EPRI
Electric Power
Research Institute

Keywords:
High-level radioactive wastes
Radioactive waste disposal
Risk assessment
Radionuclide migration
Models

EPRI TR-100384
Project 3055-2
Interim Report
May 1992

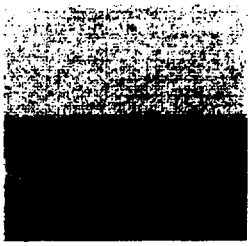

Demonstration of a Risk-Based Approach to High-Level Waste Repository Evaluation: Phase 2

Prepared by
Risk Engineering, Inc.
Golden, Colorado

REPORT SUMMARY

Demonstration of a Risk-Based Approach to High-Level Waste Repository Evaluation: Phase 2

An EPRI probability-based methodology to assess the performance of high-level nuclear waste repositories has been upgraded using realistic, credible scientific and engineering inputs. In particular, this methodology considers aqueous and gaseous pathways for release of radionuclides as well as possible releases triggered by inadvertent human intrusion and natural occurrences. Utilities and DOE can apply this methodology to identify critical technical issues that require further investigation.

INTEREST CATEGORIES

Radioactive waste management
Risk analysis, management, and assessment
Waste and water management
Waste disposal and use

KEYWORDS

High-level radioactive wastes
Radioactive waste disposal
Risk assessment
Radionuclide migration
Models

BACKGROUND With cosponsorship from Edison Electric Institute (EEI/UWASTE), EPRI revised and upgraded its high-level waste performance assessment methodology. This methodology is designed to encourage DOE to complete integrated assessments characterizing Nevada's Yucca Mountain as a prospective site for the nation's high-level waste repository. The previous phase 1 report on this project (EPRI report NP-7057) demonstrated the feasibility of a risk-based methodology and illustrated potential insights from its application.

OBJECTIVES

- To convert phase 1 results from a reasonable, illustrative model to a realistic, credible phase 2 model.
- To include new scenarios in the model, including gaseous releases; time-dependent changes in climate, infiltration, and repository temperature profile; and human intrusion.

APPROACH The project team comprised experts in climatology, surface water and groundwater hydrology, tectonics, volcanology, geochemistry, waste package design, rock mechanics, human factors, and nuclear engineering. They developed a probability-based logic tree framework for performance assessment and designated the inputs, models, and uncertainties using discrete distributions on specific input assumptions. This approach considered scientific and engineering uncertainty on the state of nature or on models and parameters used to represent future occurrences.

RESULTS The calculational methodology integrates information over all possible combinations of uncertain inputs and for each combination determines the quantity of radioactive release for 13 radionuclides. The probability distribution of releases reflects uncertainties in inputs designated by the expert in each respective field.

The methodology's calculational techniques have been applied to precipitation and surface water flow, groundwater flow, gaseous release, liquid release from the engineered barrier system, and human intrusion. The previous phase 1 model was revised to represent climate conditions, earthquake and volcanic occurrences, effect on the host rock, temperature changes, effects on the water table as a result of earthquakes, and changes in hydrologics and engineered barrier systems.

DISCLAIMER OF WARRANTIES AND LIMITATION OF LIABILITIES

ORGANIZATION(S) THAT PREPARED THIS REPORT:

RISK ENGINEERING, INC.

ORDERING INFORMATION

Requests for copies of this report should be directed to the EPRI Distribution Center, 207 Coggins Drive, P.O. Box 23205, Pleasant Hill, CA 94523, (510) 934-4212. There is no charge for reports requested by EPRI member utilities and affiliates.

ABSTRACT

This project develops and applies a probability-based methodology to assess the performance of high-level nuclear waste repositories. The particular method is an extension of the methodology demonstrated previously under Phase 1 of this project. Under the current application, aqueous and gaseous pathways for release of radionuclides are considered, as are possible releases induced by inadvertent human intrusion and by volcanic occurrences. Individual experts in the relevant scientific and engineering fields designate the inputs (and their uncertainties) for the analysis. These inputs are aggregated using the logic tree format so that calculations of levels of release for thirteen radionuclides can be made for all possible combinations of assumed input values. The probability distribution of releases reflects the uncertainties in inputs designated by the expert in each field.

The methodology is applied to the proposed repository at Yucca Mountain, Nevada. The application indicates that, for high levels of possible release, the largest quantities of nuclides will escape the repository by aqueous pathways. Gaseous release of ^{14}C may occur but will be important relative to releases by aqueous pathways only at lower levels of total release. Volcanic disturbances, earthquakes, and inadvertent human intrusion do not lead to large releases. Sensitivity studies for aqueous pathways indicate that critical factors affecting large releases are amount of groundwater infiltration, solubilities of radioelements and dissolution rate of the waste matrix, lateral diversion of the groundwater flow around the repository, characteristics of the engineered barrier system, and coupling between fracture and matrix flow.

CONTENTS

ILLUSTRATIONS

TABLES

EXECUTIVE SUMMARY

This project investigates possible releases of radionuclides that might occur from underground high-level radioactive waste repositories. The methodology developed for this purpose is an extension of that demonstrated previously under Phase 1 of this project. This methodology uses a probability-based context to quantify possible releases. Here, aqueous and gaseous pathways for release are considered, as are possible releases induced by inadvertent human intrusion and by volcanic occurrences. Individual experts in the fields of climatology, surface- and ground-water hydrology, tectonics, volcanology, geochemistry, waste package design, rock mechanics, human factors, nuclear physics, and nuclear engineering designate the inputs (and their uncertainties) for the analysis. The specific quantitative conclusions reached are a function of the input from these experts, and the overall process of probability-based performance assessment is demonstrated by the application. The inputs from the project consultants are aggregated using the logic tree format wherein discrete distributions on specific input assumptions reflect scientific and engineering uncertainty on the state of nature or on models and parameters used to represent future occurrences. The calculational methodology integrates over all possible combinations of uncertain inputs, and for each combination determines the quantity of radioactive release for thirteen radionuclides. The probability distribution of releases reflects the uncertainties in inputs designated by the expert in each field.

New calculational techniques have been advanced in several areas, from the Phase 1 study. A model of surface water flow accounts for topography, soil cover, and plant growth, giving a more physical approach to calculating net infiltration from precipitation. The groundwater flow model accounts for multiple layers and for groundwater flux that changes in time, reflecting changes from current climate conditions to pluvial conditions. The gaseous release model accounts for the release of ^{14}C as carbon dioxide, taking into account possible temperature profiles at the repository horizon caused by emplacement of radioactive waste. The source term model accounts for unsaturated, saturated, and wet-drip conditions, and accounts for the solubility limits of each radioelement and the dissolution rate of the waste_matrix. Finally, a general model of human intrusion recognizes possible changes in society, availability of knowledge about a repository site, and future value of resources, and this general model is used to derive estimates of site intrusion from drilling and excavation. In addition, previous models have been revised to represent climate conditions, earthquake and volcanic occurrences, effects on the host rock of temperature changes, effects on the water table of earthquakes and changes in hydrologic flux, and the engineered barrier system. All of these advances allow more realistic and inclusive calculations to be made of possible releases of radioactivity from a repository.

The methodology is applied to the proposed repository at Yucca Mountain, Nevada, using site-specific input assumptions designated by the consultants in each field. The application indicates that, for high levels of possible release, the largest quantities of nuclides will escape the repository by aqueous pathways. Gaseous release of ^{14}C may occur but will be important relative to releases of nuclides via aqueous pathways only at lower levels of total release. Volcanic disturbances, earthquakes, and inadvertent human intrusion do not lead to large releases. Sensitivity studies for aqueous pathways indicate that critical factors affecting the levels of nuclide release are the amount of groundwater infiltration, solubilities of radioelements and dissolution rate of the waste matrix, lateral diversion of the groundwater flow around the repository, characteristics of the engineered barrier system, and coupling between fracture and matrix flow. The possible initial pulses of release of radioelements associated with initial contact with water are also important for some radionuclides. Factors that are less important are the degree of matrix sorption, the velocity of flow in the saturated zone, repository temperature as a function of emplaced waste (the heat pulse), and the presence or absence of borehole fracturing.

Section 1

INTRODUCTION

by

Robin K. McGuire

This report summarizes the work sponsored in 1991 by the Electric Power Research Institute (EPRI) on evaluating the performance of high-level radioactive waste repositories. As in the previous application, the first objective of this effort is to develop a method to make probability-based assessments of the potential releases that might occur from a repository, and the second objective is to apply the method to the proposed repository at Yucca Mountain, Nevada. A methodology developed in the abstract matures through preliminary and subsequent applications, and it is that maturation process that we seek through the specific application for the Yucca Mountain site.

The methodology we report here relies heavily on the previous study (1) conducted under EPRI sponsorship, but extends that study in several important areas. First, the source term and thermal pulse are treated in much more detailed fashion, considering both the solubilities of radioelements and the dissolution of the waste material. Different possible temperature profiles that might occur in the vicinity of emplaced waste are also treated explicitly. This treatment allows the choice of engineered barrier system, and the estimates of possible conditions in boreholes, to be conditional on the temperature profile. Second, gaseous pathways of release are considered for ^{14}C, which is the predominant mode by which this nuclide is expected to travel to the accessible environment. Third, a model of human intrusion is included, with preliminary estimates of drilling and excavation scenarios and their probabilities. Fourth, the hydrologic transport model takes into account multiple layers of unsaturated flow and changes in flux as a function of time. Fifth, an explicit model of surface water flow and infiltration has been developed and applied that accounts for topography, soils, and vegetation. In addition to these major efforts, models of external events and the performance of the engineered barrier system have been revised and updated so that they include additional data and information. All of this brings us to performance assessment results that, while still preliminary in the sense that they are the products of single experts in each field, have the credibility associated with review, evaluation and update of models from the previous study.

Risk-based performance assessments of this type have three major purposes: (1) production of results to compare to regulatory criteria expressed in probabilistic format, (2) evaluation on a common basis of the relative importances of different data and technologies required to evaluate a site and to design and build a repository, and (3) understanding of the real performance offered by a certain repository site, and how that estimate of performance is affected by uncertainties in knowledge and data. The last is perhaps the most important objective, for it allows informed decision-making based on the safety of any particular site and based on how that perception of safety is likely to change with additional information.

This report is organized by technical area. Sections 2 through 14 discuss the scientific and engineering models that are used to create input for the performance assessment and to make calculations of releases through aqueous and gaseous pathways, through volcanic occurrences, and through human intrusion. Section 15 indicates how each of these pieces is organized into the framework for release calculations, and Section 16 presents results of application of the methodology for the proposed repository at Yucca Mountain. Conclusions from the study are stated in Section 17.

REFERENCES

1. R. K. McGuire (ed.). *Demonstration of a Risk-Based Approach to High-Level Waste Repository Evaluation*, Palo Alto, Calif.: Electric Power Research Institute, 1990. NP-7057, Research Project 3055-2.

Section 2

A PROBABILISTIC CLIMATE AND RAINFALL MODEL

by

Austin Long

INTRODUCTION

The first step in estimating the future net infiltration of water into Yucca Mountain, or any other watershed, is to assess the present-day climate and infiltration. Having established a quantitative and robust relationship between climate and infiltration under present conditions, the next step is to predict future climate conditions and how they will affect infiltration in the future. Each of these elements of the problem has its set of uncertainties, and these uncertainties are especially acute in the case of Yucca Mountain. The reasons for uncertainty in part relate to the features that make Yucca Mountain an attractive repository. For example, two of the reasons for the lack of long-term climatic data at the site are its dryness and the low population density in its vicinity. These factors are related; one of the major reasons for the low population density is the site's aridity. The site is relatively undisturbed because it is barren of economic mineralization. Infiltration would be easier to measure if boreholes or mine shafts were available for sampling and observation, but of course such disturbances would affect the permeability characteristics.

Instrumental weather records are valuable in assessing climate not only because they reveal annual averages, but also secular trends and variances in the averages. The longer the record, the better the average, and the more well-known are the variances, trends and major, low probability events. The nearest stations to Yucca Mountain began operation only in the 1950's. Thus proxy climatic indicators are necessary for defining past climates.

APPROACH TO THE PROBLEM

The lack of long-term direct measurements of meteorologic data collected at or close to Yucca Mountain requires the use of proxy indicators of climate to extend the record into the past. These paleoclimate indicators include geological deposits and paleobotanical remains. Groundwater itself can also yield paleoclimatic information. Meaningful interpretations and projections of proxy climate

data into the future must be carried out in the context of conceptual models of the meteorological processes involved and the causes of climate change. The geological record reveals that on a global scale the climate in the past was usually remarkably different from present climate. Moreover, clear periodicities of global climate change, as well as nearby paleobotanical and paleohydrological evidence suggest that Yucca Mountain was cooler and wetter at times in the past, and will experience these conditions again.

The past gives only indirect clues to how the global and local climates will respond to higher levels of greenhouse gases (CO_2, CH_4) in the atmosphere. Major DOE-sponsored efforts are directed toward the use of general circulation models (GCM's) that attempt to simulate the major global meteorologic patterns for the present, for the full glacial maximum (18ka ago) and for the present with perturbation by double the present atmospheric CO_2 content. The present study takes into account the outputs of these models in estimating the impact of greenhouse gases on Yucca Mountain climates.

This study translates the estimates of future climates into a precipitation model that simulates individual precipitation events in time, using well-known probability distributions for characterizing rain. First it simulates modern precipitation, then the model parameters for modern precipitation are adjusted to match best literature values for conditions during the full glacial maximum, about 18ka ago. Possible climatic scenarios intermediate between modern and full glacial maximum are modeled by further adjustment of model parameters.

PRESENT CLIMATE AT YUCCA MOUNTAIN

As applied here, "modern climate" means the climate that has existed for the last 10ka. Our characterization of it must include both historical and geological records. Continuous, reliable historical weather records for the Yucca Mountain vicinity extend only from the 1950's ((1), Table 2-5-1). Yucca Mountain itself has been monitored only since the mid 1980's (Alan Flint, personal communication 1991). The historical record is therefore unlikely to have registered the larger precipitation events with longer (greater than 50 years) recurrence intervals. Knowledge of these low probability events is critical to estimating net infiltration. The Holocene (last 11ka) geological record is a source of longer-term climate records. Two types of records are particularly pertinent to the question of precipitation variability during the present interglacial. One is episodic records -- those that record flood events that leave fluvial deposits at elevations higher than normal river deposits. These flood deposits can be dated and the intensity of the precipitation event estimated from the positions of the deposits (2) A more lingering episode of unusually high rainfall may leave a recharge

pulse in the groundwater, which can be radiocarbon dated. Radiocarbon dating of groundwater, though not as accurate as dating most fossils, can indicate times of recharge, hence times of more effective precipitation. The other type of paleoclimate evidence is continuous records, such as those left in lake sediments. These sediments and their fossils and isotopic content may reveal past lake levels and/or paleo salinities (3, 4).

Fluvial deposit studies by Baker and his colleagues at the University of Arizona verify that meteorological observations limited to only a few decades have not detected the major flood events that have occurred in the southwestern U.S. during the last thousand years. Their studies of flood deposits disclose increased frequencies of flooding around AD 800-1000, AD 1400-1600, and in the late 1800's (Lisa Ely, personal communication, 1991). The wide-spread nature of these deposits suggest regional rather than local climatic anomalies. Oviatt (5) interpreted fluctuating levels of lake Sevier (Utah) during the Holocene as responses to changing precipitation from westerly air masses.

Radiocarbon dating and stable isotopic analysis of groundwater in the Yucca Mountain area (6) suggests that most of the recharge to the regional aquifer in the immediate vicinity of Yucca Mountain occurred during the last glacial period, most likely by infiltration of melted snow (winter precipitation) into Forty Mile Canyon. Their study indicates that some infiltration of winter precipitation did occur during the postglacial, however, about 4000 years ago. Studies of groundwater in other arid and semiarid areas suggest episodic recharge, for example in Kenya (7) and in central Australia (8).

Sediments deposited in Lake Mojave during the past 20ka (3, 9) show evidence for pluvial conditions (higher water levels) until about 9 or 10ka ago, then interpluvial conditions (drier) to the present (Figure 2-1). The past 10ka also show several distinct episodes of pluvial-type conditions. The authors argue convincingly that these pluvial-type episodes (micropluvials) during the present interglacial represent geologically brief times, perhaps up to 100 years if varves are annual (Yehouda Enzel, personal communication 1991), during which the dominant meteorologic conditions shifted into a glacial mode. These same conditions could have brought brief pluvial intervals to the Yucca Mountain vicinity. The present Yucca Mountain model considers that if current conditions are projected into the future, the possibility exists that the climate will shift into a mode of pluvial conditions a few times per millennium. Each micropluvial might last a few decades. This probability is based on the percent of time during the past 10ka that Lake Mojave evidently experienced glacial meteorological pattern.

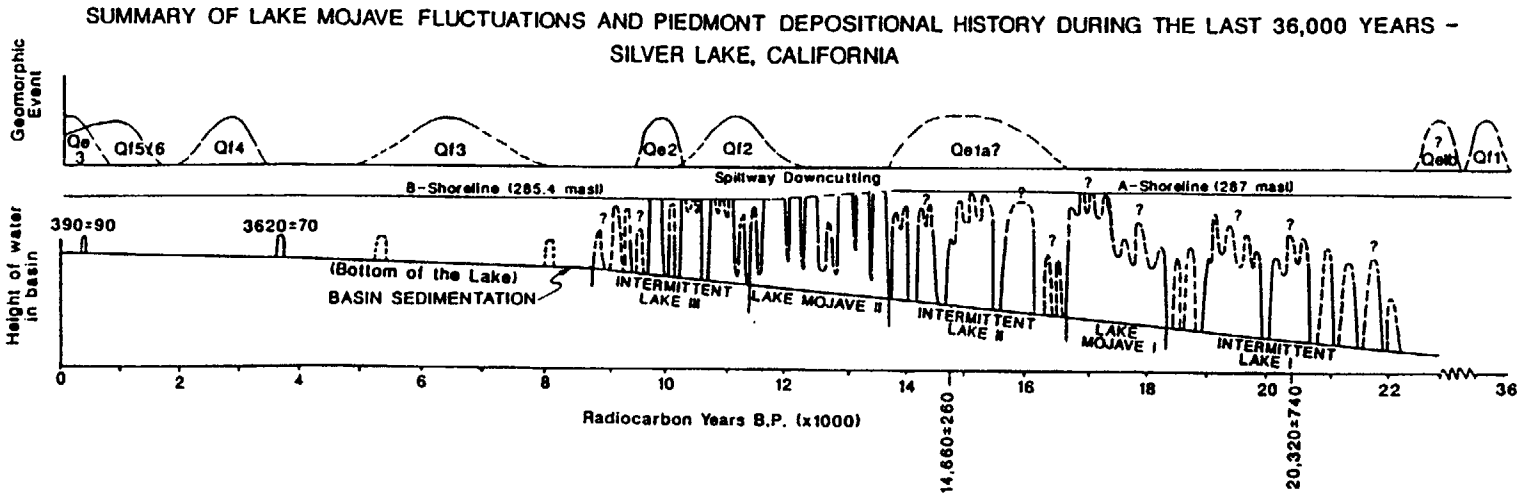

Figure 2-1. Lake Mojave sediments (from(3)).

CHARACTERIZATION OF GLACIAL CLIMATE

The Pleistocene was characterized by regular recurrence of cold periods in the high latitudes of the planet. Abundant geological and hydrological evidence supports the conclusion that glacial conditions in northern latitudes of the northern hemisphere coincided with "pluvial" climate conditions in the Great Basin of the U.S. (10, 11, 12, 13, 14). Very large lakes existed in Utah and Nevada then where merely small remnants (Great Salt Lake, Utah; Pyramid and Walker lakes, Nevada) or none at all exist today. Stable isotope measurements in ^{14}C-dated groundwater (6) and stable isotopes in groundwater-deposited carbonates (15), both in the Yucca Mountain area, suggest pluvial conditions in the vicinity during the last glacial maximum. The Winograd study further reveals several pluvial/interpluvial cycles with similar (but not exactly corresponding) periodicities that the ocean sediments recorded (Figure 2-2). Fossil spring deposits reveal groundwater discharged in southern Nevada at least during the last pluvial period (16). Fossil plant remains support the Milankovitch-based climate model's result that the pluvial regime in southwestern North American deserts was characterized by stronger westerlies and weakened monsoons (17).

Estimates of winter and summer temperature and precipitation at Yucca Mountain during the full glacial maximum (FGM) Spaulding inferred from paleobotanical remains in the Yucca Mountain area (18). His inferences are based on analysis of plant species that grew in the vicinity in the past, and the known temperature and precipitation tolerances of these species. The source of plant macrofossils was radiocarbon dated packrat middens. These values are within the range of independent estimates based on hydrologic budgets of pluvial lakes in the vicinity. Spaulding's conclusions in terms of full glacial conditions compared to today's conditions are summarized in Table 2-1.

Table 2-1

FULL GLACIAL (PLUVIAL) CONDITIONS RELATIVE TO TODAY'S CONDITIONS

Temperature		
	Winter	At least 6 C cooler
	Summer	7 to 8 C cooler
	Annual Average	6 to 7 C cooler
Precipitation		
	Winter	60 to 70% wetter
	Summer	40 to 50% drier
	Annual Average	30 to 40% wetter

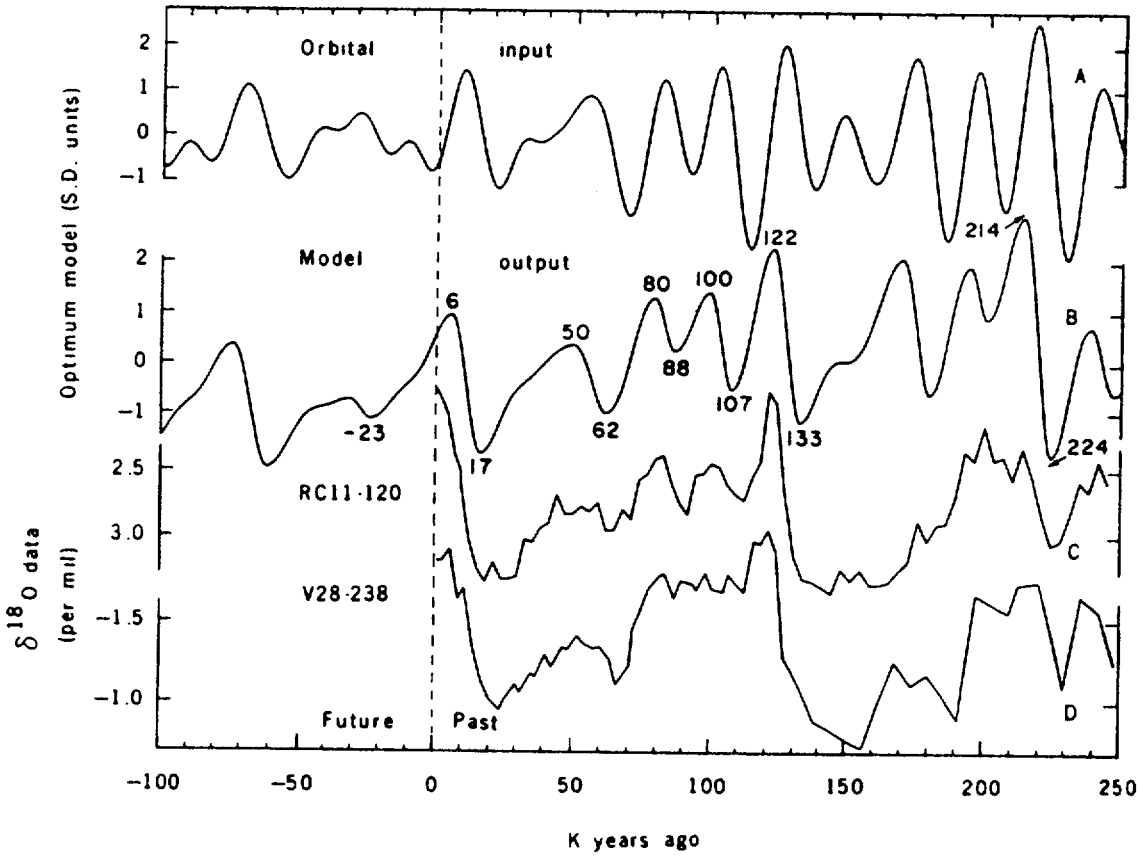

Figure 2-2. Comparison of ^{18}O records in carbonates between oceanic pelagic foraminifera and vein-filling carbonates at Devil's Hole in the Great Basin (from (15)).

PERIODICITIES OF GLACIAL/INTERGLACIAL (PLUVIAL/INTERPLUVIAL) EPISODES

Over the past 2 million years (Ma), the Pleistocene era, the Earth has experienced 17 glacial/interglacial cycles (19). These cycles consist of a 90ka duration glacial period of increasing severity followed abruptly by an interglacial of about 10ka duration. The periodicities of these cycles match periodicities in 1) the ellipticity of the Earth's orbit around the Sun, 2) the degree of the Earth's tilt with respect to the Solar orbital plane, and 3) the precession of the Earth's rotational axis (20, 21). These astronomical cycles do not change the total amount of insolation on the Earth, but do change its latitudinal distribution in time. Maximum insolation on the Northern Hemisphere occurs as glaciers begin to recede. These well-known periodicities, known as Milankovitch cycles, are considered to be triggers of the major climate changes during the Pleistocene. Smith (22) demonstrated that the long-term periodicities of lake levels in the Great Basin also registered pluvial/interpluvial conditions in coincidence with glacial/interglacial conditions in the north. Barring some major disturbance in the climate control system, the same glacial/interglacial pattern will continue into the future. As the present interglacial has lasted about 11,000 years, the onset of the next glaciation (pluvial in the Great Basin) may be considered overdue (19).

Evidence and timing for the most recent cycles derives from faunal and stable isotopic measurements in deep sea cores and stable isotopic measurements in Greenland and Antarctic ice (23). Stable isotopes in radiometrically dated groundwater (24) and in vein-filling calcite (15) (Figure 2-2) lend supporting evidence.

CHARACTERIZATION OF GREENHOUSE CLIMATE

The impact of atmospheric greenhouse gases on the future climate of Yucca Mountain is uncertain and problematic. Neither present, instrumentally measured, climatic trends, nor global circulation models (GCM's), are convincing or even in agreement about how CO_2 and other anthropogenic gases have affected or will affect climate, and if so, how they will affect climate. It is also conjectural whether the natural climatic oscillations will override the greenhouse effect, or the reverse will occur. Nevertheless, for the purposes of this risk analysis, we need to consider the possibility of a greenhouse effect on the future climate of Yucca Mountain. Again, a probabilistic approach is necessary.

The most recent precedent for atmospheric CO_2 levels at least twice pre-industrial levels occurred during the Eocene, about 30 million years ago (25). Topography and weather patterns have significantly changed since the Eocene. The Sierras were lower, consequently winter storm tracks were different from now. Because the projected atmospheric levels of greenhouse gases are

unprecedented in the Pleistocene, historic and geologic records cannot provide clear clues to greenhouse effects during interglacial times. We must rely on GCM's to suggest how greenhouse gases will affect Yucca Mountain. The models generally agree that the Earth will retain more heat with atmospheric CO_2 doubling, but disagree on how the heat will be distributed (26). Oceans are a likely sink for excess heat. Emanuel (27) has pointed out that the warmer greenhouse oceans may induce the generation of 40 to 50% more hurricanes in the Pacific off the California coast. Such deep low pressure cells migrating inland are a source of intense rain events in the southwestern U.S. now (28). Thus a possible consequence of greenhouse warming is up to 50% more rain on Yucca mountain. Additional rain from deep low pressure cells will likely be intense, tend to linger for several days and produce flooding. Carbon cycle models predict that atmospheric CO_2 could reach 475 ppm (compared to a pre-industrial level of 275 ppm, and today's level of 350 ppm) by the year 2035 (29). At that rate, doubling could occur within the next 100 years, though estimates of future CO_2 emissions as well as other sources and sinks of CO_2 have considerable uncertainty (30).

Another common element of carbon cycle models is their prediction that in a few hundred years the fossil fuels will be depleted, and in a thousand or so years natural processes will have returned the excess gases to pre-industrial levels. These natural processes include ocean circulation and carbonate deposition. Because of the compound uncertainties, it is difficult to defend estimates of the amounts or the probability that greenhouse gases will enhance rainfall on Yucca Mountain. Nevertheless, consideration is necessary, as GCM's will certainly improve and more certain assessments will ultimately become available. In this analysis we assume a rainfall enhancement, elaborated below.

THE PRECIPITATION MODEL

Based on past climatic oscillations and their regularity, and the acceptance that we understand the astronomical triggering mechanism for past climate change, we assume that these climatic oscillations will continue into the future with the same regularity. Thus, the past is the key to the future. We further assume that in the future Yucca Mountain will experience climate conditions similar to those it experienced during the Pleistocene. The best estimates, and virtually the only quantitative estimates of past climates for both winter and summer seasons in the Yucca Mountain vicinity come from Spaulding (18). (See Table 2-1.)

We cannot predict exactly when the climate will next return to glacial (pluvial) conditions. Past climatic oscillations tell us that interglacial periods, such as the one we have experienced for the last 10ka, have in the past lasted for about 10 to 12ka. The record also shows that although the changes

from glacial climate to interglacial climate have been relatively abrupt, changes from interglacial to glacial have been more gradual. An extrapolation of the past into the future would thus suggest that the onset of the next glacial period might occur within the next 1000 years, but it could take as much as 100ka to reach its fullest extent. Although past glacial periods exhibited regularity on the long term (100ka), the shorter-term climate changes superimposed on the longer-term ones prevent the past glacial periods from being exact replicas of one another. Therefore, any predictions of future conditions are necessarily probabilistic.

Even more problematic and fraught with unknowns is the impact of atmospheric greenhouse gases on the future climate of Yucca Mountain. Neither present, instrumentally measured, climatic trends, nor global circulation models, are convincing or even in agreement about how CO_2 and other anthropogenic gases have affected or will affect climate, and if so, how they will affect climate. (For a summary of the various GCM outputs for CO_2 doubling, see Grotch, (26)). It is also conjectural whether the natural climatic oscillations will override the greenhouse effect during its millennium or so of predicted effectiveness, or the reverse will occur. Again, a probabilistic approach is necessary.

The precipitation model simulates individual precipitation events in time. The model assumes that the duration of the precipitation events are exponentially distributed, and that the intensity of each event is constant throughout its duration. The model further assumes that the intensities of all the events are exponentially distributed. These assumptions are consistent with those in the precipitation model of Cowpertwait (31). The distribution of rain events in time is generally considered to be Poisson distributed (31, 32), (Entekhabi, personal communication, 1991). Thus the time between individual events will be exponentially distributed, and the time until the n^{th} event will have a gamma distribution (M. Scott, personal communication, 1991). Figure 2-3 is a representation of what the model does. Rectangular blocks represent precipitation events. Time proceeds to the right on the horizontal axis, and precipitation intensity is the vertical axis.

The model runs on the spreadsheet Lotus 1-2-3, version 2.2. The software program @RISK, an "add-in" to Lotus, performs the simulations. The model calculates time by summing the time interval between events and the duration of each event. It registers the total precipitation and the annual precipitation after each simulation trial. In addition, the model sums the precipitation events that pass a series of criteria for potential infiltration. For example, events that follow a previous precipitation event by a short time interval may be eligible for infiltration. Similarly, events that themselves exceed a minimum duration may be eligible. Note that as a consequence of this feature of the model, spacing

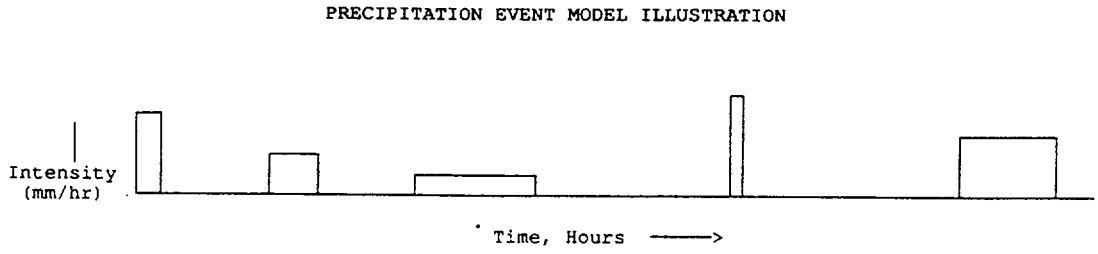

Figure 2-3. Schematic representation of the rectangular block precipitation model.

of events as well as depth of events contributes to eligibility of precipitation for infiltration. Therefore, for example, as winter precipitation increases with time into the future, the proportion (percent) of precipitation that is eligible for infiltration increases. Temperature will have a further influence on the percent of precipitation eligible for infiltration.

Simulations select values of precipitation duration, intensity and lengths of intervals according to the designated distributions using Latin Hypercube selection protocol. Though it is possible to step through the simulations one-by-one, most outputs are in the form of histograms or as seasonal and annual totals. For model simplification, years are divided into two seasons, winter (November through April) and summer (May through October).

The model has maximum built-in flexibility. Model parameters are selected to emulate as much as possible actual current conditions, then modified for the expected future climatic scenarios. Variable model parameters are:

- Average rate of winter and summer precipitation (mm/hr),
- Average time between precipitation events in winter and summer, and
- Average duration of winter and summer precipitation events.

The criteria for including an event in the summation of those eligible for infiltration (winter and summer criteria are specified separately):

- Minimum (preset) duration of current event,
- Maximum (preset) duration of previous interval, and
- Minimum (preset) duration of current event if preceded by interval of up to a preset duration.

This model allows for the fact that summer and winter precipitation events are, in general, controlled by different meteorological conditions, and consequently have different distributions. In addition, the relative contribution of winter-type and summer-type storms changed as climate changed from glacial to interglacial, and will likely change in the future. Adjustable model parameters accommodate these differences. Some evidence suggests that more than a single meteorologic configuration may produce storm events within a season. As a consequence, a single distribution function may not properly describe a summer or a winter. It is likely that major events (such as 100-yr, 500-yr storms) may not fit within same structure as the normal events.

It would not be difficult to modify the present structure to accommodate multiple distributions. One difficulty lies in obtaining the needed recurrence interval data on such long-term events. Even more vexing is the problem of assigning past events to specific meteorologic configurations.

ADJUSTMENTS OF MODEL PARAMETERS

The values for average rate of precipitation are within the range found in meteorologic records. Summer storms are generally more vigorous than winter storms. It is not clear that climate change should affect the average rates, thus this parameter was not varied with climate. The durations also reflect observations in Tucson (which receives winter and summer precipitation from the same storm track patterns as Yucca Mountain) and values in the literature. Duration may be a function of climate, but was not varied much, so that the duration, in combination with the interval between events, resulted in about the correct number of storms per year. That number for today's model precipitation is approximately 28. This number is between that of French (33), 40 days with precipitation, and that of Flint (Personal communication, 1991), about 17 precipitation events per year.

The relative amount of precipitation "today", winter vs. summer, comes from DOE/RW-0199 (1988), which shows data for seven nearby stations for the last 20 to 50 years. The differences in seasonal precipitation between today and FGM are from Spaulding (18). It should be noted that the paleobotany agrees with the GCM/CCM (general circulation model with imbedded community climate

model) for the Great Basin 18ka ago (17). The 10% and 50% FGM columns are adjusted to give precipitation 10% and 50% of the way between today and 100% FGM.

The Greenhouse scenario relies on results from GCM's. Grotch (26) summarizes the model greenhouse (double CO_2) temperature and precipitation scenarios for all major GCM's. The differences in predictions are significant. Also the grid sizes are too large to be meaningful on a local, repository-size, scale. Especially perturbing is the models' ignorance of important topographic effects, such as the Sierras (Yucca Mountain is in the Sierra's rain shadow). Nevertheless, the models show some general concordance. They mostly agree that CO_2 doubling will induce a little more rain in all seasons at this latitude. It seems likely that the summer monsoons will be more vigorous. It is also possible that with greenhouse warming Yucca Mountain will get more low pressure cells from degraded hurricanes. So the present precipitation model assumes increased precipitation in both seasons for a greenhouse scenario.

ESTIMATES OF NET INFILTRATION

Although this topic is treated from first principles in the next chapter, it was considered of interest, only for comparison, to estimate the increase in net infiltration as an add-on to the precipitation event model. The percent infiltration values (next to the last row in the first and second columns of the model) was adjusted until "today's" infiltration read 0.5 mm/yr. The other columns (climate scenarios) were given the same percentages.

RESULTS OF MODEL RUN

Table 2-2 presents the results of 10,000 iterations, and Figures 2-4 through 2-7 illustrate rainfall amount distributions for selected climate scenarios derived from the model parameters in Table 2-2.

Table 2-2

PRECIPITATION MODEL OUTPUT*

OUTPUT	TODAY-S	TODAY-W	GH-S	GH-W	FGM-S	FGM-W
Avg precip rate (mm/hr)	2	1.6	2	1.6	2	1.6
Avg duration (hr)	2.2	3.6	2.2	3.6	2.2	3.8
Avg interval (hr)	380	252	330	240	460	184
No. of seasons (years)	874	584	759	556	1055	429
Precipitation (mm/year)	49.56	99.98	58.14	103.34	37.52	142.64
Infiltration (mm/year)	0.06	0.42	0.08	0.43	0.04	0.63

*(S = summer; W = winter; GH = greenhouse; FGM = full glacial maximum)

PROBABILITIES OF THE VARIOUS CLIMATE SCENARIOS IN THE FUTURE

This section explains the probabilities listed in Table 2-3, below. Based on the sediments in Lake Mojave (3) (Figure 2-1) the estimated percent of time Yucca Mountain experienced micropluvials was about 400 years out of the past 8000, or 5% of the time. Therefore the number in cell 3 is 0.05.

A consensus of climatologists suggests that greenhouse warming will occur. They disagree on whether it has already begun, and on its most likely climatic impact. A generous estimate of skeptics would be 10%. Thus we place 0.1 in cell 1. This leaves 0.85 for cell 2. In about 1000 years the fossil fuel will have been depleted, and the oceans will have taken up most of the excess CO_2. To accommodate a sluggish recovery from the greenhouse effects, 0.02 is placed in cell 5. Micropluvials are short-lived - up to 100-year duration - pluvial climate modes. In effect, micropluvials can be represented as 5% FGM, without the global cooling. Within 10ka after the end of the previous interglacial, according to isotopic evidence from polar ice and from ocean cores, the Earth had returned to about 50% FGM. It thus seems most likely that the period between 1000 and 10ka from now will have an increasing chance of FGM as time proceeds. This increasing chance is expressed as probabilities for the whole time span. A small but finite probability exists that this time span will experience FGM.

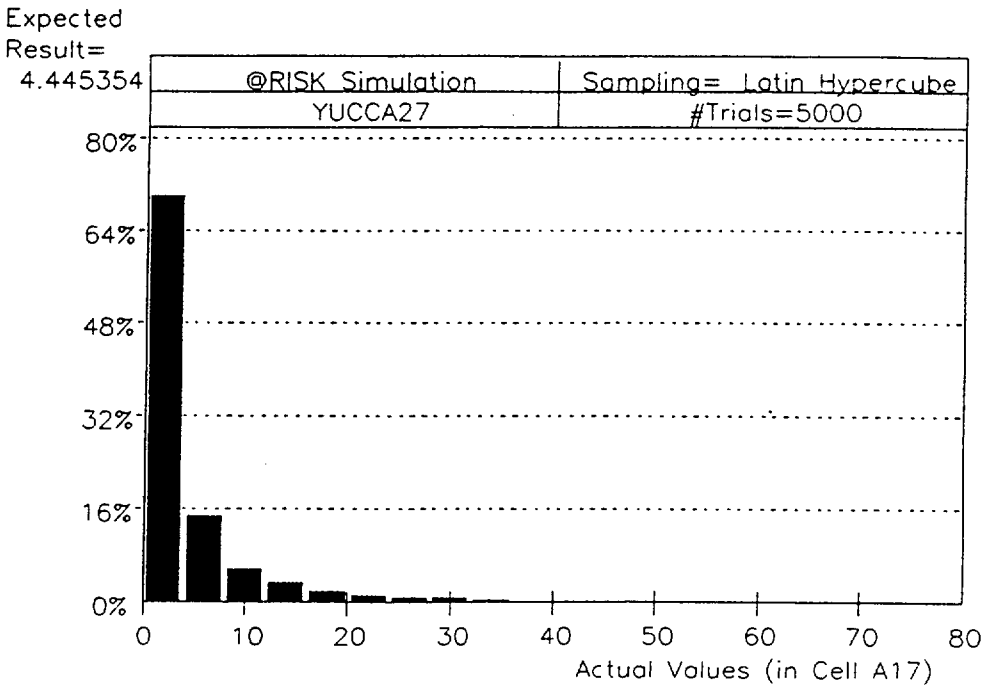

Figure 2-4. Distribution of model summer precipitation event depths, today's climate.

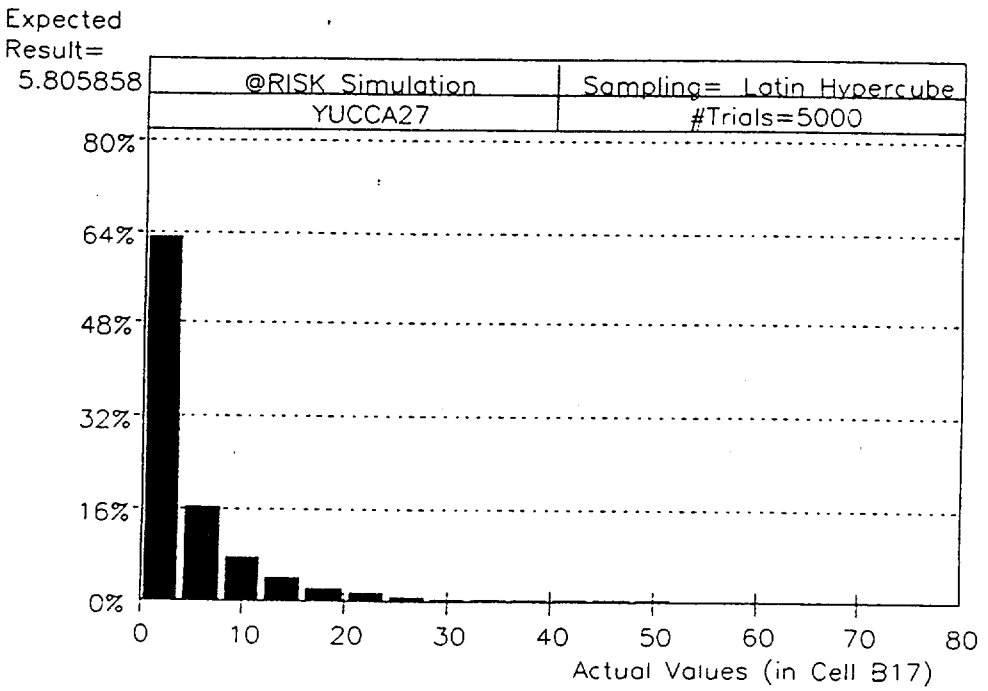

Figure 2-5. Distribution of model winter precipitation event depths, today's climate.

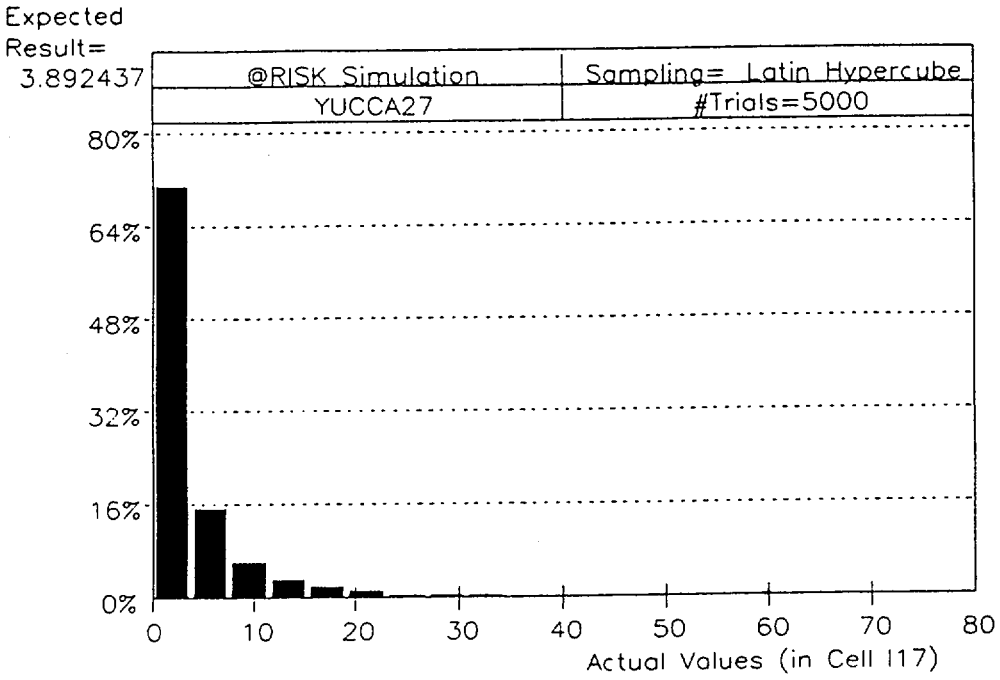

Figure 2-6. Distribution of model summer precipitation event depths, full glacial maximum.

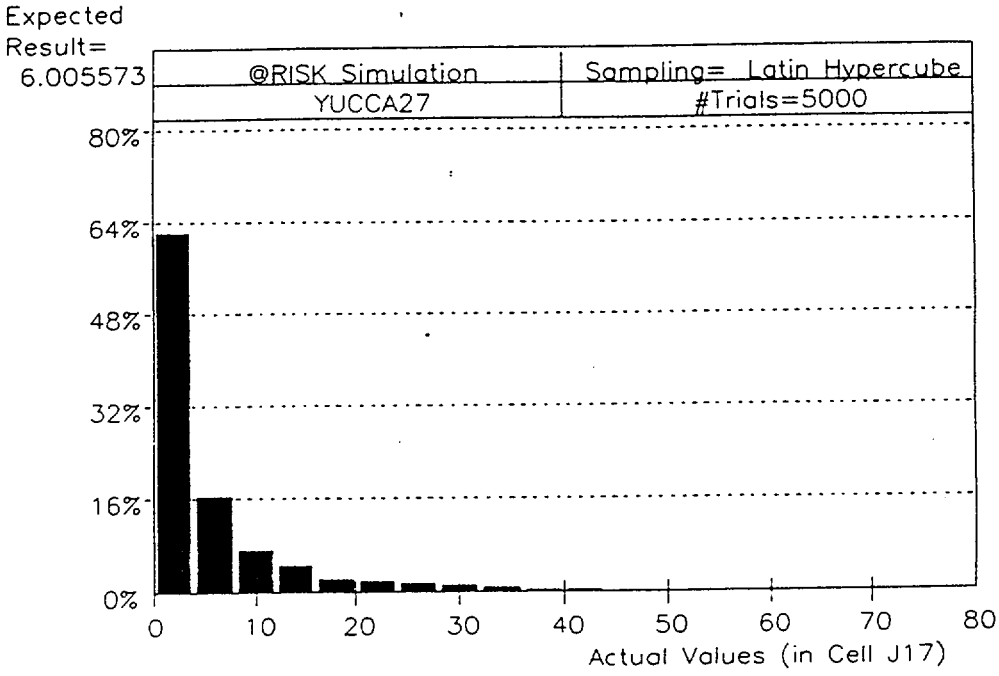

Figure 2-7. Distribution of model winter precipitation event depths, full glacial maximum.

If past rate of return to glacial (pluvial) times is a guide, the probability of FGM is taken as less than 10%. Here it is estimated it as 4%. Current conditions may resume for a while before shifting into the next pluvial. If this persists for 1000 years, then cell 4 becomes 0.1. The 50% FGM could exist for the last almost 3000 years of this 9000-yr interval (Figure 2-2), say 30%. Thus the number 0.3 is placed in cell 8. Consider micropluvials (5% FGM) to be a 1000-yr transition from current conditions to 10% FGM; thus the probability in cell 6 becomes 0.1. This leaves 0.45 for 10% FGM (cell 7). These are the values input to the Infiltration Node (Chapter 2).

DISCUSSION AND FUTURE IMPROVEMENTS

Presented here is a precipitation event model that approximates the natural system, yet runs easily on a personal computer. It employs statistical distributions of rainfall duration, intensity and timing that have been shown to match real data in other studies. The model parameters are easily adjusted to give the desired seasonal and annual precipitation. The timing and amounts of precipitation events with respect to each other, and to temperature are critical in estimating net infiltration, especially in arid and semiarid climates where potential evaporation greatly exceeds precipitation.

The present model lacks the sophistication of more advanced rainfall simulation models that emulate storm processes that account for clustering of rain cells in a frontal or convective storm system (32). The present model also does not accommodate classes of storms by weather type (34). Finally, it is likely that the extremely rare events, recorded only in the geologic record, involved storm types that do not fall within the distributions used here. Future models should accommodate these deficiencies as much as is practical given the lack of direct and proxy data available for Yucca Mountain.

Table 2-3

PROBABILITIES OF VARIOUS CLIMATIC CONDITIONS IN FUTURE*

CLIMATE	0 - 1000 yrs	1000 - 10,000 yrs
Current	(1) 0.1	(4) 0.1
Greenhouse	(2) 0.85	(5) 0.02
Micropluvial (5% FGM)	(3) 0.05	(6) 0.1
10% FGM		(7) 0.45
50% FGM		(8) 0.3
100% FGM		(9) 0.03
	1.0	1.0

*Numbers in parentheses are cell numbers discussed in text.

REFERENCES

1. DOE Site Characterization Plan. Yucca Mountain Site, Nevada Research and Development Area, Nevada, VIII Volumes, total, 1988.

2. L. L. Ely and V. R. Baker. "Large Floods and Climate Changes in the Southwestern United States." In *Hydraulics and Hydrology of Arid Lands, Proceedings of an International Symposium July 30 - August 2, 1990.* R.H. French (ed.). New York, NY: American Society of Civil Engineers, 1990, pp. 361-366.

3. S. G. Wells, R. Y. Anderson, L. D. McFadden, W. J. Brown, Y. Enzel, and J.-L. Miossec. *Late Quaternary Paleohydrology of the Eastern Mojave River Drainage, Southern California: Quantitative Assessment of the Late Quaternary Hydrological Cycle in Large Arid Watersheds.* Technical Completion Report, New Mexico Water Resources Research Institute, May 1989, 253 pp.

4. S. C. Fritz, S. Juggins, R. W. Battarbee and D. R. Engstrom. Reconstruction of past changes in salinity and climate using a diatom-based transfer function. *Nature*, vol. 352, 1991, pp. 706-708.

5. C. G. Oviatt. "Late Pleistocene and Holocene lake fluctuations in the Sevier Lake Basin, Utah, USA." *Journal of Paleolimnology*, vol.1, 1988, pp. 9-21.

6. L. Benson and H. Klieforth. "Stable Isotopes in Precipitation and Ground Water in the Yucca Mountain Region, Southern Nevada: Paleoclimatic Implications." In *Aspects of Climate Variability in the Pacific and the Western Americas*, David H. Peterson (ed.), Geophysical Monograph 55, 1989, pp. 41-59.

7. F.J. Pearson, Jr. and W. V. Swarzenki. "^{14}C Evidence for the Origin of Arid Region Groundwater, Northeastern Province, Kenya." *Proceedings of the Symposium on Isotope Techniques on Groundwater Hydrology.* Vienna: IAEA, 1, 1974, pp. 95-109.

8. G.E. Calf. "The Isotope Hydrology of the Mereenie Sandstone Aquifer, Alice Springs, Northern Territory, Australia." *Journal of Hydrology*, vol. 38, 1978, pp. 343-355.

9. Y. Enzel, R. Y. Anderson, W. J. Brown, D. R. Cayan and S. G. Wells. "Tropical and Subtropical Moisture and Southerly Displaced North Pacific Storm Track: Factors in the Growth of Late Quaternary Lakes in the Mojave Desert." In *Proceedings of the Sixth Annual Pacific Climate (PACLIM) Workshop*. J. L. Betancourt and A. M. MacKay (eds.). Asilomar, Calif.: 1990, pp. 135-139.

10. W. S. Broecker and Aaron Kaufman. "Radiocarbon Chronology of Lake Lahontan and Lake Bonneville II, Great Basin." *Geological Society of America Bulletin*, vol. 76, 1965, pp. 537-566.

11. L. V. Benson. "Paleoclimatic Significance of Lake-level Fluctuations in the Lahontan Basin." *Quaternary Research*, Vol. 16, 1981, pp. 390-403.

12. F. Street-Perrott, A. Harrison and S. P. Harrison. "Temporal Variations in Lake Levels Since 30,000 yr BP - An Index of the Global Hydrological Cycle." In *Climate Processes and Climate Sensitivity*, J. E. Hansen and T. Takahashi (eds.). Washington, DC: American Geophysical Union, 1984, pp. 118-129.

13. R. J. Spencer, M. J. Baedecker, H. P. Eugster, R. M. Forester, M. B. Goldhaber, B. F. Jones, K. Kelts, J. Mckenzie, D. B. Madsen, S. L. Rettig, M. Rubin and C. J. Bowser. "Great Salt Lake and Precursors, Utah: The Last 30,000 Years." *Contrib. Mineral. Petrol.*, Vol. 86, 1984, pp. 321-334.

14. L. Benson and Robert S. Thompson. "The Physical Record of Lakes in the Great Basin." In *North America and Adjacent Oceans During the Deglaciation*. W. F. Ruddiman and H. E. Wright, Jr. (eds.). Boulder, CO: Geological Society of America, The Geology of North America, vol. K-3, 1987.

15. I. J. Winograd, B. J. Szabo and T. B. Coplen. "A 250,000-Year Climatic Record from Great Basin Vein Calcite: Implications for Milankovitch Theory." *Science*, vol. 242, 1988, pp. 1275-1280.

16. J. Quade and W. L. Pratt. "Late Wisconsin Groundwater Discharge Environments of the Southwestern Indian Springs Valley, Southern Nevada." *Quaternary Research*, vol. 31, 1989, pp. 351-370.

17. W. G. Spaulding and L. J. Graumlich. "The Last Pluvial Climatic Episodes in the Deserts of Southwestern North America." *Nature*, vol. 320, 1986, pp. 441-444.

18. W. G. Spaulding. "Vegetation and Climates of the Last 45,000 Years in the Vicinity of the Nevada Test Site, South-Central Nevada." *U.S. Geological Survey Professional Paper 1329*, 1985, 83 pages.

19. H. W. Ellsaesser. "Atmospheric Carbon Dioxide and the Climatic Record." In *Proceedings of the Sixth Annual Pacific Climate (PACLIM) Workshop*, J. L. Betancourt and A. M. MacKay (eds.). Asilomar, Calif.: 1990, pp. 5-18.

20. J. Imbrie and K. P. Imbrie. *Ice Ages: Solving the Mystery.* Short Hills, NJ: Enslow Publ., 1979, 224 pp.

21. J. Imbrie and J. Z. Imbrie. "Modeling the Climatic Response to Orbital Variations." *Science*, vol. 207, 1980, pp. 943-953.

22. G. I. Smith. "Paleohydrologic Regimes in the Southwestern Great Basin, 0 - 3.2 m.y. ago, Compared with Other Record of 'Global' Climate." *Quaternary Research*, vol. 22, 1984, pp. 1-17.

23. G. Faure. *Principles of Isotope Geology*, 2nd edition. NY: John Wiley and Sons, 1986, 589 pp.

24. F. M. Phillips, L. A. Peeters and M. K. Tansey. "Paleoclimatic Inferences from an Isotopic Investigation of Groundwater in the Central San Juan Basin, New Mexico." *Quaternary Research*, vol. 26, 1986, pp. 179-193.

25. A. C. Lasaga, R. A. Berner and R. M. Garrels. "An Improved Geochemical Model of Atmospheric CO_2 Fluctuations over the Past 100 Million Years." In *The Carbon Cycle and Atmospheric CO_2: Natural Variations Archean to Present.* E.T. Sundquist and W. S. Broecker (eds.). Geophysical Monograph 32, 1985, pp. 397-411.

26. S. L. Grotch. "Regional Intercomparisons of General Circulation Model Predictions and Historical Climate Data. 1988, DOE/NBB-0084, 291 pp.

27. K. A. Emanuel. "The Dependence of Hurricane Intensity on Climate." *Nature*, vol. 326, 1987, pp. 483-485.

28. T. F. Saarinen, V. R. Baker, R. Durrenberger and T. Maddock, Jr. *The Tucson, Arizona Flood, of October 1983.* Washington, DC: National Academy Press, 1984.

29. J. F. B. Mitchell. "The 'Greenhouse' Effect and Climate Change." *Reviews of Geophysics*, vol. 27, 1989, pp. 115-139.

30. DOE/ER-0239, 1985.

31. P.S. P. Cowpertwait. "Further Developments of the Neyman-Scott Clustered Point Process for Modeling Rainfall." *Water Resources Research*, vol. 27, 1991, pp. 1431-1438.

32. D. Entekhabi, I. Rodriguez-Iturbe and P. S. Eagleson. "Probabilistic Representation of the Temporal Rainfall Process by a Modified Neyman-Scott Rectangular Pulses Model: Parameter Estimation and Validation." *Water Resources Research*, vol. 25, 1989, pp. 295-302.

33. R. H. French. *Daily, Seasonal, and Annual Precipitation at the Nevada Test Site, Las Vegas, Nevada.* Las Vegas, NV: Water Resources Center, Desert Research Institute, 1986, DOE/NV/10384-01, 57 pp.

34. L.E. Hay, G. J. McCabe, Jr., D. M. Wolock and M. A. Ayers. "Simulation of Precipitation by Weather Type Analysis." *Water Resources Research*, vol. 27, 1991, pp. 493-501.

Section 3

NET INFILTRATION: MODEL AND CALCULATIONS

by

Stuart W. Childs

INTRODUCTION

Performance assessment of potential high-level waste repository sites involves characterization of a number of site specific processes. As part of a larger demonstration project on repository site evaluation methodology (1), net infiltration was estimated using a probabilistic approach based on a climatological analysis, assessment of surface hydrology, and numerical simulation of the infiltration process. This Section describes calculation procedures used to assess likely effects of changing climate on the surface factors affecting net infiltration: plant community dynamics, spatial variability of soil properties, runoff-infiltration relations, evapotranspiration, and patterns of local climate.

Background

This present work was initiated after initial work by a multidisciplinary team showed that repository performance was sensitive to net infiltration estimates (1). That effort used the U.S. Department of Energy proposed repository site at Yucca Mountain, Nevada as an example for calculations. The site and the surrounding area has been studied extensively and excellent work has been done to develop a conceptual model of the unsaturated water flow environment (2, 3). In addition, field studies of unsaturated zone processes have been thorough (4, 5, 6, 7). A combination of these two approaches would be of benefit for better determining the likely range in net infiltration so that repository performance can be more accurately assessed.

A number of methods have been used to estimate net infiltration at Yucca Mountain and elsewhere. The simplest method involves assuming that a fraction of average annual precipitation becomes net infiltration (8). This approach ignores a number of details but is a useful method, especially when compared with other methods using observations that, by their nature, integrate over space, time, or both. Examples of such observations include use of spring flow data, geological observations, radiocarbon dating, paleobotany, and regional hydrologic analyses (see Chapter 2 of reference 1 for

a detailed summary of this approach). Such observations clearly demonstrate that net infiltration occurs and has varied in magnitude with time. More sophisticated analyses of climate have incorporated storm temporal distribution, intensity; and magnitude (1) or have made detailed correlations with biogeographical data (9, 10).

There have been a number of net infiltration estimates made for the Southern Nevada region. These include a variety of techniques (see 6 for a review) such as the use of chlorine tracers (11), field measurements (6, 7), tritium tracers (12), a variety of theoretically based approaches (2, 3), and analysis of climate data (1, 8). Although there is investigation currently underway (4), at present there are no detailed measurements or calculations that use a soil/plant/climate water balance approach. Field measurements have been made in support of such activities (4, 6, 12) but the combination of a physically-based model with long term climate evaluations has not yet been completed.

Objectives and Approach

The objectives of this project were to:

1. Develop a defensible and realistic conceptual model for calculating infiltration.

2. Implement a version of the model that addresses climatic variability, spatial variability, first priority physical/biological processes, and uncertainty.

Development of the conceptual model and prioritization of key factors were primary objectives. In order to accomplish these, a reasonable calculation output for the proposed Yucca Mountain repository site was required. This element of realism focused model development and provided a basis for evaluation of model assumptions as they were developed and tested.

Calculations of net infiltration can be accomplished based on models covering a wide range of complexity. For our purposes, it was important to incorporate a large array of factors in the conceptual model. Within this detailed framework, a calculating procedure was developed. The procedure emphasized factors considered to be of primary importance and de-emphasized the remaining ones for this phase of investigations. In addition, the model incorporated probability estimates of the factors and parameters specified. This was done to facilitate evaluation of model results in terms of risk analysis.

Net infiltration estimates were made for two time periods: 0 to 1,000 years and 1,000 to 10,000 years. These time periods were selected following an analysis of likely climatic occurrences based on review of past history and results of global climate modeling (see Section 2 of this report for details of this evaluation). Calculations incorporated uncertainty in several ways. The probability of various climate scenarios was directly incorporated. In addition, model calculations of water flow in soil were made for a 134 year period of variable climate conditions. This allowed consideration of compensating factors affecting year to year changes in soil/site properties. It also provided explicit assessment of likely variability in annual net infiltration.

The following sections outline the conceptual model used for this project. In addition, assumptions and calculation procedures are described. The basic components of the net infiltration modeling process used are:

1. Physical and biological processes affecting soil water flow. A numerical model of water flow was used to simulate unsaturated zone water flow through the soil profile, plant canopy water uptake, surface water runoff, plant canopy growth dynamics, and daily climate conditions.

2. Variability of climate. Climate effects on net infiltration were addressed by identifying likely climates for the next 10,000 years. These were characterized by annual precipitation, amount of annual precipitation falling between November 1 and April 30, and average annual air temperature. Details of climate modeling are in Section 2 of this report.

3. Spatial variability of net infiltration. This issue was addressed by identifying soil/hydrologic land units in the study area and developing a procedure for a real integration of net infiltration fluxes. The study area was the proposed repository location at Yucca Mountain (Figure 3-1).

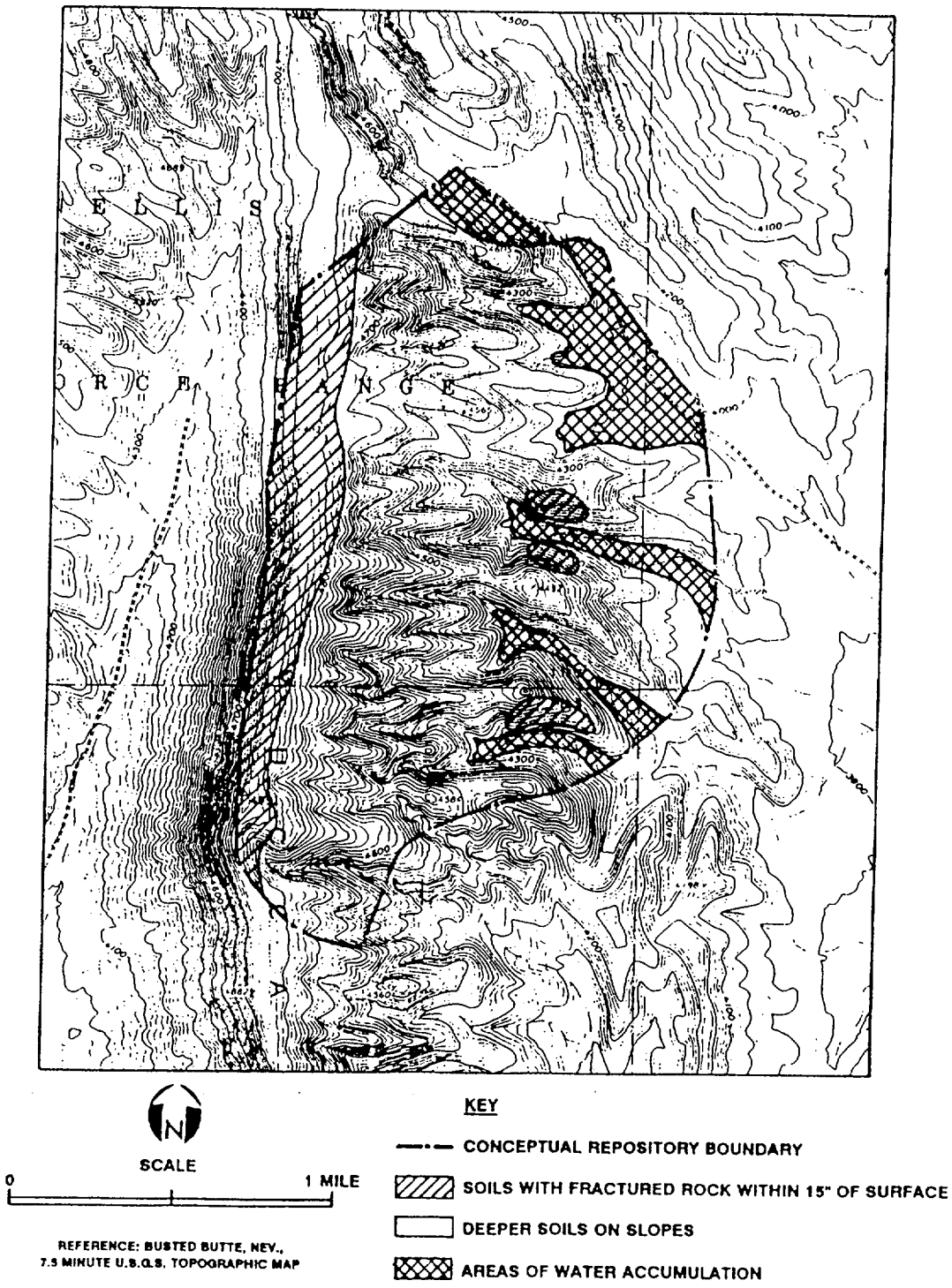

Figure 3-1. Soil/Hydrologic Units of the Proposed Yucca Mountain Repository Site.

PHYSICAL AND BIOLOGICAL PROCESSES AFFECTING NET INFILTRATION

The basis of the net infiltration conceptual model used here is a soil water budget including detailed treatment of climate. This process-oriented approach was selected because it addresses the factors known to be important. Implementation of the model required explicit treatment of spatial variability and climate variations. These are discussed below. The other factors treated were incorporated in a numerical model of soil water flow. The model, input data requirements, and calculation protocol are described below.

Soil Water Flow Model

A soil water flow model incorporating surface hydrology, soil water flow, drainage, and evapotranspiration was used for calculations. The one dimensional model of Childs and others was selected (13). This code is based on the Richards equation, the governing law for water flow in the unsaturated zone, and is appropriate for isothermal water flow through the soil matrix. Selection of this calculation approach forced a simplified treatment of the flow processes known to occur. Use of one dimensional calculations was considered appropriate because the treatment of spatial variability (see Section 3.4 of this paper) reduced the need to address lateral flow here. Spatial averaging of soil hydraulic properties and soil depth was incorporated to lessen the need to specifically address macropore or crack flow. These phenomena are known to contribute to the overall heterogeneity of the Yucca Mountain area and are particularly important below the surface few meters (14). Calculations presented here do not include thermally driven flow. Although water vapor transport is important in unsaturated zone crack flow and in near-surface soil water redistribution, it was judged to have only small impacts on profile drainage calculations made at soil depths between 0.35 and 3 meters depth.

The relationship between climate and net infiltration is indirect but of primary importance for model predictions. The soil water budget model incorporates much of the process level detail that affects precipitation when it reaches the soil/vegetation surface. Runoff, plant transpiration, direct evaporation, and infiltration into the soil profile are all treated. Calculations are made for time periods shorter than 24 hours in order to incorporate mathematical treatment of diurnal phenomena known to be of importance.

Important concepts of the soil water budget modeling procedure are summarized in Table 3-1 and additional details can be found in Childs and others (13). Background climate data requirements were high because treatment of long term and short term variability was judged to be very important. Long

Table 3-1

COMPONENTS OF NET INFILTRATION CONCEPTUAL MODEL

COMPONENT	FACTORS	SCALES REQUIRED	IMPLEMENTATION
BACKGROUND			
Climate	Precipitation, Energy Budget	Daily	Precipitation event descriptions (Duration, intensity, time between events). Use temperature as a surrogate for the energy budget.
Soil Properties	Matrix and macro pore hydraulic properties,	Arbitrary, but smaller	3 units soil/hydrologic with average hydraulic properties, depth, surface conditions.
Vegetation	Composition, leaf area and cover. Phenology. Rooting depth, water uptake pattern. Response to climate change.	Repository scale Soil profile scale Annual	Shrub and grass/forb caregories defined. Annual changes based on soil storage in September.
WATER BUDGET			
Precipitation	Storm pattern, winter vs. summer conditions.	Daily	Event description for 134 years used in simulations of 5 climate scenarios.
Evapotranspiration	Direct surface evaporation, plant water uptake from depth	Diurnal	Average annual air temperature for 134 years for each climate scenario. Average monthly extremes fit to current recorded patterns, daily values vary randomly. Solar radiation model and ET equation, % cover used to separate evaporation and plant uptake.
Infiltration/Runoff	Topography, vegetative cover, soil properties	Precipitation event	3 soil/hydrologic units with individual characteristics.
Soil Water Storage	Cracks and macropores, soil depth, hydraulic	Diurnal flow calculations	Average properties for 3 soil conditions. Numerical and solution to unsaturated flow equation, depth dependent sinks for root water extraction.
Drainage	Drainage equals NET INFILTRATION when averaged over a period of interest.	Daily with annual averaging	Sink term below the matrix flow zero-flux plane and maximum rooting depth.

term changes in climate were estimated and short term variations were incorporated by using precipitation event strings rather than annual averages. This approach incorporated large magnitude precipitation events that strongly influence the magnitude of net infiltration. Soil and vegetation properties of the site were annually averaged but process details were retained so that time and depth effects could be modeled. The water flow model used a time step shorter than one day so that diurnal soil water flow and evapotranspiration dynamics could be incorporated.

Net infiltration was calculated as the drainage term of the soil water balance. For each soil/hydrologic unit modeled, the drainage term was calculated at a depth below the root zone assumed for shrubs and grass. On occasions when daily rainfall exceeded soil profile storage, a fraction of the excess was assumed to runoff. The remainder was added to drainage.

Water flow modeling was performed for 134 realizations of annual conditions for each climate regime evaluated. This approach was adopted because the sequence of yearly climatic conditions affects net infiltration. For instance, several wet years (or wet winters) in a row are more likely to result in net infiltration than a series of alternating wet and dry years. This occurs because dry years deplete soil water storage, and wet years must fill the soil water storage reservoir before deeper percolation occurs.

VARIABILITY OF CLIMATE

Variability in climate is a primary factor determining the amount and distribution of net infiltration. For the purposes of this model, variability was evaluated in three stages to account for the important issues affecting net infiltration (see Section 2 of this report for more detail). First, likely climate scenarios were developed for the next 10,000 years. Next, these scenarios were quantified using available data on the local area, current climate, past climate, and principles of climate/storm event modeling. A model for each scenario was used to generate daily input data for the soil water flow model. The climate scenarios selected for analysis are summarized in Table 3-2. The annual characterizations shown in the table are, in fact, outcomes of the event based model used to assemble synthetic climate records for modeling. The averages for precipitation were calculated using strings of events developed in the following way:

1. Distributions of average storm intensity, average duration of event, and average time between successive events were assumed to be exponential. Also, different distributions were assumed for summer and winter conditions.

2. The six distributions for each of five climate scenarios were used to generate lists of 2000 events for summer and winter conditions. This was accomplished using a sampling software package (@RISK, Palisades Corp, Newfield, New York).

3. For each climate scenario, events were grouped into years based on the running sum of storm and between-storm durations. The shortest event string covered 134 years; this length of record was used for all climate scenarios.

Table 3-2

GENERAL CHARACTERIZATION AND PROBABILITIES FOR SIX PRESENT AND FUTURE CLIMATE TYPES

Climate Scenario	Annual Precipitation mm	Annual Precipitation % Falling November - April	Average Annual Air Temperature	Occurrence Probability 1 - 1,000 years	Occurrence Probability 1,000 - 10,000 years
Current Conditions	149.8	67	16	0.10	0.10
Greenhouse Climate	162.2	65	19	0.85	0.02
Micropluvial*				0.05	0.10
10% Full Glacial Maximum	153.2	69	15	----	0.45
50% Full Glacial Maximum	166.1	73	13	----	0.30
100% Full Glacial Maximum (FGM)	181.2	79	9	----	0.03

*This climate is considered to have of the same characteristics as 100% FGM but lasting only 30 to 50 years.

Air temperature inputs were also required for the water flow model. These were developed based on the annual values (Table 3-2) and converted to monthly values using the shape of the annual variation in monthly average temperature data provided by French for the region (15). Daily values were estimated using a random number generator to assign departures of up to 3 C from the monthly mean. The same random number was used to assign a value of percentage clear sky for use in the solar radiation model.

SPATIAL VARIABILITY OF NET INFILTRATION

Soil, geologic, and topographic factors affect the distribution of net infiltration at Yucca Mountain. The factors of most importance are soil depth, soil structure, bedrock properties, slope, and rainfall distribution. Maps of topography and geology are available for the area (16) but information about soil properties and distribution is less well documented. Some detailed studies have been performed but no detailed soil map is available (4, 5).

French and Flint have provided some information about variation in rainfall patterns including distribution of annual total precipitation from east to west and as a function of elevation (15, 17). Trends of increasing rainfall with elevation and decreasing rainfall from west to east have been noted for the Nevada Test Site as a whole. For the smaller study area of Yucca Mountain, these trends are not likely to be distinctive. For the purposes of this study, rainfall was assumed to be equal for all locations within the conceptual repository boundary.

Spatial variation of physical factors affecting net infiltration was addressed by mapping the project area using available information rather than employing more sophisticated terrain analysis methods (18). This was done using the USGS topographic map as a base and overlaying soils information, geologic information and inferences based on one visit to the site. The following soil/hydrologic units were mapped:

1. SHALLOW: Soils with bedrock within 0.35 m of the surface. These soils are typified by the shallow, flat lying soils along the ridgetop of Yucca Mountain. Soils range from 0 to 0.5 m depth and overlie fractured bedrock. Textures are loamy and soils are rocky, especially near the bedrock contact. These were delineated on the basis of slope and geology. Some steeply sloping areas of shallow soils (or exposed bedrock) were also included in this unit.

2. SLOPES: Moderately deep soils on sideslopes. This unit covers most of the proposed repository. Soils are 0.5 to 2 m deep and occur on a wide range of slopes. These areas are fairly well vegetated but are susceptible to storm runoff and erosion. Soils are loamy at the surface but generally exhibit a caliche layer at 0.2 to 0.5 meters depth. This zone has finer soil texture and is less permeable.

3. BASINS: Deep soils in areas of hydrologic accumulation. These soils tend to be somewhat finer textured and occur in small basins at the lower elevations of the study area. They are mapped as alluvium on the geology map and could also be delineated by slope. These are commonly regarded as primary areas for net infiltration and groundwater recharge in desert environments (19).

The distribution of the three soil/hydrologic units is shown in Figure 3-1. Areas mapped and physical properties estimated for each are shown in Table 3-3. Each soil unit was assumed to have a sandy loam texture with 20 percent rock fragments (30 percent for the shallow soil). The fraction of precipitation that exceeded soil storage for a given storm event was assumed to be runoff, to remain in the soil temporarily or to drain below the root zone. In addition, increased runon was assumed for the basin unit. The increase was based on standard Soil Conservation Service runoff curve methodology (20), and measured values of desert conditions in Israel (21). For the basin soil unit, daily rainfall events greater than 2 mm were assumed to provide runon equal to the total storm precipitation amount minus 2 mm. For the other soil units, runon and runoff were assumed to combine for zero net increase in water supply over the precipitation amount. No mass balance of precipitation was attempted because it was assumed that runoff events in washes would move water beyond the study site boundary.

Table 3-3

PROPERTIES OF SOIL/HYDROLOGIC UNITS

	Soil/Hydrologic Unit		
Properties	Shallow	Slopes	Basins
Percentage of Acreage Identified	17.5	70	12.5
Average Soil Depth, mm	0.35	1.5	3
Fraction of Water above Soil Storage Capactiy that is runoff	0.7	0.5	0.5
Fraction of water above Soil Storage Capacity that is net infiltration	0.02	---	0.02

MODEL CALCULATIONS AND RESULTS

Model calculations were made for 5 climate scenarios and 3 soil/hydrologic units. For each of these 15 combinations, a 134 year numerical simulation was run. Annual net infiltration for each year was calculated. Table 3-4 gives means and standard deviations for the calculations. These values incorporate effects of year to year variability, storm patterns, sequences of wet and dry years, and other variations expected in climate patterns. In fact, annual average precipitation had a coefficient of variation (standard deviation divided by the mean) of approximately 33% for each climate scenario. This variation was similar to the variation in net infiltration for the slopes soil/hydrologic unit. The variations for the shallow and basin units were much larger. The model calculated more widely-varying net infiltration because factors other than annual precipitation were incorporated in net infiltration calculations.

The relationship among net infiltration magnitudes for the three soil/hydrologic units showed interesting trends (Table 3-4). Average net infiltration is greater for the shallow soil unit than for the basin. This is different from conventional wisdom (e.g., 19) because basin locations are commonly considered to be the major locations for infiltration. In the case of a very shallow soil in an environment with small storms, the relatively small depth to bedrock allows percolation below the root zone. When basin sites accumulate runoff, they cause rather large infiltration events. This can be seen in Figure 3-2. Although average net infiltration is higher for the shallow unit, the largest annual infiltration values occur at the basin sites during wet years. That is, basin net infiltration is largest in wet years but net infiltration from shallow areas is largest in dryer years.

Figure 3-2 also serves to demonstrate the trends between net infiltration and annual precipitation. For each soil/hydrologic unit, there is a linear trend with scatter. The slope unit is lowest and least variable while the other two units have larger increases in net infiltration as precipitation increases.

INTEGRATION OF MODEL RESULTS

Soil/Hydrologic Units

Model results for the three soil/hydrologic units were combined to yield net infiltration estimates for the entire repository area. Although a number of procedures could be used, we chose to use a simple

Table 3-4

AVERAGE NET INFILTRATION FOR 3 SOIL/HYDROLOGIC UNITS AND FIVE CLIMATE SCENARIOS[1]

Climate	Mean Annual Rainfall, mm	SHALLOW Mean (Std. Dev.)	SLOPES Mean (Std. Dev.)	BASIN Mean (Std. Dev.)
Current	150.3	1.9(1.3)	0.6(0.2)	1.6(1.4)
Greenhouse	161.7	2.1(1.2)	0.6(0.2)	1.9(1.4)
-10% FGM[2]	152.7	3.0(2.0)	0.6(0.2)	2.3(2.0)
50% FGM	166.9	4.7(2.7)	0.6(0.2)	3.2(2.6)
100% FGM	180.7	7.2(4.4)	0.7(0.2)	5.0(4.0)

[1]Values shown are based on 134 year model simulations.
[2]Full Glacial Maximum

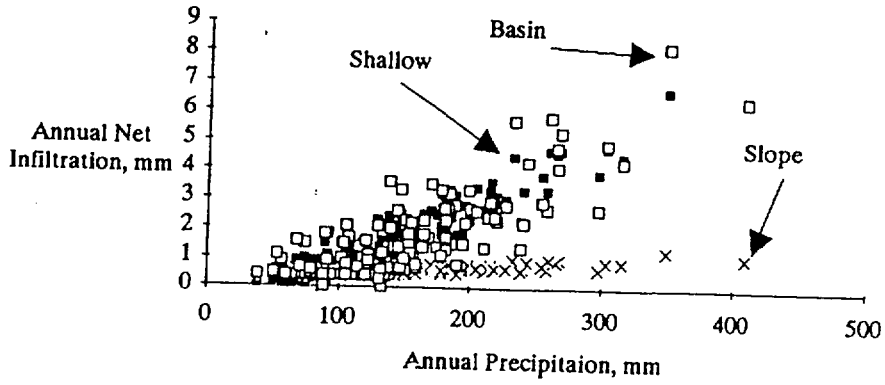

Figure 3-2. Relationship of Annual Precipitation to Net Infiltration for Three Soil/Hydrologic Units and Current Climate Conditions (134 Years shown).

weighted average of the three units based on acreage fractions. This relatively simple approach is consistent with an assumption of some subsurface mechanism for lateral water flow that makes vertical infiltration equal at all locations. There is some justification for this based on observations of subsurface stratigraphy (4).

The results of weighted averaging of the three soil units is shown in Table 3-5. Net infiltration ranges from slightly less than 1 mm/yr to more than 2.3 mm/yr for full glacial conditions. This range is large primarily because of increases in net infiltration from 30 percent of the repository area (shallow soils and basins). Net infiltration from the slopes soil unit is almost constant for the five climate scenarios modeled. Note that the coefficient of variability for net infiltration ranges from 47 to 58 percent while that for precipitation ranges from 30 to 43 percent.

Figure 3-3 shows the relationship between areal net infiltration and precipitation for two climate scenarios. The linear trends are more evident because the effect of large variability of the shallow and basin soil units has been de-emphasized by the weighting procedure. The difference between the precipitation distributions for the two scenarios is clear but both climates have similar high precipitation outliers in their 134 year simulations.

Table 3-5

NET INFILTRATION VALUES FOR FIVE CLIMATE SCENARIOS

	NET INFILTRATION, mm		RAINFALL, mm	
Climate	Mean	Standard Deviation	Mean	Standard Deviation
1. Current	.93	.52	150.3	64.8
2. Greenhouse	1.02	.48	161.7	58.7
3. 10% FGM*	1.23	.70	152.7	57.85
4. 50% FGM	1.65	.88	166.9	50.32
5. 100% FGM	2.35	1.36	180.7	58.06

*FGM = Full Glacial Maximum

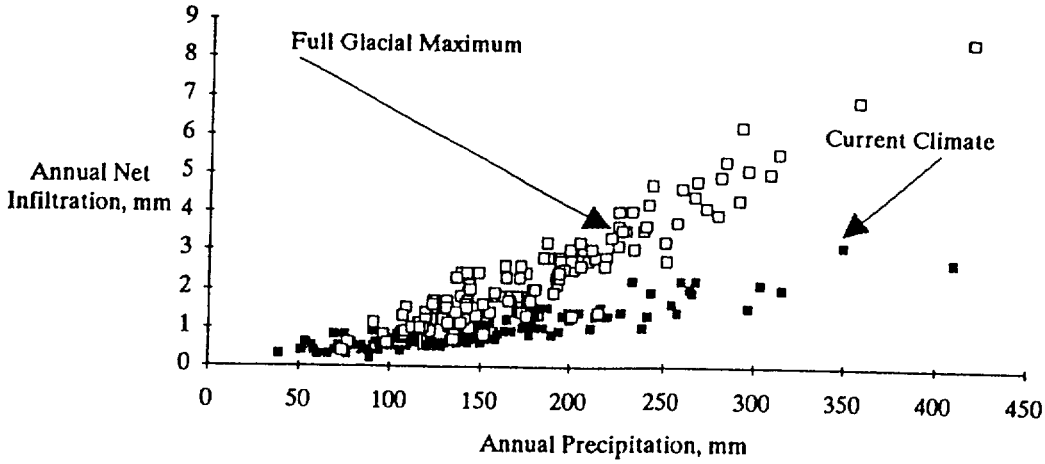

Figure 3-3. Relationship of Annual Precipitation to Net Infiltration for Two Climate Scenarios (134 years shown).

Climate Characterizations

Two climate characterizations were developed based on the climate scenarios simulated with the soil water flow model: 0 to 1,000 years and 1,000 to 10,000 years. These climates were constructed based on occurrence probabilities for the five climate scenarios (see Table 3-2). The 0 to 1,000 year climate was assumed to be dominated by greenhouse conditions while the 1,000 to 10,000 year climate had a higher probability that glacial conditions would occur. Net infiltration probability distributions were developed for these two time periods by sampling from the net infiltration distributions for the component climate scenarios. Two thousand samples were taken according to the occurrence probability proportions shown in Table 3-2. The distribution of net infiltration for the 1,000 to 10,000 year period is shown in Figure 3-4. For purposes of modeling net infiltration, this distribution was broken up into three categories as shown in Figure 3-5. A single value of 0.9 mm/yr was chosen for the 0 to 1,000 year climate because the range of net infiltration was relatively small.

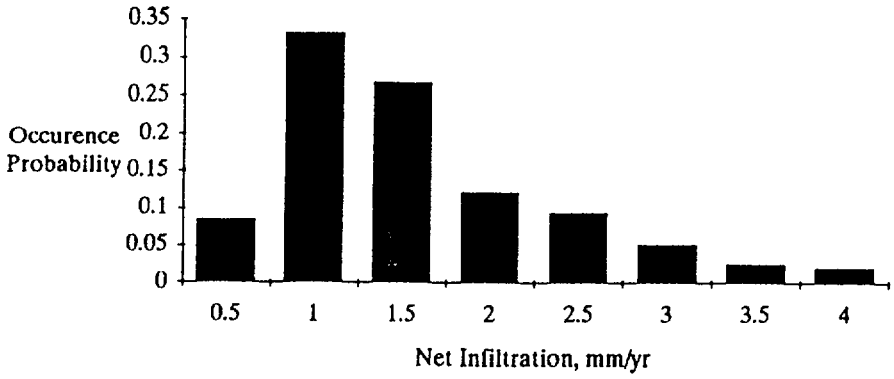

Figure 3-4. Distribution of Predicted Net Infiltration for 1,000 to 10,000 Years.

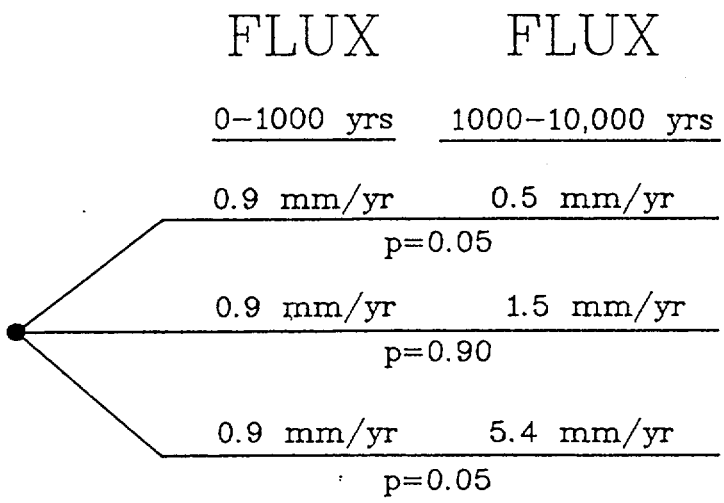

Figure 3-5. Net Infiltration Values and Probabilities.

SUMMARY AND CONCLUSIONS

A physically realistic soil water flow model was implemented as part of an effort to make realistic calculations of net infiltration. This was coupled with an analysis of soil/hydrologic units for the proposed Yucca Mountain repository site and a detailed characterization of likely climate for the next 10,000 years. This approach resulted in net infiltration calculations that incorporate areal and temporal

variability. In addition, the calculations incorporate uncertainty in terms of probability distributions for net infiltration outcomes.

The method used here for estimating climate conditions and patterns incorporates several important components. First, climate projections were made for five likely present and future scenarios. The likelihood of each was estimated to provide occurrence probabilities. Second, the precipitation model was based on events rather than annual characterizations of climate. Process based climate characterizations were used with a probability distribution to assemble a realistic weather pattern including precipitation (with different winter and summer patterns), air temperature, evaporation, and solar radiation.

The treatment of soil physical and biological factors provided an adequate conceptual model for net infiltration. Although the implementation of the model was not detailed, the structure of calculations could be revised as necessary.

The use of three soil/hydrologic units provided the opportunity to show how various combinations of physical factors result in different patterns of net infiltration. Both the shallow and basin soil units had large and variable net infiltration amounts. The relationship of each to annual precipitation was different but both combined to show larger average net infiltration values for the repository than the slopes soil unit. The differences are significant for the evaluation of likely repository performance.

REFERENCES

1. R. K. McGuire (ed.). *Demonstration of a Risk-Based Approach to High-Level Waste Repository Evaluation*, Palo Alto, Calif.: Electric Power Research Institute, 1990. NP-7057, Research Project 3055-2.

2. P. Montazer and W. E. Wilson. *Conceptual Model of Flow in the Unsaturated Zone, Yucca Mountain, Nevada.* U.S. Geological Survey Water-Resources Investigation Report, 1984, 84-4345, 55 pp.

3. S. Sinnock, T. T. Lin and J. P. Brannen. *Preliminary Bounds on the Expected Post-closure Performance of the Yucca Mountain Repository Site, Southern Nevada.* Sandia National Laboratories, Technical Report SAND 84-1492, 1984, 82 pp.

4. A. L. Flint. *Characterization of Unsaturated-Zone Infiltration.* Study Plan for Study 8.3.1.2.2.1 of U.S. Department of Energy, Office of Civilian Radioactive Waste Management, Washington DC, 1990.

5. M. R. Schmidt. "Classification of Upland Soils by Geomorphic and Physical Properties Affecting Infiltration at Yucca Mountain, Nevada." M. S. Thesis, Colorado School of Mines, Golden, CO, 1988, 116 pp.

6. K. D. Leary. "Analysis of Techniques for Estimating Potential Recharge and Shallow Unsaturated Zone Water Balance Near Yucca Mountain, Nevada." M. S. Thesis, University of Nevada, Reno, 1990.

7. D. R. Cable. 1980. "Seasonal Patterns of Soil Water Recharge and Extraction on Semi-Desert Range." *Journal of Range Management*, vol. 33, 1980, pp. 9-15.

8. P. Watson, P. Sinclair and R. Waggoner. "Quantitative Evaluation of a Method for Estimating Recharge to the Desert Basins of Nevada." *Journal of Hydrology*, vol. 31, 1976, pp. 335-357.

9. P. Neilson. "High-Resolution Climatic Analysis and Southwest Biogeography." *Science*, vol. 232, 1986, pp. 27-34.

10. R.P. Neilson, G. A. King, R. L. DeVelice, J. Lenihan, D. Marks, J. Dolph, B. Campbell, G. Glick. *Sensitivity of Ecological Landscapes and Regions to Global Climatic Change*. Report prepared for U.S. Environmental Protection Agency. EPA/600/3-89/073, 1989.

11. A. E. Norris, K. Woflsberg, S. K. Gifford, H. W. Bentley, and D. Elmore. "Infiltration at Yucca Mountain, Nevada, Traced by 36Cl." *Nuclear Instruments and Methods in Physics Research*, 1987, p. 376-379.

12. S. W. Tyler. "Review of Soil Moisture Flux Studies at the Nevada Test Site, Nyle County, Nevada." Desert Research Institute Publication 45058, University of Nevada, 1987.

13. S. W. Childs, C. Costello, and A. L. Flint. 1987. "A Soil Balance Model for Partitioning Water Use Among Crop Trees, Evaporation, and Competing Vegetation." Forest Hydrology and Watershed Management. In *Proceedings of the Vancouver Symposium*, August, 1987, Publ. no. 167. pp. 387-399.

14. G. Bloomsberg, R. E. Williams, and J. L. Osiensky. "Distribution of downward flux in unsaturated heterogeneous hydrogeology environments." *Geol. Soc. Am. Bull.*, vol. 101, 1989, pp. 1623-1630.

15. R. H. French. "Daily, Seasonal, and Annual Precipitation at the Nevada Test Site, Nevada." Water Resources Center, Desert Research Institute, DOE/NV/10384-01, 1984, 40 pp.

16. R. B. Scott and J. Bonk. *Preliminary Geologic Map of Yucca Mountain with Geologic Sections, Nye County, Nevada*. U.S. Geological Survey Open-file Report 84-494, 1984, 9 pp.

17. A. L. Flint. *Characterization of the Meteorology for Regional Hydrology*. Study Plan for Study 8.3.1.2.1.1 of U.S. Department of Energy, Office of Civilian Radioactive Waste Management, Washington, DC, 1991.

18. I. D. Moore and R. B. Grayton. "Terrain-Based Catchment Partitioning and Runoff Prediction Using Vector Elevation Data." *Water Resources Research*, vol. 27, 1991, pp. 1177-1191.

19. D. Hillel and N. Tadmor. "Water Regime and Vegetation in the Central Negev Highlands of Israel." *Ecology*, vol. 43, 1962, pp. 33-41.

20. Soil Conservation Service. *Engineering Handbook.* Washington, DC, 1972.

21. K. R. Jones. *Arid Zone hydrology for Agricultural Development.* Rome, Italy: United Nations, FAO Irrigation and Drainage Paper 37, 1981.

Section 4

CLIMATE-RELATED CHANGES IN THE WATER TABLE

by

Frank W. Schwartz

SCOPE OF EVALUATION

An important issue that technical evaluation of the Yucca Mountain site must address is how regional groundwater conditions might change in response to a changing climate. In particular, the water table position is a key variable because the engineered and geologic barriers to contaminant transport will be most effective when the rocks are unsaturated. Thus, a rising water table in the future in response to changing climates could substantially change the performance of the repository system.

Relatively few studies have examined the question of how the water table has changed in the past and may be expected to change in the future. Our analysis at this stage relies on this existing work, which is discussed below. The particular node of the logic tree that represents water table change due to climate change is discussed in detail below in "Description of the Node."

REVIEW OF EXISTING INFORMATION

Figure 4-1 illustrates the hydraulic head distribution in the upper part of the zone of saturation (1). Generally this distribution also reflects the present configuration of the water table. As the figure illustrates, the regional gradients for flow are variable. Zones of low hydraulic gradient northeast and southeast of the proposed repository are separated by a zone with relatively high gradient in the immediate vicinity of the proposed repository. This same tendency for zonation in the hydraulic gradient is also evident on a regional basis (2). Indications are (1, 3) that the water table configuration at Yucca Mountain is controlled by local variations in the hydraulic conductivity field.

Two kinds of analyses have been undertaken to estimate the extent of water table change in response to a return to the pluvial conditions. The first examines direct field evidence of water table positions during past glaciations. Winograd and Doty (4), for example, determined the distribution of historical groundwater discharge in relation to existing discharge features for the regional carbonate aquifer

system. The presence of tufas and calcite veins in sediments indicate that during the Late(?) Pleistocene discharge occurred 14 km northeast of the Ash Meadow at altitudes approximately 50 m higher than present (4). Calculations point to a maximum rise of 6 to 90 meters in the carbonate aquifer beneath central Frenchman Flat with a rise during the Wisconsin of not more than 30 m. These estimates of water table change are not directly transferable to Yucca Mountain, but help constrain the magnitude of estimates. More recently, Levy (5) examined the distribution of vitric and zeolitized tuffs at Yucca Mountain together with the structural history of the site. He found that the highest water levels occurred more than 11.6 myr ago. The water table since probably has not risen more than 60 m above its present location (5).

An alternative approach to the assessment of the historical evidence is to utilize a regional flow model to predict the water table response to an increase in infiltration flux. The area involved in such a study is that shown in Figure 4-1. The modeling assumed a 100 percent increase in precipitation, which is would correspond to extreme changes based on information from reconstructed paleoclimates (see Sections 2 and 3). Flux increases as a consequence of this increased precipitation ranged generally from two times to more than twenty times the present-day values and were greatest along Fortymile Wash. The simulation predicts a maximum rise in the water table of about 130 m at the proposed repository (1). In summary, both of the site-specific analyses of water table rise (1, 5) indicate that during pluvial conditions the water table will in all likelihood remain below the repository.

DESCRIPTION OF THE NODE

The node representing the changes in the water table is conditional on infiltration, as shown in Figure 4-2. The upper branch represents no change in water table given that infiltration is 0.5 mm/yr. The central set of nodes indicates an 0.6 probability of a 60 m rise in the water table given infiltration of 1.5 mm/yr, and an 0.4 probability of no change. Finally, the extreme infiltration of 5.4 mm/yr will likely lead to Levy's (5) value of 60 m rise (with 0.8 probability), but water table changes of + 130 m and + 230 m are also considered (with probabilities of 0.19 and 0.01, respectively). The last value is assumed to flood one-half of the repository, as the current proposed location of the repository block lies 200 to 400 m above the current water table.

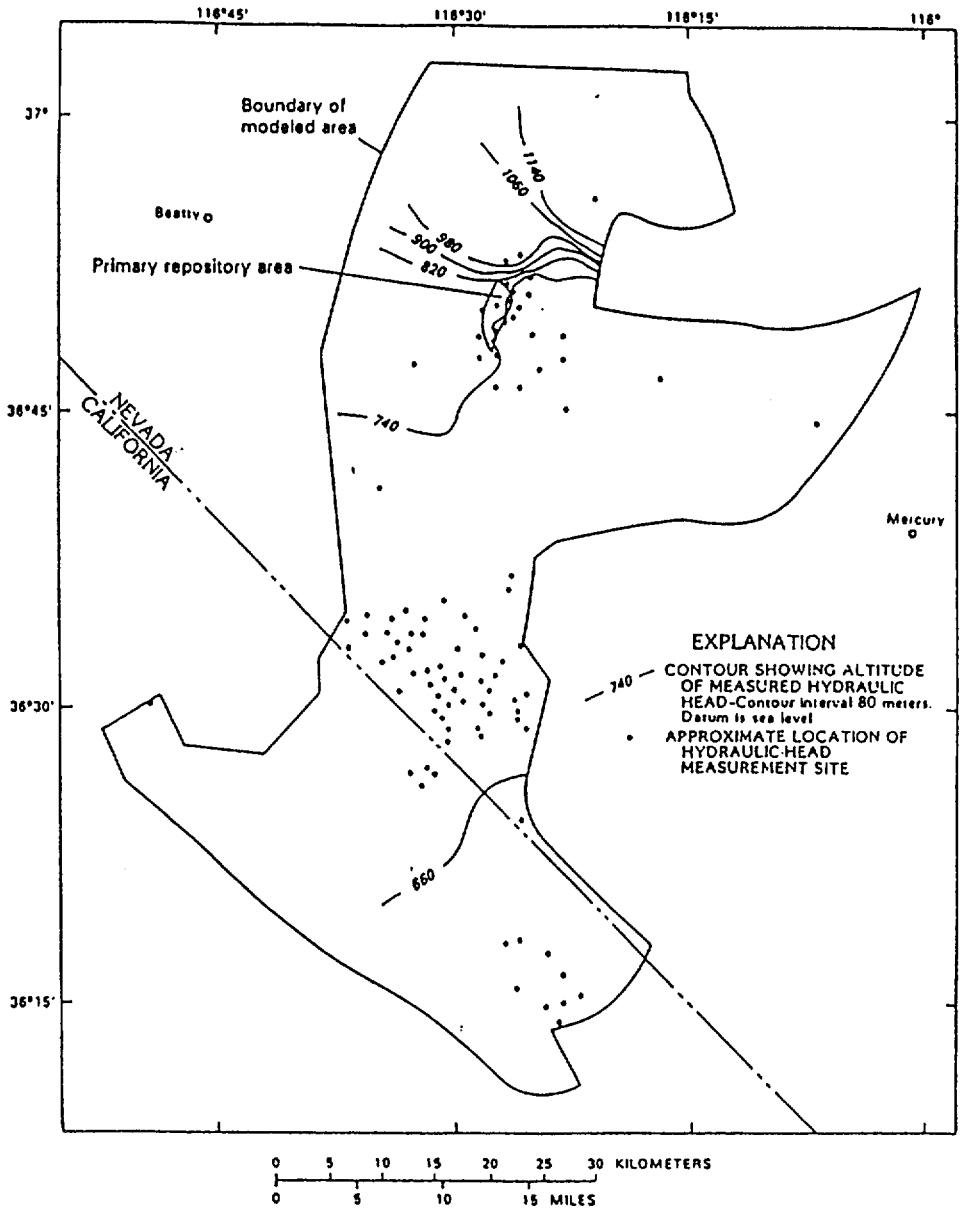

Figure 4-1. Map showing the configuration of the water table in the vicinity of Yucca Mountain (from Czarnecki, (1)).

The probabilities assigned to the bottom three branches of Figure 4-2 reflect our belief that the mineralogical data at this point provide a more reliable estimate than the model-derived estimates. Thus, larger and larger departures from Levy's (5) estimate of a maximum rise of 60 m are assigned smaller and smaller probabilities. The actual values assigned to the probabilities remain very

uncertain. At this stage of the site investigation, there are no data available to define the probabilities with more confidence. Although the probability of a water table rise of 230 m to flood the repository is low, this particular case is included to represent this extremely important condition in the overall analysis.

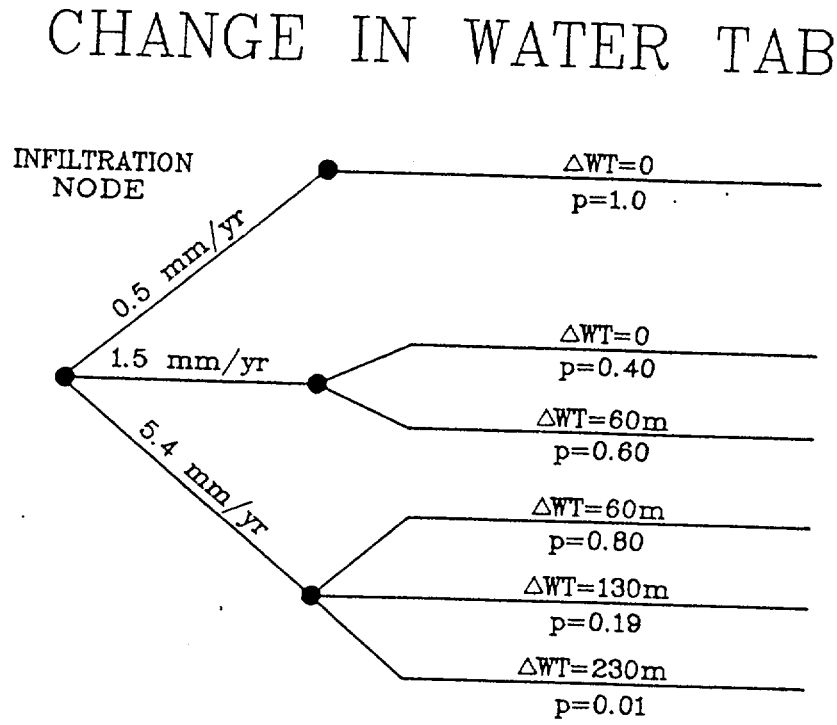

Figure 4-2. Logic tree node depicting uncertainty in change in water table.

REFERENCES

1. J. B. Czarnecki. *Simulated Effects of Increased Recharge on the Ground-Water Flow System of Yucca Mountain and Vicinity, Nevada-California.* USGS-WRI-84-4344, 1985, p. 33.

2. I. J. Winograd and W. Thordarson. *Hydrogeologic and Hydrochemical Framework, South-Central Great-Basin, Nevada-California, with Special Reference to the Nevada Test Site.* U.S. Geological Survey Professional Paper 712-C, 1975, p. 26.

3. J. S. Szymanski. *Conceptual Considerations of the Yucca Mountain Groundwater System with Special Emphasis on the Adequacy of this System to Accommodate a High-level Nuclear Waste Repository.* Draft Report, Dept. of Energy, Nevada Operations Office, 1989, 3 volumes.

4. I. J. Winnograd and G. C. Doty. *Paleohydrology of the Southern Great Basin with Special*

Reference to Water Table Fluctuations Beneath the Nevada Test Site During the Late(?) Pleistocene. U.S. Geological Survey, Open-file Report 80-569, 1980, p. 87.

5. S. S. Levy. "Mineralogic Alteration History and Paleohydrology at Yucca Mountain, Nevada." *Proc. Intern. High Level Radio. Waste Conference, Las Vegas*, 1991, pp. 477-485.

Section 5

EARTHQUAKES AND TECTONICS

by

Kevin J. Coppersmith and Robert R. Youngs

SCOPE OF EVALUATION

The objective of the earthquake and tectonics part of the model is to represent, in a physically realistic way, the magnitude, location, and likelihood of earthquake occurrence in the vicinity of the repository and the resulting effects on repository performance. The primary hazard associated with earthquakes is considered to be canister failure caused by fault rupture through the repository. Fault rupture includes movement that may occur on recognized primary faults as well as secondary faulting that may occur in the vicinity of primary faults along minor or unrecognized faults. The earthquake process is modeled by considering the activity of various faults, the three-dimensional geometry of known faults, their earthquake recurrence characteristics, and locations and displacements of fault rupture relative to the three-dimensional geometry of the repository. Knowledge and uncertainty regarding the behavior of faults is incorporated through the use of logic trees, and the pattern and amount of fault displacement is depicted by simulation of earthquakes and associated ruptures.

The basic model constructed for this analysis consists of two parts: (1) a seismic source model that defines the location, size, and frequency of earthquakes, and (2) a fault rupture model that simulates primary and secondary ruptures in three-dimensions to arrive at the likelihood of various lengths of faulting through the repository and amounts of displacement. The first part of the model is a rather standard fault-specific source characterization model that might be the first part of a probabilistic seismic hazard analysis. The details of this model were presented previously (1) and remain unchanged.

The second part of the model, which simulates the occurrence of fault displacements, has been revised in the current application. The basic approach used is the same as that developed previously, but revisions were made to the relationships used to specify the distribution and amount of secondary faulting that may be associated with a normal faulting earthquake. These revised relationships are

based on analysis of a secondary faulting database developed for this study. The database is described in Appendix A.

EVALUATION OF SECONDARY FAULTING POTENTIAL

Earthquake Source Model

Figure 5-1 shows the location of the faults that have been mapped or inferred in the vicinity of the repository. These faults are considered to be the sources of potential future significant earthquakes. Each fault was characterized in terms of its activity, geometry, maximum magnitude, and frequency of earthquake generation. The logic tree formulation shown in Figure 5-2 was used to model the uncertainty in the source characterization parameters for each of the faults. Detailed descriptions of the individual source parameters and the bases for the values selected are presented in (1). The resulting average earthquake recurrence relationships developed for each fault are shown in Figure 5-3.

Frequency of Fault-Displacement Induced Canister Failure

The primary earthquake related hazard is considered to be rupture of the waste containers induced by fault displacement. The observation of many historical surface fault ruptures often indicates that the map-view width of the zone of faulting during an earthquake is not restricted to a narrow zone along the primary fault, but is a fault zone that is several meters to kilometers wide. The rupture along the coseismic fault is termed "primary" rupture, and the zone of faulting away from the primary fault is termed "secondary" rupture. In the context of the repository, there is concern about both primary and secondary rupture for faults that actually transect the repository (the Ghost Dance fault), and secondary fault rupture associated with all faults in the site vicinity.

The formulation used to estimate the frequency of canister failure, ν_{CF} is:

$$\nu_{CF} = \sum_{n} \alpha_n(m^\circ) \int_{m} f(m) \cdot E[N_{CF}(\,|\, m \text{ on fault } n)]\, dm \qquad (5\text{-}1)$$

where $\alpha_n(m^\circ)$ is the frequency of earthquakes on fault n with magnitudes greater that a minimum magnitude of interest, m°, $f(m)$ is the density function describing the relative frequency of various magnitude earthquakes, and $E[N_{CF}(\,|\, m \text{ on fault } n)]$ is the expected number of canister failures in the repository given an earthquake of magnitude m on fault n. Parameters $\alpha_n(m^\circ)$ and $f(m)$ come directly from the earthquake occurrence model for the faults and are described by the earthquake recurrence curves shown in Figure 5-3. Parameter $E[N_{CF}(\,|\, m \text{ on fault } n)]$ is a function of the length of faulting in the repository during an earthquake, the density of canisters within the repository, and the amount

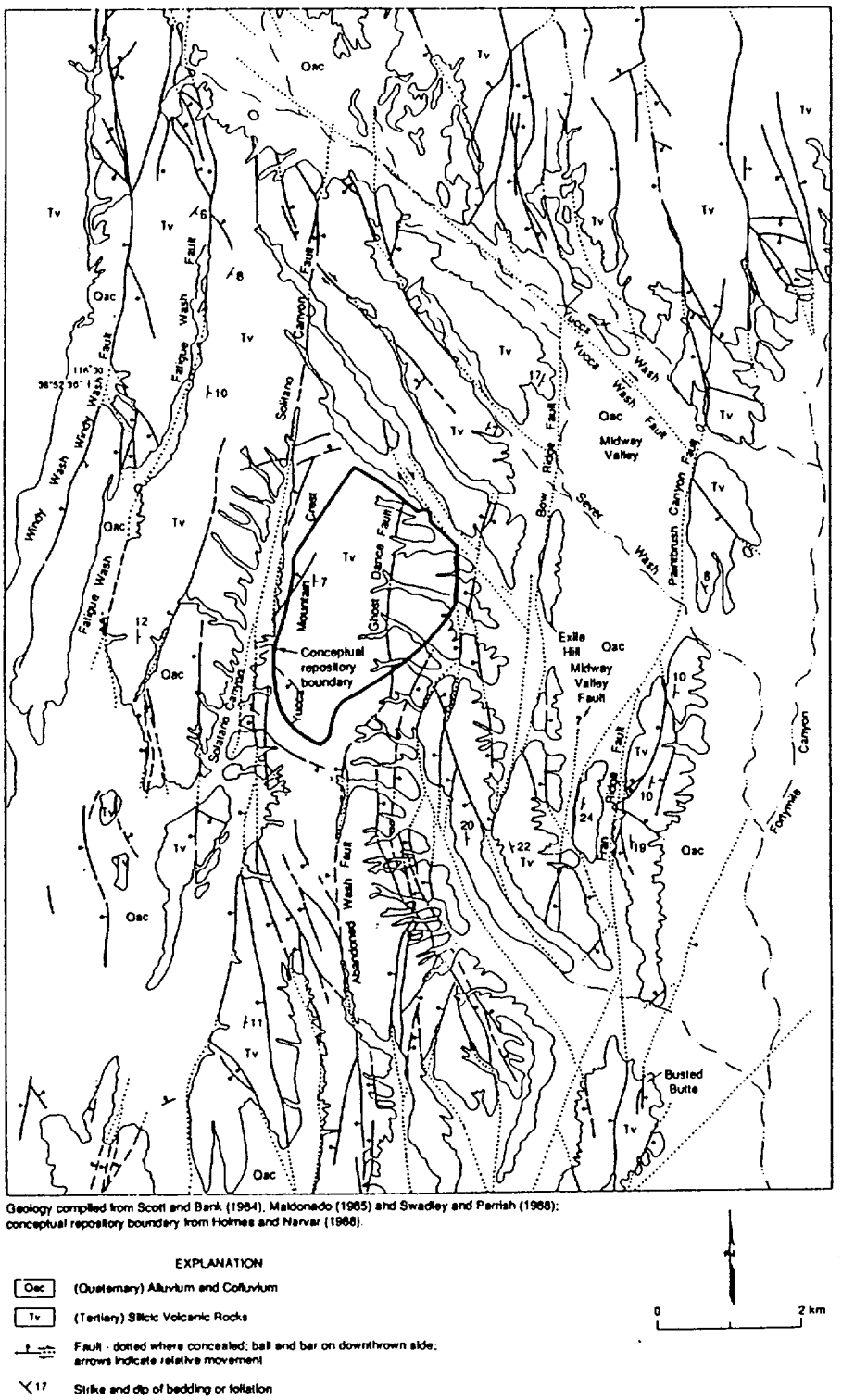

Geology compiled from Scott and Bonk (1984), Maldonado (1985) and Swadley and Parrish (1988); conceptual repository boundary from Holmes and Narver (1988).

Figure 5-1. Location map of faults considered in assessment of potential fault rupture in repository.

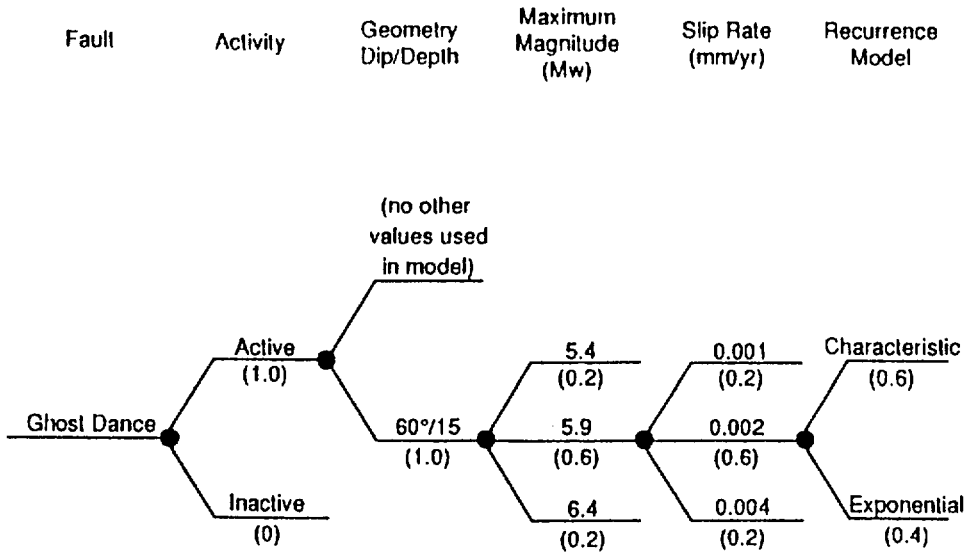

Figure 5-2. Earthquake logic tree for Ghost Dance fault.

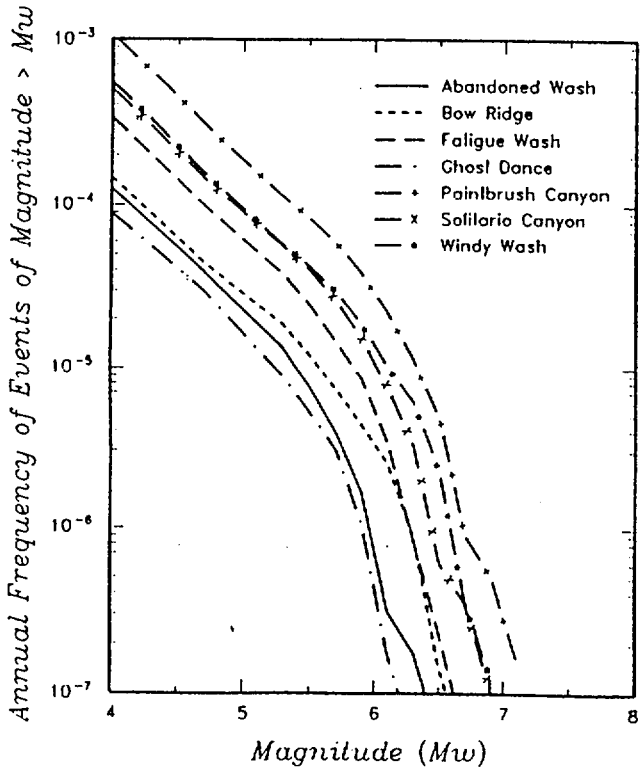

Figure 5-3. Predicted earthquake recurrence relationships for faults considered in this study.

of displacement necessary to rupture a waste canister.

The method used to estimate the number of canisters failed by an earthquake of magnitude m is illustrated schematically in Figure 5-4. Assuming vertical canister placement, then the zone over which fault displacements can intersect the waste canister is given by $L_C/tan\Theta \cdot L_F(m)$, where L_C is the canister length, Θ is the fault dip, and $L_F(m)$ is the length of faulting within the repository given a magnitude m earthquake. The expected number of canister failures is evaluated by the expression

$$E[N_{CF}(|m \text{ on fault } n)] = \frac{L_C}{\tan\Theta} \cdot E[L_F(m) \text{ for fault } n] \cdot \frac{35{,}000}{R_{area}} \cdot P(D>d_{CF}|m) \qquad (5\text{-}2)$$

where $E[L_F(m)$ for fault $n]$ is the expected length of faulting in the repository for a magnitude m earthquake, R_{area} is the total area of the repository, $35{,}000/R_{area}$ is the number of canisters per unit area, and $P(D>d_{CF} \mid m)$ is the probability that the fault displacement, D, for a magnitude m earthquake will exceed the threshold necessary to cause canister failure, d_{CF}.

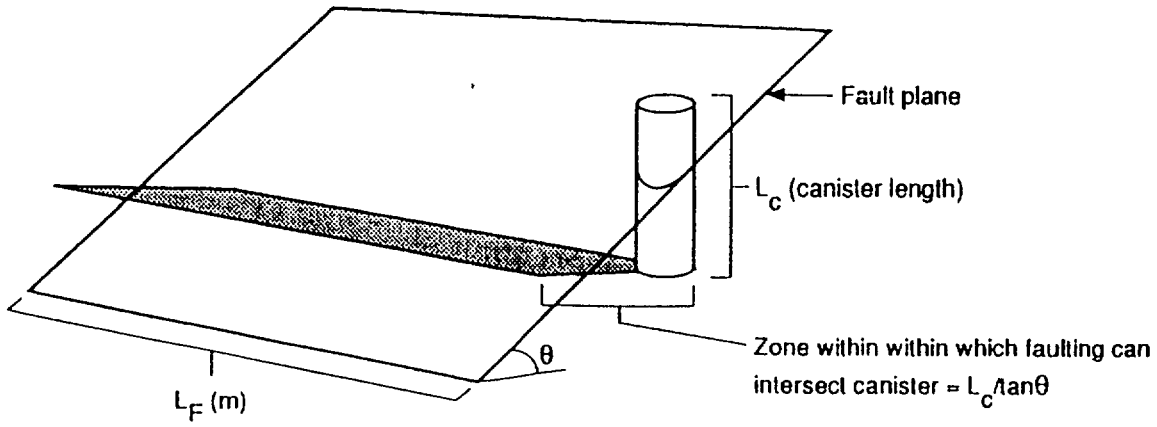

Figure 5-4. Method used to estimate the number of canisters intersected by faulting through the repository.

The expected length of faulting within the repository, $E[L_F(m)$ for fault $n]$, was evaluated using a simulation process that accounts for variability in fault zone width and the amount of secondary faulting that occurs in an earthquake. The amount of secondary rupture displacement was estimated as a variable fraction of primary displacement, which is a lognormally distributed function of the magnitude of the earthquake. The basis for these estimates are also described in Appendix A. For the current application, the frequency of canister failure was evaluated with d_{CF} set to 1, 4, and 10 cm.

For each of the faults shown in Figure 5-1, Equation 5-1 was used to compute the frequency of fault displacement-induced canister failure ν_{CF} for a given set of earthquake source parameters defined by the end branches of the earthquake logic tree (Figure 5-2). The calculation was repeated for all end branches of the earthquake logic tree for each fault, and for all faults to arrive at a discrete distribution for the frequency of canister failures. Figures 5-5, 5-6, and 5-7 show the computed distributions for d_{CF} of 1, 4 and 10 cm, respectively. Shown are the distribution of ν_{CF} considering only primary rupture (top plot), only secondary rupture (middle plot), and both types of rupture (bottom plot). As can be seen, the frequency of canister failure is controlled by the occurrence of secondary rupture.

EVALUATION OF EARTHQUAKE INDUCED STRESS CHANGES

The mechanism by which the occurrence of an earthquake may induce changes in the level of the water table is described in detail in Section 6. As indicated in that section, the increase in the elevation of the water table results from the static stress drop associated with an earthquake. This section presents the approach used to compute the probability of occurrence of various levels of stress drop.

The probability that coseismic stress drop, $\Delta\sigma$, will exceed a specified level, z, during a time period T was evaluated using the standard formulation for probabilistic seismic hazard analysis, namely:

$$P(\Delta\sigma>z) = 1-e^{-\nu(z)\cdot T} \tag{5-3}$$

where $\nu(z)$ is the frequency of exceeding stress drop z and is given by:

$$\nu(z) = \sum_{n} \alpha_n(m_o) \int_{m} f(m)\cdot P(\Delta\sigma>z\,|\,m)\,dm \tag{5-4}$$

The probability that the stress drop for a given magnitude event will exceed a specified level, $P(\Delta\sigma>z\,|\,m)$ was estimated from the relationship developed in earlier applications and shown in Figure 5-8. Individual event stress drops are assumed to be lognormally distributed about the relationship shown in Figure 5-8.

Equations 5-3 and 5-4 were was used to compute the probability of exceeding various levels of stress drop using each set of parameters defined by the end branches of the earthquake logic trees (Figure 5-2). The top plot in Figure 5-9 shows the resulting probability of exceeding various levels of stress drop for time periods of 100, 1,000, 10,000, and 100,000 years. These stress drop hazard curves were discretized to obtain probability distributions for the largest stress drop in a specified time period, as

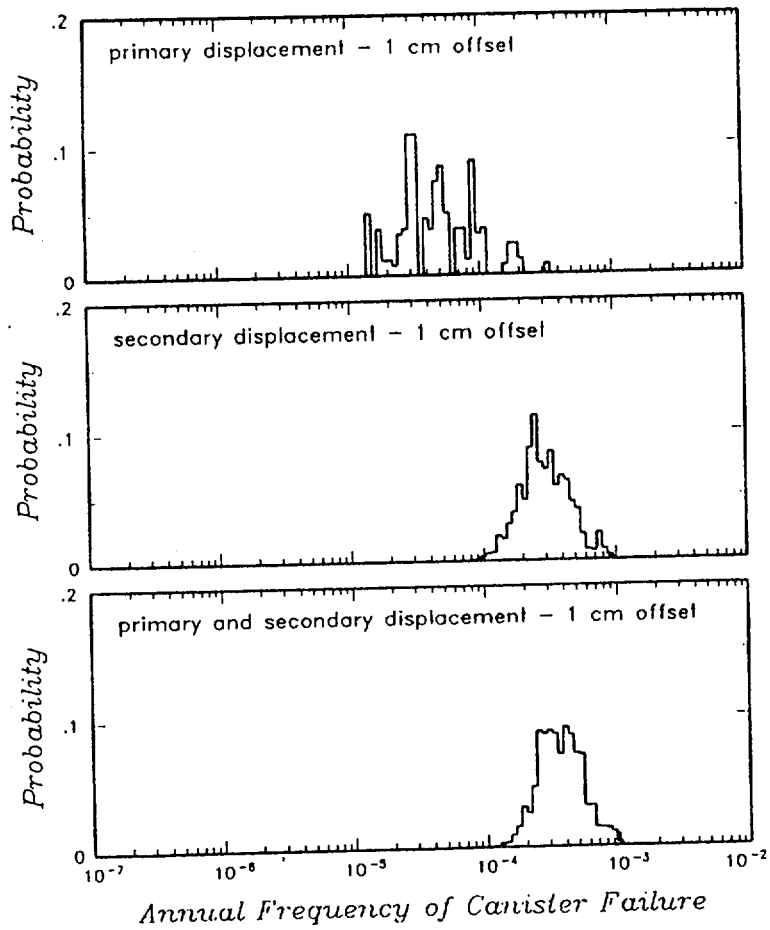

Figure 5-5. Distribution of annual frequency of canister failure due to faulting within the repository for a fault offset d_{CF} of 1 cm. Shown at the top is the effect of primary fault rupture only, in the middle plot is the effect of secondary faulting only, and at the bottom is the combined effects of primary and secondary faulting.

shown in the bottom plot of Figure 5-9. Figure 5-10 presents histograms showing the contributions of various magnitude earthquakes to the frequency of exceeding various levels of stress drop. The results presented in Figures 5-9 and 5-10 and used in Section 6 to evaluate the potential for earthquake-induced water table change.

SUMMARY

Consideration of earthquakes and tectonics leads to assessed probabilities of rupture of waste containers in the proposed repository. To incorporate this information into the overall logic tree

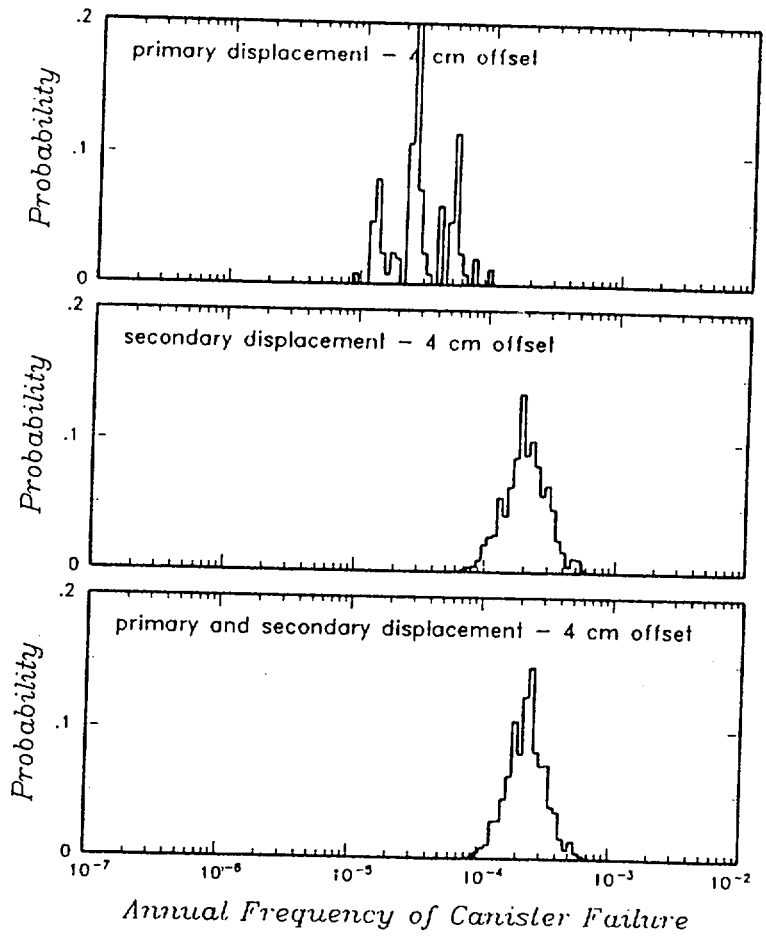

Figure 5-6. Distribution of annual frequency of canister failure due to faulting within the repository for a fault offset d_{CF} of 4 cm. Shown at the top is the effect of primary fault rupture only, in the middle plot is the effect of secondary faulting only, and at the bottom is the combined effects of primary and secondary faulting.

assessment, use is made of insights gained from the previous application of this methodology. That application suggested that earthquake-induced ruptures of waste containers is a relatively minor effect that does not contribute significantly to large off-site releases.

Thus, the earthquake effects can be treated in a simple, conservative way, to confirm whether they are small in the present application. For this, the design air gap around each container is 2 cm, so a displacement greater than 4 cm would imply contact between the container and the borehole wall. We assume, conservatively, that this implies rupture of the container. Similarly, if the airgap has failed

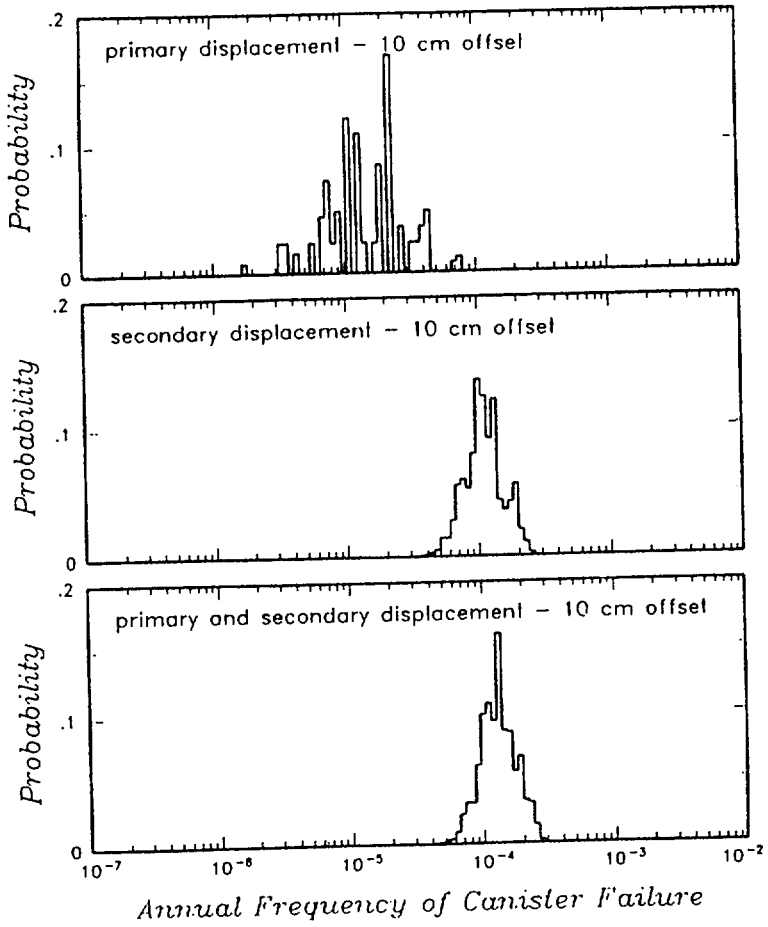

Figure 5-7. Distribution of annual frequency of canister failure due to faulting within the repository for a fault offset d_{CF} of 10 cm. Shown at the top is the effect of primary fault rupture only, in the middle plot is the effect of secondary faulting only, and at the bottom is the combined effects of primary and secondary faulting.

because of borehole fractures (see Section 8), we assume that a 1 cm fault displacement would imply container rupture. Over a 10,000 design lifetime these scenarios imply that, in expected numbers, two containers (for 4 cm offset) or three containers (for 1 cm offset) will be ruptured, out of the inventory of 35,000 containers in the proposed repository.

The earthquake effects are modeled with two branches of the master logic tree, as shown in Figure 5-11. Because of the small numbers of waste containers involved, explicit treatment of uncertainty is not appropriate, so the first branch excludes earthquake effects and the second includes them, in the

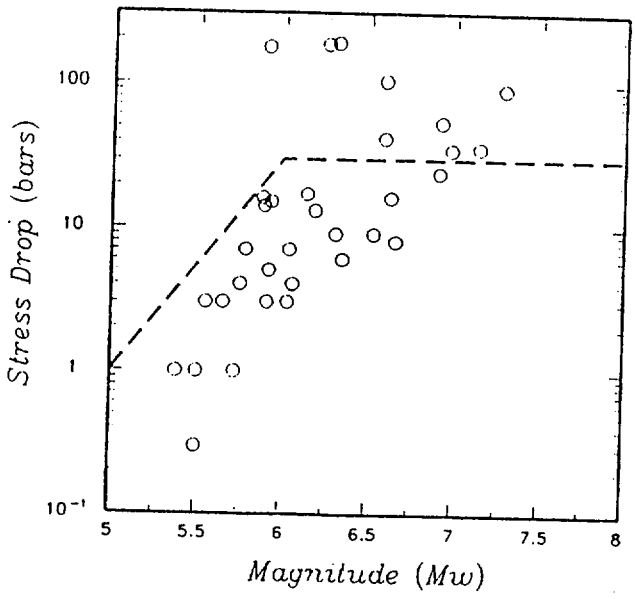

Figure 5-8. Static stress drops for Basin and Range earthquakes computed from earthquake source parameters presented by Doser and Smith (1989). Dashed line shows relationship used to estimate stress drops for specific magnitude earthquakes.

manner described above. A further simplification is that earthquakes are assumed to occur in year 1,000, which is the first time step in the temporal integration over repository effects. The alternatives in Figure 5-11 represent alternative methods of performance assessment (with and without earthquakes) and are arbitrarily assigned probabilities of 0.5 each, so that the influence of earthquakes on release levels can be investigated through sensitivity studies.

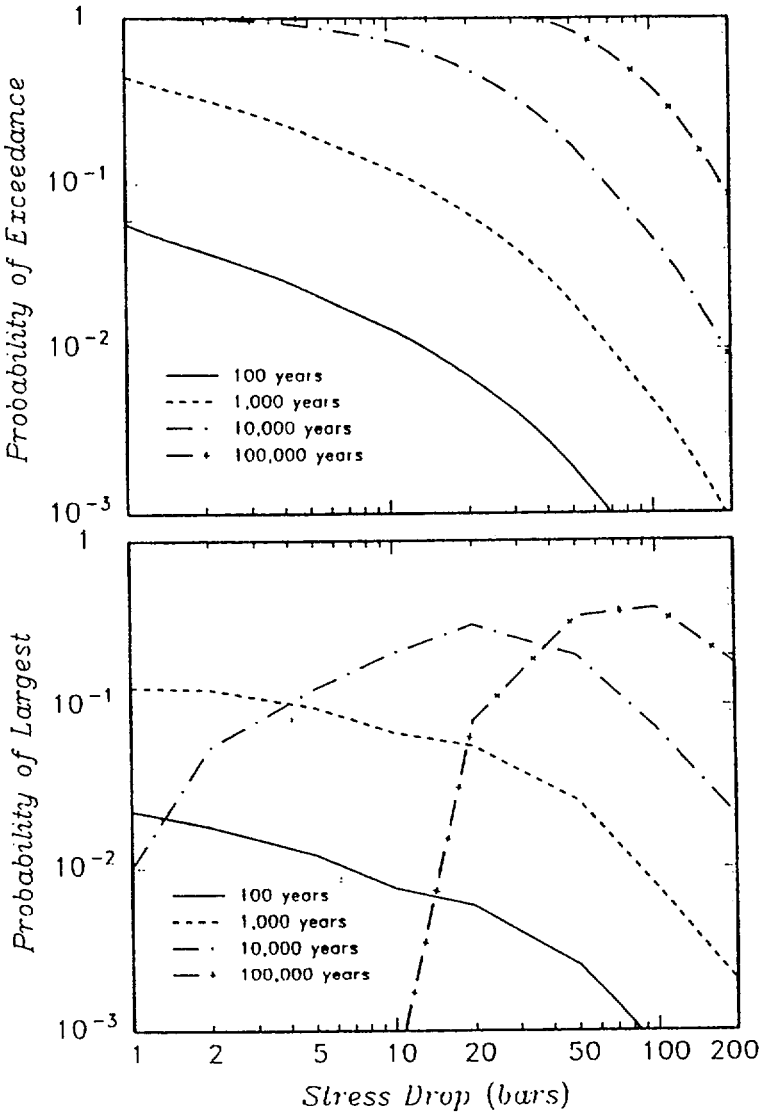

Figure 5-9. Probability of various levels of static stress drop. Shown at the top are hazard curves for the probability of exceeding various levels of stress drop as a function time period considered. Shown at the bottom are discretized hazard curves showing the probability distribution of the largest stress drop for various time periods.

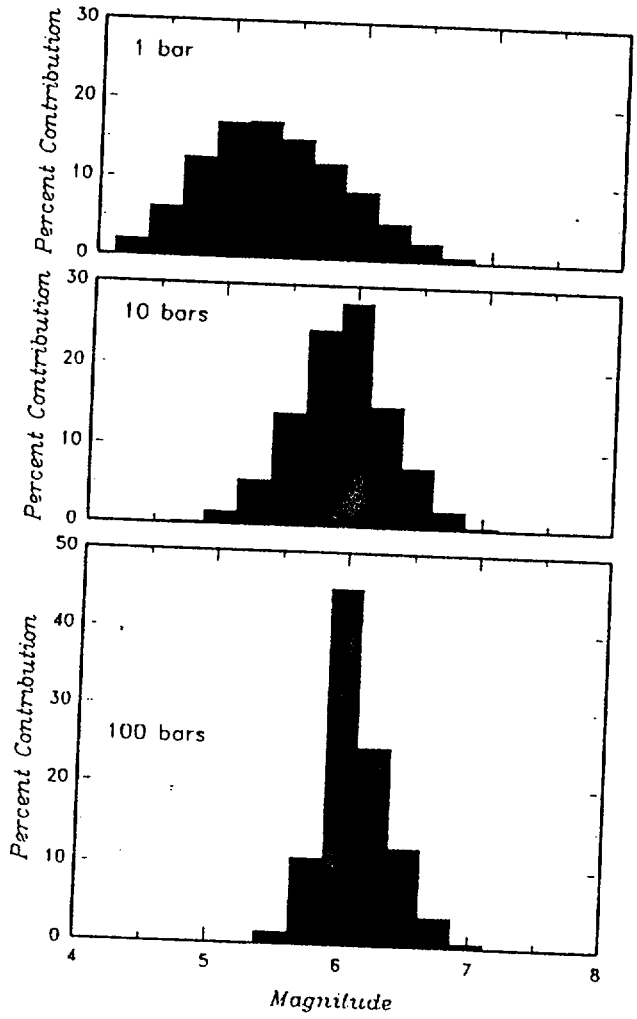

Figure 5-10. Histograms showing the contributions of various magnitude earthquakes to the frequency of exceeding various levels of stress drop.

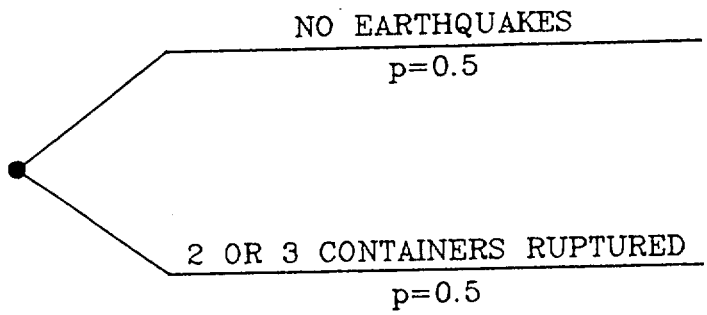

Figure 5-11. Logic tree mode depicting earthquake effects.

REFERENCES

1. R. K. McGuire (ed.). *Demonstration of a Risk-Based Approach to High-Level Waste Repository Evaluation*, Palo Alto, Calif.: Electric Power Research Institute, 1990. NP-7057, Research Project 3055-2.

Section 6

WATER TABLE CHANGE DUE TO A NORMAL FAULTING EARTHQUAKE

by

John M. Kemeny and Neville G. W. Cook

INTRODUCTION

Yucca Mountain, Nevada, is the proposed site for the underground storage of high level nuclear waste. The repository is to be located at a depth of 350 meters below the ground surface, and the water table is presently at a depth of 550 meters below the ground surface (1). The 200 meters of unsaturated rock between the repository and the water table is a natural barrier that is used to protect the regional groundwater for at least 10,000 years. Processes that could change the level of the water table (and thus the thickness of the barrier) include climatic changes, volcanism, and earthquakes. This paper focuses on the effects of normal faulting earthquakes on the level of the water table beneath Yucca Mountain. Yucca Mountain is located in a region of active normal faulting (e.g., (2, 3, 4, 5)). In particular, normal faults occur in the region immediately surrounding Yucca Mountain. The most important of these are the Solitario Canyon and Bow Ridge faults on the western and eastern flanks of Yucca Mountain, respectively, and the Ghost Dance fault, which goes directly through the proposed repository site (1).

Szymanski (6) proposed that a large rise in the level of the water table could occur following a normal faulting earthquake, due to the co-seismic redistribution of stress. Szymanski's analysis was qualitative in nature and he did not develop a model for accurately estimating the change in the level of the water table that could be expected following earthquake rupture in the Basin and Range. However, seismological and geological evidence support water table changes following Basin and Range earthquakes. For example, Whitehead (7) cites significant hydrologic changes that were observed following the Borah Peak earthquake (magnitude 7.3) on October 28, 1983. These changes include groundwater levels which rose as much as four meters, increases in the discharge in springs and streams, and the development of new springs. Also, Sibson (8, 9) showed that normal faulting earthquakes may be responsible for the upwelling of fluids along faults that result in mineral deposits.

In the past several years, models have been developed by several investigators for estimating changes in the level of the water table following normal faulting earthquakes. For instance, the EPRI model (10) estimated rises in the water table ranging from 1 to 15 meters due to large (magnitude 7) normal faulting earthquake near Yucca Mountain. This model can be summarized as follows. In an extensional regime such as the Basin and Range, a drop in shear stress along a ruptured fault results in an increase in compressive stress in the elastic Lithosphere surrounding the fault. Due to this increase in compressive stress following earthquake rupture, water will be squeezed out of pores, cracks, and faults, moving up towards the ground surface. A model for the amount of water that would be displaced was developed, based on the additional compressibility of the ground due to pores, cracks, and faults. Some additional assumptions were made about the volume over which the stress change occurred, and the porosity of the ground above the water table. Based on these assumptions, a relationship between the water table rise, Δw, the stress drop, $\Delta\tau$, and the depth of faulting, h, was derived:

$$\Delta w(\text{meters}) = \Delta\tau(\text{bars}) * 1.2\ \ 10^{-5} * h(\text{meters}) \qquad (6\text{-}1)$$

For example, for a magnitude 7 earthquake that ruptured to a depth of 15 km with a 50 bar stress drop, a water table rise of 9 meters is predicted using this relationship.

The principal drawback in the analysis described above is the large uncertainty in the compressibility of void space in pores, cracks, joints, and faults. A major improvement in the current project is the inclusion of multiple layers and the estimation of rock compressibilities using field measurements, in particular seismic wave velocity measurements from downhole borehole logs. This Section describes the development of a layered model for water table change due to a normal faulting earthquake in the vicinity of Yucca Mountain. For the ground below Yucca Mountain, a horizontally layered model with four layers above the water table (Tiva Canyon, Topopah Springs, Calico Hills, Prow Pass) and six layers below the water table (Bullfrog, Tram, Lithic Ridge, Lone Mountain, Roberts Mountain) is considered. The seismic velocities and porosities for these layers have been obtained from the Site Characterization Plan (1). A relation is derived that relates the seismic velocities and porosities in each layer with the compressibility of the void space due to pores and fractures. From this relation and the stress drop due to an earthquake rupture, the displaced volume of water is calculated. Finally, the rise in the level of the water table is calculated using assumptions about the amount of unsaturated pore space above the water table.

STRESS CHANGE FOLLOWING BASIN AND RANGE EARTHQUAKES

Following earthquake rupture, the shear stress along the fault will drop. In a normal faulting regime, the maximum principal stress will be the vertical stress due to gravity, and the minimum and intermediate principal stresses will be horizontal. In addition, the vertical stress due to gravity will remain unchanged following earthquake rupture. Figure 6-1 illustrates on a Mohr circle diagram the stress state immediately before and after fault rupture in a normal faulting regime. The shear stress will decrease, and due to the constraint that the vertical stress remains unchanged, the minimum horizontal stress will increase (become more compressive). The magnitude of the increase in compressive stress can be estimated from seismic source parameters. For a normal faulting earthquake that ruptures to the ground surface, the stress drop is estimated as:

$$\Delta\tau = \frac{8M_o}{3\pi t^2 b} \tag{6-2}$$

where M_o is the seismic moment, t is the fault depth, and b is the fault thickness (11). Assuming a normal fault with a dip θ, the increase in mean stress Δp following a normal faulting earthquake becomes:

$$\Delta p = \frac{\Delta\tau(1+\nu)}{3\sin\theta\cos\theta} \tag{6-3}$$

where ν is Poisson's ratio. Data on stress drops following Basin and Range earthquakes are available in the previous EPRI report (10). These results show that stress drop is a function of the earthquake magnitude up to magnitude 6 earthquakes, after which stress drop appears to be independent of magnitude (see Figure 6-2). Based on these data and the frequency of earthquakes of different magnitudes in the Basin and Range, the probabilities of stress drops of different sizes have been determined (see Section 5). These probabilities are presented in Table 6-1 below. For instance, the probability of a stress drop of 50 bars is 0.2. For a normal fault dipping at 60°, this gives an increase in compressive stress following earthquake rupture of about 48 bars.

The spatial extent of the increase in compressive stress can be estimated from the depth of faulting. For an edge crack in an elastic half-space, the horizontal extent of stress change in each direction from the crack is approximately equal to the crack length. Based on this, we assume that the extent of the stress change on both sides of the fault will be approximately equal to the fault depth. Basin and Range earthquakes initiate at a depth of approximately 15 km, so the extent of stress change should be approximately 15 km on each side of the fault.

Table 6-1

PROBABILITIES OF VARIOUS STRESS DROPS FOR NORMAL FAULTING EARTHQUAKES

Stress Drop (bars)	Probability
< 1	0.0015
1	0.01
2	0.054
5	0.126
10	0.208
20	0.31
50	0.20
100	0.07
> 200	0.02

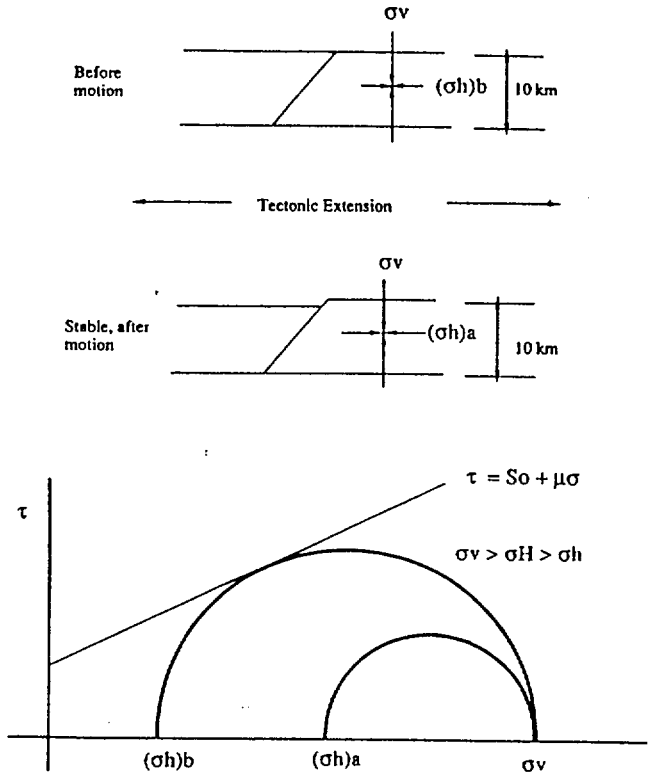

Figure 6-1. Mean Stress Changes due to Normal Faulting.

LAYERED MODEL AND THE COMPRESSIBILITY OF EACH LAYER

A layered model for the ground beneath Yucca Mountain is considered. A simplified stratigraphy is shown in Figure 6-3. The first 1800 meters below the ground surface have been broken up into 9

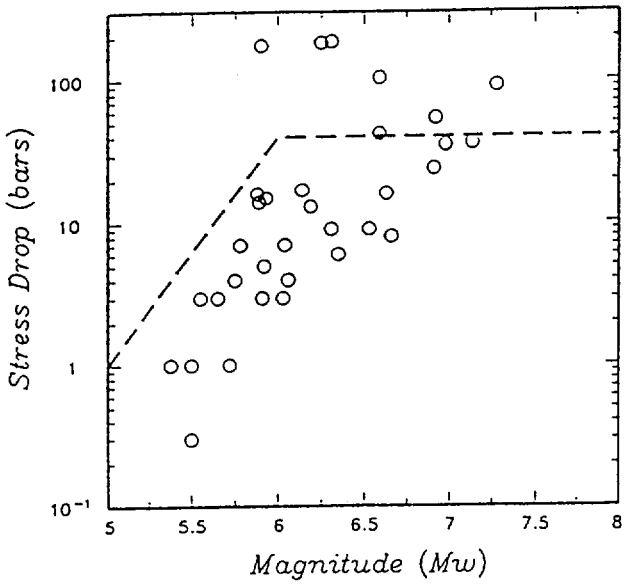

Figure 6-2. Stress drop vs. magnitude data.

layers, as shown in Figure 6-3. The water table is assumed to be at the base of the Prow Pass unit, at a depth of 350 meters. The ground between 1800 and 10,000 meters is considered to be a single layer of dolomite. Some of the known material properties for each of the layers is also shown in Figure 6-3, from DOE (1). These material properties includes the porosity, ϕ, the density, ρ, and the S and P wave velocities, α and β. In general, Figure 6-3 shows that with increasing depth from the surface to 10,000 meters, the porosity decreases (30% to 2%), the density increases (2160 to 2650 kg/m^3), and the P and S wave velocities increase (2500 to 6700 and 1500 to 3500 m/sec, respectively). The bulk compressibility, K, is a measure of the decrease in bulk volume with increasing mean compressive stress. The intrinsic bulk modulus for tuff and dolomite are about 40 GPa and 100 GPa, respectively. The effective bulk modulus, referred to as $\bar{K}$, includes the additional compressibility due to pores, microcracks, and larger scale fractures. $\bar{K}$ can be determined from seismic velocity measurements taken from borehole logs. The P and S velocities are denoted by α and β, respectively. The relationship between the P and S velocities and the effective elastic moduli are given by:

$$\alpha = \left[\frac{\bar{\lambda}+2\bar{G}}{\rho}\right]^{1/2} \qquad (6\text{-}4)$$

$$\beta=\left[\frac{\bar{G}}{\rho}\right]^{1/2} \tag{6-5}$$

where $\bar{\lambda}$ is the effective Lame's constant, $\bar{G}$ is the effective shear modulus, and ρ is density. Using the relationship:

$$\bar{K}=\bar{\lambda}+\frac{2}{3}\bar{G} \tag{6-6}$$

this gives:

$$\bar{K}=\rho\left[\alpha^2-\frac{4}{3}\beta^2\right] \tag{6-7}$$

PORE VOLUME CHANGE DUE TO STRESS CHANGE

An increase in mean compressive stress due to an earthquake will squeeze water out of pores, cracks, joints, and faults and towards the ground surface, resulting in a rise in the level of the water table. The elastic change in the pore volume due to an increase in mean stress is referred to as the pore compressibility, C_{pc}. In this section we derive a relationship between the pore compressibility, C_{pc}, the intrinsic and effective bulk moduli, K and $\bar{K}$, and the porosity, ϕ. This relationship is derived using Betti's reciprocal theorem. The reciprocal theorem is applied to a three dimensional body with volume V containing a single pore with volume v. For the reciprocal theorem, the body is subjected to two sets of applied stress, as shown in Figure 6-4. In the first set, a hydrostatic pressure p_1 is applied both externally to the body, and to the surfaces of the pore. In the second set, a hydrostatic pressure p_2 is applied only to the outside of the body. The reciprocal theorem states that the strain energy due to the first set of forces through the displacements of the second set is equal to the strain energy of the second set of forces through the first set of displacements. The volume change of the first body is p_1/K, and the volume change of the second body is $p_2/\bar{K}$. Also, the volume change of the pore in the second body is $p_2C_{pc}v$. Applying the reciprocal theorem to these two sets of boundary conditions, it follows that:

$$p_1\frac{p_2}{\bar{K}}V-p_1p_2C_{pc}v=p_2\frac{p_1}{K}V \tag{6-8}$$

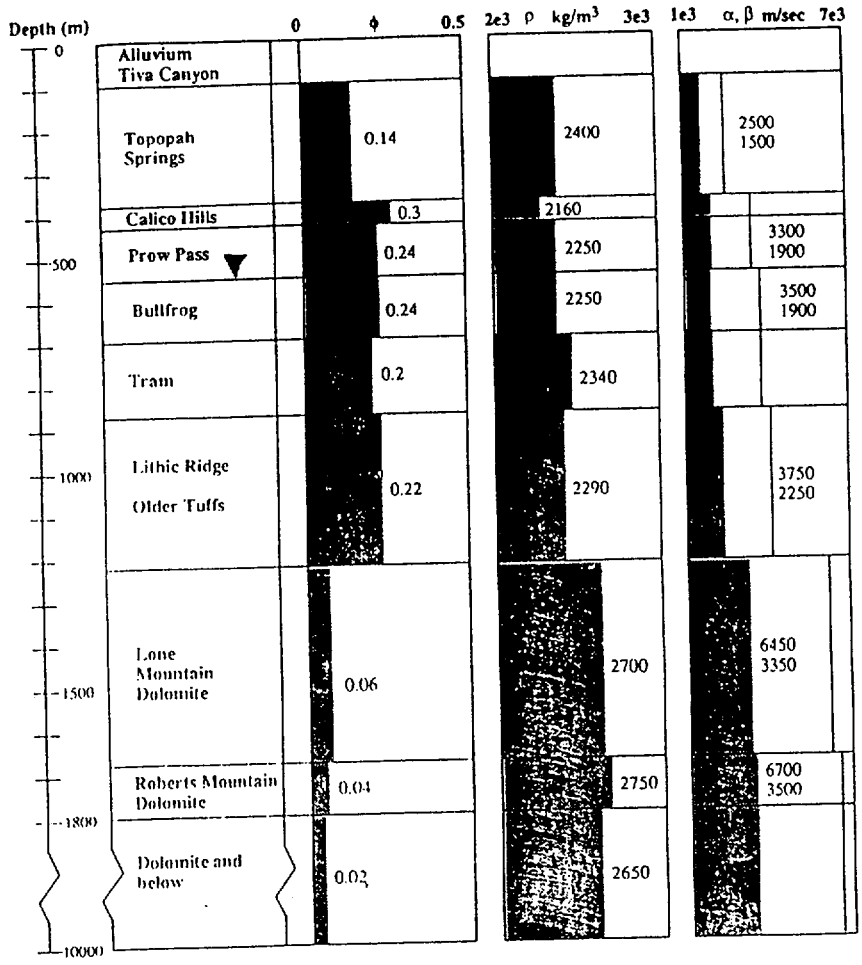

Figure 6-3. Simplified stratigraphic model of Yucca Mountain.

which upon setting $p_1 = p_2$ reduces to:

$$C_{pc}\phi = \frac{1}{\bar{K}} - \frac{1}{K} \tag{6-9}$$

where the porosity ϕ is equal to v/V. Equation (6-9) is the relationship between the pore volume change and the intrinsic and effective bulk moduli for the case when the void space is empty (or containing water but under drained conditions). In the case of an earthquake rupture, the water in the pores will not have time to drain and an increase in pore pressure will result. A formula for pore volume change under undrained conditions can be derived by considering the pore volume change due

to both an applied external pressure Δp_c and an applied pore pressure Δp_p. The change in pore volume is given by:

$$\frac{\Delta v}{v} = C_{pc}\Delta p_c - C_{pp}\Delta p_p = \frac{\Delta p_p}{K_w} \tag{6-10}$$

where C_{pp} is the compressibility due to Δp_p, and K_w is the bulk modulus of water (3.0 GPa). Rearranging, this gives:

$$\Delta p_p = \frac{C_{pc}\Delta p_c}{\frac{1}{K_w} + C_{pp}} = \frac{C_{pc}\Delta p_c}{\frac{1}{K_w} + C_{pc} - \frac{1}{K}} \tag{6-11}$$

and using equation (6-9), the formula for the instantaneous increase in pore pressure becomes:

$$\Delta p_p = \frac{\left[\frac{1}{\bar{K}} - \frac{1}{K}\right]\Delta p_c}{\frac{\phi}{K_w} + \frac{1}{\bar{K}} - \frac{1+\phi}{K}} \tag{6-12}$$

Equations (6-10) and (6-12) can now be rearranged to give the pore volume change under undrained conditions:

$$C_{pc}\phi = \frac{\frac{1}{\bar{K}} - \frac{1}{K} - \frac{\left[\frac{1}{\bar{K}} - \frac{1}{K}\right]\phi}{\frac{\phi}{K_w} + \frac{1}{\bar{K}} - \frac{1+\phi}{K}}}{1 - \frac{\left[\frac{1}{\bar{K}} - \frac{1}{K}\right]}{\frac{\phi}{K_w} + \frac{1}{\bar{K}} - \frac{1+\phi}{K}}} \tag{6-13}$$

WATER TABLE CHANGE

Based on the material properties given in Figure 6-3 and the relationships derived above, the effective bulk modulus, and instantaneous build-up in pore pressure, and the volume of water displaced (per 100 bar stress drop) are calculated for each of the layers below the water table. These results are presented in Table 6-2.

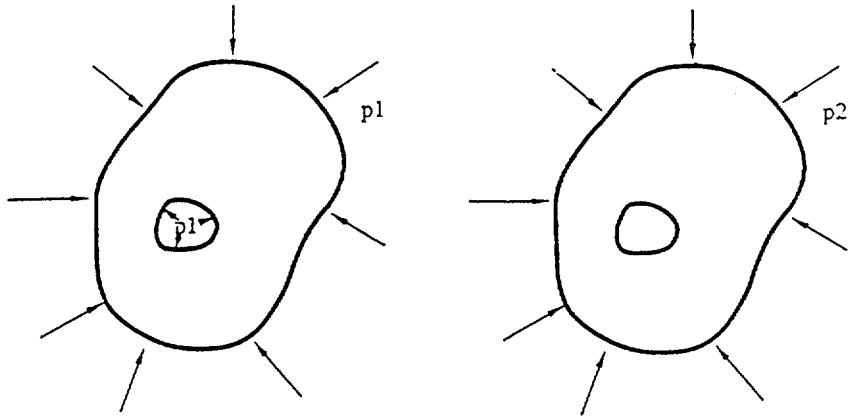

Figure 6-4. Hydrostatic pressure on free body.

Table 6-2

CALCULATED VOLUME OF DISPLACED WATER IN GEOLOGIC UNITS

Results for: $\Delta\tau$ = 100 bars, ν = 0.3, θ = 60°, ϕ above water table (Prow Pass) = 0.24, Sw above water table = 0.7

UNIT	K ($x10^9$)Pa	K ($x10^9$)Pa	Pore Pres. (MPa)	Displ. Vol. (m^3)
Bullfrog	40	16.7	2.5	0.065
Tram	40	17.4	3.0	0.078
Lithic Ridge	40	16.7	3.0	0.166
Lone Mtn. Dolomite	100	71.9	1.4	0.020
Roberts Mtn. Dolomite	100	78.5	2.2	0.004
8000m of Dolomite	100	77.1	2.8	0.322

The total displaced pore volume for the 6 layers below the water table (per unit area) is given by:

$$\Delta v = \Delta p \sum_{i=1}^{6} (C_{pc})_i \phi_i h_i \qquad (6\text{-}14)$$

If we consider a constant porosity ϕ_{unsat} and wetting phase saturation Sw_{unsat} above the water table, then the rise in the water table due to the displaced pore volume is given by:

$$\Delta h = \frac{\Delta v}{\phi_{unsat}(1 - Sw_{unsat})} \qquad (6\text{-}15)$$

If we consider a constant porosity above the water table, and a wetting phase saturation that varies from Sw_a at the top of the original water table to Sw_b at the top of the new water table, then the rise in the water table is given by:

$$\Delta h = \frac{\Delta v}{\phi_{unsat}(1 - \frac{Sw_a + Sw_b}{2})} \qquad (6\text{-}16)$$

Uncertainties in Stress Drop, Unsaturated Pore Space, Material Properties

The major uncertainties in calculating the water table change due to an earthquake are:

1. Uncertainty in Stress Drop
2. Uncertainty in the Unsaturated Pore Space above the Water Table
3. Uncertainty in Material Properties

The first uncertainty is the magnitude of the stress drop. The probability of stress drops of different sizes is given in Table 6-1.

The second uncertainty is the available unsaturated pore space above the water table. Three assumptions about the unsaturated pore space above the water table are made. The first assumption is that 70% of the pore space is filled above the water table. The second assumption is that 90% of the pore space is filled above the water table. The third assumption is that the filled pore space above the water table varies from 90% at the water table to 70% at the top of the new water table change. The probabilities assigned to these three assumptions are given as follows:

Percent saturation above the water table	Probability
70%	0.3
70-90%	0.4
90%	0.3

The third uncertainty is the material properties used to estimate the effective bulk modulus for the different layers. As a check on the results determined from seismic velocity measurements, laboratory results of the effective bulk moduli have been measured for the first two layers below the water table. These results are given as follows:

Bullfrog member	$\bar{K}$ = 4.86 GPa
Tram member	$\bar{K}$ = 7.92 GPa

These results are lower than the results obtained from seismic velocities. For these layers, the following probabilities were assigned to methods of estimating the effective bulk moduli in the Bullfrog and Tram members:

Method of obtaining $\bar{K}$	Probability
Laboratory test	0.25
Seismic velocities	0.25
Average the two	0.5

Results

Based on the nine alternatives for stress drop, three alternatives for saturation above the water table, and three alternatives for material properties, there are 81 total scenarios to be considered. Based on the results of these 81 cases, the results were reduced to 6 categories of water table rise, and a probability for each category was calculated. The results are in Table 6-3, and are shown in the logic tree format in Figure 6-5.

Table 6-3

PROBABILITIES OF DIFFERENT CHANGES IN WATER TABLE, GIVEN AN EARTHQUAKE

Water Table Rise	Probability
0 - 6 meters	0.493
6 - 15 meters	0.277
15 - 30 meters	0.161
30 - 60 meters	0.055
60 - 90 meters	0.008
90 - 130 meters	0.006

The results indicate that it is likely that due to an earthquake, the water table rise will be 15 meters or less. This is in agreement with the results in EPRI (7).

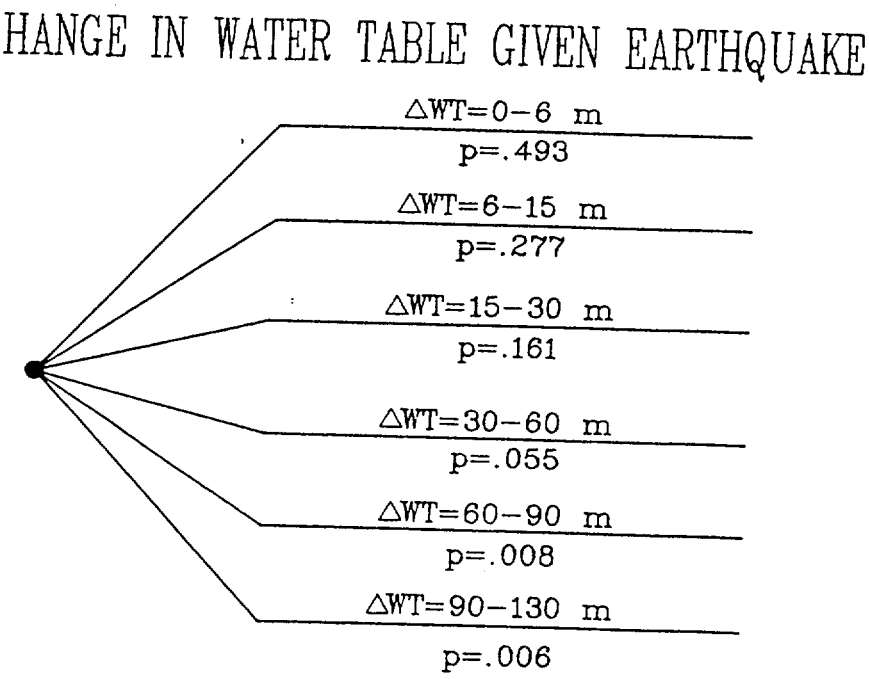

Figure 6-5. Logic tree node showing change in water table given an earthquake.

REFERENCES

1. U.S. Department of Energy. *Site Characterization Plan.* U.S. Department of Energy Report DOE/RW-0199, 1988.

2. G. A. Davis and G. S. Lister. *Detachment Faulting in Continental Extension; Perspectives from the Southwestern U.S. Cordillera.* Geological Society of America, Special Paper 218, 1988, pp. 133-159.

3. P. England and J. Jackson. "Migration of the Sseismic-aseismic Transition During Uniform and Nonuniform Extension of the Continental Lithosphere." *Geology*, vol. 15, 1987, pp. 291-294.

4. R. B. Smith and R. L. Bruhn. "Intraplate Extensional Tectonics of the Eastern Basin-Range: Inferences on Structural Style from Seismic Reflection Data, Regional Tectonics, and Thermal-mechanical Models of Brittle-ductile Deformation." *J. Geophysical Res.*, vol. 89, 1984, pp. 5733-5762.

5. R. S. Stein and S. E. Barrientos. "Planar High-angle Faulting in the Basin and Range: Geodetic Analysis of the 1983 Borah Peak, Idaho, Earthquake." *J. Geophys. Res.*, vol. 90, 1985, pp. 11355-11366.

6. J. S. Szymanski. *Conceptual Considerations of the Yucca Mountain Groundwater System with Special Emphasis on the Adequacy of this System to Accommodate a High-level Nuclear Waste Repository.* US Department of Energy, 1989.

7. R. Whitehead. *Hydrologic Changes Following the Borah Peak Earthquake.* USGS Open File Report 85-290, 1985.

8.. R. H. Sibson. "Fluid Flow Accompanying Faulting: Field Evidence and Models." From *Earthquake Prediction: An International Review, AGU.* D. W. Simpson and P. G. Richards (eds.). Washington, DC: 1981.

9. R. H. Sibson. "Earthquake Rupturing as a Mineralizing Agent in Hydrothermal Systems." *Geology*, vol. 15, 1982, pp. 701-704.

10. R. K. McGuire (ed.). *Demonstration of a Risk-Based Approach to High-Level Waste Repository Evaluation*, Palo Alto, Calif.: Electric Power Research Institute, 1990. NP-7057, Research Project 3055-2.

11. D. I. Doser. "Source Parameters and Faulting Processes of the 1959 Hebgen Lake, Montana, Earthquake Sequence." *J. Geophys. Res.*, vol. 90, 1985, pp. 4537-4555.

Section 7

VOLCANO OCCURRENCES

by

M. F. Sheridan

SCOPE OF EVALUATION

Estimation of the probability of future volcanism is an important consideration in the evaluation of volcanic risk at the proposed repository at Yucca Mountain (1, 2, 3, 4, 5, 6, 7). The probability of radionuclide migration associated with volcanism is a function of three factors: (1) the temporal probability that a volcanic event will occur, (2) the spatial probability that, given an occurence, a volcanic event will effect the proposed repository, and (3) the probable effect of volcanism on the release of radionuclides from the repository. Probability estimates for all of these considerations are presented here using the logic tree approach to characterizing and quantifying alternative events and their probabilities.

The two variables, time and space, are dependent but can be separated to simplify the analysis. The temporal analysis gives the probability in events per year of a volcanic feature associated with a specific source location. The spatial analysis gives the probability, expressed a fraction, that a volcanic feature will intersect a defined geographic area. This Section presents a new methodology for determining probability functions for various spatial models of volcanism proposed for the Yucca Mountain region that is compatible with a risk-based approach to site evaluation. The cornerstone for the new model is a Monte Carlo simulation that plots the trace of volcanic dikes specified by a set of input parameters.

The main assumption for forecasting future volcanic activity near Yucca Mountain is that the future will follow the pattern of past events in similar settings within the Great Basin. With this assumption, existing volcanic fields provide the basic data to establish probabilities for the frequency, type, and geometry of potential future volcanic events in this area. The two most important data sets for this analysis are: (1) the distribution of existing volcanic vents in time and space, and (2) the geometry of dikes associated with young volcanism.

TEMPORAL MODELS OF VOLCANISM

Temporal models for risk evaluation of historically active volcanoes are designed to predict events expected within a few months or years in the future. Risk predictions for a future eruption at extinct volcanoes are extremely difficult. Predictions for volcanic events near Yucca Mountain must extend from 10,000 to 100,000 years into the future in an area with no historic activity and relatively few extinct volcanoes. For this reason existing methodologies of prediction must be modified to be appropriate for the expanded time range of prediction.

One method used to characterize the rate of volcanism over long periods of time is to divide the number of events associated with a specified source area or volcanic field by the lifetime of the field. A better measure of volcanic activity would be a cumulative plot of the magnitude of volcanism, such as the volume or mass eruption rate, with time. However, data on volume output of lava with time is difficult to determine for older volcanic fields. Thus, typical values of eruption rates are made by dividing the age of the field by the number of identified scoria cones or lava sheets. The frequency of small or subsurface features, such as dikes, are generally not considered by this method.

Basaltic magma is generated in the mantle and moves to the surface through fracture system controlled by regional tectonics. The source regions for basalt are generally small (tens of kilometers diameter or less) and the crust in the Great Basin is relatively thin (between 20 and 30 kilometers). Because feeder dikes with dips less than 45 degrees are unlikely, geometric arguments indicate that a source field for volcanic features that could affect the area must be within a radius of less than 30 or 40 kilometers from the repository. The chance of magma being generated more than 40 km from a source is insignificant (less than 10^{-10} per year), and therefore may be disregarded as potential source for new volcanoes near Yucca Mountain.

The group of volcanoes less than 3.7 my old located in Crater Flat and Lathrop Wells is a logical choice for the most probable source field of new magmatic activity in this area. The temporal probability of a new volcano related to this field based on a study of 10 volcanoes that erupted during the past 3.7×10^6 years was estimated by Crowe (5, 6, 7) to be about 10^{-6} per year.

Confidence in the temporal rate of volcanism depends on the degree to which the age, number, and location of volcanic events related to the source field are known. A large number of events and a long duration of time better constrain the estimate of temporal probability. An important consideration in the volcanology model is the selection of the most likely source region for basaltic magma located

near Yucca Mountain.

The actual probability needed for the computer model is the temporal frequency of volcanic dikes associated with the field. Assuming that the number of dikes intruded near Yucca Mountain in the past 3.7×10^6 years is 30, the calculated probability of a new dike in the next 10,000 years is approximately 7.5×10^{-2}. This value is used in computation of the conditional logic for the probability tree calculations.

SPATIAL MODELS OF VOLCANISM

The spatial analysis of volcanic activity should be designed on a paradigm that mimics the patterns of existing volcanoes. Volcanic features in the Western United States occur in groupings or clusters at various distance scales. The problem is to choose a scale that is appropriate for the problem in hand.

The largest scale to consider includes all of the potentially active volcanoes that are present in the Western U.S. Within this region of active volcanism are large-scale (hundreds of kilometers in length) alignments or groupings of volcanoes with similar compositions and styles of eruption that define chains or broad regions, such as, the Cascade Range, the Snake River Plain, and the Columbia River Plateau. At a smaller scale (tens of kilometers in length), areas of continuous volcanic cover and a common source region define composite volcanoes, caldera complexes, or volcanic fields, each with hundreds of obvious events. At a smaller scale yet are individual volcanoes (hundreds of meters in length) which may have single or repeated eruptions. The smallest scale is illustrated by individual fissures or dikes which may be separated by tens of meters. The similarities in geometry and eruptive frequency that persist at all of the above scales make volcanoes amenable to statistical modeling which very likely has a fractal relationship in time and space.

The pattern of conduits associated with a source area define the spatial distribution of past features. New volcanic events can be predicted based on statistical assumptions about the distribution of the old conduits. In the discussion above, source areas for magma generation at distances greater than a few tens of kilometers from Yucca Mountain are shown to be irrelevant insofar as the risk to a repository at Yucca Mountain is concerned. Only the sources that produced surface lavas and scoria cones in the vicinity of Crater Flat present a finite risk to the Yucca Mountain site.

A reasonable assumption about volcanic fields in a mature or steady state is that future lavas or scoria

cones would occur within a two standard-deviation spread of the distribution of the existing volcanoes. Thus, the standard deviation of the long dimension of a volcanic source region can be used as a measure of potential field size. The volcanic exposures within 40 kilometers of Yucca Mountain occur near Crater Flat (Figure 7-1). The distribution of these volcanoes could be constrained by an ellipse with a standard deviation of about 4 kilometers, an orientation of N10°W, and an aspect ratio of 2.

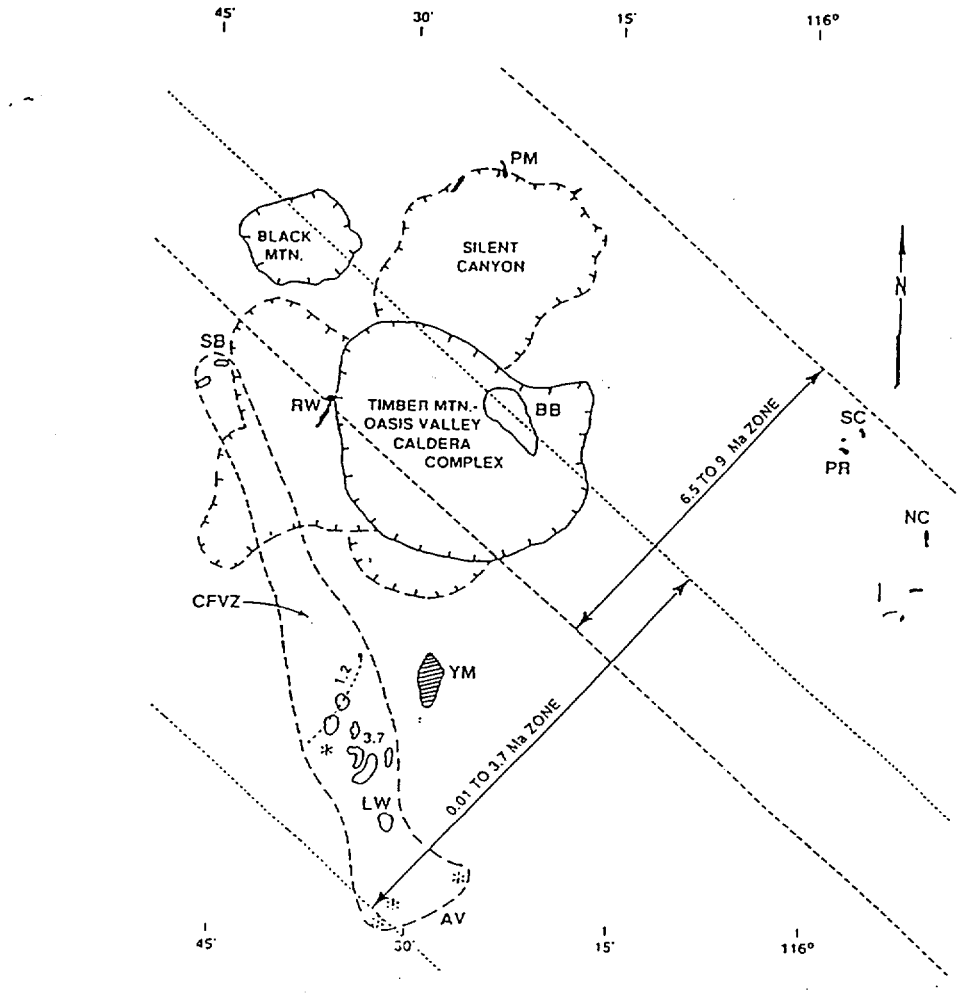

Figure 7-1. Sketch map showing the distribution of the youngest episodes of volcanism in the Yucca Mountain area [from Crowe (7)].

Crowe (1, 2, 3, 4, 5, 6, 7) has spent considerable effort developing models for volcanic risk calculations for the Yucca Mountain site. His spatial models can be incorporated into the proposed

model because they also consider the conditional probability of a volcanic event intersecting the repository contingent on an event occurring in a surrounding volcanic field.

The main difference between Crowe's older models and the proposed model is that the spatial component of his models consider an equal probability of a volcanic event anywhere within the volcanic field (4, 5, 6). This consideration dictates that the probability of a volcanic intersection is not a function of the location of the repository with respect to the geometry of the field. A consequence is that the probability of an intersection would appear to be a strong function of the size of the field and the number of expected events within the field. In other words, geometry of the repository outline, its location within the field of potential new volcanoes, the distribution of volcanic features within the field, and the size of the field do not play a significant role in these models.

In recent (1991) oral presentations, Crowe has made a new assumption of a bivariate normal distribution of conduits, as is made in the proposed model. Such a distribution exhibits an elliptical pattern and is easily mimicked by the computer code presented in this section.

Smith (8, 9) has developed a different type of model for volcanic risk evaluation for the Yucca Mountain site that uses the orientation of fracture systems and the location of the most recent volcanic vents to predict the most probable sites of future volcanism. His model consists of nested rectangles representing different levels of probable volcanic activity aligned parallel to vent systems centered within specific clusters of volcanism. The zones in this model are given relative values of probability (low, medium, and high) so they yield only qualitative information. Also, the geometry of the model field does not correspond to the shape and orientation of the existing group of volcanoes in the Crater Flat field. However, the general geometry of the preferred distribution of vents suggested by Smith can also be depicted by the model described below. With actual numbers assigned to the probability rectangles, Smith's model can be replicated with the proposed computer code and probability functions can be generated for various assigned parameters that generally correspond to his proposed field geometry.

THE PROPOSED SPATIAL MODEL

The new model for spatial probability of volcanism in this section uses a Monte Carlo simulation to plot the distribution of volcanic features that are dispersed in a bivariate Gaussian distribution about a specified magmatic source point. The main procedures of the code are to: (1) plot the position of conduits and dikes according to input parameters that specify the requisite geometry of the volcanic

field and the specific features, (2) calculate the number of conduits or dikes that intersect the proposed repository geometry or a zone surrounding this geometry, for each simulation, and (3) compute a probability of intersection based on size for the specified field and feature geometries. This probability of intersection is calculated as the ratio of the number of events within specified areas (for example near or within the repository) divided by the total number of events in the simulated field.

Example Models

Three different example models of volcanic patterns in the vicinity of Yucca Mountain are illustrated. These three field and dike geometries mimic the currently suggested ideas about volcanism in this area. In fact, any configurations allowed by the parameters could have been chosen. Each of the illustrations shows the general pattern of dike swarms generated by these three different models. They also show the location of past volcanic centers by small circles and the area of general influence of dikes on the water table by a large circle.

The general parameters on the geometry of volcanic fields and dikes was tabulated from several volcanic fields younger than 5 my in the Great Basin and surrounding areas. The source of the data includes maps from which quantitative information was extracted and published reports which directly cite the needed information. In cases where there was a significant discrepancy between values reported in publications the values used were determined by actual measurements from original maps.

Dike parameters can be selected to create dike geometries that fit any specific model. The values used in the depicted models are typical (10): mean length = 2.5 kilometers, standard deviation of length = 500 m, and standard deviation of orientation = 15°. The dike orientation for models A and B was chosen in conformance with near-surface stress conditions. Dikes in model A have a mean azimuth of N40°E and those in model B have a mean azimuth of N35°E. Model C was given a mean azimuth of N15°E to conform to the proposed model of Smith (8, 9).

Model A is considered to be the most probable geometry for future volcanism in the next 10,000 years. It assumes that new volcanic features will follow the pattern of volcanism during the past 5 my. This means that the distribution of future volcanic events will mimic the pattern of the existing volcanoes in Crater Flat and that shallow dikes will trend parallel to the current stress field, which is also in the direction of surface fissures on the existing volcanoes in this area.

For model A the following parameters were selected for the geometry of the future volcanic field: the

center is located in the middle of past volcanism in Crater Flat, the field elongation is N 10°W, and the field aspect ratio is two. The dikes generated for 1000 random events are illustrated in Figure 7-2. A much larger number of dikes (100,000) is used for the actual estimates of risk probability.

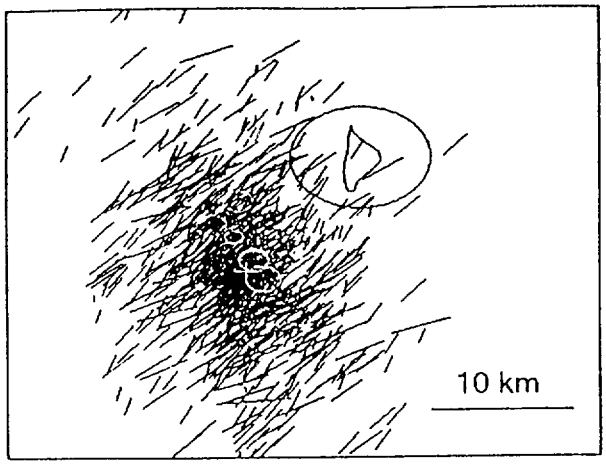

Figure 7-2. Distribution of 1,000 dikes generated by Model A.

Model B is considered to be less likely than model A. In this case the orientation of the future volcanic field is considered to trend to the NE, compatible with the near-surface stress field. The parameters used for the geometry of the volcanic field in this model are as follows: the center is located in the middle of past volcanism in Crater Flat, the field elongation is N35°E, and the field aspect ratio is two. The dikes generated for 1000 random events with a standard deviation of 10 kilometers in model B are illustrated in Figure 7-3.

Model C is considered to be the least likely scenario. This model considers that the center of renewed volcanism will be located at Lathrop Wells, the most recent of the volcanic centers. It also assumes that the aspect ratio of the new field will be narrow and that it will be oriented directly toward the proposed repository.

The parameters for the volcanic field used in model C are as follows: the center is located at Lathrop Wells, the field elongation is N15°E, and the aspect ratio is two. The dikes generated for 1000 random events with a standard deviation of 10 kilometers in model C are illustrated in Figure 7-4.

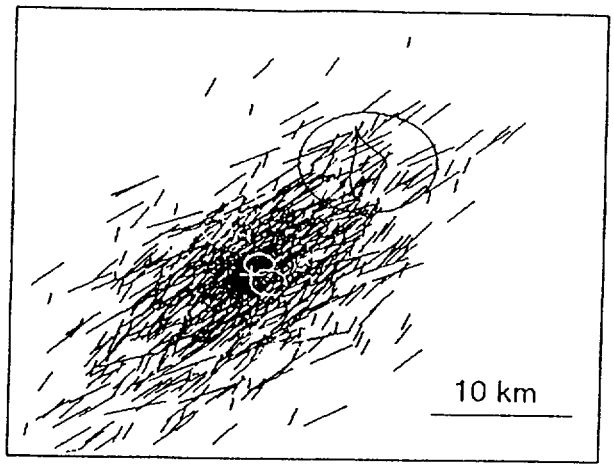

Figure 7-3. Distribution of 1,000 dikes generated by Model B.

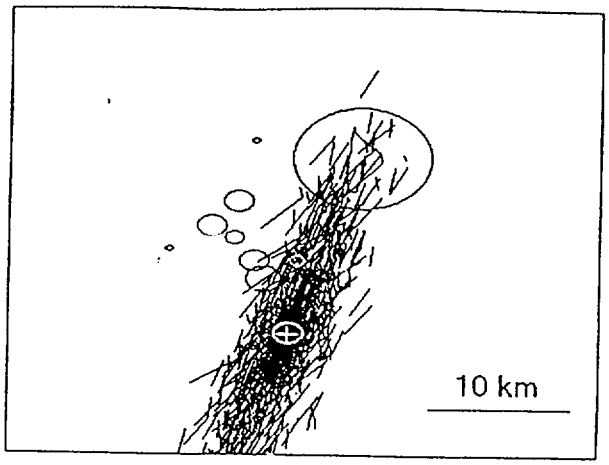

Figure 7-4. Distribution of 1,000 dikes generated by Model C.

Computer Code

The computer code for the proposed model was designed to accommodate geometries specified by various hypotheses of volcanism, including all that have been proposed in the literature. The code contains three main procedures. The first procedure generates locations for a large number of conduits

or dikes based on a set of input parameters that define the geometry of the supposed volcanic field. The second procedure traces the feeder dikes using additional parameters that specify the geometry of the dikes. A third procedure calculates the number of dikes within the proposed repository site.

The first consideration in the model is to constrain the geometry of the volcanic field because the limits of the volcanic field define the area in which dikes can occur. The shape of most volcanic fields are approximated by an elliptical outline (11, 12, 13, 14, 15). Ellipses for volcanic fields can be specified by four parameters: (1) their center point, (2) their size, in this case given by a Gaussian standard deviation of the major axis length, (3) the aspect ratio, which is the length divided by the width of the field, and (4) the orientation of the long dimension of the field. Manipulation of the standard deviation of the field size and its aspect ratio permit the generation of a wide variety of field shapes.

The second consideration in the model is the distribution of the conduits or centers of the dikes to be plotted within the bounds of the volcanic field. Surface features of volcanic fields, such as scoria cones, are more closely spaced near the center of their fields than near their margins (11, 15). With this constraint, the computer model locates the conduits or dikes based on a bivariate Gaussian distribution with a center in the midpoint of the volcanic field.

A Poisson distribution of volcanic vents has been used by some investigators (4, 5, 6). This distribution would produce somewhat larger probabilities than a bivariate Gaussian distribution. Because a Poisson distribution produces a nearly uniform spacing, it seems inappropriate for volcanic vents which deviate greatly from a nearly uniform spacing.

Considering that the location of volcanic eruptive features seem to be clustered at several scales with large gaps between clusters (11, 12, 15, 16), the distribution of the locations might better be modeled by a fractal algorithm. A fractal distribution of dikes would have a lower probability of intersection of the repository than bivariate Gaussian distributions because new dikes in a fractal model tend to cluster near existing vents which are at a great distance from the repository. The actual value of probabilities derived from a fractal distribution has not been computed.

The third consideration is the geometry of the dikes themselves. Dikes may be described by their location, length, and orientation (10). In the computer model each of these parameters is specified by a mean value and a standard deviation. After each dike is located, the length and orientation are

chosen from these Gaussian distributions according to the designated parameters. The dike routine traces a feeder dike for each volcanic event. Because of the independence of the generation of the location of dike centers and their geometry, it is possible to have a volcanic field elongated in a direction which depends on a deep feeding system and a dike field oriented in a different direction which depends on the near surface stress field.

Another procedure in the computer code counts the number of conduits or dikes that intersect the repository. Typically 100,000 dikes are plotted for each Monte Carlo simulation. The assumption is made that for such a large number of simulated dikes, the frequency of their intersections with the repository is a good estimate of the probability of such events.

The computer code can be set to loop through multiple sets of Monte Carlo simulations for a specified field and dike geometry by changing the value of the field standard deviation in increments through a specified range. These calculations create data for the variation in intersection frequencies with size of the field for each geometric model. The plot of field size versus intersection frequencies allows the probability of dike intersection with the proposed repository boundary to be estimated for various geometries of volcanic features.

Results of Monte Carlo Simulation

Points on the probability curves were calculated as the frequency of intersection of dikes with the outline of the proposed repository. Every point on the curve is based on a Monte Carlo simulation of 100,000 plotted dikes. Each curve consists of 41 points that represent the range of field standard deviations from 0 to 40 kilometers. Thus, each curve is constrained by tests of intersection for 4.1×10^6 dike locations.

The probability curves of dike intersection for each model exhibit the same general characteristics (Figures 7-5, 7-6, and 7-7). There is zero frequency of intersection for extremely small field sizes of less than about 4 kilometers. At a standard deviation larger than 4 kilometers there is a strong increase in frequency of intersections with increasing size of the field up to a well-defined maximum value. The maximum frequency occurs for standard deviations in the range of 15 to 20 kilometers. At larger standard deviations there is a gentle decrease in frequency of intersection with increasing field size. This decrease is a result of the more pronounced increase in spacing of dikes relative to their intersection rate as the field size grows.

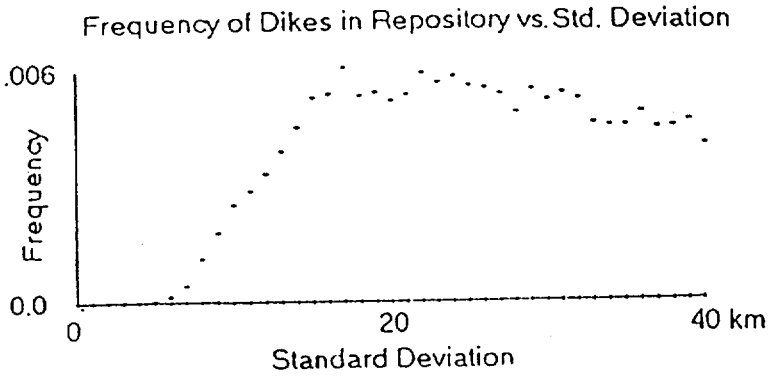

Figure 7-5. Probability function for a plot of field standard deviation vs. frequency of dike intersection for Model A.

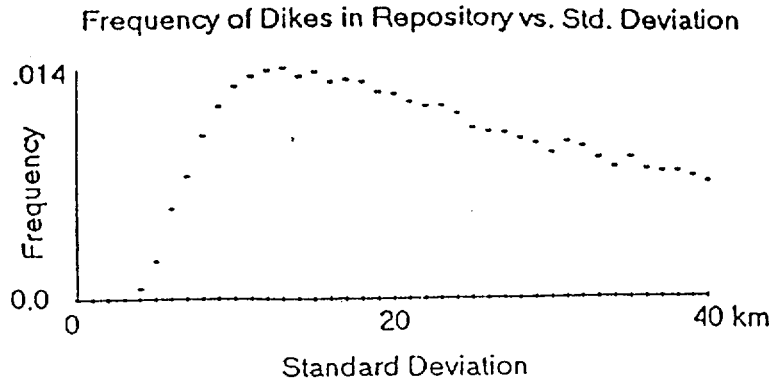

Figure 7-6. Probability function for a plot of field standard deviation vs. frequency of dike intersection for Model B.

A general interpretation of these results is that the maximum frequency value on each probability curve sets an upper bound on the frequency of a dike intersection based on geometry alone. For model A maximum probability is 6.0×10^{-3}, model B yields a maximum probability of 1.4×10^{-2}, and model C gives a maximum probability of 1.7×10^{-2}. These values serve as worst case bounds for the probability of volcanic dike intersections.

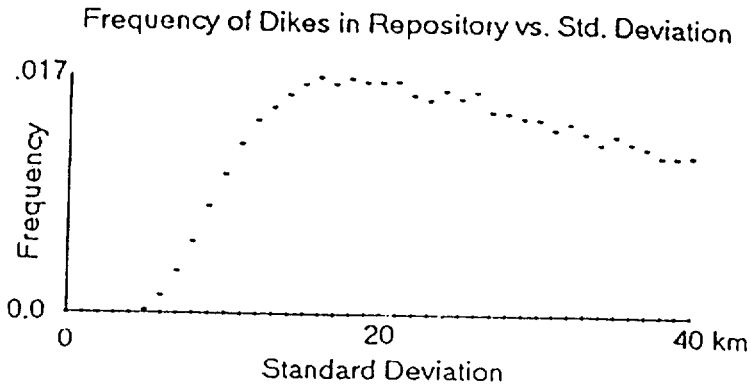

Figure 7-7. Probability function for a plot of field standard deviation vs. frequency of dike intersection for Model C.

A more reasonable estimation of the probability is to assume that the general size of a new volcanic field will be similar to that of the existing field. The present distribution of volcanic centers in Crater Flat has a standard deviation of about 8 kilometers. Using this value, the frequency of an intersection of a dike related to one of the three proposed models can be read from their respective probability curves. For model A the frequency of intersection for a standard deviation of 8 kilometers is 1.1×10^{-3}, for model B the probability at a standard deviation of 8 kilometers is 1.0×10^{-2}, and for model C the most likely probability is 5.3×10^{-3}.

EFFECT OF VOLCANISM

The effect of volcanism on the proposed repository depends on the location of the nearest volcanic source field, the frequency of volcanic events within this field, and the clustering of volcanic conduits within the field. Because the main clustering of recent volcanoes is tens of kilometers distant from the repository, certain constraints are intuitively obvious. A field with infrequent events and wide clustering or one with frequent events but a tight clustering would have extremely low probability of intersecting the repository site. Only a field with a moderate clustering of events (one standard deviation of 5 to 15 kilometers) with an average frequency of events (1.0×10^{-3} to 1.0×10^{-4} per year) would produce any significant probability of intersection with the repository.

A volcanic dike that directly intersects the proposed repository boundary has a high potential to

transport radionuclides due to the incorporation of repository materials into magma. Eruption of this material onto the surface could produce lavas or scoria and cinders that could form a cone or sheet of volcanic fragments. Conversely, the dike might not reach the surface and the lava could actually seal the canisters within the repository.

The calculations of estimated volume release of radio nuclides resulting from a dike intrusion at Yucca Mountain followed by the volume of lava production for a new volcano is schematically illustrated in Table 7-1. The value of 1.4 m^3 of radioactive waste contained in the volcanic products is the value used as a consequence of paths for models A, B, and C in the master logic tree.

Table 7-1

CALCULATION OF VOLUME OF HLW INCORPORATED INTO A DIKE

Volume of repository	3.0×10^7 m^3
Volume of lava within dike (low limit to reach surface) 1 m x 2000 m x 500 m	1.0×10^6 m^3
Average volume of erupted lava near Crater Flat	1.0×10^8 m^3
Fraction of foreign matter in erupted lava	6.0×10^{-4}
Total volume foreign matter erupted	6.0×10^4 m^3
Fraction of foreign matter actually from repository level (5 m / 300 m)	1.7×10^{-2}
Total volume of erupted material from repository level	1.0×10^3 m^3
Fraction of repository level that is actually HLW	1.4×10^{-3}
Total volume of HLW transported to the surface	1.4 m^3

The estimated release resulting from a hydrovolcanic crater within the proposed repository boundary is 281 canisters of radioactive waste. This is based on the assumption of a crater area at the repository level (430 m below the surface) of 7,850 m^2. However, due to the extremely low annual probability of such an occurrence (7.2×10^{-8}), a branch for hydrovolcanism was not included in the volcanology node of the master logic tree.

The change in water table caused by the intrusion of a volcanic dike into a zone surrounding Yucca Mountain is presented in Section 8. This calculation considers both the effects of heat and the effects of stress. Given an intrusion of a standard dike into the zone, a change of 1 m has a probability of 0.168, a change of 5 m has a probability of 0.579, and a change of 19 m has a probability of 0.253.

The spatial probabilities of dike intrusion into a zone with a radius of 10 kilometers around Yucca Mountain are computed from the Monte Carlo simulations for the three example models. The probabilities of intrusion for a field standard deviation of 8 kilometers are as follows: 1.2×10^{-2} for model A, 5.7×10^{-2} for model B, and 2.2×10^{-2} for model C. The full conditional probabilities can be computed by multiplication of the model probability, the spatial probabilities given above, and the temporal probability of a volcanic event (7.5×10^{-2}). The full logic tree would combine these factors.

LOGIC TREE FOR VOLCANISM

The volcanology node of the logic tree consists of three branches representing the three volcano models (Figure 7-8). There is no branch showing a hydromagmatic event because the calculated probability of such an event is low enough that it can be disregarded (see below).

All probabilities indicated on the logic tree assume a temporal frequency for a new dike occurrence to be 7.5×10^{-2} per 10,000 years as discussed above. The probability of a dike intersecting the repository, given a dike occurrence, is 1.1×10^{-3} for model A, 1.0×10^{-2} for model B, and 5.3×10^{-3} for model C, based on a field standard deviation of 8 km (see the discussion above of Figures 7-5 through 7-7). The frequency of dike intrusion per 10,000 yr. shown in Figure 7-8 is the product of the frequency of dike occurrence and the probability of intersection given an occurrence. The relative probabilities assigned to the three models are 0.6 for model A, 0.3 for model B, and 0.1 for model C. The calculated frequencies of occurrence are easily modified by assigning different parameters that describe different desired geometries.

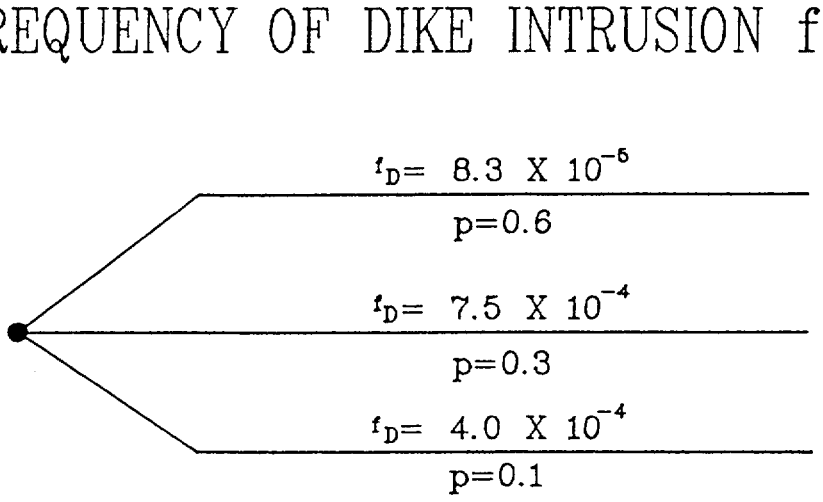

Figure 7-8. Logic tree mode showing frequency of volcanic dike intersecting repository.

Hydrovolcanism refers to volcanic events that involve an interaction between the magma and a hydrologic system. These eruptions are highly explosive and thus could present considerable risk, if they were a likely occurrence. The conditional probability for the hydrovolcanic path on the logic tree is a product of the temporal probability of a volcanic event (7.5×10^{-2}), the probability that the event is hydromagmatic (0.1), the probability that it intersects the repository (2.0×10^{-3}) and the probability that the crater is as deep as the repository level (4.8×10^{-3}). The depth of a hydromagmatic crater was taken from a Weibull distribution using the parameters (1.1, 95). This yields an expected depth of 91 meters with a maximum probability of 0.24. Only 1.3% of the hydromagmatic events would be deeper than 380 meters, the average depth of the repository. Because the conditional probability of the hydrovolcanic path is so small (7.2×10^{-8}), the risk of hydrovolcanism to the Yucca Mountain site can be considered to be negligible.

SUMMARY

This section presents a new Monte Carlo model for calculating the probabilities of volcanic risk at Yucca Mountain. The model uses temporal and spatial probabilities to calculate the conditional probability of volcanic features for various models proposed for this area.

These probabilities are assigned to volcano-related branches of the master logic tree. The generality of this framework allows consideration of any existing or new conceptual models of volcanism.

Various field and dike geometries can be plotted and their corresponding probability curves determined. Using these curves it is easy to determine the probability for any geometry including worst case scenarios. Probabilities determined by this method are useful for logic tree or other forms of probability analysis.

An interesting conclusion of this report is that upper bounds are defined for the probability of intersection of volcanic dikes with the boundary of the proposed repository, for any configuration of volcanic fields generated by the model. For very small fields (a standard deviation of field elongation less than 4 kilometers) the probability of intersection of a volcanic feature with the repository is negligible. For standard deviations of field size between 4 and 16 kilometers the probability of intersections increases up to a maximum value that depends on field and dike geometry. Increase of the field size beyond about 16 kilometers causes a decrease in the frequency of intersections. This results because the spacing between individual dikes increases at a faster rated than the frequency of intersection of dikes with the repository. Thus, the maximum probability of intersection on these curves is a worst case estimate for each field configuration. The worst case probability for bivariate Gaussian distributions of dikes is measured by this technique is between 0.01 and 0.001. These models allow the effect of volcanism near Yucca Mountain to be included in a performance assessment in a rational manner.

REFERENCES

1. B. M. Crowe, and W. J. Carr. *Preliminary Assessment of the Risk of Volcanism at a Proposed Nuclear Waste Repository in the Southern Great Basin.* Technical Report Open-file 80-357, U.S. Geological Survey, 1980.

2. B. M. Crowe, M. E. Johnson, and R. J. Beckman. "Calculation of the Probability of Volcanic Disruption of a High-level Radioactive Waste Repository Within Southern Nevada, USA." In *Radioactive Waste Management and the Nuclear Fuel Cycle.* Harwood Academic Publishers GMBH, 3(2):167-190, 1982.

3. B. M. Crowe, S. Self, D. Vaniman, R. Amos, and F. Perry. "Aspects of Potential Magmatic Disruptions of a High-level Radioactive Waste Repository in Southern Nevada." *Jour. Geol.*, vol. 91, 1983a, pp.259-276.

4. B. M. Crowe, D. T. Vaniman, and W. J. Carr. *Status of Volcanic Hazard Studies for the Nevada Nuclear Waste Storage Investigations.* Los Alamos Nat'l Laboratory, Report LA-9325-MS, 1983b.

5. B. M. Crowe. "Volcanic Hazard Assessment for Disposal of High-level Radioactive Waste." In *Active Tectonics*, Nat'l Acad. Press, 1986a, pp. 247-260.

6. B. M. Crowe, K. H. Wohletz, D. T. Vaniman, E. Gladney, and N. Bower. *Status of Volcanic Hazard Studies for the Nevada Nuclear Waste Storage Investigations.* Los Alamos Natl Laboratory Report LA-9325-MS, vol. II, 1986b.

7. B. M. Crowe and F. V. Perry. "Volcanic Probability Calculations for the Yucca Mountain Site: Estimation of Volcanic Rates." *ANS Symposium Volume*, in press.

8. E. I. Smith, D. L. Feuerbach, T. R. Neumann, and J. E. Faulds. "The Area of Most Recent Volcanism Near Yucca Mountain, Nevada: Implications for Volcanic Risk Assessment." *Proc. Intl High Level Waste Disposal*, April 1990.

9. D. L. Feuerbach and E. I. Smith. "Structural Control of Pleistocene Volcanism in Crater Flat, Nevada." *Geological Society of America Abst. with Progams*, 22, 1990.

10. A. Gudmundsson. "Form and Dimensions of Dykes in Eastern Iceland. *Tectonophysics*, vol. 95, 1983, pp. 295-307.

11. C. D. Condit, L. S. Crumpler, J. C. Aubele, and W. E. Elston. "Patterns of Volcanism Along the Southern Margin of the Colorado Plateau: The Springerville Field." *Jour. Geophys Res.*, vol. 94, no. B6, 1989, pp. 7975-7986.

12. T. Hasenaka and I. S. E. Carmichael. "The Cinder Cones of Michoacan-Guanajuato, Central Mexico: Their Age, Volume, and Distribution, and Magma Discharge Rate." *Jour. Volcan Geotherm Res.*, vol. 25, 1985, pp. 105-124.

13. R. G. Luedke and R. L. Smith. *Map Showing Distribution, Composition, and Age of Late Cenozoic Volcanic Centers in Arizona and New Mexico.* US Geological Survey Misc. Field Inves., Map I-1091-A, 1978.

14. R. G. Luedke and R. L. Smith. *Map Showing Distribution, Composition, and Age of Late Cenozoic Volcanic Centers in California and Nevada.* US Geological Survey Misc. Field Inves., Map I-1091-C, 1981.

15. D. H. Scott and N. J. Trask. *Geology of the Lunar Crater Volcanic Field, Nye County, Nevada.* US Geological Survey Prof Paper 399-I, 1971.

16. E. W. Wolfe, G. E. Ulrich, R. F. Holm, R. B. Moore, and C. G. Newhall. *Geologic Map of the Central Part of the San Francisco Volcanic Field, North-central Arizona.* US Geological Survey Misc. Field Studies, Map MF-1959, 1987.

Section 8

TEMPERATURE CHANGES CAUSED BY WASTE EMPLACEMENT

by

Benjamin Ross

INTRODUCTION

Until recently, most calculations of repository temperatures for an unsaturated-zone repository at Yucca Mountain included only conductive heat transfer and ignored gas-phase heat convection. This was due in part to the emphasis in earlier high-level waste disposal research on sites where the gas phase is not present, and in part to the difficulty of calculating convective heat transfer in the subsurface.

In the last few years, several studies of heat transfer at Yucca Mountain that include convection have been published. These analyses have greatly clarified the physical mechanisms that may be at work in the repository and provide substantial information about what temperatures may be expected given different assumptions about fluid flow mechanisms and repository operations. But, as will be seen below, none of the published studies is fully adequate to determine the temperature regime in the planned repository.

This Section will review the mechanisms that may be expected to govern heat transfer in the repository environment, survey published analyses that take convection into account, describe heat transfer regimes that the literature suggests are most likely to occur, present scenarios for repository temperature, and discuss the plausibility of each scenario.

MECHANISMS OF HEAT TRANSFER

In a porous medium, heat can be transferred by both conduction and convection. (Radiation is not significant because temperatures are relatively low and the rock matrix is opaque.) Heat transfer can be complicated because both liquid and gas phases can move and several driving forces are present. Table 10-1 lists physical processes that would play a major role in controlling heat transfer under conditions that might plausibly exist around a repository at Yucca Mountain.

Heat conduction is a relatively straightforward process; the complications arise from convection. Convection can carry both sensible and latent heat. Analyses to date indicate that, as long as temperatures are below the boiling point of water (about 96°C at repository elevation), the tuff will be wet enough to keep the relative humidity close to 100% (1, 2, 3, 4, 5).

Table 8-1

POTENTIALLY SIGNIFICANT PHYSICAL PROCESSES AFFECTING TEMPERATURE AT YUCCA MOUNTAIN

- Heat conduction
- Sensible heat convection
- Latent heat convection (with evaporation and condensation)
- Gas flow away from evaporation zones
- Buoyant gas flow
- Water removal by gas flow
- Suction-driven liquid flow
- Gas-phase diffusion
- Silica redistribution in liquid phase and precipitation
- Removal of water and heat by ventilation

In this situation, the latent heat component of convective heat transfer will be greater than the sensible heat component. At temperatures close to the boiling point but below it, the latent heat component will be much greater.[1] Only above the boiling point, when the partial pressure of water vapor no longer varies with temperature, may sensible heat be a larger component of convective heat transfer than latent heat.

---

[1]This can be seen from the following approximate argument. When a fluid through a temperature gradient, the amount of sensible heat transported is proportional to its specific heat c_p; whereas the latent heat transport is proportional to the heat of vaporization of water multiplied by the change in vapor content of the gas per unit change in temperature. For an ideal gas, the latter quantity is $(H_v/P)\ dP_v/dT$, where P is total pressure and P_v is vapor pressure. At room temperature, H_v is 539 cal/gm-K and $1/P\ dP_v/dT$ is 0.002 K^{-1}. Thus $(H_v/P)\ dP_v/dT$ is about 1 cal/gm while c_p is 0.24 cal/gm. Because dP_v/dT increases rapidly with temperature, the disproportion between latent and sensible heat transfer is even greater at higher temperatures. Use of an exact equation for heat transfer in a wet porous medium (6) does not change the qualitative conclusion of this analysis.

Two mechanisms of highly efficient latent heat transfer at Yucca Mountain have been hypothesized. These are the "heat pipe" effect and repository-scale buoyant gas flow.

The heat pipe effect can occur when the temperature of the porous medium reaches the boiling point of water. Its mechanism is as follows. Where the temperature exceeds the boiling point, the vapor pressure exceeds atmospheric pressure, and therefore, the partial pressure of water vapor must be substantially less than the vapor pressure. The liquid phase is in local thermodynamic equilibrium with the gas, so the suction is controlled by the equation for vapor-pressure lowering and must be very large, on the order of a kilobar. (Note that RT at 96°C is equivalent to approximately 1.7 kbar.) This creates an extremely strong gradient of capillary suction in the liquid phase. If liquid water is able to flow through the medium, it is drawn by this suction gradient toward the heat source. As the liquid water flows inward, it warms and evaporates, forming vapor and thus raising the gas pressure. The resulting gas-phase pressure gradient drives an outward flow of gas. When the vapor reaches cooler regions, it condenses and again returns toward the heat source under the influence of suction. By this mechanism, the same water can pass through many cycles, transporting its heat of vaporization each time.

Buoyant heat flow is driven by the temperature difference between the repository and surrounding cooler rock, reinforced by the geometry of Yucca Mountain. Gas near the repository will be warmer than gas at the same elevation elsewhere, so it will rise. Near the repository, temperatures will probably be highest at the repository elevation. The upward-moving gas will therefore warm beneath the repository, evaporating water and absorbing heat. Above the repository it will cool, condensing water and releasing heat. Thus convection will, in general, move heat from below the repository to above it, in contrast to conduction which moves heat away from the repository in both directions.

The driving force for convective gas flow depends on the total difference in weight between gas columns within and outside the repository. Just as a tall chimney draws a better draft than a short one, the gas flux driven by the repository-scale system will be greater than the flux would be in a smaller system.

The region around a nuclear waste repository in a partially saturated porous medium can be divided conceptually into three different zones, in which different heat transfer mechanisms dominate (Figure 8-1). Far from the heat source, the temperature is less than the boiling point and either conduction or convection may dominate heat transfer. Within this zone is a heat-pipe region where the

temperature is very close to the boiling point and heat is transferred very efficiently. Closest to the waste is an inner zone heated above the boiling point, in which liquid water is absent and heat transfer is dominated by conduction. Depending on the temperature attained, not all of these zones may be present.

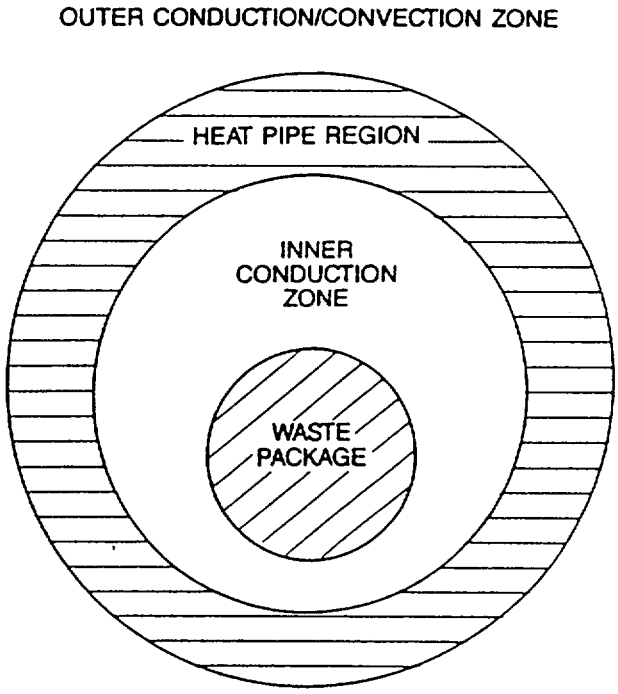

Figure 8-1. Zones of different heat-transfer regimes around an unsaturated-zone heat source, shown schematically. [Modified from (3).]

The situation is further complicated by some other processes that might modify these heat transfer mechanisms. Both heat and water will be removed in ventilation air while the repository operates. Heat removal will tend to lower temperatures, while removing water, a heat transfer medium, will tend to raise temperatures. Water could also be removed from the system by gravity drainage from zones of condensation. Water redistributed by the heat of the repository would be likely to dissolve silica, which when it reprecipitates could reduce fracture permeability (7). None of these processes has been studied very much, so their significance is difficult to assess.

ANALYSES OF REPOSITORY TEMPERATURE

All published Yucca Mountain heat transfer calculations that include convection use some version of the TOUGH computer program, which was developed by Pruess (8, 9, 10).

The first of these analyses was by Tsang and Pruess (1), who simulated a radial cross-section of a disc-shaped repository in a homogeneous block of welded tuff extending from the ground surface to the water table. The fractured porous tuff was treated as an effective continuum, using a "sequential saturation" relative permeability curve by which fractures do not conduct any appreciable amount of water until the matrix is entirely saturated. The total permeability of the fractured tuff was $1.8 \times 10^{-14} m^2$. Tsang and Pruess found that the average temperature at the repository horizon rose no higher than 93°C. (This result did not exclude the possibility of higher temperatures near waste canisters; the grid was too coarse to distinguish variations on the scale of individual waste packages or rooms.) Calculated gas fluxes (Darcy velocities) did not exceed tens of cm/yr near the repository. These fluxes were dominated by water vapor flowing away in both directions from a zone of elevated pressure caused by water evaporation coupled to gas-phase diffusion phenomena; the fluxes due to buoyancy were much smaller.

Nitao (2) used a modified version of TOUGH to simulate a tall, thin two-dimensional column of rock which reached 573 m from the ground surface to the water table but whose width extended only 18.9 m from a waste canister to the middle of the adjoining pillar. The bulk permeability of the fractured medium was $1.8 \times 10^{-14} m^2$, with a sequential-saturation relative permeability curve. Temperatures at waste canister surfaces rose to a peak value of approximately 200°C at a time 25 yr after waste emplacement. (A peak temperature value only a few degrees higher was obtained in a simulation with no convection, but convection lowered canister temperatures noticeably at times after 600 yr.) However, the area in which temperatures exceeded the boiling point extended only about 10 m from the canisters, and the central portions of pillars were in a heat-pipe region where temperatures never rose above the boiling point. The sizes of the dried-out region and the heat-pipe region reached maximums at approximately 400 yr, and at about 1200 yr the canister surface temperature fell below the boiling point. Gas fluxes were on the order of 1 cm/yr, except in the heat-pipe region where they sometimes exceeded 100 m/yr.

White and Altenhofen (11) extended Nitao's work by examining the sensitivity of temperatures to different assumptions about the permeability and porosity of the tuff and the amount of water in the system. They found that increased permeability and moisture availability had a relatively small effect

on maximum canister temperatures, but could drastically shorten the time period during which liquid water is excluded from the canister surface.

These calculations have some important common features. They all use an effective continuum approximation for the fractured porous tuff, with a sequential-saturation model for the relative permeability. They also do not fully treat buoyant gas flow, either because of a low value of permeability (3, 4) or geometrical limitations (2, 11).

The effective continuum approximation (by which the fractures and matrix pores are approximated by a single porous medium) was analyzed in detail by Pruess et al. (3, 4), who derived criteria for its validity. Generally, the acceptability of the approximation improves for more permeable rock matrix and larger times. At times of less than one year, the approximation is marginally acceptable for permeabilities like those of welded tuff matrix. At later times, the acceptability of the approximation improves. Considering the many other imperfections in temperature calculations, the calculations of Pruess et al. (3, 4) indicate that the effective continuum approximation is a minor source of uncertainty in long-term repository temperature calculations at Yucca Mountain.

The effect of the sequential-saturation assumption was studied by Doughty and Pruess (5), using a semianalytical solution for the transient two-phase fluid flow and heat transfer around a linear heat source. This solution incorporates all of the phenomena included in the TOUGH simulations except gravity and temporal decay of the heat source. Space and time dependences are combined into a single variable, making the results easier to visualize. While this solution cannot be applied to realistic repository geometries, it clarifies the nature of controlling physical processes and the roles played by the various parameters of the problem. Calculations with a permeability of 10^{-11} m^2 and sequential saturation yielded results consistent with those of Nitao (2) and White and Altenhofen (11), with a heat pipe region of moderate size. When parameters were changed to make water more mobile in the fractures, the heat pipe expanded to traverse nearly an order of magnitude of the combined space and time variable. Numerical simulations by Pruess et al. (4) with a similar geometry, a transient heat source, and discrete fractures in the tuff yielded similar results, with canister-surface temperatures never exceeding the boiling point when water was mobile in the fractures.

The potential significance of buoyant gas flow can be assessed by using gas flow simulations by Ross et al. (12), which assumed a welded-tuff permeability of 10^{-11} m^2. Calculated gas fluxes were tens of cm/yr under pre-construction conditions and rose to values of several m/yr when the repository horizon

reached a temperature of 57°C. This is nearly two orders of magnitude larger than the gas fluxes calculated by Nitao. Yet in Nitao's calculations, convection reduced calculated temperatures by about 5° to 10°C even in regions where temperatures remained below the boiling point (see especially his Figures 10 and 11).[2] It is therefore plausible that the much larger convective fluxes calculated by repository-scale simulations could play a dominant role in heat removal. The same suggestion is made by the observation that under current conditions as much geothermal heat may be transferred upward through the Yucca Mountain unsaturated zone by gas convection as by conduction.

SCENARIOS FOR HEAT TRANSFER AT YUCCA MOUNTAIN

The above considerations suggest three different heat transfer regimes that might plausibly occur at Yucca Mountain:

- A regime in which the fractured tuff has a relatively low gas permeability, as simulated by Tsang and Pruess (1). Heat transfer is conduction-dominated and there is little buoyant flow. Liquid water is drawn toward the waste by suction and evaporates, raising the gas pressure. Gas moves away by pressure-driven mass flow.

- A regime in which the tuff has a high bulk permeability and a sequential-saturation relative permeability curve. A heat-pipe region develops, but its effectiveness depends on the matrix permeability of the tuff. A strong buoyant flow develops, but near the waste there may be a dried-out region in which conduction dominates heat transfer and buoyant flow does not remove heat effectively.

- A regime in which the tuff has a high bulk permeability and liquid water can flow relatively easily in fractures. Buoyant gas flow will remove heat quite effectively by latent-heat convection. If the temperature reaches the boiling point, a strong heat-pipe effect will develop.

---

[2]Some of the temperature effect of convection is due to one-time removal of heat of vaporization when water evaporates with rising temperature. This contribution would not be increased with a greater gas flux. However, it is doubtful that all or even most of the temperature lowering by convection shown in Nitao's results is due to this effect. One-time heat removal would cause a symmetrical temperature lowering above and below the repository. In Nitao's results, the temperature is lowered roughly twice as much below the repository as above. This is consistent with an effect of buoyant gas flow, which transfers heat from below the repository to above.

Even if the heat transfer regime were known, there would still be uncertainty about repository temperatures. For example, in the high-permeability sequential-saturation regime, it still is uncertain how much water will be removed by ventilation and drainage and how strong the effect of water removal would be. Furthermore, the published heat-transfer calculations are all based on the heat output of 8.5-year-old waste; some or all of the waste will be older when placed in the repository. How much cooler the repository would be if older waste is buried is uncertain, but conduction-only temperature calculations by Altenhofen and Eslinger (13) suggest that the effect could be substantial.

Maximum canister temperatures above the boiling point, at the boiling point, or below the boiling point thus all are possible.

In addition, no matter what the heat-transfer regime, the waste canisters will not all be at the same temperature. Initially, canisters will differ substantially in age and heat output; this alone will cause a substantial temperature variability (13). Temperatures will also be lower near the edge of the repository. Emplacement holes intersected by highly permeable fractures will experience better convective cooling than holes poorly connected with the fracture network. Holes toward which liquid water drains along fractures will be better cooled than others. These inhomogeneities may be amplified by hydrodynamic instabilities, which are common in fluid systems heated from below.

TEMPERATURE SCENARIOS

The uncertainty in repository temperature leads to three alternative scenarios. To allow the scenarios to be defined clearly, specific mechanisms that determine temperatures have been identified in each scenario. Other mechanisms might also be important, but they would probably yield scenarios similar to those defined here, because the three scenarios span a wide range of plausible repository temperatures.

The first scenario corresponds to sequential saturation of fractures with the heat-pipe effect and buoyant gas flow playing a limited role. Repository conditions are generally as predicted by Nitao (2). However, 10% of the canisters, which have lesser heat output or are located in a wet zone, reach temperatures no higher than the boiling point.

In the second scenario, a stronger heat pipe restrains temperatures. This might occur because water is mobile in fractures or because the repository's heat output is less than assumed in past calculations.

Temperatures of most canisters are held at the boiling point by the heat pipe effect. Some 10% of the canisters are in poor contact with the fracture network and have temperatures that rise higher.

In the third scenario, convective heat transfer by buoyant gas flow is very effective, and the repository temperature never even reaches the boiling point.

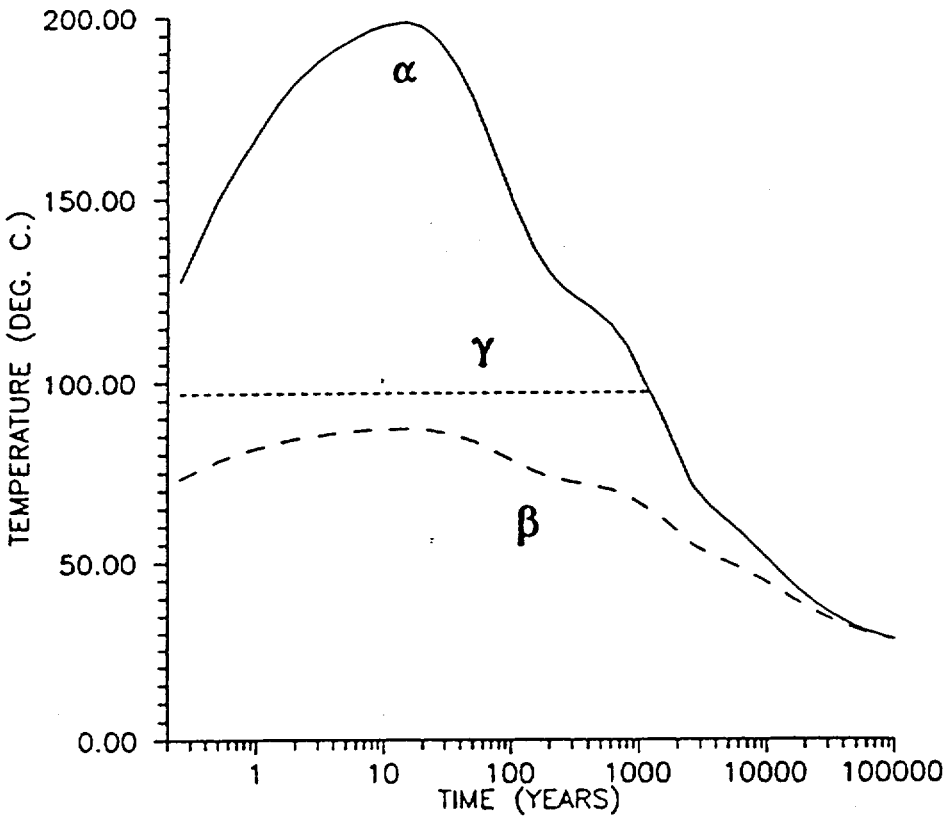

Figure 8-2. Three alternative curves showing temperatures at the outer surface of a waste emplacement hole as functions of time.

Curves showing the evolution of canister surface temperature over time are presented in Figure 8-2. These curves are intended as rough approximations that characterize different heat-transfer regimes. No effort was made to actually compute temperatures by mechanistically modeling the phenomena

discussed above.Curve α describes canisters whose temperature exceeds the boiling point. It is largely taken from Nitao (2). Nitao's calculations end at 2567 yr. Temperatures for times between 2567 and 100,000 yr were obtained by scaling the temperature increase (over an assumed final temperature of 27°C) at 2567 yr in proportion to the heat output of pressurized water reactor waste (taken from (14)). This extrapolation will be accurate to the extent that heat transfer away from the repository has reached a quasi-steady state by 2567 years. Close correspondence between the scaled heat transfer curve and Nitao's repository temperature curve for times shortly before 2567 years suggests that heat transfer may indeed have become quasi-steady by this time.

Curve β represents a case in which buoyant gas flow efficiently removes heat from the repository. It was obtained by scaling Curve α downward. The scaling factor was written as unity plus a term proportional to the temperature derivative of vapor pressure. The constant in the formula was chosen so that the maximum temperature was 87°C (an arbitrary value chosen to be slightly below the boiling point). The resulting formula was:

$$T_\beta = 27 + \frac{T_\alpha - 27}{.1 + 1.881\times10^{11}\,\exp\dfrac{-4883}{T_\beta + 273.14}\Big/(T_\beta + 273.14)^2} \qquad (8\text{-}1)$$

where the second term in the denominator is the temperature derivative of vapor pressure, using the Clausius-Clapeyron equation. The equation was solved by Newton's method.

Curve γ describes canisters whose temperatures are prevented by the heat-pipe effect from exceeding the boiling point. It was obtained from Curve α by reducing all higher temperatures to 96°C.

As discussed above, some scenarios have canisters following more than one temperature curve. The fraction of waste canisters following each of the three curves is given in Table 8-2.

SCENARIO LIKELIHOOD

Because the existence of three alternative scenarios reflects uncertainty in our scientific knowledge, the probabilities assigned to each scenarios are determined by the strength of the arguments that it is the correct one. We therefore will briefly present some of these arguments. (Future repository designs might lower repository temperatures or increase waste densities to maintain planned temperatures;

these possibilities are ignored here, and the present evaluations are based on currently planned waste densities.)

The primary argument for Scenario 1 is the high canister temperatures that have been calculated in all attempts to simulate heat flow at Yucca Mountain. As discussed above, each of these simulations omits at least one potentially important heat transfer mechanism, but there are also processes that could keep temperatures as high as calculated or even higher. Any mechanism that removes all the water from a region around the waste canisters will render ineffective such heat transfer mechanisms as the heat pipe and buoyant gas flow. In addition to the effects of high heat input and poor liquid return flow, which are included in published simulations, there are other water removal mechanisms not included in calculations to date. These include ventilation, gravity drainage through pillars and cooler portions of the repository, and possibly rapid drainage along large fractures passing through hotter areas. Field heating tests in tuff, although on different scales in time and space, do show substantial drainage of water out of the system and drying out (15, 16). Plugging of fractures by mineral precipitation might also block convective fluid flow.

Lower temperatures might be caused by several mechanisms. Buoyant gas flow, as discussed above, appears capable of removing large quantities of heat from a repository and has not been fully taken into account. Heat output from the waste also seems to be overestimated in the available calculations. Heat removal by ventilation might be substantial, especially if ventilation continues until the end of the period of waste retrievability.

Water might also be able to move in fractures more easily than assumed in calculations, strengthening the heat-pipe effect. There are several ways this might happen:

- If fracture linings composed of mineral precipitates or weathered tuff have properties intermediate between intact tuff matrix and open fractures, the sequential-saturation model for water transmission could be inapplicable.

- Water would move readily through fractures if the tuff matrix is initially saturated (5). If unsaturated-zone water flow at Yucca Mountain is controlled by a capillary barrier, a simple model (17) suggests that the tuff matrix in the repository horizon is currently saturated.

- The buoyant gas flow will cause more water to condense above the repository than below. Even if suction forces cannot effectively draw water through fractures, gravity would tend to drain this water down toward the heat source.

Notwithstanding these considerations, the majority of technical opinion currently holds that waste canister temperatures will exceed the boiling point of water. We therefore assign a probability of 0.6 to Scenario 1, in which the rock around most canisters dries out. Scenario 2, in which the heat-pipe effect dominates, is assigned a probability of 0.3, and Scenario 3, the coolest, is given a probability of 0.1.

Table 10-2 summarizes the three scenarios. For each scenario, it gives the probability of the scenario and the fraction of canisters following each of the three temperature histories shown in Figure 8-2.

Table 8-2

SUMMARY OF TEMPERATURE SCENARIOS AND FRACTIONS OF REPOSITORY AREA FOLLOWING EACH TEMPERATURE CURVE

Scenario	Probability	Curve α	Curve β	Curve γ
1	0.6	0.9	0	0.1
2	0.3	0.1	0	0.9
3	0.1	0	1.0	0

Figure 8-3 shows the corresponding logic tree node for repository temperature, with assigned probabilities for each branch.

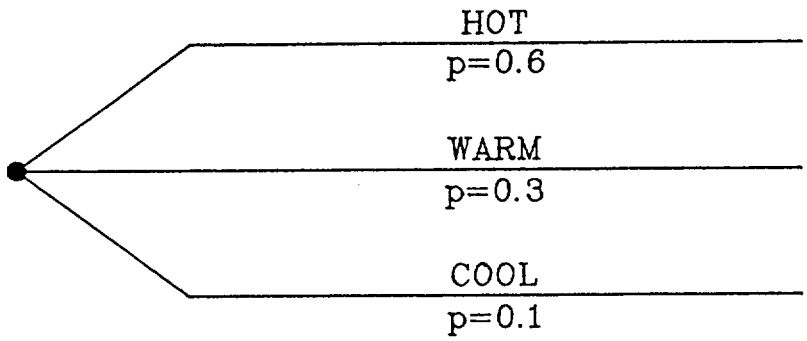

Figure 8-3. Logic Tree Node for Repository Temperature.

REFERENCES

1. Y. W. Tsang and K. Pruess. "A Study of Thermally Induced Convection Near a High-level Nuclear Waste Repository in Partially Saturated Fractured Tuff." *Water Resour. Res.*, vol. 23, 1987, pp. 467-479.

2. J. J. Nitao, *Numerical Modeling of the Thermal and Hydrological Environment Around a Nuclear Waste Package Using the Equivalent Continuum Approximation: Horizontal Emplacement.* Lawrence Livermore National Laboratory Report UCID-21444, May 1988.

3. K. Pruess, J. S. Y. Wang, and Y. W. Tsang. "On Thermohydrologic Conditons Near High-level Nuclear Wastes Emplaced in Partially Saturated Fractured Tuff: 1. Simulation Studies with Explicit Consideration of Fracture Effects." *Water Resour. Res.*, vol. 26, 1990, pp. 1235-1248.

4. K. Pruess, J. S. Y. Wang, and Y. W. Tsang.. "On Thermohydrologic Conditons Near High-level Nuclear Wastes Emplaced in Partially Saturated Fractured Tuff: 2. Effective Continuum Approximation." *Water Resour. Res.*, 26, 1990, pp. 1249-1261.

5. C. Doughty and K. Pruess. "A Similarity Solution for Two-phase Water, Air, and Heat Flow Near a Linear Heat Source in a Porous Medium, Lawrence Berkeley Laboratory Preprint LBL-30051, to be published in *Jour. Geophys. Research*, 1992.

6. S. Amter, N. Lu, and B. Ross. "Thermally Driven Gas Flow Beneath Yucca Mountain, Nevada. To be presented to American Society of Mechanical Engineers, Atlanta, December 1991.

7. W. Lin. "Variation of Permeability with Temperature in Fractured Topopah Spring Tuff Samples." In *Proc. High-Level Radioactive Waste Management*, Las Vegas, April-May 1991, pp. 988-993.

8. K. Pruess and J. S. Y. Wang. "TOUGH -- A Numerical Model for Nonisothermal Unsaturated Flow to Study Waste Canister Heating Effects. In *Scientific Basis for Nuclear Waste Management VII*, Mat. Res. Soc. Symp. Proc., vol. 26, edited by G. L. McVay, pp. 1031-1038, Elsevier, New York, 1984.

9. K. Pruess, *TOUGH User's Guide*. Lawrence Berkeley Laboratory Report LBL-20700 (also available as U. S. Nuclear Regulatory Commission Report NUREG/CR-4645), 1987.

10. K. Pruess, *TOUGH2 -- A General-Purpose Numerical Simulator for Multiphase Fluid and Heat Flow*. Lawrence Berkeley Laboratory Report LBL-29400, 1991.

11. M. D. White and M. K. Altenhofen. "A Sensitivity Study of Near-field Thermal and Hydrological Conditions in Tuff. In *Proc. Nuclear Waste Isolation in the Unsaturated Zone*, Las Vegas, September 1989, pp. 20-29.

12. B. Ross, S. Amter, and N. Lu. *Numerical Studies of Rock-Gas Flow in Yucca Mountain.* Disposal Safety Inc. Report 32, submitted to Sandia National Laboratories, February 1991.

13. M. K. Altenhofen and P. W. Eslinger. "Evaluation of Near-field Thermal Environmental Conditions for a Spent Fuel Repository in Tuff." In *Proc. High-Level Radioactive Waste Management*, Las Vegas, April 1990, pp. 402-409.

14. A. J. Mansure. "Thermal Decay Curves for PWR and BWR SF Waste." Memorandum to R. Hill, Sandia National Laboratories, February 13, 1985.

15. T. A. Buscheck and J. J. Nitao. "Modeling Hydrothermal Flow in Variably Saturated, Fractured, Welded Tuff During the Prototype Engineered Barrier System Field Test of the Yucca Mountain Project." Presented to TOUGH Workshop, Berkeley, September 1990.

16. T. A. Buscheck. "Field Heater Test, G-Tunnel." Presented to Workshop on Flow and Transport Through Unsaturated Fractured Rock, Tucson, January 1991.

17. B. Ross. "Quasi-linear Analysis of Water Flow in the Unsaturated Zone at Yucca Mountain, Nevada, USA." *Mem. Int. Assn. Hydrogeol.*, vol. 22, 1990, pp. 166-173.

Section 9

TIME-DEPENDENT, THERMO-MECHANICAL DAMAGE IN THE NEAR-FIELD ENVIRONMENT

by

John M. Kemeny and Neville G. W. Cook

INTRODUCTION

Yucca Mountain, Nevada is the proposed site for the underground storage of high level nuclear waste. The repository will be located in Topopah Springs tuff at a depth of approximately 350 meters. The host rock surrounding the underground repository will be subjected to thermal loads from the emplacement of the nuclear waste. Based on the current design as given in the Site Characterization Plan (1), the waste canisters will heat up the surrounding rock to a maximum temperature of 206°C twenty years after emplacement, followed by a rock temperature above 100°C for over 1000 years. This design does not consider the heat convection effects of water vapor in the rock near the canisters, which could put a ceiling on the rock temperatures at about 96°C. The design also assumes that the waste canisters are placed in the repository "hot", rather than letting them cool before emplacement. Understanding the thermomechanical response of the host rock to various thermal scenarios is one of the important issues for the design of the underground facility. In particular, the thermal load will result in a thermal stress in the rock, which, in conjunction with the pre-mining stress state, could damage the integrity of the near-field environment. For instance, microcracking and fracturing of the host rock near the waste canisters could increase groundwater flow. This could also result in a reduced life for the waste canisters, either by canister crushing from rock instability, or by causing a contact between rock and canister, and thereby increasing the likelihood of canister corrosion.

Models for predicting the response of the host rock to thermal loads should take into account the thermomechanical processes of rock damage that are occurring near the canister boreholes. These processes include microcrack growth, and the coalescence of microcracks into fractures and faults. The models must also take into account the time-dependence of rock deformation and failure. Finally, the models must give parameters that can be used to assess the changes in flow characteristics of the host rock and assess the potential for rock instability that could impact canister deterioration. Previous

experimental studies on rocks have shown that there are many different mechanisms by which extensile microcracks can initiate and grow under differential compressive stresses (2, 3, 4, 5, 6, 7). The result of these processes is a gradual degradation of the rock, starting well below the compressive strength and continuing past the peak stress into the strain softening region. Experimental studies have also shown that both time and rate-dependent behavior in brittle rocks is controlled by processes acting at the tips of cracks where stress concentrations exist (8, 9, 10). This time-dependent crack growth occurs at values of the stress intensity factor below the fracture toughness of the material, and is referred to as sub-critical crack growth. The time dependence of crack growth in tuff is of particular importance to predicting the 10,000 year behavior of the host rock at Yucca Mountain.

The work described in this paper focuses on the near-field environment in the repository, and is an extension of the works of EPRI (11) and Kemeny and Cook (12). In these works, a damage model was developed to analyze the stability of a two-dimensional circular opening in rock subjected to both far-field loading and a time-dependent temperature pulse at the boundary of the opening. Time dependency in rock deformation under compression was modeled by considering an elastic body containing cracks that grow under compressive stresses due to subcritical crack growth. The thermal and mechanical properties for TSw2 tuff were used, and the far field boundary conditions in the model considered the tectonic setting at Yucca mountain. Also, the temperature profile in the model was based on the placement of high level nuclear waste in a canister borehole. The damage model was initially used to determine the subcritical crack growth parameters for TSw2 tuff. Using these properties, the model was then run for 10,000 years under various scenarios of material strength, in-situ stress state, and temperature loading. It was found that under many realistic scenarios, borehole slabbing was predicted prior to 10,000 years. More specifically, based on likely variations in the material properties of the host rock and the in-situ stress state at Yucca Mountain, 38% of the boreholes were predicted to slab within 10,000 years.

The works of EPRI (11) and Kemeny and Cook (12) looked only at the rock conditions at the boundary of the canister boreholes. For this reason, those results did not give information on the extent of damage around the canister boreholes, or the change in the flow properties within the damage zone. In this paper the results have been improved, by implementing the damage model into a two-dimensional finite-element program. The results from this program now give the likelihood for slabbing of the borehole to occur, the extent of damage that occurs around the canister boreholes, and the increase in crack density in the damage zone. From the increase in crack density in the damage zone, the changes in the flow properties can be calculated. The final results of this analysis are

presented in the form of probabilities of different rock damage scenarios as a result of heat pulse associated with waste borehole construction and the emplacement.

STRESS AND TEMPERATURE BOUNDARY CONDITIONS

The boundary conditions for the problem are presented in Figure 9-1. A two-dimensional circular opening (plane strain) is subjected to far-field principal stresses σ_1 and σ_2, and to the walls of the borehole a uniform but time-varying temperature is applied. Here it is assumed that the canister boreholes will be located in TSw2 tuff (nonlithophysal Topopah Springs unit) at a depth of approximately 350 m. Our knowledge of the mechanical and thermal properties of the TSw2 tuff are limited, due to the limited number of core samples from this unit that have been tested. For the analysis presented here, the mechanical and thermal properties of TSw2 tuff are taken from Chapter 2 (Geoengineering) of the Site Characterization Plan (1). These properties are presented in Table 9-1.

Table 9-1

MATERIAL PROPERTIES USED IN THE DAMAGE MODEL

Material Property	Value(s) used in damage model	Source
Young's Modulus, E	3×10^{10} Pa	(1)
Poisson's Ratio, ν	0.25	(1)
Coef. Thermal Exp., α	8.8×10^{-6}/ C	(1)
Angle of initial microcracks, β	45°	(12)
Initial crack density, χ	0.4	(12)
Microcrack coef. of friction,	0.2	(12)
Length of initial cracks, l_o	0.0015 m	This work
Initial Microcrack Spacing l_o/b	0.23	(12)
Subcritical exponent, n	25	(12)
Subcritical constant, A	$5x10^{-2}$, $5x10^{-4}$, $5x10^{-6}$	(12)
Activation Enthalpy, H	$6x10^4$ J/mole	(10)

Thermal Stresses Due to Temperature Boundary Condition

The walls of the canister boreholes will heat up due to the high-level waste in the canisters. Due to uncertainties in the heat transfer effects of water vapor in the near-field environment, three scenarios are considered for the temperature distribution due to canister heating. The first scenario considers the case where heat transfer is conduction-dominated. This is the original conceptual design as described in the SCP (1). In this scenario, the temperature at the wall of the canister boreholes rises to 206°C after 20 years of emplacement, followed by a slow cooling over the next several thousand

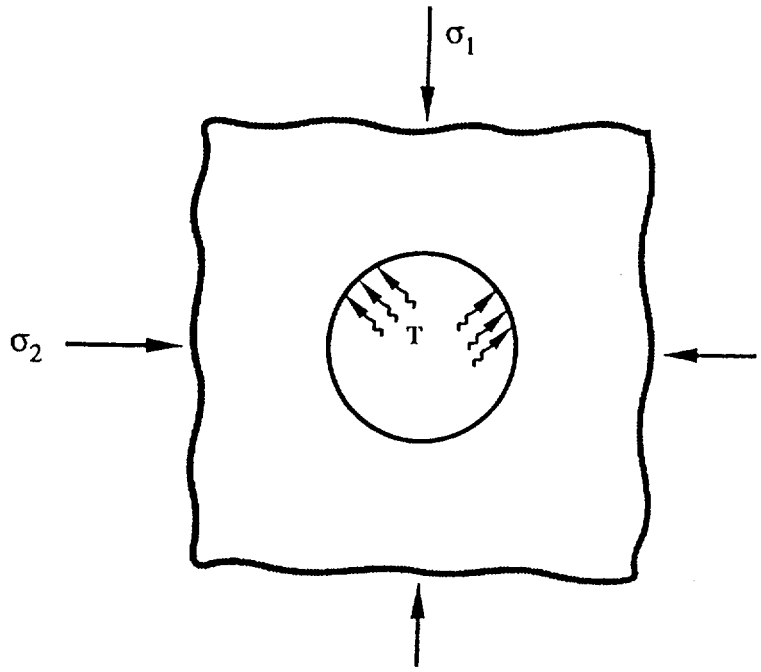

Figure 9-1. Boundary conditions for stress-temperature problem.

years (1). The second and third scenarios consider the phenomena of the heat-pipe effect and repository-scale buoyant gas flow. The second scenario considers a plateau in rock temperature at 96°C for the time period when the canisters are above the boiling point of water. The third scenario considers a maximum temperature of 87°C in the host rock. Details of these temperature scenarios are given in Section 8 of this report. The temperature distributions at the wall of the canister borehole for these three scenarios are approximated with the following functions:

Temperature Scenario I (Hot repository):

$$T(t) = 1.307 * t + 180 \qquad t < 20 \text{ years}$$
$$T(t) = 347.7 * t^{-0.1745} \qquad t \geq 20 \text{ years} \qquad (9\text{-}1)$$

Temperature Scenario II (Warm repository):

$$T(t) = 96 \qquad t < 1600 \text{ years}$$
$$T(t) = 347.7 * t^{-0.1745} \qquad t \geq 1600 \text{ years} \qquad (9\text{-}2)$$

Temperature Scenario III (Cool repository):

$$T(t) = 1.0*t + 67 \qquad t < 20 \text{ years}$$
$$T(t) = 147 * t^{-0.1745} \qquad t \geq 20 \text{ years} \qquad (9\text{-}3)$$

Based on the induced thermal stress due to a temperature imposed on the boundary of a circular opening in an infinite body (13), the thermal stresses due to the above imposed temperature boundary conditions are given by:

$$\sigma_r(\text{thermal}) = \frac{\alpha E(T(t) - T_o)}{2(1-\nu)}\left(1 - \frac{a^2}{r^2}\right) \tag{9-4}$$

$$\sigma_\theta(\text{thermal}) = \frac{\alpha E(T(t) - T_o)}{2(1-\nu)}\left(1 + \frac{a^2}{r^2}\right) \tag{9-5}$$

where α is the linear coefficient of thermal expansion, T_o is the ambient ground temperature (25°C used here), r is the radial distance to a position in the ground, a is the radius of the borehole, E is Young's modulus, and ν is Poisson's ratio.

Mechanical Stresses Due to Far-Field Loading

The mechanical stress in the near field depends on a number of factors, including the size, shape, and orientation of the underground drifts, the size, shape, and location (wall or floor of underground drift) of the canister boreholes, the in-situ stress state, and the material properties of the ground. Yucca Mountain is located in the Basin and Range Province, which is an extensional regime, cut by a series of normal faults. The exact in-situ stress state at Yucca Mountain is not known at the present time. The in-situ stress state at Yucca Mountain is most likely to be within the bounds of lithostatic and normal faulting as estimated below for the repository depth of 350 m:

Lithostatic

$$\sigma_v = \sigma_H = \sigma_h = 8\text{MPa} \tag{9-6}$$

Normal Faulting Limit

$$\sigma_v = 8\text{MPa};\ \sigma_h = 3\text{MPa};\ \sigma_H = 6\text{MPa} \tag{9-7}$$

where σ_H and σ_h are the magnitudes of the maximum and minimum principal horizontal stresses, respectively.

THERMO-MECHANICAL DAMAGE MODEL

Subcritical Crack Growth

Laboratory investigations have revealed that time-dependent rock deformation in brittle rocks at low and medium temperatures is associated with the growth, interaction, and coalescence of microcracks (8, 9). The actual time dependence of crack growth is due to rate-controlled processes acting at the tips of cracks, where stress concentrations exist. This time dependent crack growth occurs at values of the stress intensity factor below the fracture toughness of the material, and is referred to as subcritical crack growth. Subcritical crack growth can be caused by several different mechanisms, such as stress corrosion, diffusion, dissolution, ion exchange, and microplasticity (10, 14). The most common empirical equation used to describe subcritical crack growth in rocks is based on a power law formulation (15) given by:

$$\text{crack velocity} = A \exp(-H/RT)K_I^n \tag{9-8}$$

where H is the activation enthalpy, R is the gas constant, T is the absolute temperature, and where A and n are constants. K_I is the mode I crack tip stress intensity factor (16). As discussed by Atkinson and Meredith (14), A and n are functions of the material properties of the rock and changes in environmental conditions (humidity, type of reactive species, etc.). Here K_I is normalized with respect to an average K_{IC} for rock of 1 MPa$\sqrt{m}$, which leaves A with the units of m/sec.

Time-Dependent Damage Model

A damage model has been developed based on subcritical crack growth. The model considers an array of microcracks subjected to principal stresses σ_1 and σ_2, as shown in Figure 9-2. The growth of cracks under compressive stresses is formulated using the "sliding crack" model, which considers extensile crack growth caused by the sliding along pre-existing cracks. These extensile cracks grow in the direction of the maximum principal stress. Eventually some of these cracks will coalesce to form a large scale splitting fracture. Variables in this model include the angle of the microcracks β, the length of the initial microcracks l_o, the coefficient of friction along the microcracks , the average spacing between cracks b, and the crack density χ. The stress intensity factor for the sliding crack model which includes collinear crack interaction is given by:

$$K_I = \frac{2l_o\tau^*\cos\beta}{\sqrt{b\sin(\pi l/b)}} - \sigma_2\sqrt{2b\tan(\pi l/2b)} \tag{9-9}$$

where:

$$\tau^* = \frac{1}{2}\left[(\sigma_1 - \sigma_2)\sin 2\beta - (\sigma_1 + \sigma_2 + (\sigma_1 - \sigma_2)\cos 2\beta)\right] \quad (9\text{-}10)$$

The stress intensity factor solution, when combined with equation (9-6), becomes a nonlinear ordinary differential equation involving the time-varying stresses σ_1 and σ_2, crack length l, and time. When integrated numerically, it gives crack length as a function of time.

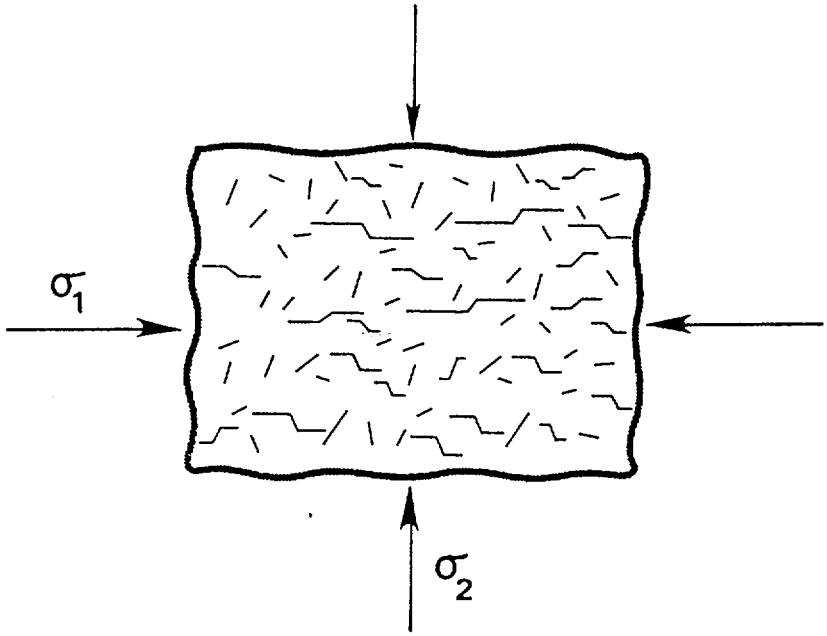

Figure 9-2. Model of microcracks subjected to principal stresses.

Single Element Example

As an example of the damage model under thermal and mechanical loads, consider the thin section of rock near the edge of the canister boreholes. For this thin rock area, the radial stress will be close to zero, and the tangential stress will have components due to both the mechanical and thermal loads. For this example, consider the thermal stress due to Temperature Scenario I in equation (9-1), and mechanical tangential stresses at the borehole boundary that vary from 0 to 30 MPa (referred to as $\sigma_\theta$mechanical). For this example, the subcritical parameters A and n are set to 5×10^{-4} and 25, respectively. The elastic and thermal properties used are for TSw2 tuff and are listed in Table 9-1. The micromechanical properties used are those that have been developed for TSw2 tuff from Kemeny and Cook (11) and are also listed in Table 9-1.

The tangential stress vs. time behavior near the borehole boundary under these conditions is shown in Figure 9-3. This shows a buildup of tangential stress for the first 20 years, followed by a decrease over the next several thousand years. The crack length vs. time behavior for the section of rock near the borehole under these conditions is presented in Figure 9-4. The crack lengths are normalized with respect to the distance between cracks, *b*. The normalized crack length, *l/b*, is a damage parameter that varies from l_o/b initially to 1 when the cracks have coalesced to form a macroscopic splitting fracture. For the three cases of $\sigma_\theta$mechanical=0, 10, and 20, Figure 9-4 shows that the relative crack lengths initially increase, and then stabilize at approximately t=20 years to *l*/b values of 0.22, 0.31, and 0.47, respectively. The reason for the stabilization is the decrease in tangential stress due to the canister cooling starting at 20 years. For the case of $\sigma_\theta$mechanical=30 MPa, however, the relative crack length approaches 1 prior to t=20 years and goes unstable.

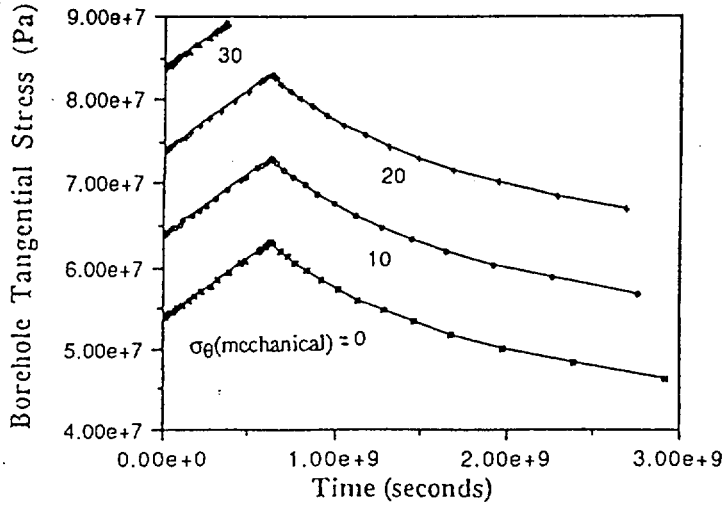

Figure 9-3. Tangential stress vs. time near borehole boundary.

Strain vs. time curves an also be calculated by utilizing relationships between effective rock moduli and crack length (17). Using these relationships, a plot of strain vs. time for the four cases of $\sigma_\theta$mechanical is presented in Figure 9-5. This shows that for the three stable cases, the strain initially increases and then unloads when cooling starts to occur, and for the unstable case, the strain only increases and becomes unbounded at t=11.6 years.

DETERMINATION OF SUBCRITICAL CRACK GROWTH PARAMETERS FOR TSW2 TUFF

The time-dependent properties, A and n, are normally determined from mode I fracture tests such as the double torsion test (14). These tests have not been conducted for TSw2 tuff. However, tests at different strain rates have been conducted, from which A and n an be determined with the use of the damage model described in the previous section. The damage model is modified to consider an applied uniaxial strain rate $\dot{\varepsilon}_o$ at the boundary of the rock rather than the time-varying stresses discussed previously (see (17)). For example, the results for two strain rates, 10^{-5}/sec and 10^{-7}/sec, have been analyzed using values for A and n of $5x10^{-4}$ and 25, respectively.

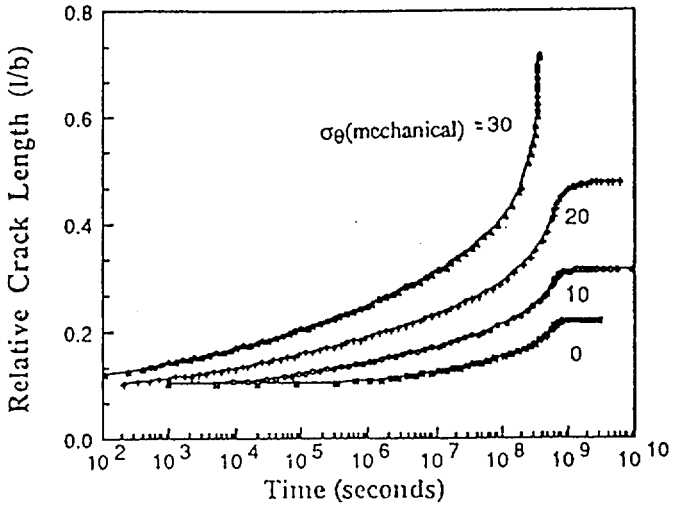

Figure 9-4. Relative crack lengths vs. time.

A comparison of the results from these runs with those of TSw2 tuff from the Site Characterization Plan (1) at the same strain rates are:

Strain Rate	Strength(model)	Strength(lab)	ε at failure(model)	ε at fail(lab)
10^{-5}/sec	171 Mpa	160 MPa	0.0043	0.0045
10^{-7}/sec	143 MPa	123 MPa	0.0036	0.0038

Based on the results above, values for A and n of $5x10^{-4}$ and 25, respectively, are used to represent the average strength values for TSw2 tuff. Significant variations in the strength values occur for TSw2 tuff, with values ranging from 45 to 320 MPa (1). This variation in strength can be simulated in the

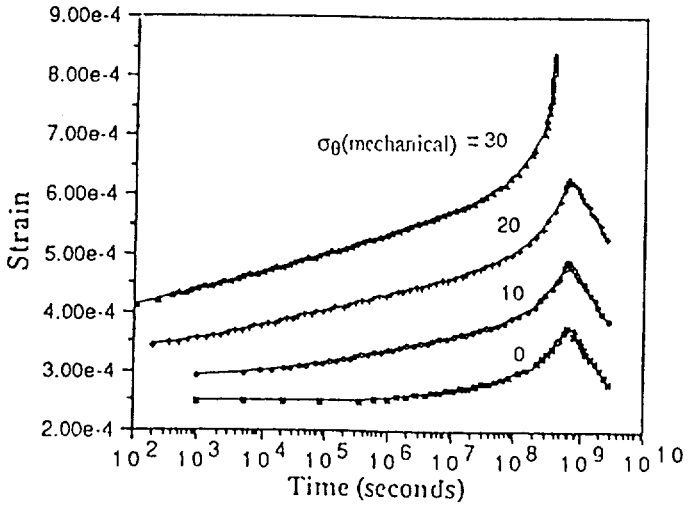

Figure 9-5. Strain vs. time near borehole boundary.

model by varying parameters A and n. For example, varying the parameter A from $5x10^{-2}$ to $5x10^{-6}$ (same properties as above, with $\dot{\varepsilon}_o = 10^{-7}$, n=25) results in strength changes from 110 to 180 MPa. Varying the exponent n from 15 to 35 results in only modest strength changes from 137 to 147 MPa. Based on this, we model weak, medium, and strong TSw2 tuff using A values of $5x10^{-2}$, $5x10^{-4}$, and $5x10^{-6}$, respectively (and using n=25).

FINITE ELEMENT FORMULATION

The damage model described above has been implemented into a two-dimensional (plane strain) finite-element code. In each of the elements, an initial distribution of cracks is considered that can grow, interact, and coalesce due to subcritical crack growth. Initially, an elastic solution at t = 0 is obtained. This elastic solution considers the effect of the initial distribution of cracks in each of the elements. From this elastic solution, the rate of crack growth in each of the elements is evaluated using equations (9-6) and (9-7). The model then marches forward in time, and the cracks are allowed to grow at the appropriate rate in each of the elements using equation (9-7) with an explicit Euler algorithm. Following an increment of crack growth at each time step, the elastic solution is recalculated. The changing crack lengths in each of the elements modifies the effective elastic properties for those elements. For a body that is initially isotropic, crack growth in the direction of the maximum principal stress will render the material anisotropic, and this must be taken into account

in the finite element calculations. In the case of an initially isotropic body, crack growth in the direction of the maximum principal stress will render the material transversely isotropic. The 3x3 matrix of material properties (5 independent elastic constants) that relates the two dimensional stress components with the two dimensional strain components for transverse isotropy is a measure of the damage that occurs in each of the elements due to crack growth and interaction. Details of this are given in (17).

The time-dependent temperature boundary condition at the boundary of the canister borehole results in a time-dependent thermal stress in the rock. The thermal stress is calculated using the formulas given in equation (9-4). These formulas give the radial and tangential thermal stresses as a function of time for the different temperature scenarios. The total stress in each element is the thermal stress calculated from equation (9-4) plus the mechanical stresses that result from the finite element equations. Changes in crack growth will probably result in changes in the coefficient of thermal expansion and thermal diffusivity. These changes have not been considered in this analysis.

The finite element mesh used to model the canister boreholes is shown in Figure 9-5. The mesh contains 112 elements. Far field stresses σ_1 and σ_2 are applied to the boundaries of the mesh. As an example, the results of a run with σ_1 = 20 MPa and σ_2 = 4 MPa, weak TSw2 tuff, and temperature scenario I is shown in Figure 9-5. This shows the relative crack growth, *l/b*, in each of the elements at t = 10,000 years. Figure 9-5 shows the formation of a thin damage zone around the opening. The extent of the damage zone is greatest in the direction perpendicular to σ_1.

FINITE ELEMENT RESULTS

The primary variables to be considered are the in-situ stress state, the material properties of the host rock, and the temperature distribution imposed on the wall of the canister boreholes. The approach taken here is to estimate probabilities associated with these different variables. A set of finite element runs is then made, and probabilities associated with the final results are determined.

In-Situ Stress State

Two bounds on the in-situ stress state are considered, normal faulting and hydrostatic, as given in equation (9-5). In addition, the canister boreholes can be situated either in the wall or floor of the underground drifts, and the parts of the canister borehole close to the drift will be subjected to stress concentrations from these drifts (the stress concentration from a circular-shaped drift is assumed). Also, for the normal faulting scenario, the drifts can be aligned either parallel or perpendicular to σ_h.

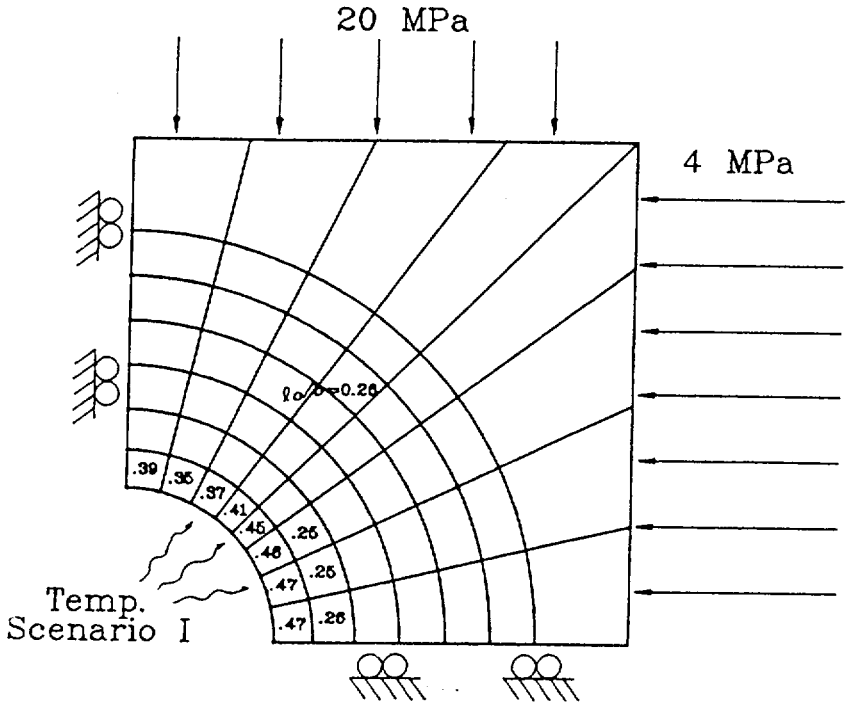

Figure 9-6. Finite element mesh and results for J_1 = 20 MP_a and σ_2 = 4 MP_a.

Overall, there are 12 scenarios for in-situ stress, and each of these 12 scenarios is given the same probability of occurrence (0.0833). The 12 possibilities are:

In-Situ Stress	Location-Orientation	Position along Borehole	Probability	σ_1, σ_2 (MPa)
Hydrostatic	wall	near drift	0.0833	16,8
Normal Faulting	wall - parallel to σ_h	near drift	0.0833	18,3
Normal Faulting	wall - perp. to σ_h	near drift	0.0833	21,3
Hydrostatic	floor	near drift	0.0833	16,8
Normal Faulting	floor - parallel to σ_h	near drift	0.0833	10,3
Normal Faulting	floor - perp. to σ_h	near drift	0.0833	6,1
Hydrostatic	wall	away from drift	0.0833	8,8
Normal Faulting	wall - parallel to σ_h	away from drift	0.0833	8,3
Normal Faulting	wall - perp. to σ_h	away from drift	0.0833	8,6
Hydrostatic	floor	away from drift	0.0833	8,8
Normal Faulting	floor - parallel to σ_h	away from drift	0.0833	8,6
Normal Faulting	floor - perp. to σ_h	away from drift	0.0833	6,3

These 12 scenarios have been reduced to four scenarios with grouped probabilities as given below:

σ_1	σ_2	Probability
20 MPa	4 MPa	0.17
16 MPa	8 MPa	0.25
8 MPa	8 MPa	0.25
6 MPa	2 MPa	0.33

Material Properties

Three rock material properties are considered; weak, medium, and strong. As discussed above, A values of 5×10^{-2}, 5×10^{-4}, and 5×10^{-6} are appropriate for weak, medium, and strong TSw2 tuff, respectively. The probability for each material property is based on the test results given in the Site Characteristics Plan (1). The results are:

Material	A	Probability
Weak	5×10^{-2}	0.31
Medium	5×10^{-4}	0.35
Strong	5×10^{-6}	0.34

Temperature Distribution

Three scenarios for the temperature loading of the canister boreholes are considered, as given in equations (9-1), (9-2), and (9-3). In addition, three sets of probabilities for the likelihood of these temperature scenarios are given, as discussed in Section 8. The three sets of probabilities for the temperature scenarios are labeled α, β, and γ, as given below:

	α	β	γ
Temperature Scenario I	0.9	0	0.1
Temperature Scenario II	0.1	0	0.9
Temperature Scenario III	0	1.0	0

Results

Based on four scenarios of in-situ stress, three scenarios of material property for the host rock, and three scenarios for temperature distribution, 36 runs were made with the thermomechanical damage model. A typical result is shown in Figure 9-6. The important aspects of the results include the

extent of the damage in the rock surrounding the borehole and the increased density of cracks in this damaged region. The crack density is defined by:

$$\chi = \frac{Nl^2}{V} \qquad (9\text{-}11)$$

where l is the half crack length, N is the number of cracks, and V is the volume (unit thickness is assumed). An initial value for crack density, χ_o, of 0.25 is assumed in each of the elements. With increasing crack growth, the crack density increases. The final crack density in the damaged zone at 10,000 years, χ_D has been calculated for each of the runs that have been made. In order to compare different runs, we take the final crack density in the damage zone for a given run to be the highest crack density for all the elements in the damage zone for that run. Also, from the modeling of TSw2 tuff we know that a macroscopic fracture will occur when the relative crack length, l/b, gets to approximately 0.5. For the material properties used in this analysis, this translates to a ratio of final crack density to initial crack density of 2.9 for a spalling fracture to occur. Finally, the extent of the damage zone is calculated for each of the runs that were made. Based on the criteria given above, the 36 runs were each put into one of the following four deformation patterns:

Deformation Pattern	Local Failure	Extent of Damage	Increased crack Density
Type 1	spalling	$r_D/r_o = 1.35$	$\chi_D/\chi_o > 4.8$
Type 2	spalling	$r_D/r_o = 1.16$	$\chi_D/\chi_o = 2.9 - 4.8$
Type 3	no spalling	$r_D/ro = 1.16$	$\chi_D/\chi_o = 2.0 - 2.9$
Type 4	no spalling	$r_D/ro = 1.16$	$\chi_D/\chi_o < 2.0$

Based on the probabilities for the different scenarios given above, the probability for the different deformation patterns is as follows:

Deformation Pattern	Hot Repository	Warm Repository	Cool Repository
Type 1	0.047	0.005	0
Type 2	0.303	0.034	0
Type 3	0.392	0.125	0.112
Type 4	0.258	0.836	0.888

These results are presented in the logic tree format in Figure 9-7.

Overall, the results indicate that the damage zone will be in most cases be limited to a thin zone around the borehole. The result indicate that under the present design of a "hot" repository, 35% of the boreholes will experience some kind of rock failure. This result agrees with the simplified analysis in Kemeny and Cook (12).

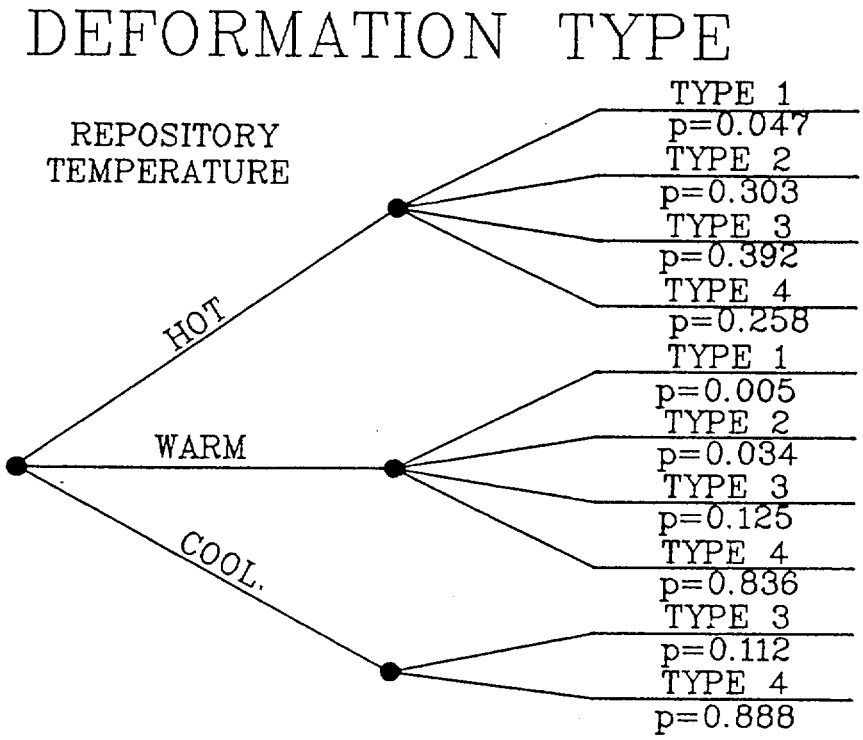

Figure 9-7. Logic tree for rock deformation

REFERENCES

1. DOE. *Site Characterization Plan*, U.S. Department of Energy report DOE/RW-0199, 1988.

2. W. R. Wawersik and W. F. Brace. 1971. "Post-failure Behavior of a Granite and Diabase." *Rock Mech.*, vol. 3, 1971, pp. 61-85.

3. T.-f. Wong. 1990. "A Note on the Propagation Behavior of a Crack Nucleated by a Dislocation Pileup." *J. Geophys. Res.*, vol. 95, 1990, pp. 8639-8646.

4. R. L. Kranz. "Microcracks in Rocks: A Review." *Tectonophysics*, vol. 100, 1983, pp. 449-480.

5. J. T. Fredrich and T.-f. Wong. 1986. "Micromechanics of Thermally Induced Cracking in Three Crustal Rocks." *J. Geophys. Res.* vol. 91, 1986, pp. 12743-12764.

6. Fredrich, J. T., Evans, B. and Wong, T.-f. 1989. Micromechanics of the brittle to plastic transition in Carrara marble. J. Geophys. Res. 94:4129-4145.

7. J. Zhang, T.-f. Wong and D. M. Davis. "Micromechanics of Pressure-induced Grain Rushing in Porous Rocks." *J. Geophys. Res.*, 1989, in press.

8. O. Sano, I. Ito, and M. Terada. 1981. "Influence of Strain Rate on Dilatancy and Strength of Oshima Granite Under Uniaxial Compression." *J. Geophys. Res.*, vol. 86, 1981, pp. 9299-9311.

9. N. L. Carter, D. A. Anderson, F. D.Hansen and R. L. Kranz. 1981. "Creep and Creep Rupture of Granitic Rocks." In *The Mechanical Behavior of Crustal Rocks*, Washington, DC: Geophysical Monograph 24, AGU, 1981.

10. B. K. Atkinson. "Subcritical Crack Growth in Geologic Materials." *J. Geophys. Res.*, vol. 89, 1984, pp. 4077-4114.

11. R. K. McGuire (ed.). *Demonstration of a Risk-Based Approach to High-Level Waste Repository Evaluation*, Palo Alto, Calif.: Electric Power Research Institute, 1990. NP-7057, Research Project 3055-2.

12. J. M. Kemeny and N. G. W. Cook. *Time-dependent Borehole Stability Under Mechanical and Thermal Stresses: Application to Underground Nuclear Waste Storage, Rock Mechanics as a Multidisciplinary Science.* Roegiers (ed.). Rotterdam: Balkema, 1991a, pp. 977-986

13. S. Timoshenko and J. Goodier. *Theory of Elasticity.* NY: McGraw-Hill, 1970.

14. B. K. Atkinson and P. G. Meredith. "The Theory of Subcritical Crack Growth with Applications to Minerals and Rocks. In *Fracture Mechanics of Rock*, B. K. Atkinson (ed.). London: Academic Press, 1987. pp 111-166.

15. R. J. Charles. "Static Fatigue of Glass." *J. Appl. Phys.* vol. 29, 1958, pp. 1549-1560.

16. B. R. Lawn and T. R. Wilshaw. 1975. *Fracture of Brittle Solids.* Cambridge: Cambridge University Press, 1975.

17. J. M. Kemeny and N. G. W. Cook. 1991b. "Micromechanics of Deformation in Rocks." In *Toughening Mechanisms in Quasi-Brittle Materials.* S. P. Shaw (ed.), Dordrecht, the Netherlands: Kluwer Academic Publishers, 1991b.

18. T.-f. Wong. 1982. "Micromechanics of Faulting in Westerly Granite." *Int. J. Rock Mech. Min. Sci.*, vol. 19, 1982, pp. 49-64.

19. T.-f. Wong. "Geometric Probability Approach to the Characterization and Analysis of Microcracking in Rocks." *Mech. of Mat.*, vol. 4, 1985, pp. 261-276.

20. D. K. Hallbauer, H. Wagner and N. G. W. Cook. "Some Observations Concerning the Microscopic and Mechanical Behavior of Quartzite Specimens in Stiff, Triaxial Compression Tests." *Int. J. Rock Mech. Min. Sci.*, vol. 10, 1973, pp. 713-726.

Section 10

ENGINEERED BARRIER SYSTEM FAILURE

by

Daniel B. Bullen

INTRODUCTION

The performance of the Engineered Barrier System (EBS) for containment of high-level radioactive waste in the deep geologic repository proposed for Yucca Mountain will significantly impact the total system performance of the facility. Previous studies by the EPRI-sponsored team (1) have shown that container lifetime is one of the critical parameters controlling the cumulative release of radionuclides from the repository. The current design of the EBS employs a single, thin-walled metal barrier comprised of an austenitic or copper-based alloy as the container as shown in Figure 10-1 (2). This metal barrier provides a vessel for handling and transporting the waste from a surface facility to the underground repository horizon. The metal barrier also acts as a containment barrier to provide "substantially complete containment" of the waste for a period of 300 to 1000 years after repository closure. For a period of up to 10,000 years, the container is projected to act as an isolation barrier, along with other components in the EBS, to limit the release of radionuclides to one part in 10^5 of the 1,000 year inventory of each radionuclide in accordance with the requirements of the Code of Federal Regulations (10 CFR 60, 40 CFR 191).

The use of thin walled containers in the Yucca Mountain environment is currently being reevaluated by the Yucca Mountain Project. The Nuclear Waste Technical Review Board (NWTRB) has recently stated that "high priority should be assigned to developing a more robust engineered barrier system" (3). This engineered barrier system could include the use of multiple, redundant barriers for waste containment, as well as the use of more corrosion resistant container materials. The potential use of alternate materials and multiple redundant engineered barrier systems provides an even greater challenge for the development of performance assessment models to accurately predict the release and transport of radionuclides to the accessible environment.

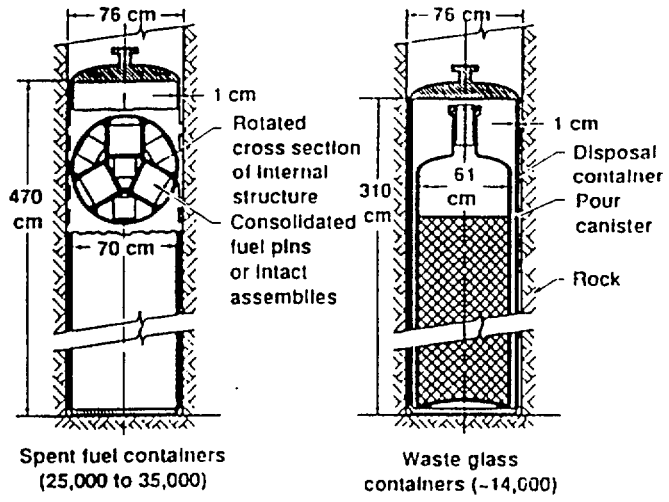

Figure 10-1. Schematic of proposed Yucca Mountain Project waste containers for spent fuel and borosilicate glass wastes.

The EBS failure model used in (1) identified a probabilistic model describing the cumulative container failure rate as a function of three parameters; (1) the mean container lifetime, (2) the threshold container failure time, and (3) the failure rate at the mean container lifetime. These parameters were the inputs for the Weibull distribution. This Section will describe the refinements to the model of engineered barrier system failure, which were developed as a part of the current effort. The modifications to the EBS failure model described in this Section include the development of mechanisms to evaluate the impact of "early container failures" on the performance of the overall EBS, the ability to evaluate multiple barriers with different performance characteristics, and the capability to address the potential impact of waste form failure rates (cladding failure rates and glass pour canister failure rates) on EBS performance.

EBS FAILURE MODELING

Although the current candidate materials for the EBS container include austenitic and copper-based alloys, a number of new container concepts have recently been proposed for HLW packages. Evaluation of the degradation mechanisms of these new materials and container concepts will require an extensive literature review and laboratory research effort. An extensive review of the literature to determine the potential degradation modes and failure mechanisms for the austenitic and copper-based candidate materials has already been completed (4). This review identified a number of possible

failure scenarios for the design basis, single metal, thin-walled container. These scenarios included failure due to general oxidation and corrosion, localized corrosion (crevice and pitting corrosion), stress corrosion cracking (primarily at the closure seal), degradation due to metastable microstructure, and embrittlement due to hydride formation. The most probable failure mechanism for the container is a function of the service environment, container material, method of closure, and the thermo-mechanical history of the material. Although it is difficult to predict the actual failure mechanisms, an assessment of the critical issues relating to container degradation centers on localized corrosion (pitting) or stress corrosion cracking associated with the closure seal of the metal barrier.

Numerous failure models for the candidate metal barrier materials have been reviewed by Farmer et al. (5). This review was completed to determine the applicability of models of candidate alloy degradation to the prediction of the long-term performance of the containers under repository conditions. The models address uniform oxidation and corrosion, localized corrosion, and stress corrosion cracking failure mechanisms. Due to the complexity of the degradation modes and the associated uncertainty in the actual environment of the repository horizon, an accurate evaluation of these models for the purpose of performance assessment is extremely difficult. Therefore, it was necessary to take a different approach to the development of an EBS failure mechanism and radionuclide release rate model.

The application of statistical techniques to the modeling of the failure of containers was undertaken to permit the development of a model for waste container failure rate. These statistical techniques included the utilization of the Weibull distribution, which is employed in many fields of engineering for component life prediction (6). Previous studies of the applicability of Weibull statistics to high-level radioactive waste container failure prediction were completed by Thomas (7). Thomas suggests that the three-parameter Weibull function may be applicable to the determination of EBS container failure rates. The cumulative distribution function for the Weibull distribution, C(t), which is the fraction of containers that have failed up to time (t), is given by:

$$C(t) = 1 - \exp\left[- \left(\frac{t-x}{f} \right)^b \right] \qquad (10\text{-}1)$$

where x is the lower limit of container lifetime, f is the mean container lifetime, and b is the Weibull slope (represents the failure rate at the mean lifetime).

Equation (10-1) is the basis of the model for EBS failure developed in this study. Weibull distributions are utilized in this study to represent the failure rates of individual barriers in a multiple barrier system.

The EBS failure model must also address the possible container failures that occur due to abnormal localized conditions, fabrication flaws, incorrect emplacement, and other parameters that may impact a small fraction of the total container population. These conditions could lead to early container failure. To address the need for an "early container failure" component of the EBS failure model, an additional exponential factor was added to the failure rate equation. This factor, D(t), which represents the fraction of containers that fail prior to the threshold failure time, is defined as follows:

$$D(t) = c_1 \left(1-\exp\left[-\left(\frac{t}{t_1}\right)\right]\right) \qquad (10\text{-}2)$$

where c_1 is the fraction of containers susceptible to early failure, and t_1 is the mean time for early container failure.

The failure rate of the waste form may also significantly impact the release rate of radionuclides from the EBS. This waste form failure rate will be dictated by the failure rate of the cladding material for spent fuel waste forms or by the failure rate of the pour canisters for borosilicate glass waste forms. The use of an additional Weibull distribution in the EBS failure model permits the evaluation of the impact of the waste form failure rate. The combination of the parameters for a single metal barrier container including waste form failure rates and the potential for "early container failures" yields an equation for the EBS failure rate given by:

$$C(t) = c_1 \left(1-\exp\left[-\left(\frac{t}{t_1}\right)\right]\right) + sa \left(1-\exp\left[-\left(\frac{t-x_1}{f_1}\right)^{b1}\right]\right)\left(1-\exp\left[-\left(\frac{t-x_2}{f_2}\right)^{b2}\right]\right) \qquad (10\text{-}3)$$

where:

- c_1 = fraction of containers susceptible to early failure
- t_1 = mean time for early container failure
- sa = step function operator
- x_1 = lower limit of metal barrier lifetime
- f_1 = mean metal barrier lifetime

b_1 = failure rate of the metal barrier at the mean lifetime (Weibull slope)

x_2 = lower limit of cladding lifetime

f_2 = mean cladding lifetime

b_2 = failure rate of the cladding at the mean lifetime (Weibull slope)

Equation (10-3) permits the evaluation of the impact of a number of parameters on the failure rate of a single metal barrier container under repository conditions. Values for the parameters employed in this equation can be derived from data available in the literature as described below.

The final adaptation of the EBS failure model addresses the use of a multiple barrier system with different failure rate parameters for each barrier material. The multiple barrier EBS may easily be modeled through the utilization of one additional Weibull distribution. The previous single barrier failure rate equation is multiplied by this additional Weibull distribution to produce a cumulative failure distribution. The cumulative failure distribution for the multiple barrier waste containers is given by:

$$C(t) = c_1\left(1-\exp\left[-\left(\frac{t}{t_1}\right)\right]\right)+sa\left(1-\exp\left[-\left(\frac{t-x_1}{f_1}\right)^{b1}\right]\right)\left(1-\exp\left[-\left(\frac{t-x_2}{f_2}\right)^{b2}\right]\right)\left(1-\exp\left[-\left(\frac{t-x^3}{f_3}\right)^{b3}\right]\right) \quad (10\text{-}4)$$

where:

c_1 = fraction of containers susceptible to early failure

t_1 = mean time for early container failure

sa = step function operator

x_1 = lower limit of metal barrier 1 lifetime

f_1 = mean metal barrier 1 lifetime

b_1 = failure rate of metal barrier 1 at the mean lifetime (Weibull slope)

x_2 = lower limit of metal barrier 2 lifetime

f_2 = mean metal barrier 2 lifetime

b_2 = failure rate of metal barrier 2 at the mean lifetime (Weibull slope)

x_3 = lower limit of cladding lifetime

f_3 = mean cladding lifetime

b_3 = failure rate of the cladding at the mean lifetime (Weibull slope)

Additional waste container barriers can easily be modeled through the application of additional Weibull distributions. Therefore, this model of container failure can be adapted to meet any design modifications required when site specific environmental data become available and container design modifications are made.

EVALUATION OF EBS PARAMETERS

The successful application of the EBS failure model described in the previous section requires the determination of applicable parameters, which describe the projected behavior of EBS container materials under repository conditions. The identification and evaluation of applicable parameters requires the evaluation of a system of deterministic models that describe container performance. Application of these models will also require the interpretation of currently available data that may be relevant to the behavior of candidate container materials under repository conditions.

The repository environment is projected to evolve as a function of time from an initially hot or warm, dry condition to a cool, moist condition as described in Section 8. This change in condition will occur over a period of 1,000 to 10,000 years depending upon the age and the areal power density of the emplaced waste. The accurate evaluation of the EBS failure rate input parameters requires some initial assumptions regarding container design, environmental conditions, and failure mechanisms. The initial EBS model developed under this project (1) employed scenarios in which mean container lifetimes ranged from 1,000 to 50,000 years. These lifetimes represented estimates for various container materials and designs. To provide a more quantitative justification for EBS failure rate parameter selection for the current study, simple models for EBS failure have been evaluated based on: (1) general oxidation and corrosion failure mechanisms for the hot, dry repository conditions, and (2) localized corrosion (pitting) for the cool, moist repository conditions. A brief review of applicable models for general corrosion and pitting corrosion for metals in a subsurface environment has been completed by Sullivan and Suen (8) for low-level radioactive waste disposal containers. These models are based upon currently available data for a number of metallic materials and may be applicable to the conditions expected for high-level radioactive waste disposal containers.

General Corrosion Model

General corrosion is assumed to be the dominant failure mechanism for the metal barrier materials in

the hot, dry repository environment. The general corrosion rate of a metal can be calculated assuming that the corrosion rate is constant and independent of time, as shown below:

$$d = gt \tag{10-5}$$

where d is the depth of corrosion, g is the general corrosion rate (m/yr), and t is time.

The independence of the general corrosion rate with time can be considered a conservative assumption since data from the National Bureau of Standards (9) for long-term exposures of metals in various subsurface environments indicate that the corrosion rate decreases with time. General corrosion is also assumed to be uniform over the entire surface of the container. The general corrosion model is applicable to materials that are not susceptible to localized corrosion under repository conditions.

Pitting Corrosion Model

Pitting corrosion is primarily an electrochemical process that occurs due to potential differences between points connected by an electrolyte. A recent review of pitting corrosion with respect to metals exposed to soils systems has been completed by Mughabghab and Sullivan (10). The factors identified in this review that significantly impact corrosion of metals exposed to subsurface environments include:

1. Aeration factors that influence the amount of oxygen and moisture that reach the metal.

2. Electrolyte factors that address local water chemistry (e.g., pH, resistivity, Cl^-, SO_4^{-2}, and CO_3^-).

3. Electrical factors that define size, number, and location of anodic areas.

4. Miscellaneous factors that include microbial corrosion, differential aeration, and the area effect.

Empirical correlations have been developed by Mughabghab and Sullivan (10) that address the role of the first two items on the pitting process.

The extensive subsurface corrosion investigations have been completed by the National Bureau of Standards (NBS) (NBS has recently been renamed the National Institute of Standards and Technology (NIST)). Early investigations by Romanoff (9) tested 333 different materials in 128 different environments for extended time periods. Based upon the corrosion data for ferrous materials in 47 different environments for time periods of up to 18 years, Romanoff developed a correlation of the

maximum pit depth as a function of time:

$$h(t) = kt^n \tag{10-6}$$

where h is the maximum penetration of the pit in mils (1 mil = 0.001 inch), k is the pitting parameter for maximum pits in mils/year^n, t is the exposure time in years, and n is the pitting exponent which is near-field environment dependent parameter.

Other empirical correlations have been attempted. However, Mughabghab and Sullivan state that the correlation expressed in equation 10-6 is the most common expression used to estimate the rate of maximum pit growth. In the NBS study (9), the value of n was found to be correlated with the degree of aeration of the subsurface environment and the parameter k reflected the corrosivity of the environment.

Evaluation of the relevant data presented in the NBS study (9) requires an adaptation of the empirical relation presented in equation 10-6. Based on these data, the maximum pit depth takes the form:

$$h(t)=kt^n\left(\frac{A}{372}\right)^a \tag{10-7}$$

where:

h = maximum penetration of the pit in cm

k = pitting parameter for maximum pits in cm/year^n

t = exposure time in years

n = pitting exponent (near-field environment dependent parameter)

A = surface area of the container in cm^2

Constant = 372 cm^2 = scaling factor that arises from the fact that the original test coupons which were used to obtain the data for determining the values of k and n were 372 cm^2

a = experimentally derived correlation coefficient

Extensive studies by Logan (11) indicated that values of "a" for ferrous materials ranged from 0.08 to 0.32 with a mean value of 0.15. Values of "n" have been calculated through empirical expressions derived from the NBS data based upon the degree of aeration of the subsurface environment. Values of "n" over the range 0.26, 0.39, 0.44 and 0.59, represent good, fair, poor, and very poor aeration,

respectively. The value of the pitting parameter "k" has been determined to be a function of the pH of the environment, as described in the following relationships:

$$\begin{aligned} k &= 0.1458\ (10 - pH) && pH < 6.8 \\ k &= 0.0457 && 6.8 < pH < 7.3 \\ k &= 0.0256\ (pH - 5.13) && 7.3 < pH \end{aligned} \qquad (10\text{-}8)$$

Application of these failure models to the proposed EBS container designs and projected repository environments permits an evaluation of each scenario with respect to the relevant Weibull parameters. Acquisition of additional data pertaining to the degradation of candidate container materials under repository conditions will permit further refinement of the selected empirical parameters employed in the corrosion models.

Cladding Failure

Although cladding is currently ascribed no containment capabilities under current regulations, it may be desirable to evaluate the potential impact of cladding failure rates on radionuclide release rates. The primary cladding failure mechanisms that have been identified include creep rupture and hydride reorientation (12). Creep rupture results from the long-term creep deformation of Zircaloy cladding due to internal stresses resulting from fission product gas pressure. Gilbert et al. (12) applied theoretical deformation and fracture theory to develop cladding fracture maps for use in evaluating dry cask storage options for spent nuclear fuel. These maps indicated that with temperatures less than 400°C and stresses less than about 200 MPa, there would be very limited failure of the cladding material. The cladding breach failure rate under these conditions would be less than 1% of the spent fuel rods in the 40 year period for dry cask storage of spent fuel.

The failure mechanism identified was pinhole penetration through the cladding. The pinhole cracks were typically less than 10 m in diameter. The driving force for the continuation of crack growth would be internal gas pressure. Since this pressure was relieved by the pinhole rupture, the mechanism for continued cracking was essentially deactivated. After the gas pressure was relieved, the remaining stresses were too low for continued cladding degradation. Therefore, even though the cladding has failed, the diameter of the pinhole failure was usually 10 m or less. This could significantly impact the release rate from failed fuel pins and will be addressed in the evaluation of mass transfer rates from failed fuel pins in Section 11.

Hydride reorientation was identified as another potential failure mechanisms for spent fuel pins. Significant efforts by Marshall (13, 14) and Cheadle (15, 16, 17) described the mechanisms for hydride orientation in Zircaloy and Zr - 2.5 Nb alloys, respectively. Marshall studied the impact of fabrication technique on hydride orientation, while Cheadle evaluated the reorientation of hydrides under various conditions that resulted in Hydrogen Induced Delayed Cracking (HIDC). Additional work by Hardie and Shanahan (18) studied the reorientation of Zr - 2.5 Nb alloys. This study noted that for internal pressures of less than 200 MPa and temperatures less than about 300°C, hydride reorientation was not a significant effect.

The internal pressure of the fuel pin provides the driving force for both failure mechanisms. Estimates by Gilbert, et al. (12) may have been significantly conservative and subsequent evaluations by Johnson (19) suggest that failure times may be 2 orders of magnitude longer at lower temperatures. These parameters are easily evaluated with the present Weibull failure distribution model by employing a mean time to cladding failure of 4000 years instead of 40 years, as described previously. These failure times are employed in the sample container failure rate evaluations completed in the following subsection.

At the temperatures and internal pressures of interest, it appears that there will be limited degradation of the cladding material under nominal repository conditions. The mean time to failure for fuel pin cladding may be on the order of 40 to 100 years due to creep rupture for high temperatures and may be as long as 4,000 years for low internal pressures and/or low temperatures. In addition, it should be noted that the failure of the pins results in very small (less than 10 m) egress pathways for the radionuclides. This will significantly influence the mass transfer rate of radionuclides from failed pins. Hydride reorientation will have a limited effect on the failure of fuel pins. Once the fuel pin has been breached, the driving force for additional hydride reorientation will be eliminated. Both of these failure modes are operational prior to failure of the container and are significantly influenced by increases in temperature.

EXAMPLE EVALUATIONS

Three container designs and associated environmental scenarios, which result in three different container lifetimes, are presented here. The scenarios are evaluated with respect to the applicable failure models and the associated Weibull parameters are selected to describe the expected mean time to failure. These cases represent the range of conditions and container performance characteristics that

may be expected in the repository.

The first scenario employs a 1 cm thick, single metal barrier design that is constructed of a moderately corrosion resistant material, such as Type 304L stainless steel. Utilization of this material could result in a sensitized microstructure at the closure seal. This sensitized microstructure would result in the onset of localized corrosion (pitting corrosion) due to stress corrosion cracking at the closure joint. Since pitting has been identified as the probable failure mechanism, the pitting corrosion model described above (Equation 10-7) using the data from Romanoff (9) is applied with the following parameters:

k = 0.0457 (neutral pH, 6.8 < pH < 7.3)

A = 114,455 (surface area of the container in cm^2)

a = 0.15 (mean value of the experimentally derived correlation coefficient)

n = 0.32 (pitting exponential - selected to represent "moderate" aeration)

Application of these parameters yields a pit penetration rate as a function of time as shown in Figure 10-2. This figure indicates that at approximately 1000 years, the 1 cm wall thickness would be penetrated. This figure also suggests that the failure rate at 1000 years appears to be increasing. Based upon these results, the following parameters were selected for the Weibull distributions employed in the first model:

c_1	=	0.01	fraction of containers susceptible to early failure
t_1	=	300 yr	mean time for early container failure
x_1	=	300 yr	lower limit of metal barrier lifetime
f_1	=	10000 yr	mean metal barrier lifetime
b_1	=	2.0	failure rate of the metal barrier at the mean lifetime
$x_2 = x_1+0$	=	300 yr	lower limit of cladding lifetime
$f_2 = f_1+40$	=	1040 yr	mean metal barrier lifetime
b_2	=	2.0	failure rate of cladding at the mean lifetime

Substitution of these parameters into equation 10-3 yields the cumulative container failure distribution shown in Figure 10-3.

The second scenario envisioned also employs a 1 cm thick, single metal barrier that is constructed of a much more corrosion resistant alloy, such as the high-nickel Alloy 825. This material is much more

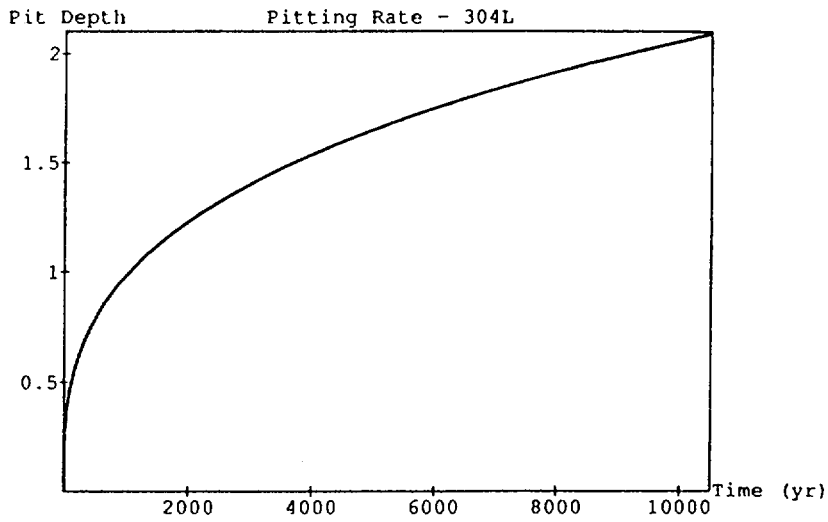

Figure 10-2. Pit penetration depth as a function of time for Type 304L stainless steel using the data from Romanoff (9).

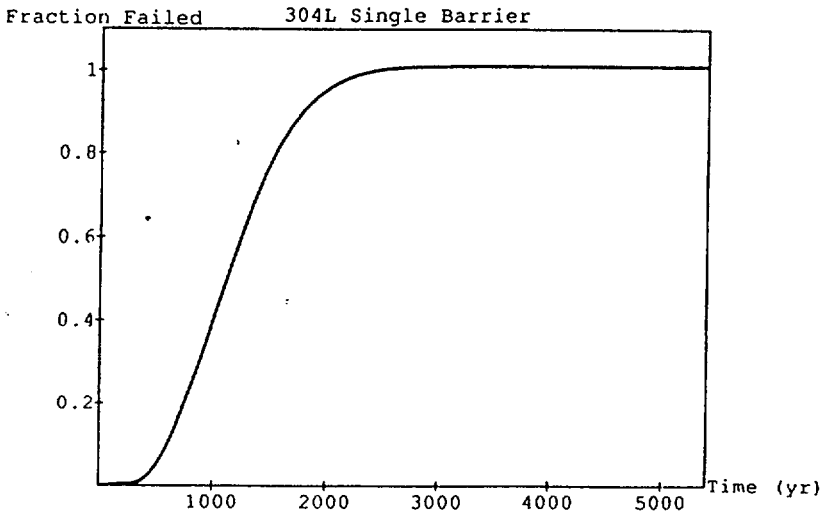

Figure 10-3. Fraction of containers failed as a function of time for a Type 304L stainless steel single metal barrier.

resistant to sensitized microstructure formation, pitting corrosion, and stress corrosion cracking. However, as in the previous calculation, localized corrosion will most likely be the predominant failure mechanism. Although pitting has been identified as the probable failure mechanism, the pitting should

be somewhat less severe. This leads to the selection of parameters for the pitting model that are somewhat different from those selected for 304L stainless steel. The pitting corrosion model described by Equation 10-7 using the data from Farmer (4) is applied with the following parameters:

k = 0.0457 (neutral pH, 6.8 < pH < 7.3)

A = 114,455 (surface area of the container in cm^2)

a = 0.15 (mean value of the experimentally derived correlation coefficient)

n = 0.26 (pitting exponential - represents greater pitting resistance than 304L)

Application of these parameters yields a pit penetration rate as a function of time as shown in Figure 10-4. This figure indicates that at approximately 5000 years, the 1 cm wall thickness would be penetrated. This figure also suggests that the failure rate at 5000 years appears to be increasing at a relatively constant rate. Based upon these results, the following parameters were selected for the Weibull distributions employed in the second model:

c_1	=	0.005	fraction of containers susceptible to early failure
t_1	=	500 yr	mean time for early container failure
x_1	=	500 yr	lower limit of metal barrier lifetime
f_1	=	5000 yr	mean metal barrier lifetime
b_1	=	2.0	failure rate of the metal barrier at the mean lifetime
$x_2 = x_1+0$	=	500 yr	lower limit of cladding lifetime
$f_2 = f_1+40$	=	5040 yr	mean cladding lifetime
b_2	=	2.0	failure rate of cladding at the mean lifetime

Substitution of these parameters into Equation 10-3 yields the cumulative container failure distribution shown in Figure 10-5.

The third scenario investigated in these calculations results from a significant improvement in the lifetime of the container due to the utilization of a multi-barrier system. This system includes a 0.5 cm thick, highly corrosion resistant titanium outer covering and a 1 cm thick, inner metal barrier of corrosion resistant high-nickel alloy (C-4). The titanium outer layer is not susceptible to pitting corrosion in the projected repository environment. This layer is assumed to fail by general corrosion according to Equation 10-5. The general corrosion rate for titanium is estimated to be approximately

0.0001 cm/yr based upon the observed corrosion rates for Grade 12 titanium alloy in salt solutions as measured by Braithwaite and Molecke (20). This corrosion rate yields the container penetration rate as shown in Figure 10-6. The outer 0.5 cm thick layer failure time is approximately 5000 years.

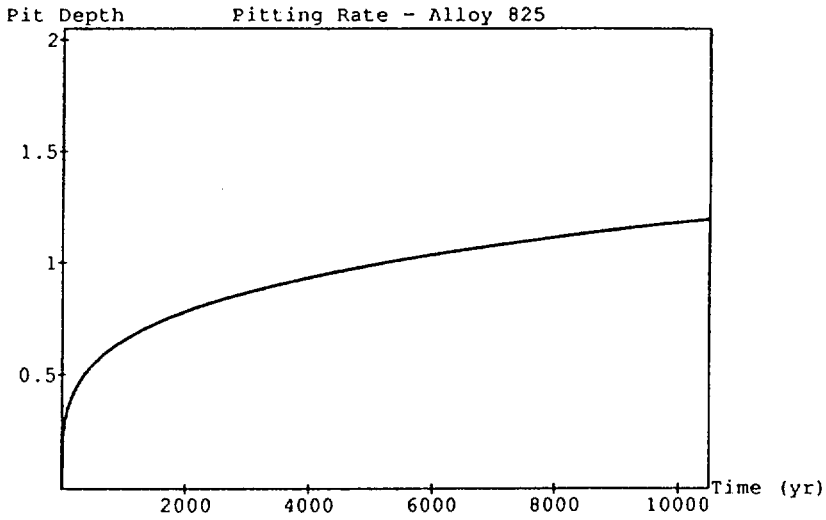

Figure 10-4. Pit penetration depth as a function of time for Allow 825 using the data from Farmer et al. (4).

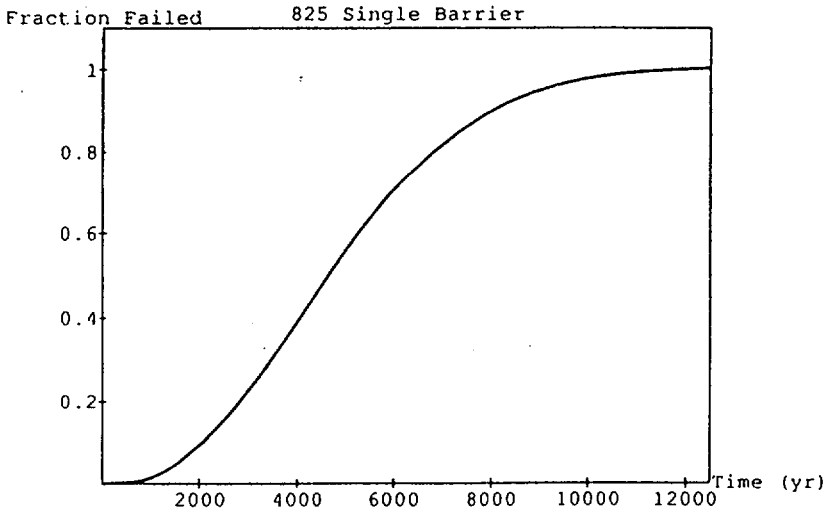

Figure 10-5. Fraction of containers failed as a function of time for an Alloy 825 single metal barrier.

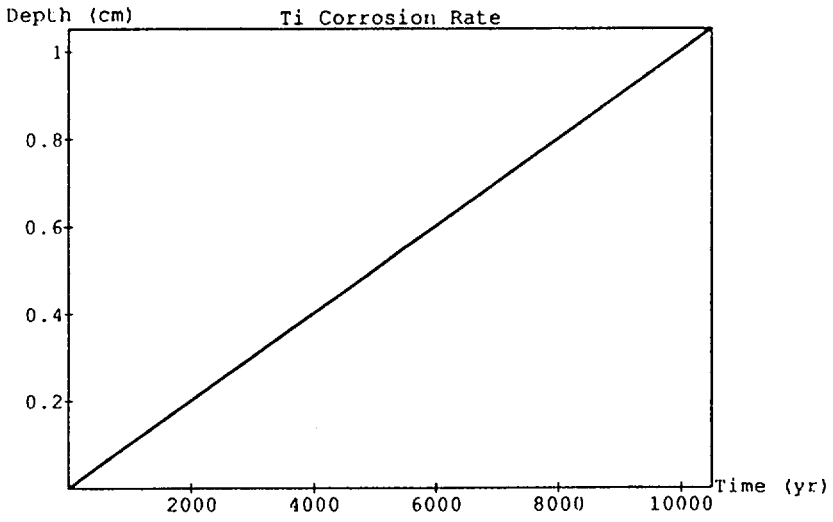

Figure 10-6. General corrosion rate for titanium (Grade 12) alloy using the data from Braithwaite and Molecke (20).

Pitting corrosion is assumed to be the dominant failure mechanism for the C-4 high-nickel alloy. Since the C-4 alloy is even more resistant to pitting corrosion than Alloy 825, the pitting corrosion model described by Equation 10-7 using the data from Jackson and van Rooyen (21) is applied with the following parameters:

k = 0.0457 (neutral pH, 6.8 < pH < 7.3)

A = 114,455 (surface area of the container in cm^2)

a = 0.08 (lowest value of the experimentally derived correlation coefficient)

n = 0.26 (pitting exponential - represents greater pitting resistance than 304L)

Application of these parameters yields a pit penetration rate as a function of time as shown in Figure 10-7. This figure indicates that at approximately 25000 years, the 1 cm wall thickness would be penetrated. This figure also suggests that the failure rate at 25000 years appears to be slowly increasing. Based upon these results, the following parameters were selected for the Weibull distributions employed in the third model:

c_1	=	0.005	fraction of containers susceptible to early failure
t_1	=	1000 yr	mean time for early container failure
x_1	=	1000 yr	lower limit of barrier 1 lifetime

f_1	=	5000 yr	mean barrier 1 lifetime
b_1	=	1.0	failure rate of barrier 1 at the mean lifetime
$x_2 = x_1+1000$	=	2000 yr	lower limit of barrier 2 lifetime
$f_2 = f_1+20000$	=	25000 yr	mean barrier 2 lifetime
b_2	=	1.0	failure rate of barrier 2 at the mean lifetime
$x_3 = x_2+1000$	=	3000 yr	lower limit of cladding lifetime
$f_3 = f_2+4000$	=	29000 yr	mean cladding lifetime
b_3	=	2.0	failure rate of cladding at the mean lifetime

Substitution of these parameters into Equation 10-4 yields the cumulative container failure distribution shown in Figure 10-8.

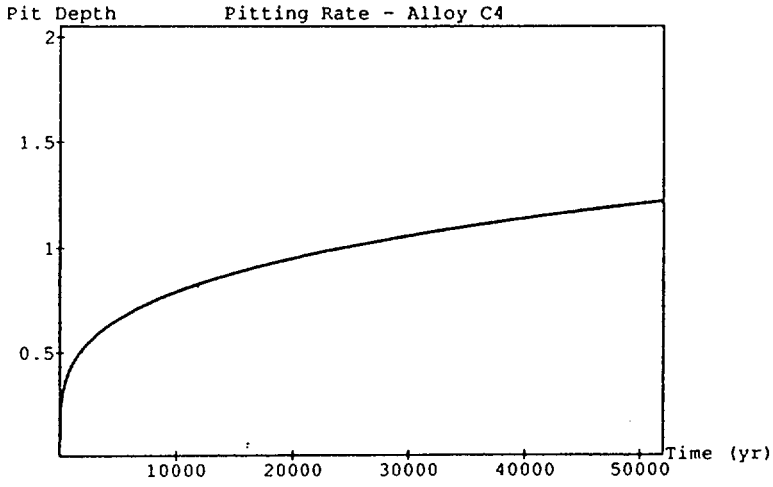

Figure 10-7. Pit penetration depth as a function of time for Alloy C-4 using the data from Jackson and van Rooyen (21).

DISCUSSION

The results presented in the previous section represent a wide range of container design parameters and repository conditions. These results show that a significant improvement in the mean container lifetime may be achieved through the utilization of a more robust container design. This variation in container design results in a change in the mean container lifetime from 1,000 years for Type 304L stainless steel single metal barriers, to 5,000 years for an Alloy 825 single metal barrier, and to 35,000 years for an multiple barrier Ti/C-4 container.

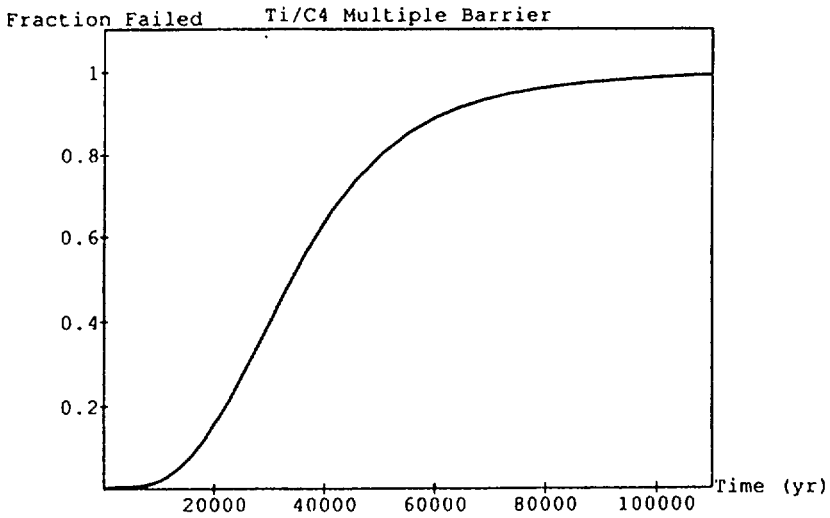

Figure 10-8. Fraction of containers failed as a function of time for a Ti/C-4 multiple metal barrier.

It should be noted that the first two container failure distributions (304L and 825 single metal barriers) did not take any significant credit for the potential containment capabilities of the Zircaloy cladding material. These calculations assume a mean cladding failure time of 40 years and a failure rate parameter (Weibull slope) of 2.0. Selection of these parameters provided no significant change in the calculated cumulative container failure distribution. The multiple barrier container design did incorporate the cladding as a significant containment barrier. This enhanced containment contribution increased the mean container lifetime from approximately 30,000 years to 35,000 years.

The projected temperature scenario will have a significant impact on the container design selected for use in the repository environment. The three temperature scenarios, which are presented in Section 8 of this report (Hot, T > 96°C, Warm, T = 96°C, and Cold, T < 96°C), represent dramatically different initial repository environments for the EBS. Selective container design, based upon the areal power density that resulted in these temperature scenarios, will most likely be completed as repository temperature data become available during site characterization. These scenarios are best addressed in the current model by judicious selection of the probabilities assigned to the respective container designs for each temperature scenario.

The Hot scenario would suggest a high probability (P = 0.7) for the use of the single metal Alloy 825 container, while the probability for the use of the Type 304L stainless steel container would be lower

(P = 0.2) and the probability for the use of the multiple barrier Ti/C-4 container would be even lower (P = 0.1). These probabilities were selected to represent the current container design considerations for the high temperature environment.

The Warm environment would provide the potential for a very aggressive container environment. This might suggest almost equal probabilities of the use of a corrosion resistant alloy such as Alloy 825 (P = 0.50) or a multiple barrier system (P = 0.49). There would be a relatively low probability of using the Type 304L alloy due to its susceptibility to pitting corrosion in wet environments (P = 0.01). The EBS failure models and their dependence on temperature environment are shown in Figure 10-9.

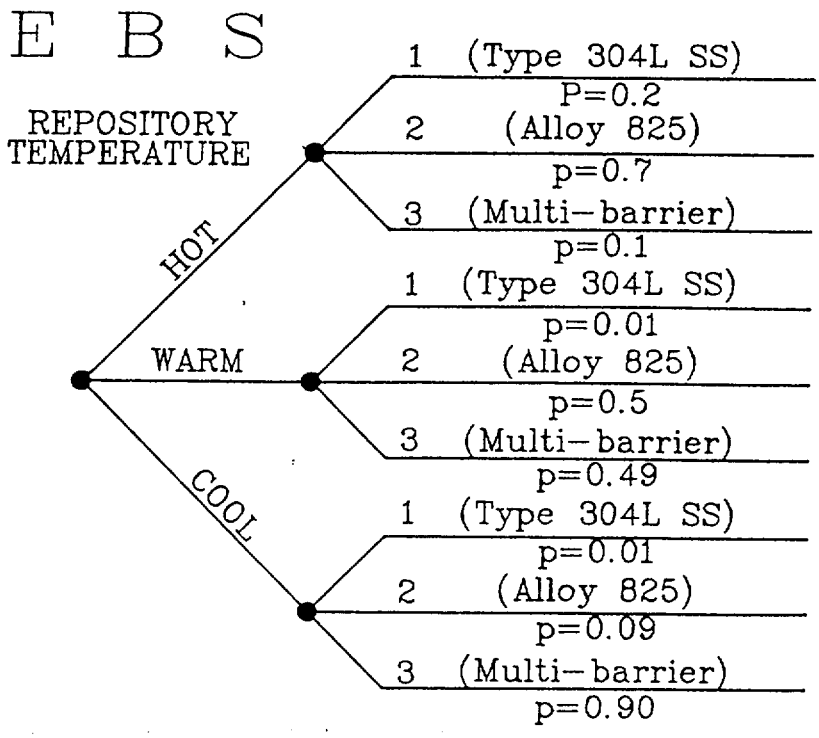

Figure 10-9. Logic tree nodes for EBS model (conditional on repository temperature).

The Cold environment could require a significantly more robust container design. This might suggest a significantly higher probability for the use of a multiple barrier system (P = 0.90). This assumption would then suggest a relatively low probability of employing a corrosion resistant Alloy 825 single

metal barrier system (P = 0.09). There would again be a very low probability of using the Type 304L alloy due to its susceptibility to pitting corrosion in wet environments (P = 0.01).

The thermal environment may also impact the various failure rate parameters defined in the general corrosion and pitting corrosion models developed in this study. The data used in this study were the best available data for corrosion in subsurface environments. In situ experimental efforts will be required to determine additional parameter modifications that may be necessary at higher temperatures. Previous results by Tait (22) suggest that at higher temperatures (90°C vs. 20°C) there may be as much as a three-fold increase in the pitting corrosion rate. However, these results were reported for nonpassivating mild steels, not stainless steels or high-nickel alloys. Hence, changes in the pitting and general corrosion parameters based on increases in temperature were not incorporated into this study.

SUMMARY AND CONCLUSIONS

An EBS failure model was developed during previous EPRI studies (1). This model employed a probabilistic approach describing the cumulative container failure rate as a function the mean container lifetime, the threshold container failure time, and the failure rate at the mean container lifetime. The original model was modified for the current study to include the addition of a mechanism to evaluate the impact of "early container failures" on the performance of the overall engineered barrier system, the ability to evaluate multiple barriers with different performance characteristics, and the capability to address the potential impact of waste form failure rates (cladding failure rates and glass pour canister failure rates) on EBS performance.

A system of deterministic sub-models was developed to provide a quantitative justification for the selection of various Weibull parameters. These parameters were employed as the input for the Weibull distributions that represented the modified EBS failure rate models. This methodology provides significant flexibility for the application of additional quantitative sub-models, which should be based upon actual experimental data generated during site characterization.

The results of the EBS failure rates calculated in this section suggest that a significant improvement in container lifetime will have an extremely favorable impact on the performance of the repository. Sensitivity analyses studying the impact of enhanced container performance on radionuclide release and transport in the Yucca Mountain environment can now be completed using this probabilistic model with deterministic sub-models.

REFERENCES

1. R. K. McGuire (ed.). *Demonstration of a Risk-Based Approach to High-Level Waste Repository Evaluation*, Palo Alto, Calif.: Electric Power Research Institute, 1990. NP-7057, Research Project 3055-2.

2. W. C. O'Neal and D. W. Gregg. *Preclosure Analysis of Conceptual Waste Package Designs for a Nuclear Waste Repository in Tuff.* LLNL Report UCRL-53595, November 1984.

3. Nuclear Waste Technical Review Board. *Third Report to the U.S. Congress and the U.S. Secretary of Energy.* Washington, DC: U.S. Government Printing Office, May 1991, pp. 13-16.

4. J. C. Farmer, R. D. McCright, J. N. Kass, D. B. Bullen, G. E. Gdowski, R. A. Van Konynenburg, M. J. Strum and H. Weiss. *Survey of Degradation Modes of Candidate Materials for High-Level Radioactive Waste Disposal Containers.* Lawrence Livermore National Laboratory Report UCID-21362, Vols. 1-8, June 1988.

5. J. C. Farmer, G. E. Gdowski, R. D. McCright and H. S. Ahluwalia. *Corrosion Models for Performance Assessment of High-Level Radioactive Waste Containers.* Lawrence Livermore National Laboratory Report UCRL-JC-103517, May 1990.

6. E. J. Dudewicz and S. N. Mishra. *Modern Mathematical Statistics.* NY: John Wiley & Sons, 1988, pp. 150-153.

7. R. E. Thomas. *A Feasibility Study Using Hypothesis Testing to Demonstrate Containment of Radionuclides Within Waste Packages.* Battelle Memorial Institute Report BMI/ONWI-599, April 1986.

8. T. M. Sullivan and C. J. Suen. *Low-Level Waste Shallow Land Disposal Source Term Model: Data Input Guides.* U.S. Nuclear Regulatory Commission NUREG/CR-5387, July 1989.

9. M. Romanoff. *Underground Corrosion.* National Bureau of Standards Circular 579, 1957, 227 pages.

10. S. F. Mughabghab and T. M. Sullivan. "Evaluation of the Pitting Corrosion of Carbon Steels and Other Ferrous Metals in Soil Systems." *Waste Management*, vol. 9, 1989, pp. 239-251.

11. K. H. Logan. "Engineering Significance of National Bureau of Standards Soil-Corrosion Data." *Journal of Research of the National Bureau of Standards*, vol. 22, January 1939.

12. E. R. Gilbert, W. J. Bailey, A. B. Johnson, Jr., and M. A. McKinnon. "Advances in Technology for Storing Light Water Spent Fuel." *Nuclear Technology*, vol. 89, Feb. 1990, pp. 141-161.

13. R. P. Marshall. "Influence of Fabrication History on Stress-Oriented Hydrides in Zircaloy Tubing." *Journal of Nuclear Materials*, vol. 24., 1967, pp. 34-48.

14. R. P. Marshall. "Control of Hydride Orientation in Zircaloy by Fabrication Practice," *Journal of Nuclear Materials*, vol. 24., 1967, pp. 49-59.

15. B. A. Cheadle, C. E. Ells and W. Evans. "The Development of Texture in Zirconium Alloy Tubes." *Journal of Nuclear Materials*, vol. 23, 1967, pp. 199-208.

16. B. A., Cheadle, C. E. Coleman, and H. Licht. "CANDU-PHW Pressure Tubes: Their Manufacture, Inspection and Properties." *Nuclear Technology*, vol. 57, 1982, pp. 413.

17. B. A., Cheadle, C. E. Coleman, and M. Ipohorski. "Orientation of Hydrides in Zirconium Alloy Tubes." In *Zirconium in the Nuclear Industry*, ASTM STP 824, 1982, pp. 210-221.

18. D. Hardie and M. W. Shanahan. "Stress Reorientation of Hydrides in Zirconium-2.5% Niobium." *Journal of Nuclear Materials*, vol. 55, 1975, pp. 1.

19. A. B. Johnson, Jr., unpublished data, private communication, April 1991.

20. J. W. Braithwaite and M. A. Molecke. "Nuclear Waste Canister Corrosion Studies Pertinent to Geologic Isolation." *Nuclear and Chemical Waste Management*, vol. 1, 1980, pp. 37-50.

21. R. P. Jackson and D. van Rooyen. "Crevice Corrosion of Some Ni-Cr-Mo-Fe Alloys in Laboratory Tests." *Localized Corrosion - Cause of Metal Failure*. ASTM-STP 516, American Society for Testing and Materials, 1972, pp. 210-221.

22. W. S. Tait. "Effect of Physical Parameters on the Pitting Corrosion of Mild Steel at Low Total Dissolved Solid, Oxygen Bearing Waters: A Nonpassivating Metal/Environment System," *Corrosion*, vol. 35, 1979, pp. 296-300.

Section 11

SOURCE-TERM MODELS FOR THE WASTE PACKAGE

by

M. J. Apted

INTRODUCTION

The feasibility of permanent disposal of radioactive high-level waste (HLW) in repositories located in deep geologic formations is being studied world-wide. The most credible release pathway is interaction between groundwater and nuclear waste forms, followed by migration of radionuclide-bearing groundwater to the accessible environment. Under hydrologically unsaturated conditions, vapor transport of volatile radionuclides is also possible. The primary components of repositories that mitigate release are the near-field and the far-field subsystems. The near-field encompasses the waste packages composed of engineered barriers (e.g., man-made materials, such as vitrified waste forms, corrosion-resistant containers), while the far-field includes the natural barriers (e.g., host rock, hydrologic setting). Taken together, these two subsystems define a series of multiple, redundant barriers whose purpose is to assure the safe isolation of nuclear waste.

In the U.S., the Department of Energy (DOE) is investigating the feasibility of safe, long-term disposal of high-level nuclear waste at the Yucca Mountain site in Nevada. The proposed repository horizon is located in non-welded tuffs within the unsaturated zone (i.e., above the water table) at Yucca Mountain.

The purpose of this Section is to describe the source-term models for radionuclide release from the near field. While these models have been developed specifically for the waste package design and conditions of the Yucca Mountain site, many of the models are broadly applicable to a range of waste package designs and repository conditions.

DESCRIPTION OF NEAR FIELD

Because of the hydrologically unsaturated conditions at the Yucca Mountain site, the design of the engineered barrier system (EBS) by the DOE is somewhat unique compared to other international

waste-package designs based on a saturated repository formation. Diagrams of possible waste package designs for the Yucca Mountain site are shown Figure 11-1. Key barrier materials include the nuclear waste form (either HLW borosilicate glass or spent nuclear fuel), a disposal container, and an air gap between the container and the surrounding tuff (1).

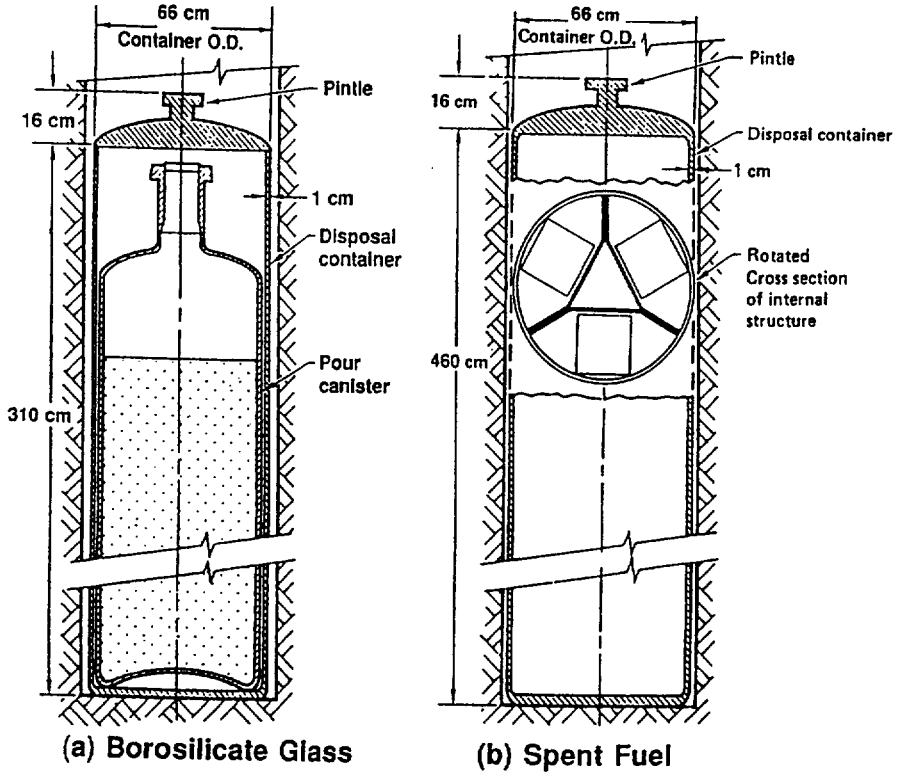

Figure 11-1. General waste-package configuration for Yucca Mountain Site (12).

This study exclusively focuses on waste packages containing spent nuclear fuel. As will be discussed below, spent nuclear fuel is composed of several sources (i.e., UO_2 matrix, cladding, gap/grain boundary phases) that contain different proportions and amounts of radionuclides, and react differently with water. The container is designed to assure compliance with regulatory containment objectives. A key element of these designs is a small air gap between the waste container and the edge of the emplacement hole in the surrounding tuff. Table 11-1 presents dimensions and waste loading characteristics for a reference waste package.

Table 11-1

DIMENSIONS AND WASTE LOADING CHARACTERISTICS FOR A REFERENCE WASTE PACKAGE (Apted et al. 1990)

Waste Package Height	4.6 m
Waste Package Outside Diameter	0.71 m
Waste Package Overall Volume	1.73 m^3
Waste Package Internal Void Volume (V)	1.22 m^3
Waste Package Waste Loading	2.1 MTHM
Surface Area of Intact Fuel (A)	140 m^2
Air Gap Between Waste Container and Emplacement Hole (b)	0.03 m

CONCEPTUAL RELEASE MODELS

Upon breaching of the containment barriers, which may include multiple container materials, there will be the potential for radionuclide release from the waste package to the far field. Three general modes of release can be identified: (1) "dry", (2) "wet-drip", and 3) "moist/wet-continuous" models (1). These modes are shown schematically in Figure 11-2. Specific mathematical models for each of these conceptual models are presented below.

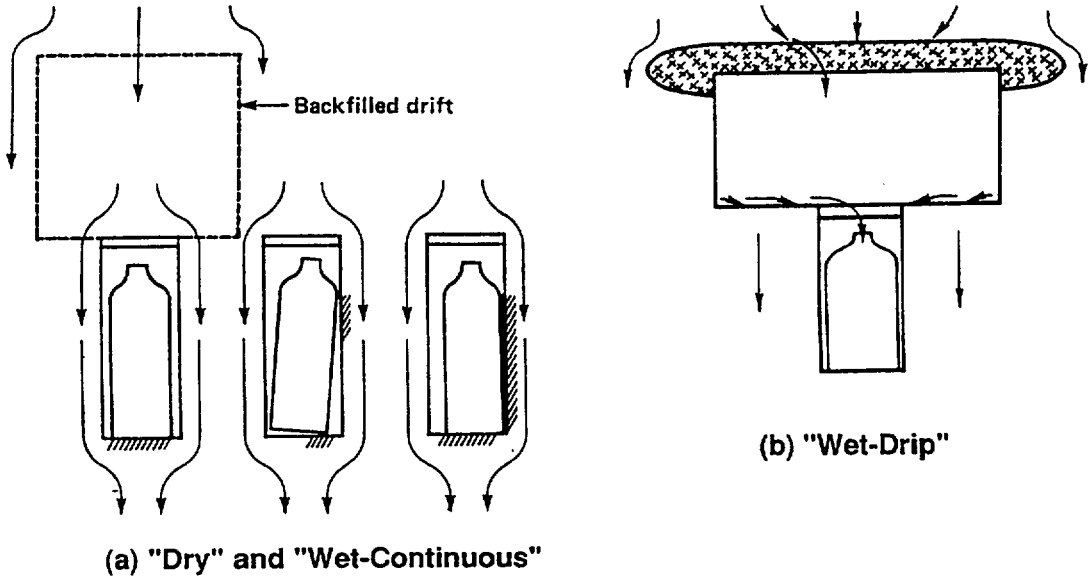

Figure 11-2. Schematic diagram for possible release modes from the waste package (12).

Dry Release

The air gap is intended to provide a hydrologic break between the waste and the hydrologic system,

thereby preventing the aqueous transfer of radionuclides from the waste package to the far field. With an intact air gap under anticipated unsaturated conditions, there would be no continuous pathway for water to contact the waste form and remove radionuclides. Under such dry conditions, gaseous transport of volatile radionuclides (e.g., C-14) is the only available pathway for release.

Wet-Drip Release

For some emplacement holes, there is a possibility that local variations in rock permeability and fracturing may divert water flow into the emplacement hole. If this occurs, water may drip onto the waste package. If this dripping were to lead to the breaching of the containment barriers, dripping water could penetrate the waste container, contacting the spent fuel. Depending on drip rates, the interior volume of the waste container may eventually fill up to the breach point. This would result in radionuclide-bearing water being released into the host rock at a rate equal to the drip rate of water into the container.

Moist/Wet-Continuous Release

If the waste container directly contacts the host rock, either by physical displacements within the emplacement hole or by sedimentation of rubble into the air gap, a continuous pathway for release of dissolved radionuclides would result. Formation of such a pathway would permit diffusive/ advective transport of radionuclides to occur, even under hydrologically unsaturated conditions. For anticipated unsaturated conditions, radionuclide releases out of the waste package would be restricted to diffusive transport along films of water on the surfaces of pore within the intact or rubblized tuff (Figure 11-3). This same mode of release would pertain if hydrologically saturated conditions were to develop around the waste package, whether or not the air gap remained intact. In this case, the release of radionuclides out of the waste package would be either diffusion or diffusion/advection controlled, depending on the pore-water flow rate around the waste package. Certain conditions might lead to the formation of a waste package in which only the lower half is under saturated conditions ("wet-feet" condition); modeling such an occurrence would require only a trivial normalization of the release equations that are presented below.

Conca (2) has experimentally determined the effective diffusion coefficient (Db, in m^2/yr) for tuff gravel as a function of volumetric water content (Figure 11-4). Assuming the tuff gravel has a porosity of 45%, the following approximate fit to Conca' s data can be made:

$$\log (Db) = 2.14 \log (\Psi) - 1.5 \qquad (11\text{-}1)$$

where Ψ is the dimensionless degree of hydrologic saturation of contacting rock or rubble. Note that the degree of saturation for a tuff gravel is always less than the degree of saturation in the adjoining intact tuff host rock.

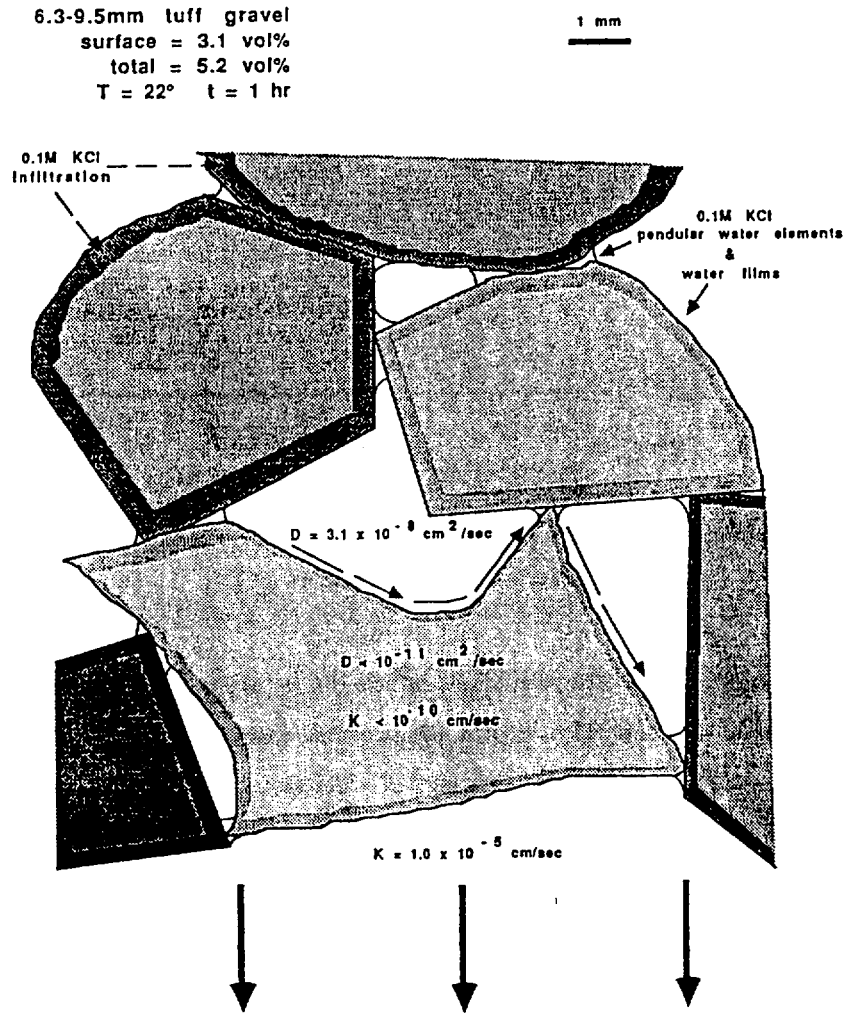

Figure 11-3. Inferred water distribution on partially saturated tuff gravel (2).

SPENT FUEL CHARACTERISTICS

To develop appropriate release models for the near field, the relevant characteristics of spent fuel must be understood. Interested readers may refer to more detailed publications for further information (3). Of prime concern is the abundance of radionuclides contained within the spent fuel after reactor operations. The radionuclide content used in these calculations is for a reference 33,000 MWd per

MTIHM pressurized water reactor (PWR) fuel (see (3), Tables 3-4, 3-6 and 3-10). The abundances of individual radionuclides change over time from radioactive decay and ingrowth.

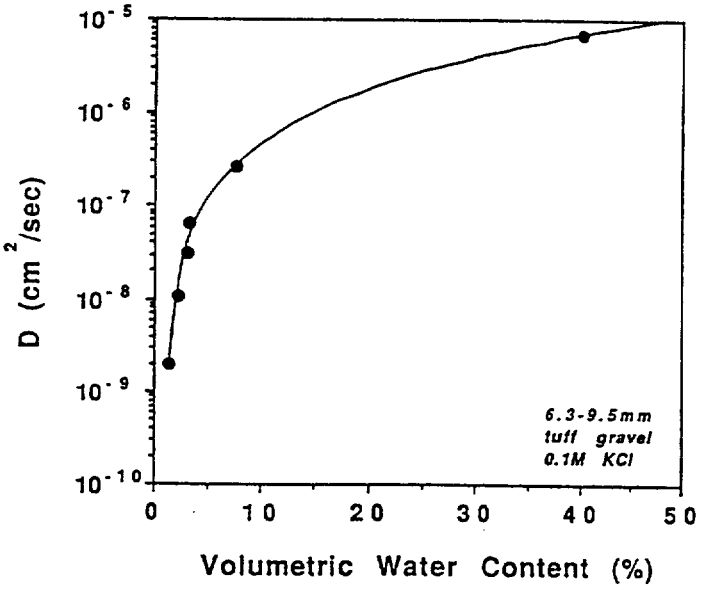

Figure 11-4. Effective diffusion coefficient as a function of water content in tuff gravel (2).

Abundance of radionuclides is not sufficient information, however. The location and relative "accessibility" of these radionuclides is not uniform because the fuel itself is not of uniform composition. As a waste form, "spent nuclear fuel" includes both the reactor assemblies and the individual spent fuel rods. The spent fuel rods, in turn, can be subdivided into the following general source-regions based on physicochemical characteristics (Figure 11-5):

- UO_2 matrix,
- Zircaloy cladding, and
- phases of volatile fission-products that form in the matrix-cladding "gap" and along UO_2 grain boundaries during the high temperatures of reactor operation.

The Zircaloy cladding, in turn, may develop a surface layer that has characteristics different from the bulk cladding material.

Table 11-2 shows an estimate of the proportion of key radionuclides within the separate regions of spent fuel. The 1-2% for volatile fission products in the gap/grain boundary phase is an approximation

based on limited study of PWR fuel; certainly there will be a distribution around this estimated mean value. Likewise, the location and abundance of C-14 in spent fuel is not well established. It appears that some C-14 on the surface of the cladding may be related to sources external to the activation of N-14 impurities in the fuel; hence, the amount and chemical form of this C-14 is problematical at this stage.

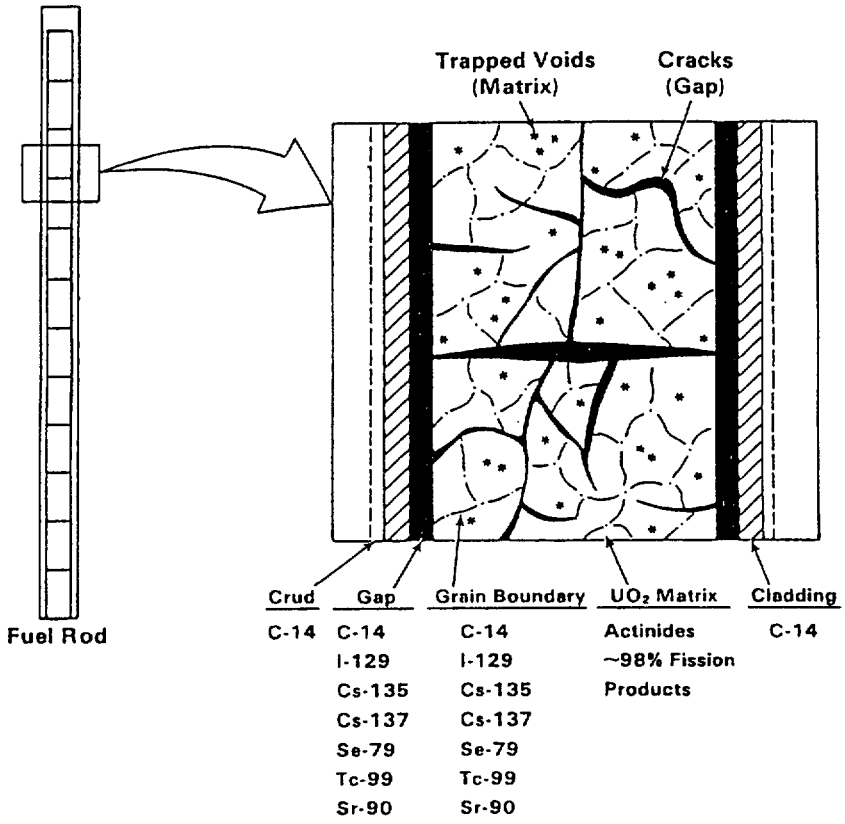

Figure 11-5. Schematic diagram of spent fuel showing different source regions with characteristic radionuclides (13).

CHEMICAL CONSTRAINTS ON RELEASE

The release of radionuclide from nuclear waste forms will be controlled by one of two limiting processes. The first is the dissolution (or alteration or reaction) rate ($gm/m^2/year$) of the waste form. So-called leaching data have been collected for a variety of waste forms, including spent fuel to provide such a limiting constraint. The second process for controlling the release of radionuclides in the near field is radioelement solubilities, imposed either by the primary waste form or by formation of new alteration phases by precipitation from solution. Limited studies on radioelement solubilities has also been conducted. Note that spent fuel dissolution rate and solubility data are ***not*** functions of the degree of hydrologic saturation; these chemical data can be obtained under fully saturated test

conditions. The effect of partial saturation on source-term releases is accounted for by separate factors in the release-rate equations.

Table 11-2

ESTIMATED PERCENT OF TOTAL RADIONUCLIDE INVENTORIES WITHIN THE SEPARATE REGIONS OF SPENT FUEL (1)

Nuclides	UO_2 Matrix	Gap (+ Grain Boundary)	Cladding	Surface Layer
C-14	35	1	63	1
Se-79	98	2	---	---
Tc-99	98	2	---	---
Sn-126	100	---	---	---
I-129	98	2	---	---
Cs-135	98	2	---	---
U-234	100	---	---	---
U-238	100	---	---	---
Np-237	100	---	---	---
Pu-239	100	---	---	---
Pu-240	100	---	---	---
Pu-242	100	---	---	---
Am-241	100	---	---	---
Am-243	100	---	---	---
Cm-245	100	---	---	---

The relative importance of these two processes in controlling radionuclide release from the near field may be determined from mass-transfer theory. Zavoshy et al. (4) and Pigford and Chambrè (5) have derived a derived relationship for a dimensionless ***flux ratio***, θ:

$$\theta = \frac{jo\ f\ ro}{\varepsilon\ Db\ cs} = \frac{\text{dissolution-rate per unit area}}{\text{diffusive-transport rate}} \qquad (11\text{-}2)$$

where:

- jo = forward-reaction rate of the waste form per unit area ($gm/m^2/yr$),
- *ro* = radius of the waste form (m),
- ε = porosity of the surrounding rock (dimensionless),
- Db = effective diffusion coefficient (m^2/yr),
- cs = solubility for the specific radioelement (gm/m^3).

The f term is the time-dependent mass fraction of a given radionuclide in the waste form:

$$f = \frac{M^{\circ}_{j} \exp(-\lambda_j t)}{M^{\circ}_{M} \exp(-\lambda_M t)} = \frac{M^{\circ}_{j}}{M^{\circ}_{M}} \exp[-t(\lambda_i - \lambda_M)] \approx \frac{M^{\circ}_{j}}{M^{\circ}_{M}} \exp[-\lambda_i t] \qquad (11\text{-}3)$$

where:

M°_{i} = initial mass inventory of nuclide i (gm),

λ_i = radioactive decay constant of nuclide i (years^{-1}),

M°_{M} = initial mass inventory of waste matrix (gm),

λ_M = radioactive decay constant of matrix component U-238 = 1.54 x 10^{-10} years^{-1},

For $\theta \ll 1$, diffusive transport is much more rapid than reaction rate of the waste form, and the release will be limited by dissolution, while for $\theta \gg 1$, diffusive transport will limit the release of radionuclides. Under diffusion-limited release, the concentration of dissolved radioelements at the waste-form surface will increase with time, eventually leading to attainment of solubility-limiting conditions. Using representative values of the above parameters, it can be calculated whether solubility-limited diffusional mass-transfer rate or waste-form dissolution rate will control release rate from the waste package. Note that solubilities and reaction rate are functions of environmental conditions (e.g., temperature, Eh, pH, water composition) that may vary over time and space within a geological repository system.

In general, release models for both bounding processes must be developed to assure that realistic release conditions are modeled. The most ***soluble*** radionuclides, such as ^{14}C, ^{129}I, and ^{79}Se, are reasonably expected to be controlled by the reaction rate of spent fuel. Releases of the remaining, ***insoluble*** radionuclides are expected to be constrained by solubility limits. Which process will control the release of a given radionuclide can be determined by comparing the predicted steady-state release rates of the two models for a given release mode; the equation that predicts the lower release rate is used to estimate expected releases from the proposed repository.

MATHEMATICAL MODELS FOR RELEASE

This subsection describes the mathematical models for calculating the release-rate and concentration for given radionuclides exiting from individual waste packages. The approach adopted here is equivalent to that used elsewhere by DOE contractors for near-field assessment (1). The release models described below do differ from those employed by the DOE researchers, basically because these

current models have been simplified for incorporation into a much larger computer code for total system assessment. However, there should be only minor differences between the results calculated here and those of Apted et al. (1), and these differences will occur at times longer than 10,000 years.

Dry Release Model

Insoluble Radioelements:

No releases of insoluble radioelements are anticipated for unsaturated conditions in which the air gap remains intact and there is no dripping water on the waste container. Without an aqueous phase, only gaseous species can be released. These conditions are often referred to as "dry", signifying the absence of liquid water contacting the waste matrix.

Soluble Radioelements:

Only ^{14}C in a gaseous form (CO_2) is expected to be released under these conditions. There is expected to be an initial "pulse" of ^{14}C corresponding to 1-2% of the inventory of ^{14}C being released from the surface of the Zircaloy cladding immediately upon failure of the container. An additional 58% of the inventory of ^{14}C will be released from the waste package at rates corresponding to the separate moist-air oxidation rates of Zircaloy and UO_2 matrix. Assuming uniform distribution of immobile ^{14}C within the cladding, exhaustion of this source will occur only after complete alteration of the Zircaloy and the UO_2. The remaining 40% of the inventory of ^{14}C is assumed to be immobile and is never released in gaseous form.

Wet-Drip Release Model

Insoluble Radioelements:

Sadeghi et al. (7) have developed a set of equations for calculating the release rate of solubility-limited radioelements for unsaturated conditions with water dripping into a breached waste container:

$$M_i = \begin{cases} 0, & 0 \le t \le t_2 \\ Q\, c_s, & t_2 \le t \end{cases} \qquad (11\text{-}4)$$

where:

$Q=FA_{wp}$ = volumetric flow rate of water into and out of the waste container, assumed to be constant (m^3/year),

F = infiltration rate through tuff (m/year),

A_{wp} = cross-sectional area normal to infiltrating water that diverts flow into the waste container (m^2),

cs = constant concentration (solubility) of the species within the container (gm/m^3), and

t_2 = time after emplacement when the waste container is full (years).

The time to actually fill the waste container, t_f, is:

$t_f = t_2 - t_1 = V/Q$,

t_1 = time after emplacement that the waste container is penetrated (years),

V = interior volume of waste container (m^3).

For radioelements in which the solubility is shared among several radioisotopes, the time-dependent solubility ($c_{s/i}$) for a given radioisotope i of the radioelement is:

$$c_{s/i}(t) = [M_i(t)/M_\Sigma(t)]\, c_s = \phi_i(t)\, c_s \qquad (11\text{-}5)$$

where:

$M_i(t)$ = mass of radioisotope i in waste form (gm),

$M_\Sigma(t)$ = total mass of all isotopes of the radioelement in waste form (gm),

$\phi_i(t)$ = mass fraction of radioisotope i among all isotopes (dimensionless),

Note that these last three terms are time dependent because of radioactive decay:

$$M_i(t) = M^\circ_i [\exp(-\lambda_i t)] \qquad (11\text{-}6)$$

where:

M°_i = initial mass inventory of nuclide i at time of waste emplacement (gm),

λ_i = radioactive decay constant for nuclide i (= ln 2/ half-life) ($years^{-1}$),

t = time after emplacement of waste (years).

Also note that $\phi_i(t) = 1$ for single-isotope radioelements (e.g., ^{99}Tc, ^{126}Sn). Based on the above equations, the concentration of a given radionuclide exiting the waste package, c_i, is:

$$c_i = M_i / Q = \phi_i(t)\, c_s \qquad (11\text{-}7)$$

A side condition must be imposed to track the depletion of radionuclides within the waste matrix. Over sufficient lengths of time, it is possible that a nuclide might completely disappear from the waste matrix, by the combination of release and radioactive decay. The actual release behavior of nuclides that approach exhaustion is somewhat complicated and beyond the intent of these computationally simple models. However, the total released mass as a function of time for each radionuclide is checked against the inventory of that radionuclide to ensure that release rates are not artificially driven to higher cumulative amounts than are physically possible.

Soluble Radioelements:

Sadeghi et al. (7) have also developed a calculation release model for soluble radionuclides under these conditions, assuming alteration commences when the waste container is filled with water. Two models are derived; the first is for the case in which the fill time, t_f, is much longer than the alteration time, $1/f_a$, of the waste form:

$$M_i=\alpha\exp[-\lambda_i t-\alpha t]f_a M^{\circ}{}_i\{(\frac{1}{\alpha}+t_1+\frac{1}{f_a})\ (\exp[\alpha t]-\exp[\alpha t_2])-\alpha\frac{[\exp[\alpha t](\alpha t-1)}{\alpha^2} \qquad (11\text{-}8)$$

$$-\ \frac{\exp[\alpha t_2](\alpha t_2-1)]}{\alpha 2}\}+\frac{\alpha\exp[-\lambda i t_2]M^{\circ}\,i}{(t_2-t_1)}(t_2-t_1-\frac{1}{2f_a})\exp[(-\lambda_i-\alpha)\ (t-t_2)]$$

The second is for when the fill time, t_f, is less than the alteration time, $1/f_a$:

$$M_i = f_a M^{\circ}{}_i\{(\exp[\alpha(t_2+\frac{1}{f_a})]-\exp[\alpha t_2])+\frac{1}{2}\alpha(t_2-t_1)\exp[\lambda t_2]\}\exp[-(\alpha+\lambda_i)t] \qquad (11\text{-}9)$$

where:

α	=	Q/V (years^{-1}) = $1/t_f$,
Q	=	volumetric flow rate (m^3/yr),
V	=	interior volume of waste container (m^3),
λ_i	=	radioactive decay constant for nuclide i (= ln 2/ half-life) (years^{-1}),
t	=	time after emplacement of waste (years),
f_a	=	[jo A]/ M°_M, = fractional alteration rate of waste matrix (years^{-1})
A	=	surface area of waste form (m^2),
jo	=	forward-reaction rate of the waste form per unit area (gm/m^2/yr),
M°_M	=	initial mass inventory of waste matrix (gm),
M°_i	=	initial mass inventory of nuclide i at time of waste emplacement (gm),
t_1	=	time after emplacement that the waste container is penetrated (years),

t_2 = time after emplacement when the waste container is full (years).

Note that these release equations are appropriate only up to the time that the waste form becomes completely altered ($t = t_2 + 1/f_a$). The release rate falls off after this time, and Sadeghi et al. [7] derive exact release-rate equations for $t > t_2 + 1/f_a$. In an effort to streamline the source-term portion of the code, these equations were not implemented. Instead, the above release-rate equations are conservatively applied until all of a given radionuclide has exited the waste package.

The time-dependent concentration exiting the waste package, c_i, is:

$$c_i = M_i / Q \tag{11-10}$$

where Q the volumetric flow rate into and out of the package. Many of the terms for these equations will be identical for each different soluble radionuclide, greatly simplifying the computational effort required to calculate the release rates or concentrations of multiple radionuclides.

Moist/Wet-Continuous Release Model

Insoluble Radioelements:

If the waste package is displaced within the emplacement hole, or if the air gap is compromised, radionuclides may be released by diffusive transport along water coating the pores of the unsaturated tuff. Likewise, the development of saturated conditions would permit the diffusive/advective transport of radionuclides from the waste container. Many mass-transfer models have been developed for diffusive/advective transport in the near field (5). A particularly elegant solution has been derived by Chambré (8). This solution is for steady-state mass transport of a radioactive species from a spherical-configuration waste package having a backfill/buffer surrounded by porous rock with diffusive-advective mass transfer. This simplified geometry, while not realistic, reasonably approximates the waste cylinder and can provide basic evaluations on near-field release. The steady-state mass-transfer rate, M_i, and the steady-state concentration, c_i, at the backfill-rock interface are:

$$M_i = \frac{4 \pi \varepsilon \Psi D_b r_o c_s [Sh\, r_1 \sqrt{k}]}{[(Sh - 1) \sinh d + r_1 \sqrt{k} \cosh d]} \tag{11-11}$$

$$c_i = \frac{c_s r_o \sqrt{k}}{[(Sh - 1) \sinh d + r_1 \sqrt{k} \cosh d]} \tag{11-12}$$

where:

ε = porosity of backfill (dimensionless),

Ψ = degree of hydrologic saturation of contacting rock (dimensionless),

D_b = effective diffusion coefficient (m^2/yr),

r_o = waste-form radius (m),

r_1 = radius of backfill/rock interface (m),

b = backfill thickness = $r_1 - r_o$,

c_s = concentration (solubility) of the species at the waste-form surface (gm/m^3),

Sh = Sherwood number = $1 + \dfrac{0.5\,Pe}{1 + 0.63\sqrt{Pe}}$

Pe = Peclet number = $\dfrac{r_1 U}{D_b}$

U = groundwater pore velocity (m/yr),

k = $\dfrac{\lambda R}{D_b}$

R = retardation coefficient for nuclide i in tuff = $1 + \rho\,[(1 - \varepsilon)/\varepsilon\,\Psi]\,K_d$, (dimensionless),

K_d = sorption distribution coefficient (m^3/kg),

ρ = bulk density of tuff (kg/m^3),

d = $(r_1 - r_o)\sqrt{k}$ = $b\sqrt{k}$

Several relations are immediately obvious. The release rate, M_i, is directly proportional to the solubility, the diffusion coefficient, and the backfill porosity; decreases in the values of any of these parameters translates into a proportional decrease in release rate. Note that as U$\rightarrow$ 0, $Pe\rightarrow$ 0 and $Sh\rightarrow$ 1, the release rate does ***not*** go to 0, but reaches a diffusive steady-state value that is proportional to [1/cosh d]. This term represents the decrease in steady-state release arising from radioactive decay of the species as it is retarded by sorption on the backfill. For d > 23 (i.e., high R), the release rate is reduced by more than 10 orders of magnitude, while for d < 0.1 (low R), there is less than 1% reduction in the release rate.

The release rate from the waste package is assumed to be related to the degree of hydrologic saturation (Ψ). At Ψ = 1, the release rate equation becomes that used for fully saturated conditions. If the system becomes completely dry (Ψ = 0), the predicted release rate is zero, as required. Note that both Db and R, however, are also dependent on Ψ.

Soluble Radioelements:

For radionuclides that do not reach solubility limits at the waste-form surface ($\theta \ll 1$), the release rate of these radioelements will be controlled by the alteration/dissolution rate of the waste matrix rather than by mass-transport constraints of convective or diffusive flow. Workers at the University of California, Berkeley (7) have developed a model for the release of readily soluble radionuclides controlled by the alteration/dissolution rate of the waste matrix. Their solution involves the iterative calculation of "instant" release pulses that are summed over a series of relatively small time steps. This summation technique was judged unsuitable for the large number of system calculations required by the overall performance assessment model being implemented on this project (6).

As a simple yet conservative alternative, it is assumed that the steady–state release rate for a given radionuclide species at the boundary of the emplacement hole is constant and equal to the mass-transfer rate for the species at the surface of the waste matrix. This model conservatively ignores the potential attenuation on release rate by retardation during transport to the emplacement hole, which is relatively insignificant for the 0.03 m distance. This latter rate is proportional to the product of matrix alteration/dissolution rate, surface-area, and the time-dependent mass fraction of nuclide i (f):

$$M_i = \Psi\, j_o\, A\, f = \Psi\, j_o\, A\, \frac{M^\circ_i \exp(-\lambda_i t)}{M^\circ_M \exp(-\lambda_M t)} = \Psi\, f_a\, M^\circ_i \exp[-t(\lambda_i - \lambda_M)] \qquad (11\text{-}13)$$

where:

- Ψ = degree of saturation in tuff (dimensionless),
- j_o = matrix alteration/ dissolution rate (gm/m^2/year),
- A = the surface area of the dissolving waste matrix (m^2) = $4\,\pi\, r_o^2$,
- M°_i = initial mass inventory of nuclide i (gm),
- λ_i = radioactive decay constant of nuclide i (years^{-1}),
- M°_M = initial mass inventory of waste matrix (gm),
- λ_M = radioactive decay constant of matrix component U-238 (years^{-1}),
- f_a = fractional alteration rate of waste matrix (years^{-1}) = $[j_o A]/ M^\circ_M$.

Because the decay constant for U-238 is so long (1.54×10^{-10} years^{-1}), the above equation can be reduced to the following approximation:

$$M_i \approx \psi\, f_a\, M^\circ_i \exp(-\lambda_i t) \qquad (11\text{-}14)$$

The steady-state concentration of solution for a given radionuclide exiting the waste package, c_i, is

obtained by the following relationship derived by Chambrè (8) for spherical coordinates:

$$c_i = \frac{Mi}{4\,\pi\,r_o^2\,h} = \frac{Mi\;r_o}{A\;Sh\;\varepsilon\;D_b} = \frac{A\;j_o\;f\;r_o}{A\;Sh\;\varepsilon\;D_b} = \frac{c_s\;\theta}{Sh} \qquad (11\text{-}15)$$

Note that there is a finite duration, t_a, following contact by water for the application of the above equations:

$$t_a = M^{\circ}_M/(j_o\;A) = 1/f_a$$

At the end of this duration the waste matrix is, by definition, completely altered.

The predominant amount of readily soluble nuclides are located within the matrix; however, there is a significant fraction of these nuclides that is readily released upon first contact with water following the loss of containment. Specifically, this readily released fraction is related to the "gap" region of the cladding/matrix for nuclides such as ^{79}Se, ^{99}Tc, ^{129}I, and to the surface "layers" on the Zircaloy cladding for ^{14}C. For the purposes of these simplified source-term models, these mass amounts are conservatively assumed to be "pulses" that will be released within the first year following contact (loss of containment).

Data Base for Release Calculations

Tables 11-3 and 11-4 presents selected values for several physical and chemical parameters that are identified above in the mathematical models. Where possible, these data have been obtained from recent experimental and modeling studies conducted specifically for the Yucca Mountain and materials under expected repository conditions at Yucca Mountain. Table 11-4 shows low, median, and high solubilities that have been selected for radioelements.

These estimated solubility values were derived from a variety of reported sources on radionuclide solubilities for a repository in tuff (6, 9, 11, 13; personal communication from R. Stout, Lawrence Livermore National Laboratory), as well as for a generic "granitic" oxidizing groundwater (10). The "low" values of Table 11-4 correspond to the lowest solubility values cited from reports on a repository located in tuff. The exceptions to this procedure were the "low" solubility for Se, taken from (10), and the "low" solubility values of C and I (for which there were no reliable data reported other than "high") that were set approximately equal to 1.0 gm/m^3. All three of these radioelements are expected to be controlled by UO_2 reaction rate rather than their own solubilities, so this

approximation is not deemed to introduce any significant effect on the calculated results. The "high" solubility values for all radioelements were taken from the highest values reported among these sources. The "medium" values were then selected between these extremes.

Table 11-3

RADIONUCLIDE CHARACTERISTICS

Element	Half life, Years	Amount (Ci/MTHM)	Activity (Ci/gm)
^{14}C	5.73×10^{3}	1.38	4.45
^{79}Se	6.50×10^{4}	0.50	6.97×10^{-2}
^{99}Tc	2.15×10^{5}	13.0	1.70×10^{-2}
^{129}I	1.59×10^{7}	.0315	1.74×10^{-4}
^{135}Cs	3.00×10^{6}	0.345	8.82×10^{-4}
^{226}Ra	1.62×10^{3}	3.12×10^{-3}	0.988
^{234}U	2.47×10^{5}	2.03	6.18×10^{-3}
^{235}U	7.10×10^{8}	0.01	2.14×10^{-6}
^{238}U	4.51×10^{9}	0.01	3.33×10^{-7}
^{237}Np	2.14×10^{6}	0.999	7.05×10^{-4}
^{239}Pu	2.44×10^{4}	305.	6.13×10^{-2}
^{240}Pu	6.58×10^{3}	4.78	0.226
^{242}Pu	3.79×10^{5}	1.72	3.90×10^{-3}

Table 11-4

SOLUBILITIES OF RADIOELEMENTS, IN gm/m^3

Element	Low	Moderate	High
C	1.0	1.4	1.4×10^{2}
Se	7.9×10^{2}	7.9×10^{3}	5.5×10^{5}
Tc	3.5×10^{-2}	1.0×10^{2}	9.9×10^{5}
Sn	1.3×10^{-4}	3.2×10^{-3}	2.2×10^{-2}
I	1.0	3.9×10^{2}	1.0×10^{5}
Cs	1.2	3.9×10^{2}	2.1×10^{3}
Ra	1.0×10^{-5}	4.0×10^{-4}	0.1
U	0.5	2.4	5.0×10^{1}
Np	4.0×10^{-4}	3.6×10^{2}	7.2×10^{2}
Pu	6.0×10^{-5}	9.6×10^{-4}	4.3×10^{-1}
Am	1.5×10^{-7}	9.6×10^{-2}	9.6×10^{-1}
Cm	2.4×10^{-9}	9.6×10^{-2}	9.6×10^{-1}

Summary of Source-Term Calculations

The approach adopted for calculating radionuclide-release rates for use in the EPRI computer software contains the following elements:

1. All relevant release modes (unsaturated conditions, saturated conditions and wet-drip conditions) are identified, with no a priori judgement regarding probability of occurrence,

2. Models are developed for each mode and parameters identified,

3. The proportion of waste packages that are releasing by any given mode are conceptually related to the conditions and events that have previously occurred for a given scenario; these include:

   - Seismic disturbances,
   - Mode and timing of containment failure,
   - Thermally induced failure of the air gap,
   - Elevation of the water table,

   - Number and flow properties of water-bearing fractures intersecting the repository horizon,
   - Time at which temperature for formation of liquid water is attained at the container surface.

4. Within the proportion of waste packages that are undergoing release by a certain mode, individual waste packages having different parameters can be independently simulated,

5. Available data on the performance of engineered barrier materials have been obtained from the literature and communications with the Department of Energy contractors studying the Yucca Mountain site. These data have not been critically examined and their use in this report in no way constitutes a confirmation of their correctness.

6. Release rates (grams per year) and concentrations (gm/m^3) into the tuff host rock are calculated. These values can be readily normalized by 1000-year inventories of

radionuclides to compare with proposed EPA release-rate performance objectives for the proposed repository.

It must be noted that certain simplifications and assumptions are made in these models to permit incorporation within the computer software for performance assessment over multiple scenarios. Among these simplifications/ assumptions are:

- The geometry of the waste package has been generalized to a sphere in some cases. Such an approximation introduces differences of less than 10% from the exact cylindrical geometry; given the order-of-magnitude uncertainty (or more) in many parameters, this variation is not deemed significant.

- Steady-state, rather than transient, release rates are calculated. While the release model does incorporate a term to describe the attenuation of final release rate arising from combined sorption and radioactive decay on tuff gravel, use of this steady-state model neglects the effect of sorption on delaying the time to reach final release rate from the waste package. Given the fact that the current design for waste packages at Yucca Mountain does not contain any buffer/ backfill barrier for sorption, the relatively short pathway (0.03 cm) from the waste container to the host rock, and the uncertain aggregate properties of tuff material that may fill this air gap, ignoring sorptive delay in reaching steady state is a conservative and justifiable assumption.

- Radioactive decay within the waste form and during transport are included. Decay-chain in-growth (i.e., Np-237 growing in from Am-241 that has been previously released and is migrating in the near-field) is excluded. This may be a significant factor in treating the release of Ra-226 and Th-230 at time periods greater than 100,000 years. Depending on the relative solubility and sorption behavior of Am (having short-lived isotopes) relative to Pu, Np, and U (with longer-lived daughters), decay in-growth may be a significant factor.

- Two groups of radioelements are identified; "insoluble" radioelements that are expected to be solubility limited in their release (e.g., Cs, Sn, U, Np, Pu, Am) and "soluble" radioelements that are released at a rate corresponding to the alteration/dissolution rate of the UO_2 matrix (e.g., Se, Tc, I) or corrosion rate of Zircaloy/structural hardware (C).

- Certain volatile radionuclides (e.g., ^{135}Cs, ^{137}Cs, ^{79}Se, ^{129}I) are found to escape from the UO_2 matrix of spent fuel during reactor operation and become trapped with noble fission gases in the "gap" between the fuel matrix and cladding. By equating the release of these "gap" radionuclides with measurements of noble fission gases released from failed fuel pins, it is assumed here that 1-2% of these soluble "gap" radionuclides will be released within the first year following loss of containment by the Zircaloy cladding. These "gap" nuclides are expected to be important contributors to overall repository performance because of the rapid release of a significant amount of their inventory, their generally non-sorbing behavior, and long half-lives.

  The actual percentage of "gap" radionuclides will be a function of fuel burnup and power history, although there are not extensive statistical data on these effects for light-water reactor (LWR) fuel. In addition, the 1:1 relationship between "gap" radionuclides and noble fission gases is probably a conservative assumption. By analogy to CANDU fuel (14), "gap" nuclides such as ^{79}Se, ^{135}Cs and ^{129}I are present in the "gap" at percentages of their total abundance that are significantly lower than the percentages of the abundances of the noble fission gases. Again, exact information for LWR is difficult to obtain and may be further complicated by possible imprecisions in codes such as ORIGEN (3) that are used to calculate total radionuclide inventories. Clearly additional work will be needed to refine and confirm these estimates of "gap" inventories.

- Under hydrologically unsaturated conditions, it may be assumed that there is inconsequential convective flow occurring; transport by either dripping water or diffusion through partially-filled pores is assumed for such conditions. The release model could be extended to handle episodic saturated flow through tuff if that mode is deemed likely.

- Several of the parameters affecting release are temperature-dependent. These include solubilities, sorption coefficients, diffusion coefficient, and degree of saturation. While data exist on some of these temperature dependencies (e.g. (9)), the estimated size of temperature-dependent variations between 90°C and 25°C is small (less than one order of magnitude) compared to the uncertainties in the absolute magnitudes of these parameters. It would be misleading, therefore, to explicitly include such temperature

dependencies into the source-term model at this time. Selection of high, median, and low values for radioelement solubilities has been implemented instead, in an effort to capture the effect of these uncertainties on the overall performance of a geologic repository. The logic tree node used to represent uncertainty in solubility and dissolution rate is shown in Figure 11-6.

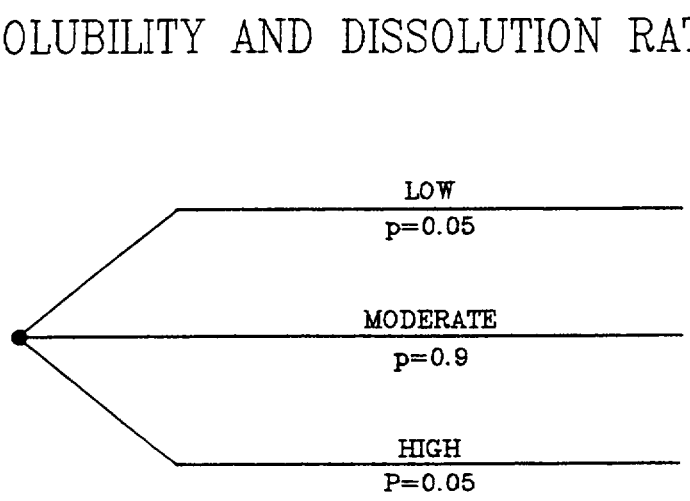

Figure 11-6. Logic tree node showing uncertainty in solubility and dissolution rate.

Certainly there are other, more advanced models for calculating transient release rates of radionuclides from waste packages over a full range of conditions (10, 15). Given the constraints of the current project, none of these codes could be used. If more detailed analysis of the near field proves warranted, the use of such codes as linked, supporting codes could be considered for future versions of this probabilistic code. Linkage could be established directly, or through means of creating data arrays of release-rate profiles that could abstracted by the performance assessment code. Such linkage would provide more rigor in calculated release calculations, permit inclusion of processes and parameters currently excluded, yet would permit the EPRI code to retain its useful, compact structure and ease of operation.

REFERENCES

1. M. J. Apted, W. J. O'Connell, K. H. Lee, A. T. MacIntyre, T.-S. Ueng, T. H. Pigford and W. W.-L. Lee. "Preliminary Calculations of Release Rates from Spent Fuel in a Tuff Repository." In *Proceedings of the 2nd International Conference on High Level Radioactive Waste Management*, Vol. 2. LaGrange Park, IL: American Nuclear Society, 1991, pp. 1080-1090.

2. J. Conca. "Diffusion Barrier Transport properties of Unsaturated Paintbrush Tuff Rubble Backfill." *High-Level Radioactive Waste Management*, vol. 1, 394, American Nuclear Society, 1990.

3. J. W. Roddy, H. C. Claiborne, R. C. Ashline, P. T. Johnson, and B. T. Rhyne. *Physical and Decay Characteristics of Commercial LWR Spent Fuel.* ORNL/ TM–9591 Oak Ridge, TN: Oak Ridge National Laboratory, 1986.

4. S. J. Zavoshy, P. L. Chambré and T. H. Pigford, "Mass Transfer in a Geologic Environment." *Scientific Basis for Nuclear Waste Management VIII.* Pittsburgh, PA: Materials Research Society, vol. 44, 1985, p. 311.

5. T. H. Pigford and P. L. Chambré. "Near-Field Mass Transfer in Geologic Disposal Systems: A Review." *Scientific Basis for Nuclear Waste Management XI.* Pittsburgh, PA: Materials Research Society, vol. 112, 1988, p. 125.

6. R. K. McGuire (ed.). *Demonstration of a Risk-Based Approach to High-Level Waste Repository Evaluation*, Palo Alto, Calif.: Electric Power Research Institute, 1990. NP-7057, Research Project 3055-2.

7. M. M. Sadeghi, T. H. Pigford, P. L. Chambré and W. W.-L. Lee. *Equations for Predicting Release Rates for Waste Packages in Unsaturated Tuff. LBL-29254.* Berkeley, Calif: Lawrence Berkeley Laboratory, 1990.

8. P. L. Chambré. *Steady-State Mass Transport of a Radioactive Species from a Sphere into a Backfill Surrounded by Porous Rock, with Diffusive-Advective Mass Transfer in the Rock.* Berkeley, Calif.: LBL- Lawrence Berkeley Laboratory, in press.

9. C. J. Bruton and H. F. Shaw. "Geochemical Simulation of Reaction Between Spent Fuel Waste Form and J–13 Water at 25°C and 90°C" *Scientific Basis for Nuclear Waste Management XI.* M. Apted and R. Westerman (eds.). Pittsburgh, PA: Materials Research Society, 1988, 485 p.

10. Statens Kårnkraftinspektion (SKI). *SKI PROJECT-90*, SKI TR 91-23, Stockholm, Sweden, 1991.

11. M. J. Apted, A. M. Liebetrau, and D. W. Engel. *The Analytical Repository Source-Term (AREST) Model: Analysis of Spent Fuel as a Nuclear Waste Form.* PNL-6347. Richland, WA: Pacific Northwest Laboratory, 1989.

12. W. J. O'Connell and R. S. Drach. *Waste Package Performance Assessment: Deterministic System Model Program Scope and Specification.* Livermore, Calif.: UCRL–53761, Lawrence Livermore National Laboratory, 1986.

13. U.S. Department of Energy. *Environmental Assessment: Yucca Mountain Site, Nevada Research and Development Area, Nevada.* DOE/RW-0073. Washington, DC: vol. 2 of 3, Office of Civilian Radioactive Waste Management, 1986.

14. N. C. Garisto, E. R. Vance, S. Stroes-Gascoyne and L. H. Johnson. *Instant-Release Fractions for the Assessment of Used Nuclear Fuel Disposal.* AECL-9892. Pinawa, Manitoba, Canada: Whiteshell Nuclear Research Establishment, 1989.

15. M. J. Apted, "Engineered Barrier System of the Near Field: The 'Little Brother' of Performance Assessment," Proceedings of the 1989 Paris Symposium on Safety Assessment of Radioactive Waste Repositories, 471, OECD/ Nuclear Energy Agency, Paris, France (1990).

Section 12

GROUNDWATER FLOW AND MASS TRANSPORT

by

Frank W. Schwartz

SCOPE OF EVALUATION

This Section describes features of the hydrogeological system at Yucca Mountain and explains how these elements are represented in the overall risk-based approached. As a basis for understanding the logic tree for groundwater and the models for contaminant transport, the next subsection describes the conceptualization of the hydrogeologic setting. A detailed description of the modeling approach is presented in subsection titled "Flow and Transport Modeling"; the subsection titled "Logic Tree" summarizes the groundwater logic tree and its component nodes.

CONCEPTUALIZATION OF THE HYDROGEOLOGIC SETTING

The strategy for storing nuclear waste in a mined repository relies in part on geologic and hydrogeologic barriers to control the release and spread of contaminants. At the Yucca Mountain site, the capability of the geosphere to perform this function, judged in terms of well-defined performance standards, is a major component of the site characterization study. Early consideration of the site was prompted by two important hydrologic features, the arid climate and the thick unsaturated zone, both of which at the present time apparently limit the potential fluxes of nuclides.

Understanding and representing the hydrogeological setting is made difficult by a relatively complex pattern of geologic layering with an attendant variability in hydraulic and transport properties, and by the presence of faults and fractures. Following several recent studies (1, 2), the stratigraphy is idealized in terms of a small number of major units. The Tiva Canyon unit is a partially saturated, densely fractured, welded tuff (Figure 12-1). The tabulation of data by Dudley and others (3, their Table 2-1-2) shows the saturated hydraulic conductivity of the matrix is approximately 9.7×10^{-12} m/s with a porosity of about 8%. The unit is quite fractured (20 fractures/m^3) with the fractures having a hydraulic conductivity many orders of magnitude higher than the matrix (3, Table 2.1-2).

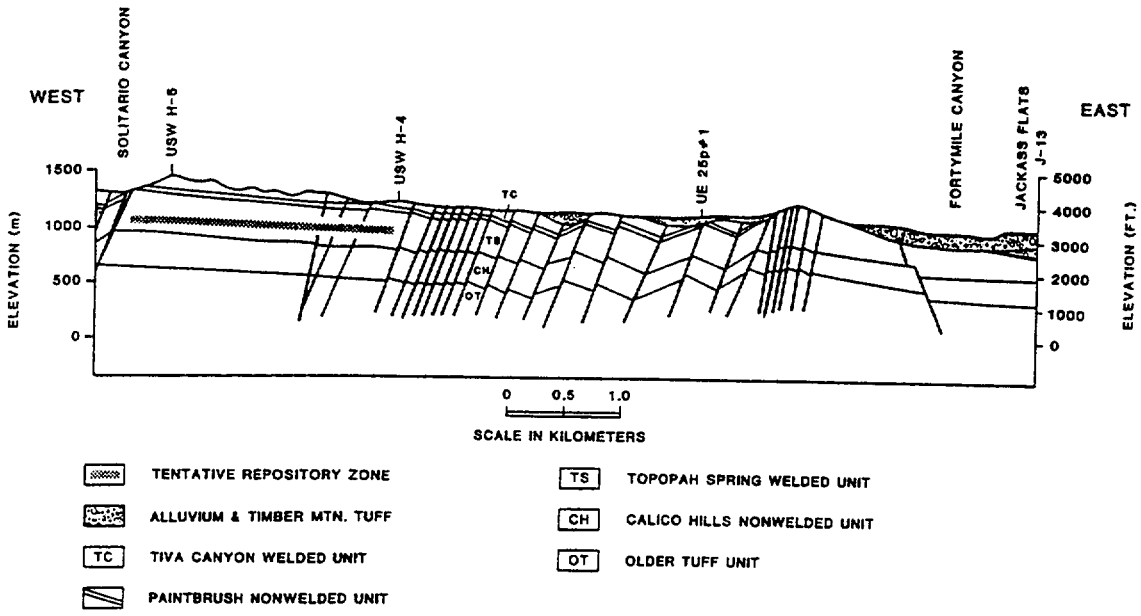

Figure 12-1. East-west geologic cross-section for the Yucca Mountain site showing the most important hydrostratigraphic units (modified from (6)).

Next stratigraphically is the Paintbrush unit, which is a nonwelded ash-fall tuff. Typically this unit has low fracture densities (1 fracture/m^3), a porosity of about 40%, and a matrix conductivity of 3.9×10^{-7} m/s (3, Table 2-1-2). The underlying Topopah Spring unit in which the repository is planned to reside has been divided into an upper and lower half (Figure 12-1). Both of these units are presently considered to have similar matrix conductivities (1.9×10^{-11} m/s) and porosities (11%) but differ in terms of the fracture properties. The fracture densities and fracture conductivities are 40 and 8 fractures/m^3, and 2.2×10^{-5} and 1.7×10^{-5} m/s for the upper and lower portions respectively.

The underlying Calico Hills nonwelded tuff contains both vitric and zeolitic facies. A detailed analysis of the history of alteration by Levy (4) indicates that a zone 100 m or more above the water table has been zeolitized. Thus, the Calico Hills unit for our analysis is provided with the zeolitic set of parameters for nonwelded tuff described in Dudley and others (3). As Gauthier and others (2) show, performance of the repository generally is not sensitive to this particular characterization. Older tuff units underlie the Calico Hills unit and, for example include the Prow Pass, Bullfrog, and Tram units. These deeper units are also fractured with a modest intergranular permeability.

Along the line represented by the cross-section shown in Figure 12-1, the water table is almost flat lying and occurs at a depths ranging from approximately 500 to 650 m from the ground surface. Regionally, however, the water table configuration is more complicated. Zones having a low water-table gradient (north east and southeast of the proposed repository) are separated by a zone having a relatively high hydraulic gradient (just north of the proposed repository). The occurrence of these different zones has been related to large scale variations in hydraulic conductivity that may or may not remain constant with time (5). Eventually, the water table occurs at the ground surface to the south in the Amaragosa desert where it forms a playa.

Fracture/Matrix Coupling

Flow in a fractured porous medium is described mathematically in its most complete form by writing a separate nonlinear flow equation for the matrix and the fracture network. Terms in these equations account for the coupling between the two systems. While it is possible to solve the pair of coupled equations, simplifications are often made to make the modeling easier. One approach is to assume that differences in pressure head that develop within a fracture are instantaneously redistributed within the matrix or vice versa (3). This assumption about the coupling yields a single flow equation in which the key model parameters are represented as bulk or "composite" values. For example, hydraulic conductivity and capacitance terms are defined as the volume weighted contributions from the matrix and the fractures.

This approach can be illustrated with the hydraulic conductivity versus pressure head curves for the zeolitic Calico Hills unit (Figure 12-2). Curves of this type are usually determined experimentally and represented mathematically by the van Genuchten or other similar constitutive equations.

As Figure 12-2 illustrates, the curves for the fracture system and the matrix each have their own distinctive shape. The composite relationship in effect is the single curve that represents the combined effects of the fractures and matrix. Inspection of the composite curve shows that as the medium becomes drier (higher negative pressure heads) the matrix conductivity is controlling, and as the medium becomes wetter, the fracture conductivity is controlling.

Just as there is coupling of flow between the matrix and fracture systems, there is also the possibility of coupling as dissolved mass is transported through the system. The process involves the diffusion of mass between the fracture and the pores of the unfractured rock blocks. Following Dudley and others (3), our conceptual model of mass transport provides for both "strong" and "weak" diffusive

coupling. Strong coupling assumes that the mass is redistributed instantaneously between the matrix and fracture systems. This coupling effectively means that mass transport is described in terms of a composite velocity, which Dudley and others (3) express as:

$$v^i = \frac{q}{\theta_m R_m^i + \theta_f R_f^i} = \frac{q}{\theta_m R_m^i} \qquad (12\text{-}1)$$

where v is the advective velocity of the ith constituent, q is the Darcy velocity for water flow, R is the moisture content, subscripts m and f refer to the matrix and fractures respectively, and θ is the retardation factor for the ith constituent.

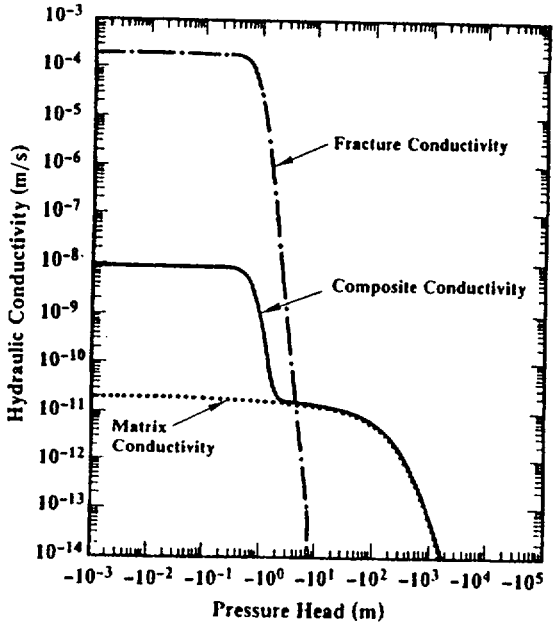

Figure 12-2. Example of a conductivity curve developed for unit CHnz (from Dudley and others (3)).

Weak coupling is assumed to occur when mineral precipitates along the fractures reduce the rate of diffusive transport between the fracture and matrix. The effect of weak coupling is most evident with relatively large groundwater fluxes when contaminants moving along fractures can be far in front of mass traveling along in the matrix (3).

Other Main Elements

Ideally, to capture the essence of the complex flow through Yucca Mountain requires that the complete

saturated/unsaturated system be modelled with a transient, multi-dimensional model that reflects the complex pattern of layering and disruptions due to fault development. Unfortunately, the requirement for many separate transport calculations within a performance assessment code usually means that simpler models must be used that provide less fidelity with the actual hydrogeologic setting. With this point in mind, following here is a discussion of three features of the hydrogeological setting that we feel should be captured by the simpler models. The detailed modeling studies by Prindle and Hopkins (1) indicate that changing hydraulic conductivities with depth and the major faults may produce distinctly two-dimensional patterns of flow. As Figure 12-3 illustrates, under relatively large net infiltration fluxes, water is diverted laterally downdip as a result of the large contrast in hydraulic conductivities between Paintbrush nonwelded unit and the underlying Topopah Springs Unit. Open faults or the zones alongside sealed faults could provide the pathway for further vertical flow. Lateral flow above the repository not only shields it from increases in the applied flux but generally promotes vertical flow in units below the repository. Figure 12-4 taken from Prindle and Hopkins (1), shows that this shielding effect may begin at fluxes above 0.20 mm/yr and become particularly pronounced as fluxes increase above 1.0 mm/yr.

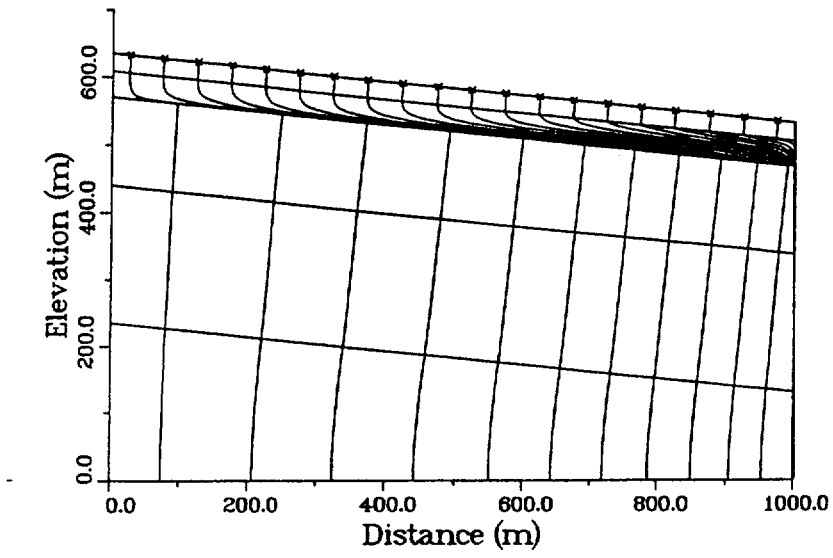

Figure 12-3. Simulation results showing lateral flow diversion within the Paintbrush unit to a down-dip fault (from (1)).

Another feature related to the complex setting is the possibility for storage within the Paintbrush unit perhaps to delay the onset of changes in the surface infiltration rate at the repository level (3). For example, Dudley and others (3) compute that a flux change from 0.1 to 0.2 mm/yr will be felt at the repository approximately 10,000 years after it occurs at the surface. As surface fluxes increase above about 1.0 mm/yr, the effect becomes insignificant. These delay times will be important in models like ours that pick flow up at the repository.

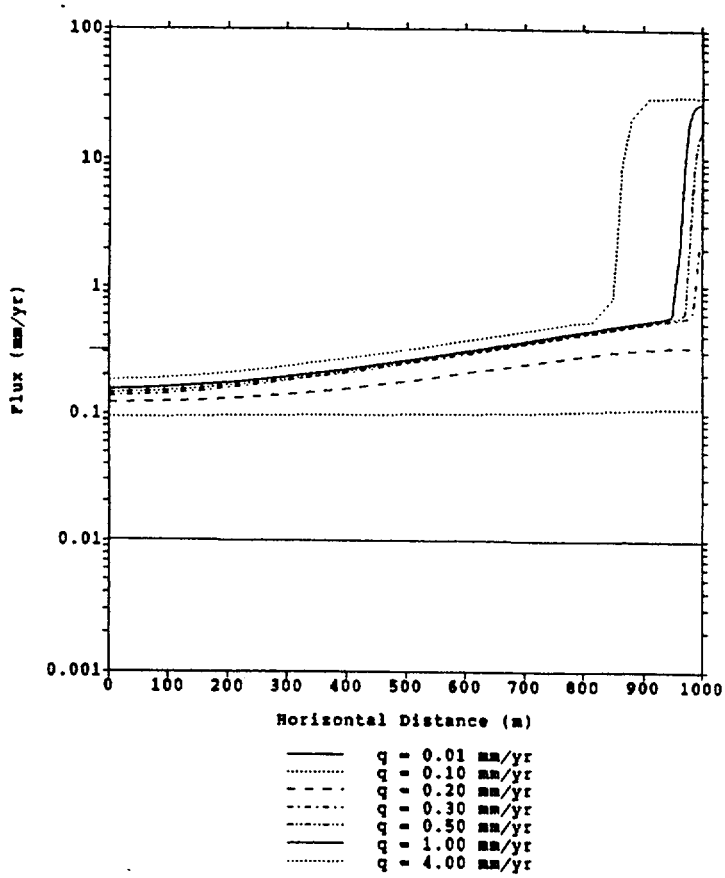

Figure 12-4. Variation in flux at the repository as a consequence of lateral diversion of flow in the Paintbrush unit (from (1)).

The possibility for lateral flow and transport below the water table has not been considered generally in most analyses (1, 3) or to only a limited extent (6). However, this part of the system may contribute in a meaningful way to the system performance. Although data on the zone of saturation beneath the site are limited, there is less uncertainty about the conceptual model for flow. Fractures provide the dominant pathways for flow under a relatively low hydraulic gradient. The direction of

flow in the saturated groundwater system is generally southward. Sinnock and others (7) suggest that the upper portion of the saturated system (i.e., water table to 1200 m) behaves as an unconfined aquifer because the hydraulic head is constant and independent of depth. At greater depth there is an apparent increase in hydraulic head that provides evidence of an upward component of flow (5, 8). Syzmanski (5) interprets these higher heads at depth as caused by changes in the distribution of hydraulic head due to tectonic straining. Sinnock and others (7) cite the results of ^{14}C determinations and other studies that indicate seepage velocities from 1 to 50 m/yr.

FLOW AND TRANSPORT MODELING

To understand fully the groundwater portion of the logic tree requires a detailed description of the capabilities and limitations of the flow and mass transport model. With the logic tree representing the significant processes and events that might affect the repository and the uncertainty about these processes, the purpose of the flow and transport code is to predict the performance of the barrier/repository system in relation to existing regulations concerned with travel times and release rates. These types of performance assessments by DOE will form the basis for demonstrating compliance with the regulations (8).

Flow and transport codes that are used for performance assessments must treat a large number of scenarios. For this reason, these codes typically cannot provide the same level of sophistication and detail as the more rigorous research codes that are designed to understand processes. However, to the extent possible, performance assessment codes must represent the hydrogeologic setting in a realistic manner.

Mathematical Formulation of the Problem

The main features of the conceptual model for flow and transport described above are represented in the code developed for this study. The problem domain consists of a one-dimensional unsaturated pathway from the proposed repository to the water table and a connected saturated pathway that transports nuclides laterally 5 km to the boundary of the accessible environment (Figure 12-5). The position of the water table varies as a function of other elecments in the master logic tree. The unsaturated portion of the pathway includes the lower half of the Topopah Springs unit and approximately 130 m of the Calico Hills unit.

The following equation describes the flow of groundwater in a one-dimensional, unsaturated medium (9):

$$\frac{\partial}{\partial z}\left\{ K_{*}(\psi)\ \frac{\partial\ (\psi+z)}{\partial z} \right\} = \frac{\partial \theta}{\partial t} \qquad (12\text{-}2)$$

where z is the vertical coordinate, positive upward, K_* is the unsaturated hydraulic conductivity which is a function of the pressure head, ψ (negative for unsaturated flow), θ is the moisture content, and t is time.

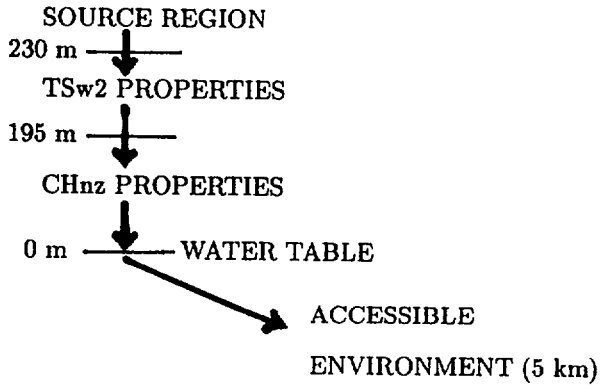

Figure 12-5. Transport pathways to the accessible environment.

In order to solve an unsaturated flow equations like equation (12-2) it is necessary to specify functions that define the relationship between hydraulic conductivity, moisture content and pressure head. Because the analytical approach of Srivastava and Yeh (9) will be used to solve equation (12-2), these simple constitutive relationships are chosen:

$$K_{*} = K_{s}\, e^{\alpha\psi} \qquad (12\text{-}3a)$$

$$\theta = \theta_{r} + (\theta_{s} - \theta_{r})\, e^{\alpha\psi} \qquad (12\text{-}3b)$$

where K_s is the saturated hydraulic conductivity, θ_r is the residual moisture content, θ_s is the saturated moisture content, and α is a soil pore-size distribution parameter. It is generally well known that the constitutive relationships in (12-3a) and (12-3b) relative, for example, to the van Genuchen equations have considerable limitations in their ability to represent experimentally derived relationships and the behavior of soils close to saturation (9). Their use here is a concession to the need to find a computationally simple solution to the flow equation. Later analyses will show that these simplified relationships do in fact provide reasonable results.

Clearly, the simple relationships in equations (12-3a) and (12-3b) are not able to represent the complex composite conductivity curves like the one shown in Figure 12-2. However, they can approximate the individual matrix and fracture conductivity curves reasonably well. The approach we follow is to utilize the future net groundwater flux at the repository, I_{r2}, to determine whether the fracture or matrix curves predominate and thus avoid specifying the full composite curve. The cutoff value was determined to be 0.6 mm/yr. For those cases that involve both matrix and fracture dominated flow, the fracture curve is selected to be conservative. In most instances, the change to the future flux occurs at 1000 years making the resulting errors on calculated releases small.

One-dimensional mass transport is described by the following form of the advection-dispersion equation (10):

$$D_z\frac{\partial^2 C}{\partial z^2}-v_x\frac{\partial C}{\partial z}-R_f\lambda C=R_f\frac{\partial C}{\partial t} \qquad (12\text{-}4)$$

where C is concentration, D_z is the dispersion coefficient in the z-direction, v is the unsaturated flow velocity, λ is the decay rate constant or 0.693 divided by the radioactive half-life, z is distance, R_f is the retardation factor that accounts for the equilibrium sorption of the nuclide and diffusion into the matrix, and t is time.

The flow and mass transport equations are coupled through the velocity term in equation (12-4) and by concentrations in cases where the density of the contaminant plume is different from the ambient groundwater. The description below summarizes how forms of these equations are solved to provide the pressure head, moisture content, and radionuclide concentrations as a function of depth and time. This information provides the basis for calculating the cumulative mass released at the accessible environment, for comparison to EPA regulations for allowable releases.

Boundary and Initial Conditions

In order to provide a specific solution to equations (12-2) and (12-4), initial and boundary conditions need to be specified. Further, it is with the help of the boundary conditions that the major elements of the conceptual model are represented. For example, the specified inflow to the problem domain (Figure 12-4) may be reduced to account for lateral diversion higher in the stratigraphic section. In other words, the flux of ground water through the repository, I_r, in general is less than or equal to the net infiltration flux at the ground surface, I_s. The logic tree defines the range of uncertainty in exactly how these variables are related. Waste stored in the repository is assumed not to interact with the

water that is diverted laterally.

The boundary and initial conditions used to develop the analytic solution to equation (12-2) are quite complex mathematically. Interested readers can refer to Srivastava and Yeh (9) for a detailed definition. Operationally, the boundary at the repository has flux specified in terms of an initial flux (I_{r0}), and a flux at times greater than zero (I_{rt}). Because the initial condition is essentially the steady state distribution of pressure head due to I_{r0}, the time at which the flux changes need not be zero and can be specified in the future. This lets us simulate, for example, a change in climate at 1000 years in the future that causes infiltration rates, for instance, to increase from a present-day value to a pluvial value. The notation adopted here is to represent the present flux conditions as I_{r1*} and the flux due a change in the climate in the future as I_{r2*}. The "*" indicates the timing for the flux change has to consider the time lag in the flux change.

The actual time that a flux change is felt at the repository must be adjusted from the surface value to account for the time required for water to reach the repository. To establish this value in our case, the following transfer function was developed based on simulation results presented by Dudley and others (3):

$$t_{rep} = t_{surf} + t_{adj} \quad \text{where} \quad t_{adj} = 25 \exp(-I_{s2}/0.22) \qquad (12\text{-}5)$$

where t_{rep} is the time (millennia) when a flux change occurs at the repository, t_{surf} is the time (millennia) when the net infiltration flux changes at the surface, t_{adj} is the time lag (millennia) and I_{s2} is the new net infiltration rate at the surface when the climate changes. Sample calculations provided in Table 12-1 illustrate the relationship between I_{s2} and t_{adj}.

Table 12-1

VALUES OF t_{adj} AS A FUNCTION OF I_{s2}

I_{s2}	t_{adj}
0.1	15.8
0.2	10.0
0.5	2.5
1.0	0.2
2.0	0.0

NOTE: I_{s2} is in m/millenium, t_{adj} is in millenia

The lower boundary for calculations involving the unsaturated domain is the water table along which the pressure head is fixed at zero. Because the water table is a boundary to the system, its position remains fixed throughout time. Thus, any processes that might produce a change in the water table position are assumed to have occurred when the simulation begins. This assumption, although conservative in the safety analysis, will undervalue the importance of the thick unsaturated zone at Yucca Mountain in some scenarios. Within the zone of saturation, a solution to the flow equation is assumed by providing constant values of velocity.

In terms of mass transport, it is assumed that initially all radionuclides have a zero concentration throughout the system. Mass loading rates as a function of time at the repository are determined with the source loading and container failure models. Mass reaching the boundary with the accessible environment leaves there.

Modeling Methodology

A semi-analytical approach is utilized to solve the flow and transport problem. The method as it is typically implemented involves an using an analytical solution for the flow equation and numerical solution to the mass transport equation (11). Here, Srivastava and Yeh's (9) analytical solution for transient, unsaturated flow in a layered system provides estimates of pressure potential at a series of equally spaced points from the repository to the water table. The solution is particularly complicated so that we have chosen not to reproduce it here.

The calculated pressure heads together with hydraulic conductivity $K_*(\psi)$, moisture content (θ) and elevation are used in the Darcy equation to determine linear groundwater velocities or the velocity of advective mass transport. In the saturated groundwater system, the velocity is not calculated but simply provided as input. Under the particular conditions, when there is no zone of saturation, the code simply skips the calculations for the unsaturated zone.

The moving particle approach (12) models flow subject to advection, retardation due to sorption, and radioactive decay. In order to simplify the numerical procedure, dispersion and radionuclide ingrowth due to decay chains are not considered. The method works by adding a reference particle to the flow field at the repository at the beginning of each time step. During this time step, the particle is moved a distance along the one-dimensional pathway that is determined by the size of the time step (Δt) and the contaminant velocity (v_c) according to the following equation:

$$\Delta z = v_c \Delta t$$

In practice, the size of the time is kept relatively small to provide an appropriate sampling of the velocity field. The contaminant velocity is related (7) to the linear groundwater velocity (v) that is calculated from the flow equation by:

$$v_c = v/R_f \qquad (12\text{-}7)$$

where R_f is $(1 + \rho_b K_d/\theta_m)$ with θ_m as matrix moisture content, ρ_b as the bulk density of the medium, and K_d as the distribution coefficient. For the present study, transport in the saturated system is assumed to occur with a R_f of one.

Each of the moving particles carries along with it a certain mass of the given radionuclide. The amount of mass is determined from the waste leaching and the container failure models. With time, the mass on the particle is reduced using a first-order kinetic expression to account for radioactive decay. By knowing the flow rate of groundwater through the repository, it is a simple matter to calculate the cumulative mass outflow to the accessible environment.

This formulation of the unsaturated transport equation represents the case of strong coupling discussed in section "Fracture/Matrix Coupling" that is comparable to the approach in TOSPAC (3). The way we model transport precludes an equivalent development for the case of weak coupling. However, by using an effective moisture content in the velocity determinations, it is possible to approximate the case of weak coupling. The present model uses effective moisture contents of 4.6×10^{-3} and 18×10^{-3} for the Calico Hills and lower Topopah Springs units respectively.

Input Parameters

A variety of input data is required for a flow and transport calculation. A summary of parameter values is shownn in Table 12-2.

Model Verification

The flow and transport model has been checked through a series of cross-verification trials with TOSPAC (3). A version of TOSPAC was made available to this project through the co-operation of researchers at Sandia National Laboratories. A series of TOSPAC model runs was conducted to replicate certain base cases. After slight modifications to the project code to include the congruent leach and container failure models used by TOSPAC, the project model should provide comparable

results from the repository to the water table.

Table 12-2

SUMMARY OF PARAMETERS REQUIRED FOR THE FLOW AND MASS TRANSPORT SIMULATIONS

$l_{1,2}$	- thickness of layers 1 (CHnz) and 2 (TSw2-3)
$K_{s1,s2}$	- saturated hydraulic conductivity values for layers 1, 2
$\alpha_{1,2}$	- soil pore-size distribution parameters for layers 1,2
$\theta_{r1,r2}$	- residual moisture content for layers 1, 2
$\theta_{s1,s2}$	- saturated moisture content for layers 1, 2
$I_{r1,r2}$	- groundwater flux at the repository for times 1, 2
$\theta_{e1,e2}$	- effective moisture content for layers 1, 2
v_{sat}	- linear groundwater velocity in the saturated zone
$m_0(t)$	- time variation in the mass loading at the source
λ_i	- radioactive decay rate constant for ith nuclide
$(\rho_b K_d)_{1,2}$	- dimensionless distribution coefficient for ith nuclide in layers 1, 2

The cross-verification test presented here is the second example problem of Gauthier and others (2), with a set of changes involving the surface infiltration rates and the extent of coupling. The only change in the basic data from example 2 (2) was to reduce the dispersion lengths in TOSPAC to 1 m to account for the fact that our code neglects dispersion.

In all, four test are run with the following variations: Test A - strong coupling, flux 4 mm/yr, ^{129}I; Test B - strong coupling, flux 0.5 mm/yr, ^{129}I; Test C - strong coupling, flux 4.0 mm/yr, ^{99}Tc; and Test D - weak coupling, flux 4.0 mm/yr, ^{129}I. The model results (labelled "FLOAT" in the figures) for the tests with strong coupling are quite similar (Figures 12-6, 12-7, and 12-8). Typically, TOSPAC exhibits earlier breakthrough with small quantities of contaminant because some dispersion is still occurring in the TOSPAC simulations. The small differences in the two sets of results are due mainly to the differences in moisture contents predicted by TOSPAC and the project model. These differences are due to differences in the constitutive relationships between the two models.

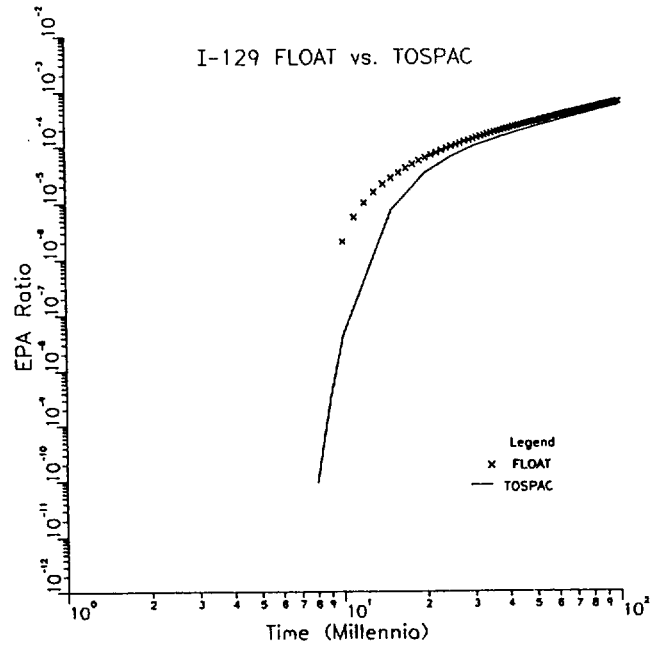

Figure 12-6. Comparison of results with TOSPAC in Test A for ^{129}I transport under conditions of strong coupling and a surface flux of 4mm/yr.

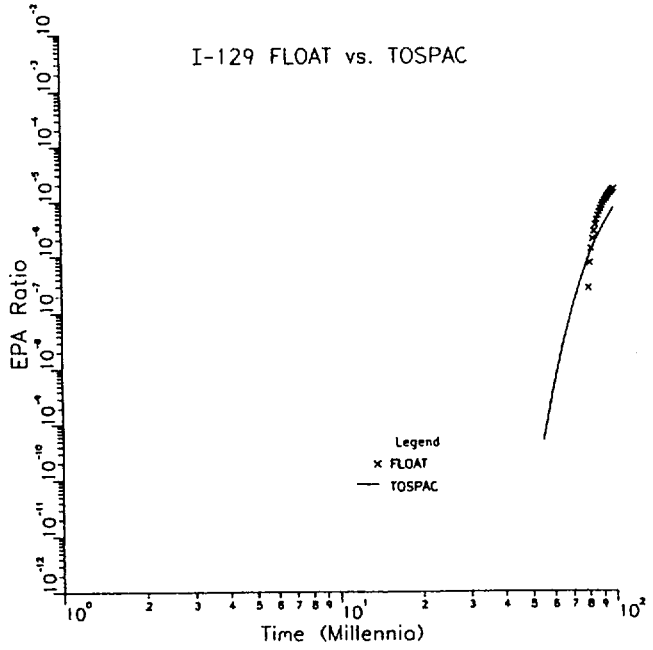

Figure 12-7. Comparison of results with TOSPAC in Test B for ^{129}I transport under conditions of strong coupling and a surface flux of 0.5 mm/yr.

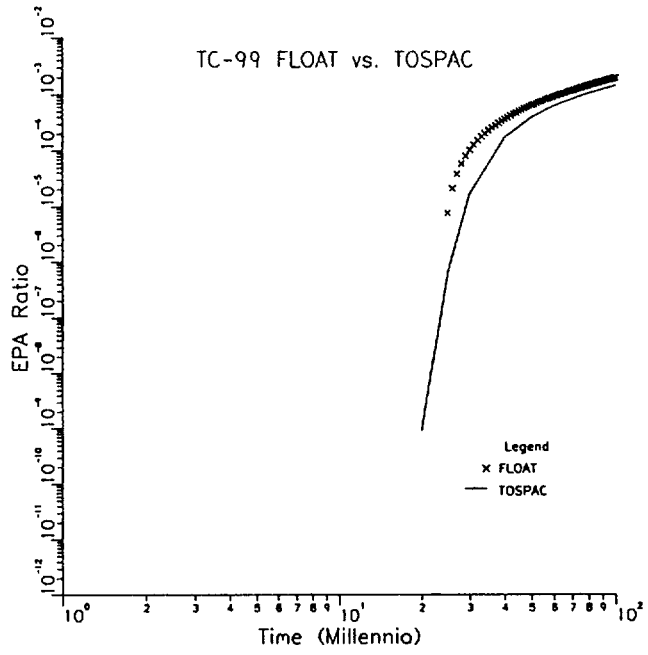

Figure 12-8. Comparison of results with TOSPAC in Test C for ^{99}Tc transport under conditions of strong coupling and a surface flux of 4 mm/yr.

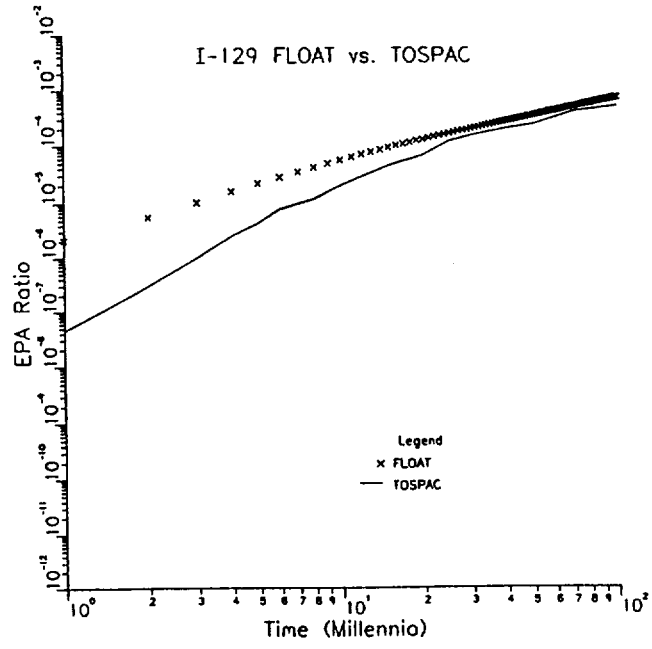

Figure 12-9. Comparison of results with TOSPAC in Test C for ^{99}Tc transport under conditions of weak coupling and a surface flux of 4 mm/yr.

For the test with weak coupling, the lack of sophistication of our model relative to TOSPAC is reflected in the comparison (Figure 12-9). Nevertheless, the results are considered acceptably close given the broad range of uncertainties elsewhere in the simulation problem. Overall, the successful cross-comparison of our simple code with TOSPAC provides confidence that in spite of simplification the approach taken here is valid.

LOGIC TREE

The groundwater system is represented by a logic tree consisting of four different nodes. As illustrated in Figure 12-10, the nodes represent: (1) the groundwater flux at the repository, (2) fracture/matrix coupling within the Topopah Springs and Calico Hills units, (3) sorption within the matrix, and (4) groundwater flow within the saturated portion of the system. Branches on the resulting logic tree (Figure 12-10) for all four nodes represent uncertainty in how the various processes manifest themselves during transport.

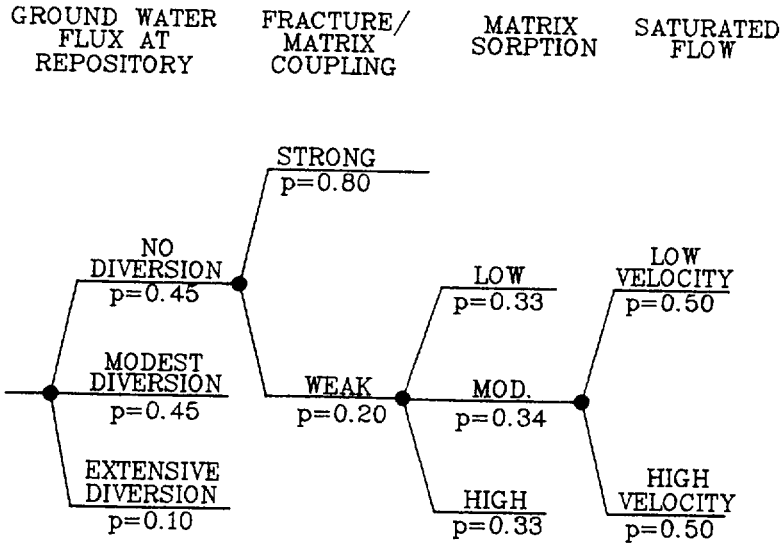

Figure 12-10. Logic tree for parameters describing groundwater and radionuclide flow.

Groundwater Flux

The main uncertainty associated with infiltration flux at the repository is knowing the extent to which lateral diversion of flow will occur, as the present conceptualization suggests. The top middle and bottom branches for this node (Figure 12-10) consider the following three possibilities: no lateral redistribution [p=0.45], modest lateral redistribution [p=0.45], and extensive lateral redistribution [p=0.10] respectively. The top branch is represented mathematically as:

$$I_{r1*} = I_{s1} \quad \text{and} \quad I_{r2*} = I_{s2} \tag{12-9}$$

or in words, the groundwater flux through the repository is equal to the net infiltration flux at the surface.

The middle branch assumes that some fraction of the surface flux is redistributed laterally. As before, a mathematical function for flux can be developed. It is based on the results of Prindle and Hopkins (1) shown in Figure 12-4 at the midpoint of the repository, and that show (i) at fluxes less than about 0.2 mm/yr there is no lateral diversion, and (ii) fluxes through the repository reach a maximum of about 0.3 mm/yr. This relationship is represented in the following manner

$$I_{r1*} = I_{s1} \quad \text{and} \quad I_{r2*} = I_{s2} \quad \text{when} \quad I_{s1}, I_{s2} \leq 0.2 \text{ mm/yr} \tag{12-10}$$
$$I_{r1*} = 3I_{s1}/(1 + 10I_{s1}) \quad \text{and} \quad I_{r2*} = 3I_{s2}/(1 + 10I_{s2}) \quad \text{when} \quad I_{s1}, I_{s2} > 0.2 \text{ mm/yr}$$

The lower branch represents an extreme case of lateral diversion that was produced by Prindle and Hopkins by modifying the constitutive relationships in the unsaturated zone. Mathematically, the fluxes at the repository and surface are related as follows:

$$I_{r1*} = I_{s1} \quad \text{and} \quad I_{r2*} = I_{s2} \quad \text{when} \quad I_{s1}, I_{s2} \leq 0.7 \text{ mm/yr} \tag{12-11}$$
$$I_{r1*} = 0.07 \text{ mm/yr} \quad \text{and} \quad I_{r2*} = 0.07 \text{ mm/yr} \quad \text{when} \quad I_{s1}, I_{s2} > 0.7 \text{ mm/yr}$$

The probabilities assigned to these branches cannot now be determine with any degree of certainty. The present values represent a belief that there is a strong possibility that lateral diversion may not develop because of local scale heterogeneity in hydraulic conductivity due to faulting, which could exist at a scale smaller than was considered by Prindle and Hopkins (1). The relatively small probability assigned to the lower branch reflects the feeling that a strong diversion of flow has a relatively low likelihood of occurrence.

Fracture/Matrix Coupling

The node for matrix coupling represents the extent to which diffusion into the matrix operates as an attenuation mechanism. The top branch represents a case of strong coupling where mass is assumed able to diffuse instantaneously from the fractures into the matrix. The lower branch represents weak coupling where diffusion into the matrix is limited and the mass in the fractures outruns the mass that is moving through the matrix. Simulation trials (3) suggest that this effect occurs when groundwater

fluxes at the repository (I_r) are greater than 1 mm/yr. The present conceptualization considers that with weak coupling that there is no retardation due to sorption within the fractures.

There are no firm data available to establish the probability that should be attached to the various coupling models. The probabilities assigned in Figure 12-10 represent the belief that strong coupling is most likely, but that weak coupling is a reasonable possibility as well.

Matrix Sorption

The third node of the groundwater portion of the logic tree represents uncertainty in establishing values of $\rho_b K_d$ or dimensionless distribution coefficients for the Calico Hills unit ($\rho_b K_{d1}$) and the Topopah Springs unit ($\rho_b K_{d2}$). The values defining the base case or middle branch of the logic tree (Table 12-3) are based on the K_d values presented in Table 6.48 (13) except for the value for Se which comes from Table 6.23b (13). The demonstration trials with TOSPAC (2) for Yucca Mountain also used these values. The top and bottom branches of the logic tree represent a range in variability that is 5x smaller and 5x larger than the base case values (Table 12-3).

Table 12-3

VALUES OF THE DIMENSIONLESS DISTRIBUTION COEFFICIENT FOR NINE ELEMENTS AND THREE BRANCHES

Element	Low value (0.33)		Base-case value (0.34)		High value (0.33)	
	$\rho_b K_{d1}$	$\rho_b K_{d2}$	$\rho_b K_{d1}$	$\rho_b K_{d2}$	$\rho_b K_{d1}$	$\rho_b K_{d2}$
Pu	45	30	225	150	1120	750
Np	3.6	3.2	18	16	90	80
U	1.7	0.8	8.5	4.1	42	20
C	0	0	0	0	0	0
Se	1.0	3.2	4.8	16	24	81
I	0	0	0	0	0	0
Cs	2500	133	12500	667	62500	3300
Tc	0	.14	0	.69	0	3.5
Ra	8000	12000	40000	58000	200000	290000

$\rho_1 = 1.61$ g/cm^3; $\rho_2 = 2.30$ g/cm^3

The probabilities in Figure 12-10 consider that each of the three sets of distribution coefficients is

equally probable.

Saturated Groundwater Flow

The last groundwater node of the logic tree represents mass transport laterally within the zone of saturation. As was previously discussed, this transport is assumed to be affected only by advection and thus the process is characterized by an average linear groundwater velocity. The two values, 1 m/yr and 10 m/yr, represent the uncertainty in estimating velocity that was discussed earlier. It is assumed that both velocities are equally probable.

REFERENCES

1. R. W. Prindle, and P. Hopkins. *On Conditions and Parameters Important to Model Sensitivity for Unsaturated Flow Through Layered, Fractured Tuff: Results of Analyses for HYDOCOIN Level 3 Case 2.* SAND89-0652, Sandia National Laboratories, 1989, 63 p.

2. J. H. Gauthier, M. L. Wilson, R. R. Peters and A. L. Dudley. *Total System Performance Assessment Code (TOPSAC) Volume 2: User's Guide.* SAND85-0004, Sandia National Laboratories, 1985.

3. A. L. Dudley, R. R. Peters, J. H. Gauthier, M. L. Wilson, M. S. Tierney and E. A. Klavetter. *Total System Performance Assessment Code (TOPSAC) Volume 1: Physical and Mathematical Bases.* SAND850002, Sandia National Laboratories, 1985, 203 p.

4. S. S. Levy. "Mineralogic alteration history and paleohydrology at Yucca Mountain, Nevada." *Proceedings High Level Waste Conference*, Las Vegas, 1991, pp. 477-485.

5. J. S. Szymanski. *Conceptual Considerations of the Yucca Mountain Groundwater System with Special Emphasis on the Adequacy of this System to Accommodate a High-level Nuclear Waste Repository.* Draft Report, Dept. of Energy, Nevada Operations Office, 1989, 3 volumes.

6. R. W. Barnard and H. A. Dockery (editors). "Summary Report on the PACE-90 Radionuclide Transport Problem for a "Nominal" Hydrogeologic Configuration." SLTR-3001, *Letter Report.* Sandia National Laboratories, 167 p.

7. S. Sinnock, Y. T. Lin and J. P. Brannen. "Preliminary Bounds on the Expected Postclosure Performance of the Yucca Mountain Repository Site, Southern Nevada." *J. Geophys. Res.*, vol 92, No. B8, 1987, pp. 7820-7842.

8. DOE. *Site Characterization Plan, Yucca Mountain Site, Nevada Research and Development Area, Nevada.* U.S. Dept. of Energy, Office of Civilian Radioactive Waste Management, 1988, 9 volumes.

9. R. Srivastava and T.-C. J. Yeh. "Analytical Solutions for One-dimensional, Transient Infiltration Toward the Water Table in Homogeneous and Layered Soils." *Water Resources Research*, 1991, pp. 753-762.

10. J. Bear. *Dynamics of Fluids in Porous Media.* Elsevier, 1972, 764 p.

11. P.A. Domenico and F. W. Schwartz. *Physical and Chemical Hydrogeology.* NY: John Wiley, 1990, 815 p.

12. F. W. Schwartz and A. S. Crowe. *A Deterministic-Probabilistic Model for Contaminant Transport.* NUREG/CR-1609, Nuclear Regulatory Comm., 1980, 158p.

13. DOE. *Environmental Assessment-Yucca Mountain Site, Nevada Research and Development Area, Nevada.* DOE/RW-0073, U.S. Department of Energy, Washington, 1986.

Section 13

GAS-PHASE TRANSPORT

by

Benjamin Ross

INTRODUCTION

Because the proposed nuclear waste repository at Yucca Mountain is designed to be located in the unsatured zone, radioactivity, if released from waste containers, could migrate in the gas phase as well as the liquid phase. Carbon-14 is the nuclide most likely to reach the surface in this way.

Field observations (1, 2) show that large-scale flows of air through Yucca Mountain are driven by the combination of topographic relief and temperature differences between the surface and subsurface. Because the subsurface is, on average, warmer than the atmosphere, there is a "chimney effect" that causes warm gas inside the mountain to rise. This flow is most rapid in winter and partially reverses itself in summer. Lesser but significant contributions to rock gas flow are made by barometric pressure fluctuations, aerodynamic effects of wind flowing over the mountain, and the effect on density of the humidity difference between rock gas and air.

GAS FLOW CALCULATIONS

We have simulated gas flow at Yucca Mountain using TGIF, a model of rock-gas flow driven by temperature and humidity differences. The derivation and numerical development of this model have been described elsewhere (3, 4). TGIF, which calculates steady-state flows, cannot simulate flows driven by driving forces that change so fast that pressures cannot equilibrate through the system; examples of such driving forces at Yucca Mountain are barometric pressure fluctuations and temperature differences between day and night. These rapidly oscillating flows do not cause net movement of gas at depth. Consequently they should not significantly affect contaminant transport. Another phenomenon not treated by the model, wind, does appear to drive a substantial net gas flux at depth (2); further research is needed to devise a way to model this effect.

Using the TGIF model, we calculated the annual-average rock-gas flow through Yucca Mountain. For each simulation, travel paths were determined for particles traveling to the surface from points distributed throughout the proposed repository area. Carbon-14 travel times were calculated along each path line.

The calculations used four equally spaced cross-sections along the east-west lines shown in Figure 13-1. The sections, depicted in Figure 13-2, were mostly taken from computer-generated sections presented by Prindle and Hopkins (5). The dashed lines in Figure 13-2 represent parts of the cross-sections that were extrapolated using the geologic map by Scott and Bonk (6).

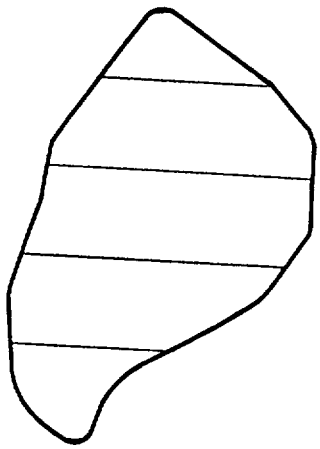

Figure 13-1. Location of simulated cross-sections relative to proposed repository.

The cross-sections contain three hydrostratigraphic subdivisions of the Paintbrush Tuff formation dipping approximately six degrees to the east. The upper and lower layers, the Tiva Canyon and Topopah Spring welded tuff units, were assigned a permeability of 10^{-11} m^2. This value, based on downhole measurements of barometric pressure changes (7), is relatively reliable insofar as it is derived from a large-scale field measurement.

The Paintbrush nonwelded unit, which lies between the two welded units, was assigned a permeability of 10^{-13} m^2 in most places. This value was selected because previous sensitivity studies (8) have shown that a permeability contrast between welded and non-welded tuff of 100 or more leads to formation of two separate flow systems above and below the nonwelded layer. Isotopic studies of

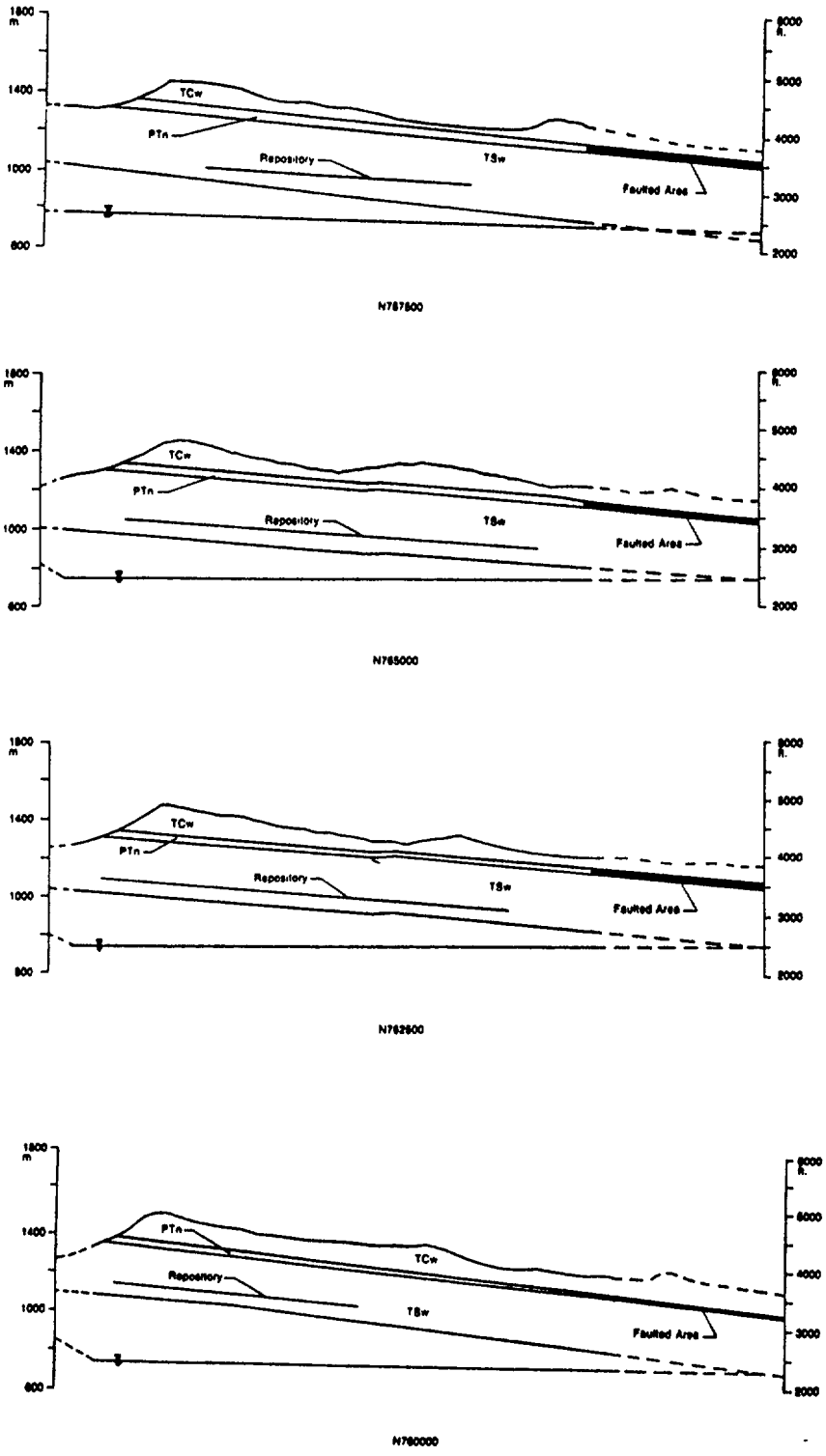

Figure 13-2. Cross-sections used in gas-flow simulations. TCw, PTn, and TSw are the Tiva Canyon welded, Paintbrush nonwelded, and Topopah Spring welded hydrostratigraphic units. Solid line indicate cross-section from (5) dashed lines indicate extrapolation.

rock gas at Yucca Mountain indicate that the two welded tuff units differ substantially in age, suggesting that the nonwelded unit provides substantial confinement (9). To the east of the repository block, there is a zone of intense faulting. In this area, the Paintbrush nonwelded unit was assigned a permeability of 10^{-12} m^2. The nonwelded units beneath the Topopah Spring unit were excluded from the simulation because their relatively small permeability and the presence of a non-flow boundary at the water table imply that little gas will flow through them.

The system was simulated with a natural geothermal temperature gradient of 0.02° K/m and with the repository heated to 42°C, 57°C, and 87°C. Results from the simulations with the natural gradient and the repository at 42°C and 57°C were reported previously (3); the case with the repository at 87°C was simulated for this study. Temperature fields were obtained by solving the heat conduction equation; this approximation is necessary because effects of convection cannot currently be simulated with a reasonably modest effort (see Section 8).

The Darcy fluxes calculated by the gas-flow simulations are converted to seepage velocities by dividing by the drained (gas-filled) porosity. Drained porosity values of 0.04, 0.18, and 0.05 were used for the Tiva Canyon welded, Paintbrush nonwelded, and Topopah Spring welded units.

The results of the gas-flow calculations were used to compute travel times for ^{14}C migration from the repository to the surface. The movement of gas-phase $^{14}CO_2$ is affected by interaction with carbon in the aqueous and solid phases. We conservatively ignored precipitation of ^{14}C into the solid phase and considered only water-gas exchange. Isotopic equilibrium between gaseous and aqueous phases can safely be assumed, but the amount of dissolved bicarbonate depends on the water chemistry (10).

The concentration of dissolved bicarbonate can be specified by assuming thermodynamic equilibrium with solid calcite and the measured composition of the rock gas. These concentrations had previously been calculated with the PHREEQE model, using concentrations of major ions that do not interact with the gas phase measured by Yang et al. (11). The ratio of gas velocity to ^{14}C velocity, known as the "retardation factor," also depends on the relative amounts of gas and water in the rock; saturation values of 0.67 in the Tiva Canyon welded unit, 0.61 in the Paintbrush nonwelded unit, and 0.64 in the Topopah Spring welded unit were used (12). The retardation factors that resulted from these calculations were reported by Doctor et al. (13) and are shown in Figure 13-3. For temperatures greater than 60°C, the straight lines shown in the figure were extrapolated.

To follow the trajectories of individual particles from the repository to the surface, a particle-tracking program called PATHLINE was used. This program uses the method of explicit integration of velocity within each grid block originally developed by Pollock (14). Pollock's method, which was developed for use with a block-centered finite difference model, was slightly adapted and reprogrammed for use with the lattice-centered finite difference method used in TGIF (3).

RESULTS

Travel times were calculated for 323 particles with starting points evenly distributed throughout the repository. One starting point was located randomly on each 25-meter interval within the intersection of each simulated cross section with the repository. The results of these calculations are presented in Figures 13-4 through 13-7 as histograms of ^{14}C travel times. Each histogram represents the distribution of travel times throughout the repository (combining all four cross-sections) for a given repository temperature. These histograms were used to calculate amounts of ^{14}C released to the atmosphere.

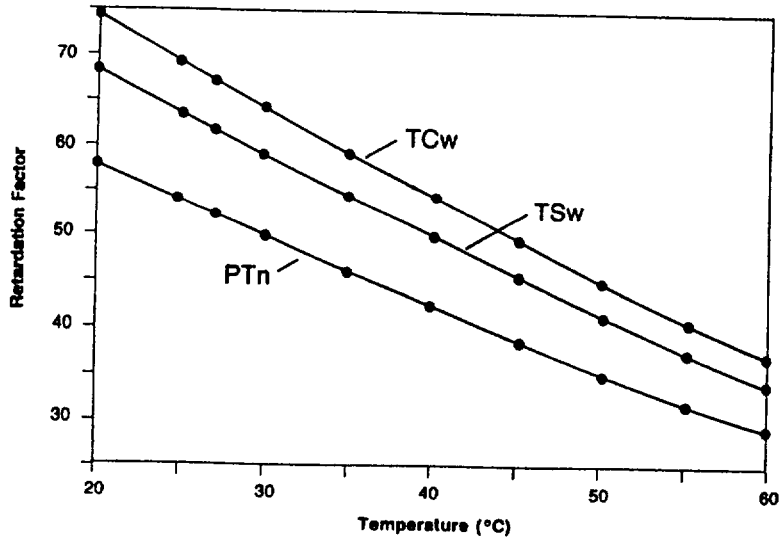

Figure 13-3. Carbon-14 retardation factor as a function of temperature [from 13].

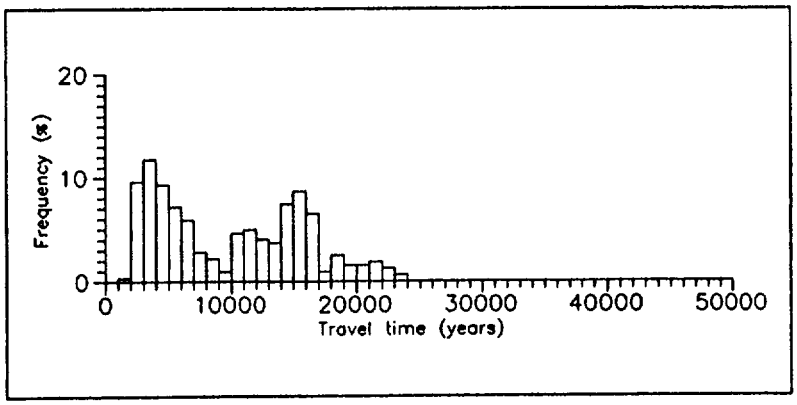

Figure 13-4. Distribution of ^{14}C travel times from the repository to the atmosphere with geothermal temperature gradient.

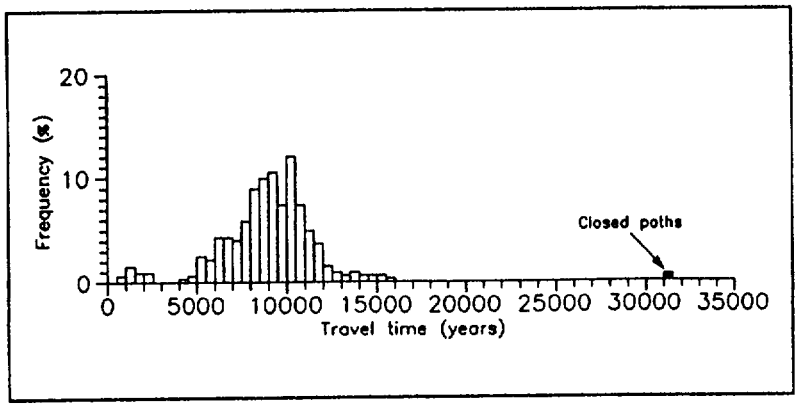

Figure 13-5. Distribution of ^{14}C travel times from the repository to the atmosphere with repository heated to 42°C.

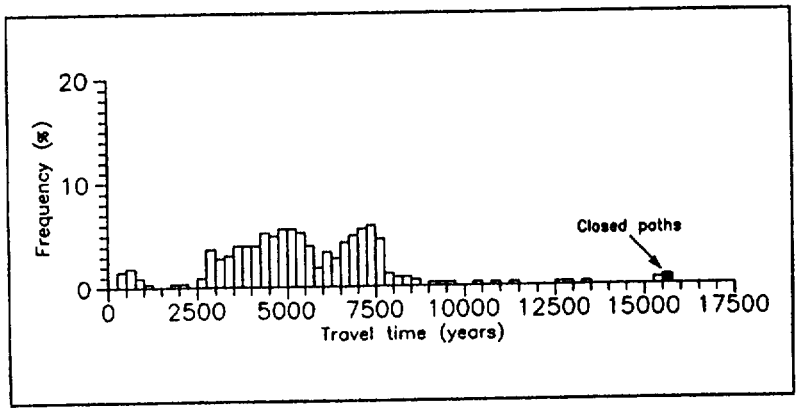

Figure 13-6. Distribution of ^{14}C travel times from the repository to the atmosphere with repository heated to 57°C.

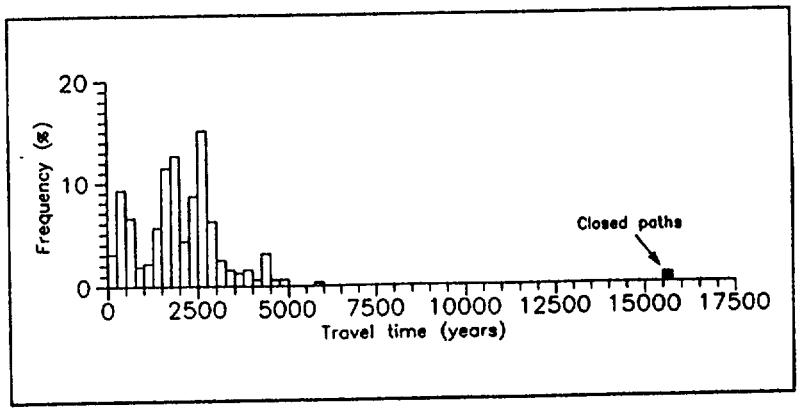

Figure 13-7. Distribution of ^{14}C travel times from the repository to the atmosphere with repository heated to 87°C.

REFERENCES

1. E. P. Weeks. " Effect of Topography on Gas Flow in Unsaturated Fractured Rock--Concepts and Observations." In *Flow and Transport Through Unsaturated Fractured Rock*, D.D. Evans and T.J. Nicholson (eds.). Geophysical Monograph 42, American Geophysical Union, pp. 165-170, 1987.

2. E. P. Weeks. *Does the Wind Blow Through Yucca Mountain.* Presented to Workshop on Flow and Transport Through Unsaturated Fractured Rock, Tucson, January 1991.

3. B. Ross, S. Amter, and N. Lu. *Numerical Studies of Rock-Gas Flow in Yucca Mountain.* Sandia National Laboratories Report, SAND 91-7034, February 1992.

4. S. Amter, N. Lu, and B. Ross. "Thermally Driven Gas Flow Beneath Yucca Mountain, Nevada." In *Multiphase Transport in Porous Media*, R. R. Eaton at al., (eds.). ASME, 1991, pp. 17-23.

5. S. Sinnock, personal communication, 1991.

6. R. B. Scott and J. Bonk. *Preliminary Geologic Map of Yucca Mountain, Nye County, Nevada, with Geologic Sections.* U. S. Geological Survey Open-File Report 84-494, Denver, CO., 1984.

7. P. Montazer, E. P. Weeks, F. Thamir, S. M. Yard, and P. B. Hofrichter. "Monitoring the Vadose Zone in Fractured Tuff, Yucca Mountain, Nevada." In *Proceedings of the NWWA Conference on Characterization and Monitoring of the Vadose (Unsaturated) Zone*, Denver, November 19-21, 1985, pp. 439-469.

8. N. Lu, S. Amter, and B. Ross. "Effect of a low-permeability layer on calculated gas flow at Yucca Mountain," In *Proceedings of the 2nd Intl. High Level Waste Conference*, Las Vegas, April 1991.

9. D. C. Thorstenson. "The Composition and CO_2 Carbon Isotope Signature of Gases from Borehole USW UZ-6, Yucca Mountain, Nevada. Presented to Workshop on Flow and Transport Through Unsaturated Fractured Rock, Tucson, January 1991.

10. B. Ross. "Gas-phase Transport of Carbon-14 Released from Nuclear Waste Into the Unsaturated Zone." In *Scientific Basis for Nuclear Waste Management XI.* M.J. Apted and R.E. Westerman (eds.). Pittsburgh, PA: Materials Research Society, 1988, pp. 273-284.

11. I. C. Yang, A. K. Turner, T. M. Sayre, and P. Montazer. "Triaxial-Compression Extraction of Pore Water from Unsaturated Tuff, Yucca Mountain, Nevada." *U. S. Geological Survey Water-Resources Investigations Report 88-4189*, 1988.

12. P. Montazer and W. E. Wilson. "Conceptual Hydrologic Model of Flow in the Unsaturated Zone, Yucca Mountain, Nevada." *U. S. Geological Survey Water-Resources Investigations Report 84-4345*, 1984.

13. P. G. Doctor et al. *Yucca Mountain Candidate Site Preliminary Post-Closure Risk Assessment.* Pacific Northwest Laboratory draft report, 1991.

14. D. W. Pollock. "Semianalytical Computation of Path Lines for Finite-difference Models." *Ground Water*, vol. 26, 1988, pp. 743-750.

Section 14

A MODEL OF HUMAN INTRUSION AT YUCCA MOUNTAIN

by

Ralph L. Keeney

INTRODUCTION

One major concern for the proposed repository at Yucca Mountain is that humans might inadvertently intrude and release radionuclides at some time in the future. These radionuclides might through some pathway reach a population of individuals and consequently cause health effects to some of those individuals. Because of regulations and the long lives of the radionuclides, the period of concern is for 10,000 years.

This Section describes an illustrative model to indicate how human intrusion could be addressed in performance assessment. The results reflect only the views of the author, although numerous ideas used in the model were gathered from reading literature on human intrusion possibilities at repositories for nuclear waste.

There are several components addressed in the model to help estimate the likelihood that radionuclides are released to the environment in the future. However, the essential features of the model for performance assessment are the results that indicate probabilities that various numbers of bore holes intersect waste containers in the repository, the probabilities that these bore holes are then continued to the water table level, and the probabilities and consequences of any excavation of part or all of the proposed repository. These probabilities are calculated for two time periods after closure: from 0 to 1000 years and from 1000 to 10,000 years.

A GENERAL MODEL

A general model for estimating the likelihood of human intrusion is illustrated in Figure 14-1. It consists of five major components:

- Status of society

- Knowledge of the site
- Value of potential site resources
- Activities at the site in the future
- Intrusion given such activities

Each of these components is briefly described below.

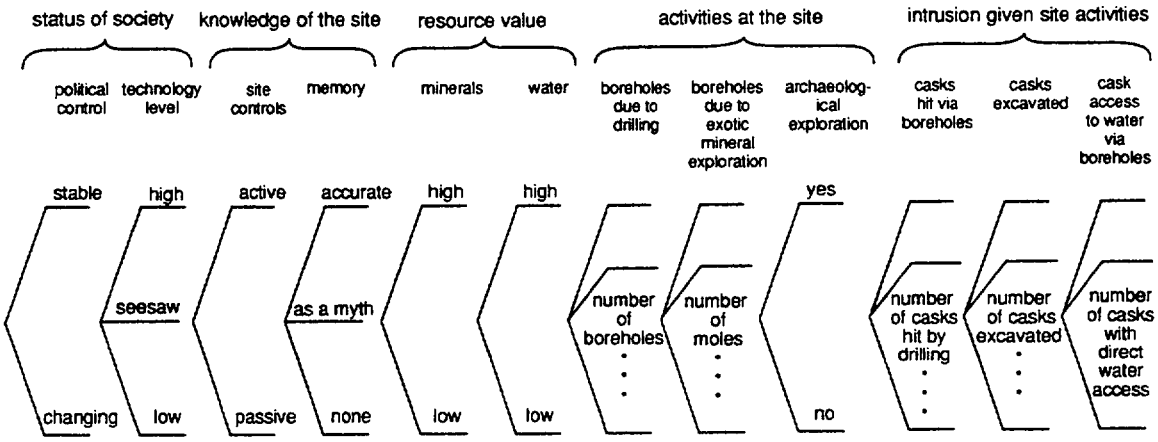

Figure 14-1. A general model of inadvertent human intrusion.

There are two aspects to the status of society. One concerns what political control exists over the site and the second concerns the level of technology that society has. Political control is of concern mainly in terms of whether it is stable into the future or whether there is change in control, as it is more likely that records are lost with changes in political control. The technology level as well as changes in the technology level is important. A high technology level is necessary to be able to drill through or excavate the repository. However, a changing technology level which declines from our present high level and then returns to a high level may be more likely to result in activities that would attempt to enter the repository.

The knowledge of the site is explained in terms of two aspects: whether or not there are active site controls, and the degree to which memory of the repository is preserved. There may be a total loss of any memory that a repository exists, or the memory could be accurate or inaccurate.

Two different types of resources are considered at the site in the component addressing the value of potential site resources. The resources of interest may be minerals or water. If the value of either of

these resources is high relative to today's value, it will naturally enhance the likelihood that drilling will take place at the site to obtain those resources. In a detailed model, it may be more likely the drilling would continue to the water level if the water resource value is high.

There are three types of activities at the site that could result in inadvertent human intrusion that are addressed in the model. These are conventional drilling similar to that currently done in oil exploration, exotic mineral exploration through remote controlled drilling vehicles (a subterrine, to travel under land, analogous to a submarine), and archaeological explorations that would excavate the repository. Potential expansions of the repository and the future mining of materials placed in the repository, which are not considered inadvertent intrusion, are not addressed here.

The fifth component of the model concerns what occurs with regards to releasing radioactivity if the various activities at the site take place. Specifically, the concern is with the number of waste containers intersected by either conventional drilling or drilling with subterrines, whether such drilling continues to the water table level, and the number of waste containers brought to the surface or exposed during excavation.

As indicated by Figure 14-1, one could develop a detailed model of each of the components in the general model of human intrusion. Different expertise could be used to gain insight about the likelihoods of various scenarios in terms of those component models. These could then be integrated to provide estimates of the likelihood of human intrusion at the repository. However, there would be major uncertainties about the likelihoods of various scenarios, partly because of the long time periods concerned. Thus it seems reasonable, especially for our illustrative purposes, to use this general model as a basis for a simpler model to be used in the initial aspects of performance assessment.

A SPECIFIC MODEL OF HUMAN INTRUSION

The components in Figure 14-1 are aggregated to provide a simpler model of inadvertent human intrusion illustrated in Figure 14-2. The general principle used in this aggregation is to combine descriptions from Figure 14-1 that naturally fit together into a consistent scenario. For instance, regarding the status of society, we felt that stable political control is consistent with a high technology level. Thus, one of the possible levels of the status of society in our simplified model of Figure 14-2 is a stable society with high technology. If there is a change in political control, then the technology level could either decrease or decrease and then increase again-- in other words, a seesaw.

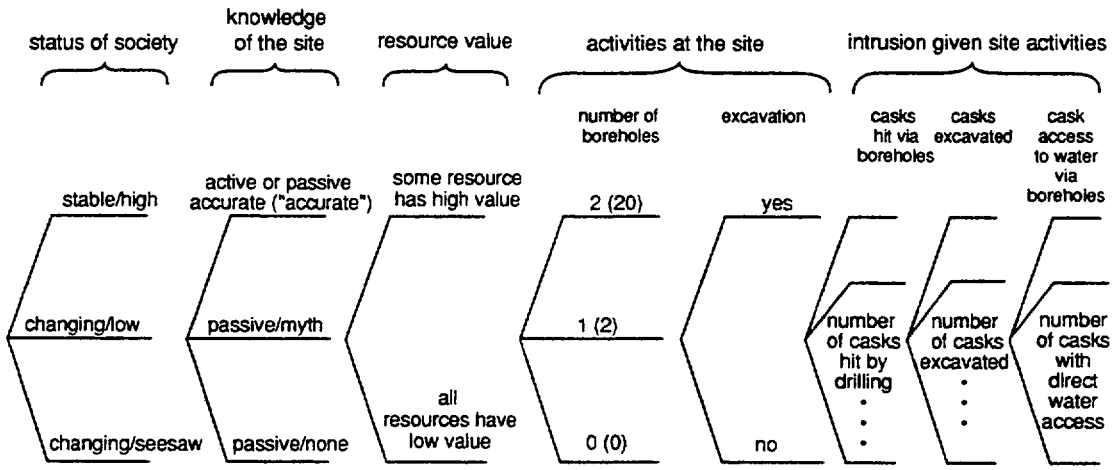

Figure 14-2. Model for inadvertent human intrusion at Yucca Mountain. NOTE: The first number of boreholes is for the 1,000 year period until the year 3,000; the number in parentheses indicate number of boreholes from 3,000 to 12,000 A.D.

Regarding knowledge of the site, it seems likely that if active controls are present, then there would be an accurate memory of what is stored at the site. Hence, the situation where there are active controls or passive controls with an accurate memory are combined as the consequences of both of those circumstances will likely be similar. If there are only passive controls, there is a chance that either a myth will exist about the site, which may be somewhat accurate, or all memory of the site may be forgotten.

Regarding resource value, we felt that the key aspect is whether or not some resource at the site has a high value, and how that high value compares to the value of other resources taking into account the inflation that will occur over long periods of time.

Document 40 CFR 191 of the Environmental Protection Agency states that the maximum number of bore holes that need be considered in 10,000 years is three per square kilometer. This works out to be approximately 20 bore holes for the 1690 acre repository. Dividing by 10, the maximum number of holes in a 1000 year period is 2. Hence, in the simplified model of human intrusion, the number of bore holes at the site for the first 1000 years are modeled to be either 0, 1, or 2. For the period from 1000 to 10,000 years, which is indicated by the numbers in parenthesis on that part of the model

in Figure 14-2, we assume 0, 2, or 20 bole holes. Whether or not archaeological excavation occurs is simply indicated by yes or no.

Intrusion given the site activities is usually calculated using basic probabilistic models and some judgmental assumptions about probabilities. For instance, it was calculated that the likelihood of a single bore hole hitting a waste container is approximately 0.003. This is simply based on the ratio of the area of the containers to the area of the repository assuming there will be 45,000 containers with a 76 centimeter diameter placed vertically in the repository. If 20 bore holes are drilled, a Bernoulli probability model is used to estimate the likelihood that various numbers of containers would be intersected. We assumed the probability that any bore hole reached water is 0.6, and this was independent of whether any other bore hole reached water. Thus, given the number of containers intersected, we used the Bernoulli model to determine the number of those for which the bore hole was continued to reach the water level. For excavation likelihoods, we directly assumed that excavation in the period from 0 to 1000 years was approximately one percent as likely as bore holes drilled into the repository. For the period from 1000 to 10,000 years we assumed excavation was ten percent as likely as bore holes drilled into the repository. If excavation occurred, we assumed one containers would be dug up in the first period and four in the second period.

ILLUSTRATIVE DATA USED

All of the illustrative data used in calculating the likelihoods of intrusion are indicated in Tables 14-1 through 14-5. It is worthwhile mentioning that, although the relationship of the likelihoods to each other make sense, the absolute magnitudes of these probabilities are not based on existing data simply because there is none.

Table 14-1 indicates the status of society. In the period from 0 to 1000 years, we assume it is unlikely that society will drop down to a low technology level and then return to a high level. Hence this probability is 0, although this is not the case for the 10,000 year period.

Table 14-2 indicates the knowledge of the site given the status of society. Naturally it is more likely that our knowledge is accurate at the site for the shorter time period and if society is stable rather than changing. The likelihoods of various levels of knowledge at the site depend only on the status of society.

Similarly, the likelihood that resource values are high or low depend only on the status of society and not on knowledge of the site. If society is stable and technology levels remain high, then it is more

Table 14-1

STATUS OF SOCIETY

Status	Period	
	0 - 1000 Years	1000 - 10,000 Years
Stable/high technology	.7	.4
Changing/low tech.	.3	.2
Changing/seesaw tech.	0	.4

Table 14-2

KNOWLEDGE OF SITE GIVEN STATUS OF SOCIETY

	Period					
	0 - 1000 Years			1000 - 10,000 Years		
Knowledge of Site	Stable	Change/ Low	Seesaw	Stable	Change/ Low	Seesaw
Accurate	.7	.4	--	.5	.1	.1
As a myth	.3	.3	--	.3	.2	.4
None	0	.3	--	.2	.7	.5

Table 14-3

RESOURCE VALUE GIVEN STATUS OF SOCIETY

	Period					
	0 - 1000 Years			1000 - 10,000 Years		
Resource Value	Stable	Change/ Low	Seesaw	Stable	Change/ Low	Seesaw
Some high	.6	.3	--	.3	.2	.5
All low	.4	.7	--	.7	.8	.5

likely that resource values are high than is the case when the technology level is low. In the long term, with a stable society, it is likely that we will not require the same mineral resources as now. However, if there is a seesaw circumstance with our technology, then the same resources that we prize now may be valued at a later time.

Table 14-4(a) indicates the site activities that might be likely given the status of society, the knowledge of the site, and resource values. In general, site activities may depend on all three of these factors. Also in general, it is more likely that activities will take place with a stable society than with a changing society in the short term (i.e. 1000 years) or the long term (i.e. the period from 1000 to 10,000 years). With the latter period, however, it seems reasonable to make the same assumptions about intrusions into the repository given a high level of technology that has resulted from a stable political climate or one that has resulted from a changing political climate with the seesaw in technology. This is indicated in Table 14-4(b).

Table 14-4

SITE ACTIVITIES GIVEN STATUS OF SOCIETY, KNOWLEDGE OF THE SITE, AND RESOURCE VALUE*

a) Number of holes in 0 - 1000 years

Society Status	Stable						Changing/Low						Seesaw					
Knowledge	acc.		myth		none		acc.		myth		none		acc.		myth		none	
Resource value	hi	lo	hi	lo	hi	lo	hi	lo	hi	lo	hi	lo	hi	lo	hi	lo	hi	lo
Number of Holes																		
2	.1	0	.8	.2	-	-	0	0	.2	0	.4	0	-	-	-	-	-	-
1	0	0	0	0	-	-	0	0	0	0	0	0	-	-	-	-	-	-
0	.6	1	.2	.8	-	-	1	1	.8	1	.6	1	-	-	-	-	-	-

b) Number of holes in 1000 - 10,000 years

Society Status	Stable						Changing/Low						Seesaw					
Knowledge	acc.		myth		none		acc.		myth		none		acc.		myth		none	
Resource value	hi	lo	hi	lo	hi	lo	hi	lo	hi	lo	hi	lo	hi	lo	hi	lo	hi	lo
Number of Holes																		
20	.2	0	.2	0	.2	0	0	0	0	0	0	0	.2	0	.2	0	.2	0
2	.6	.2	.6	.2	.6	.2	.2	0	.2	0	.2	0	.6	.2	.6	.2	.6	.2
0	.2	.8	.2	.8	.2	.8	.8	1	.8	1	.8	1	.2	.8	.2	.8	.2	.8

*Probability of excavation in the period from 0-1000 years is 0.01 times the probability that any holes are drilled. The probability of excavation in the period from 1000-10,000 years is 0.1 times the probability that any holes are drilled.

The probabilities of intrusion given various site activities are indicated in Table 14-5. As indicated above, the 0.003 probability that a drill hole hits a waste container is calculated and the other probabilities are arbitrarily chosen.

ANALYSIS

The analysis using the basic data is presented in Tables 14-6 through 14-10. In Table 14-6, the distribution for the number of holes drilled in the repository is calculated. This is done by simply multiplying the likelihood of the scenarios described by the society status, knowledge of the site, and

Table 14-5

INTRUSION GIVEN SITE ACTIVITY

Event	Probability
Any drillhole hits a cask	0.003
Any drillhole reaches water	0.6
Number of casks dug up by excavation	1 in 0 - 1000 year period 4 in 1000 - 10,000 year period

resource value, times the probabilities in Table 14-4 and then adding up the likelihoods of the number of bore holes. For any number of bore holes, we use the Bernoulli probability model to calculate the number of containers intersected. For instance, if twenty bore holes are drilled the probability of hitting exactly one cask, given the probability that a single bore hole hits a cask is 0.003, is given by:

$$20(0.003)(0.997)^{19} = 0.05667 \qquad (14\text{-}1)$$

which is approximately 0.056 as indicated in Table 14-7.

Table 14-8 indicates the probabilities for the number of containers intersected by drilling. This just multiplies the likelihoods of various numbers of bore holes drilled, from Table 14-6, times the conditional probability that the specified numbers of containers are hit, from Table 14-7. In other words, the probability that one container is hit in the period from 1000 to 10,000 years is given by:

$$0.064(0.056) + 0.296(.006) = 0.00536 \qquad (14\text{-}2)$$

as indicated in Table 14-8.

If two containers are hit, the likelihood that the drill hole for exactly one continues to water is:

$$2(0.6)(0.4) = 0.48. \qquad (14\text{-}3)$$

If one drill bore hole is drilled, the likelihood that this is continued to hit water is 0.6. For the period 0 to 1000 years, the likelihoods of hitting one or two containers are multiplied times the respective probabilities that exactly one of the bore holes is continued to hit water, which gives:

$$0.0000025(0.48) + 0.0015(0.6) = 0.0009012 \qquad (14\text{-}4)$$

which is approximately 0.001 as indicated in Table 14-9.

Table 14-6

DISTRIBUTION OF HOLES DRILLED IN THE REPOSITORY

0 - 1000 Years		1000 - 10,000 Years	
No. of holes	Probability	No. of holes	Probability
0	0.754	0	0.64
1	0.162	2	0.296
2	0.084	20	0.064

Table 14-7

DISTRIBUTION OF CASKS HIT BY DRILLING GIVEN THE NUMBER OF HOLES DRILLED

	0 - 1000 Years				1000 - 10,000 Years		
	Holes Drilled				Holes Drilled		
Casks hit	2	1	0	Casks hit	20	2	0
0	.994	.997	1	0	.942	.994	1
1	.006	.003	0	1	.056	.006	0
2	0	0	0	2	.002	.0	0
				3	0	0	0
				4	0	0	0

Table 14-8

CALCULATED DISTRIBUTION OF CASKS HIT BY DRILLING*

	Period	
No. Casks Hit	0 - 1000 Years	1000 - 10,000 Years
0	.9985 (.998)	.9942 (.99)
1	.0015 (.002)	.00536 (.01)
2	.0000025 (0)	.000128 (0)
3	0 (0)	0 (0)
4	0 (0)	0 (0)

*Numbers in parenthesis are round-off suggestions

There are two parts of Table 14-10 addressing excavation. The first multiplies the probabilities that bore holes are drilled, indicated in Table 14-6, times 0.01 to determine the probability of excavation

Table 14-9

CALCULATED DISTRIBUTION FOR DRILL HOLES THAT HIT A CASK AND CONTINUE TO HIT WATER*

(Note: Each hit cask has a 0.6 chance of continuing to water)

Casks Hit Plus Water	Period	
	0 - 1000 Years	1000 - 10,000 Years
0	.9991 (.999)	.99667 (.994)
1	.0009 (.001)	.00328 (.006)
2	.0000015 (0)	.000046 (0)
3	0 (0)	0 (0)

*Numbers in parenthesis are round-off suggestions

Table 14-10

LIKELIHOOD OF EXCAVATION AND CASKS DUG UP*

Period	Probability Of Excavation	Number Of Casks Dug Up If Any
0 - 1000 years	.00246 (.002)	1
1000 - 10,000 years	.36 (.004)	4

*Numbers in parenthesis are round-off suggestions

in the first 1000 year period. The probability of bore holes in the period from 1000 to 10,000 years is multiplied by 0.1 to find the corresponding probability of excavation in Table 14-10. The number of containers dug up given excavation are directly assumed as given in Table 14-5; these are based on judgments of the author. These numbers are necessary to calculate the amount of radionuclides released to the environment as a result of excavation.

RESULTS

Since the numbers indicated in Tables 14-6 through 14-10 are calculations based on other numbers, the relative precision indicated does not relate to the extent of our knowledge. Hence, it seems reasonable to round these numbers off considerably for use in an illustrative analysis of possible

repository performance in a performance assessment. One set of suggestions for such rounded off probabilities is indicated in parenthesis in Tables 14-8 through 14-10.

It may be useful to conduct an even simpler sensitivity analysis. Using the Environmental Protection Agency's guideline of 3 bore holes per square kilometer for 10,000 years, the maximum number of bore holes is 2 for a 1000 year period and 20 for the 9000 year period were determined. Thus, we might assume that this is the number of bore holes that would definitely be drilled. Given this, the probabilities that various numbers of casks are hit by the drilling are indicated in Table 14-7. For further simplification, we can assume that each of these bore holes is continued until it reaches the water table. In this simplified sensitivity analysis, it could either be assumed that excavation does not take place or that the probabilities and implications in Table 14-10 are appropriate.

Two documents [1, 2] were mainly used to develop the ideas used in this Section. As both of these documents are available for information only and not to quote, only ideas were taken from the documents and embellished or altered using the author's judgment.

REFERENCES

1. S.C. Hora, D. von Winterfeldt, and K.M. Trauth. *Expert Judgment on Inadvertent Human Intrusion into the Waste Isolation Pilot Plant.* SAND 90-3063, Sandia National Laboratories, 1991.

2. G. Barr, R. Barnard, and E. Dunn. *Progress Report on the Construction of Event Trees in Support of Scenario Development.* SLTR 90-2001, 1991.

Section 15

METHODOLOGY FOR PERFORMANCE ASSESSMENT

by

Robin K. McGuire

OVERVIEW

The methodology for performance assessment uses the logic tree as the basic representation of uncertain models and parameters, in the manner of previous efforts on risk-based performance assessment (1). Project participants found the concept of logic trees to be the most effective means of organizing and expressing their uncertainties with respect to conditions and processes potentially affecting a repository. A "logic tree" is a generalization of the "fault tree" and "event tree" approach (see, for example (2)), in which specific sequences of faults or events are not modeled in time but where uncertainties in states of nature and in the occurrences of future events is modeled. The logic tree approach has been used with success to quantify expert opinion in other fields, most particularly in the evaluation of earthquake hazards. The logic tree is ordered so that independent effects are to the left side (upstream), and dependent effects are to the right (downstream) of any node representing an effect upon which it is conditioned. Each branch is assigned a probability that represents the conditional probability (conditional on the values of the previous branches leading to that node) of that branch correctly representing future occurrences or the state of nature. Probabilities for branches emanating from each node must sum to unity.

The product of the logic tree is a set of end branches with associated probabilities and parameters obtained from the intermediate branches. The design of the logic tree is critical, for it represents which inputs are independent and which are dependent, and consequently which probability assessments can be made independently and which must be made conditionally. It also requires each technology to estimate parameters that are needed by downstream technologies, in order to make the subsequent assessments.

The value of the logic tree is that it organizes the inputs and their interactions in a coherent fashion, both for analysis and review. The structure of the logic tree is a critical component of an integrated

site evaluation and must be developed cooperatively with the scientists and engineers knowledgeable about the processes at work. Also, the logic tree must be changeable as new ideas and their interactions are understood. The probabilities assigned to the alternative branches at each node may come from statistical analysis, deterministic sensitivity studies (perhaps using a more detailed logic tree to derive a set of parameters and their probabilities), scientific and engineering judgment from one or a group of participants, or a combination of these.

The overall use of the logic tree is outlined in Figure 15-1. Interpretations of scientific and engineering issues that may affect potential releases of radionuclides are represented by logic tree nodes and branches. These interpretations are assembled into a "master logic tree" as illustrated in Figure 15-1a. The format of this logic tree keeps nodes representing independent models and variables on the left, so that nodes representing dependent models and variables can be placed to the right of them, and conditional probabilities can be assigned based on branches leading to the conditional nodes. Assignments of models and variables are made by experts in each field, as summarized in previous Sections of this report.

The logic tree format means that the path leading to each end branch represents a complete collection of assumptions (models and variables) that is used for a performance assessment. From each such set of assumptions a source term model and a hydrological model are used to estimate levels of release at the accessible environment as a function of time (Figure 15-1b). In the current application releases are calculated from time zero to 20,000 years, in steps of 1000 years. Each end branch therefore results in an estimate of total releases at year 10,000, and this estimate is assigned a probability that is the product of the probabilities on the logic tree branches leading to that end branch. Figure 15-1c illustrates the collection of release curves that result from numerous end branches of the logic tree.

The final step for each nuclide is to form a complementary cumulative distribution function (CCDF) that indicates the probability of various levels of release at 10,000 years (Figure 15-1d). This is measured by a normalized level of release, the normalization being the allowable level of release at 10,000 years developed by the EPA (2). The normalization is 100 curies released per thousand metric tons of initial heavy metal for many nuclides, but is larger for some nuclides. The CCDF shows the probability that any normalized level of release will be exceeded at 10,000 years for that nuclide; it is calculated at each release level simply by adding the probabilities of release curves (Figure 15-1c) yielding releases larger than that level. The CCDF thus indicates probabilities of various levels of release given uncertainties in inputs.

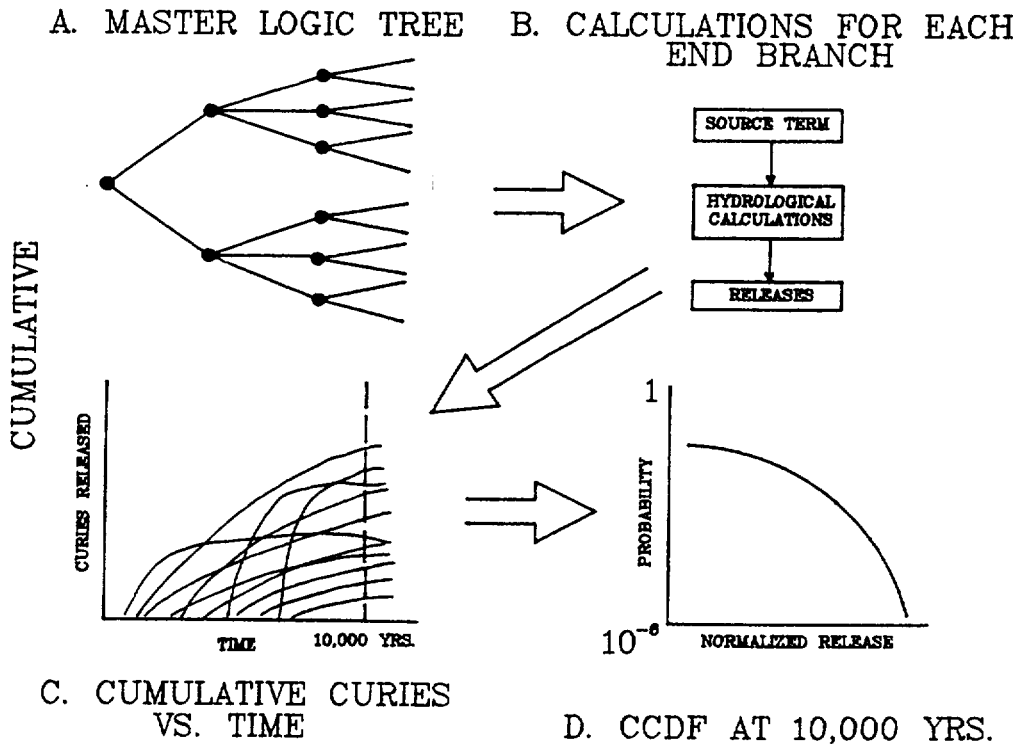

Figure 15-1. Steps in quantification of repository performance.

To derive a CCDF considering all nuclides released, the source term and hydrological models are run for all nuclides for each path through the logic tree. Then, for that path, the releases at 10,000 years for each nuclide are divided by the appropriate EPA standard, and the resulting normalized levels of release are summed to obtain a total, normalized level of release (sometimes called the "EPA sum"). This total level is assigned the probability of that path. When all calculations have been completed, a CCDF of these values is created in the usual way; this represents the CCDF of the total normalized releases from all nuclides. This total CCDF can be compared to allowable levels of release as defined by EPA.

The remainder of this Section describes the inputs used for the performance assessment, as derived from analyses documented in previous Sections. These analyses are not reviewed here, as they are adequately described in each Section. Rather we present the results of each analysis that are used in the master logic tree, and describe any interpretations that are made to the original analysis in order to use it for the performance assessment. We also summarize the source term model and the

hydrological model used for the actual calculations of radionuclide release.

INPUTS

The models used to estimate net hydrologic flux at the Yucca Mountain site are described in Sections 2 and 3. These models represent the future climate, precipitation, absorption, and runoff at the site, and quantify possible levels of hydrologic infiltration. The quantification used in the master logic tree is shown in Figure 15-2; it is exactly that presented in Section 3 as the levels of infiltration over the next 1000 years, and between 1000 and 10,000 years, and the associated probabilities.

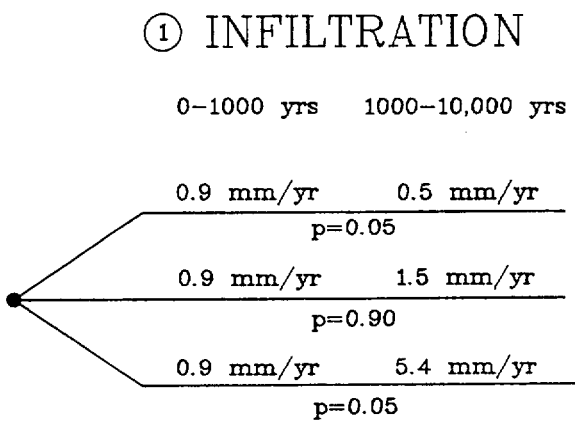

Figure 15-2. Logic tree node representing infiltration.

Possible changes in the water table as a result of changes in infiltration are described in Section 4. These changes are not thought to depend on any lateral redistribution of hydrologic flux, because such redistributions would merely rechannel the flux toward adjacent drainages or alternate pathways, and the effects on the water table would be the same. The node used to describe water table changes as a function of infiltration level are shown in Figure 15-3; these are the same as presented in Section 4.

The logic tree node representing earthquake occurrences is shown in Figure 15-4. Here we make use of previous experience (described in (1)) that suggests that the effect of earthquakes on repository performance is small. We assume that a 10 cm offset is required to rupture a waste container. (One representative conceptual design indicates a 3 cm air gap surrounding each waste container, so a 6 cm fault movement across a borehole would be required to simply have the borehole walls contact the container. It is assumed that a further 4 cm of displacement is required to rupture the container.) We use the results from Figure 5-7 to estimate that, over 10,000 years, an estimated two containers would

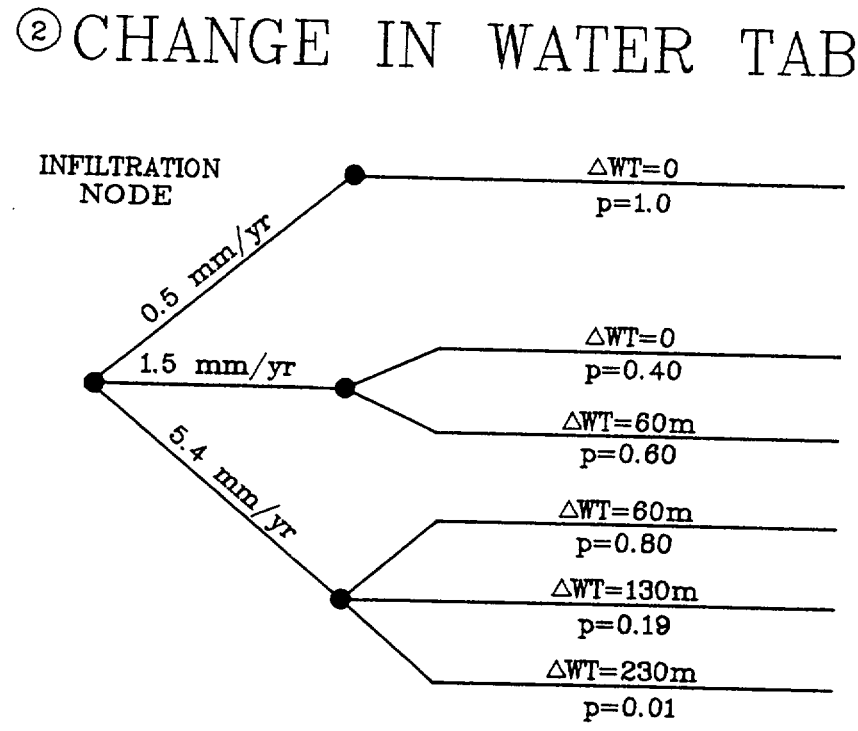

Figure 15-3. Logic tree node representing change in water table as a function of infiltration.

be ruptured in this way. We further assume, conservatively, that this earthquake occurs in year 1000, and that if part of the repository is flooded, the ruptured containers occur in the flooded part. As will be shown in the next Section, these conservative assumptions make little difference in the calculated releases. To compare results with and without earthquake effects, we use logic tree node no. 3 shown in Figure 15-4. The choice of probability of 0.5 for each branch is arbitrary; as the effects of earthquakes on releases are small, the choice of probability level does not influence the calculated releases.

The changes in water table associated with an earthquake are also shown in Figure 15-4. For the branch representing "no earthquakes" there is no possible change in water table. For the second branch, where earthquakes are assumed to occur in year 1000, three possible changes in the water table are assumed. These levels and the associated probabilities have been derived by combining the levels and probabilities from Table 6-3 into three groups. For instance, changes of less than 30 m from Table 6-3 are considered to be no change in water table in Figure 15-4, and the associated probability

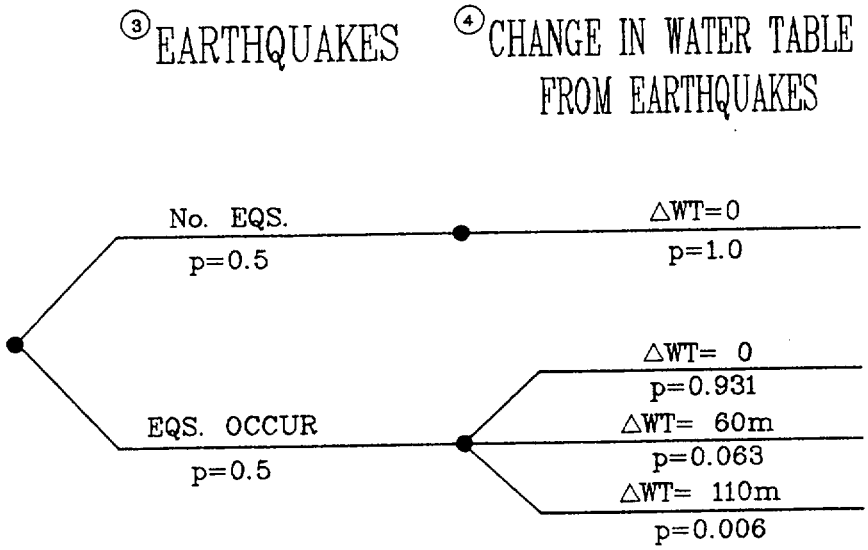

Figure 15-4. Logic tree node for earthquakes and associated water table change.

is the sum of probabilities indicated in Table 6-3 for changes of less than 30 m. This combination of water table changes allows us to represent the entire range of results, without being unduly burdened by calculations of small changes.

Occurrences of volcanoes are treated in node no. 5 of the logic tree. As Figure 15-5 indicates, the likelihood of a volcano occurring and producing a basaltic dike that intersects the repository is 0.0014 over a period of 10,000 years. This is calculated as the probability of volcanism occurring in a 10,000 year time period (8 x 10-2) times the probability of intersection given an occurrence (1.7×10^{-2}, from model C of Section 7, which is the worst case geometry for dike formations relative to the Yucca Mountain site). The complementary probability of 0.9986 indicates the likelihood that no volcanic event affects the repository during 10,000 years. The impact on release of a volcanic dike intersecting containers and carrying radioactive waste to the surface is calculated from the analysis presented in Section 7. That is, 1.4 m^3 of waste material is assumed to be transported immediately to the accessible environment. This amounts to the contents of 1.15 waste containers out of 35,000 planned for the repository, or 3.3×10^{-5} of the material stored. For reasons of calculational efficiency this scenario is treated as being mutually exclusive of gaseous and aqueous modes of release; it amounts to a minor amount of release by comparison to the other pathways, as will be demonstrated in the next Section. Similarly, possible changes of water table resulting from volcanic dikes in the vicinity of the repository are ignored. These changes are estimated to be 19 m or less, and these changes are much smaller than possible water table changes from other causes.

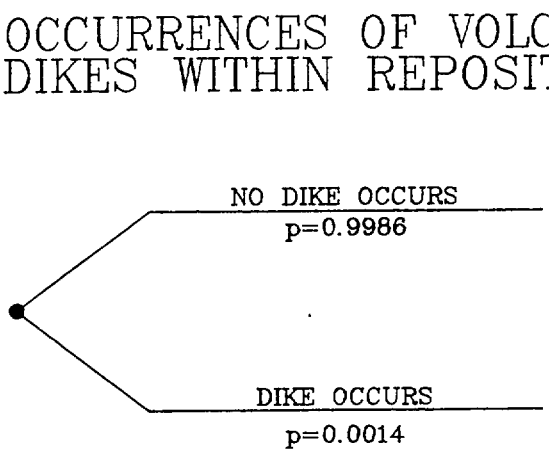

Figure 15-5. Logic tree node for occurrences of volcanic dikes within repository.

Possible temperature pulses from the emplacement of radioactive waste material are described in Section 8. The possible scenarios and their probabilities are shown in Figure 15-6, taken from that Section. Recall that the "hot" scenario means that 90% of the repository follows a hot temperature profile (curve α in Figure 8.2) and 10% follows a warm profile (curve γ). Likewise, "warm" means that 90% of the repository follows a warm profile and 10% follows a hot profile. The "cool" scenario means that 100% of the repository follows the cool profile, curve β in Figure 8-2.

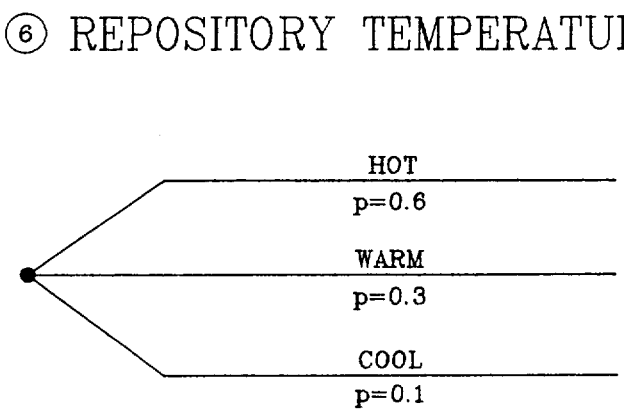

Figure 15-6. Logic tree node for repository temperature.

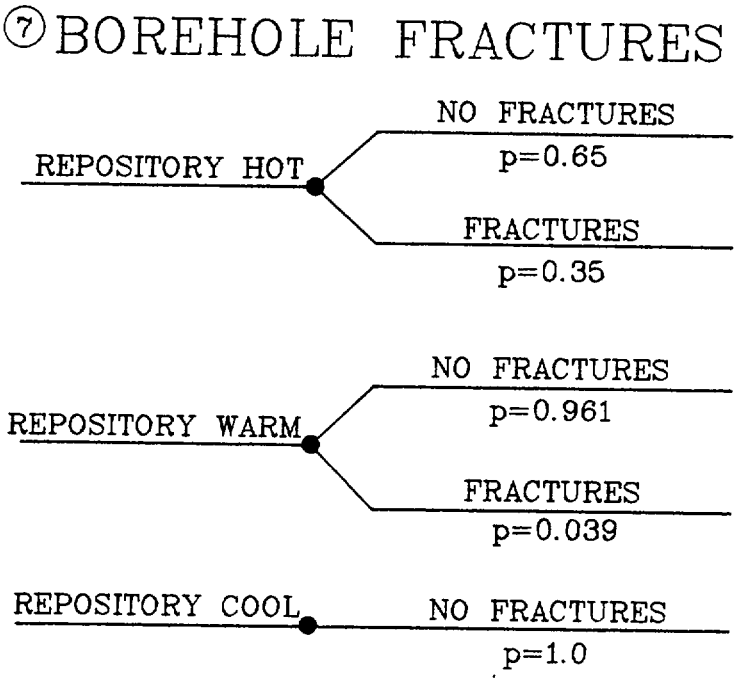

Figure 15-7. Logic tree node for borehole fractures.

Borehole fractures that might occur as a result of the temperature pulse are described in Section 9, and the input used to the performance assessment is summarized in Figure 15-7. Borehole fractures are conditional on the temperature profile that occurs after emplacement of waste material, and the values shown in Figure 15-7 are obtained by combining the Type 1 and 2 deformation patterns described in Section 9 to estimate a total probability that borehole fractures will occur, and combining the Type 3 and 4 deformation patterns to estimate a total probability that borehole fractures will not occur. This combination is appropriate because the Type 1 and 2 deformation patterns are assumed to produce spalling of the borehole wall that will fill the air gap and provide a pathway for unsaturated flow and transport of nuclides, whereas Type 3 and 4 deformation are not associated with spalling or failure of the air gap.

The engineered barrier system (EBS) selected for the repository also depends on the temperature environment. This is treated as an uncertainty in this analysis, as the design of the EBS is not fixed

at this date. The values presented in Section 10 are depicted in Figure 15-8; three choices of EBS are represented, with the a probability that each will be chosen. These probabilities represent a combined likelihood that more will be known about the repository temperature behavior at the time container design is finalized, and that a design similar to those indicated will be chosen, given what is known about the temperature profile at the time container design is selected.

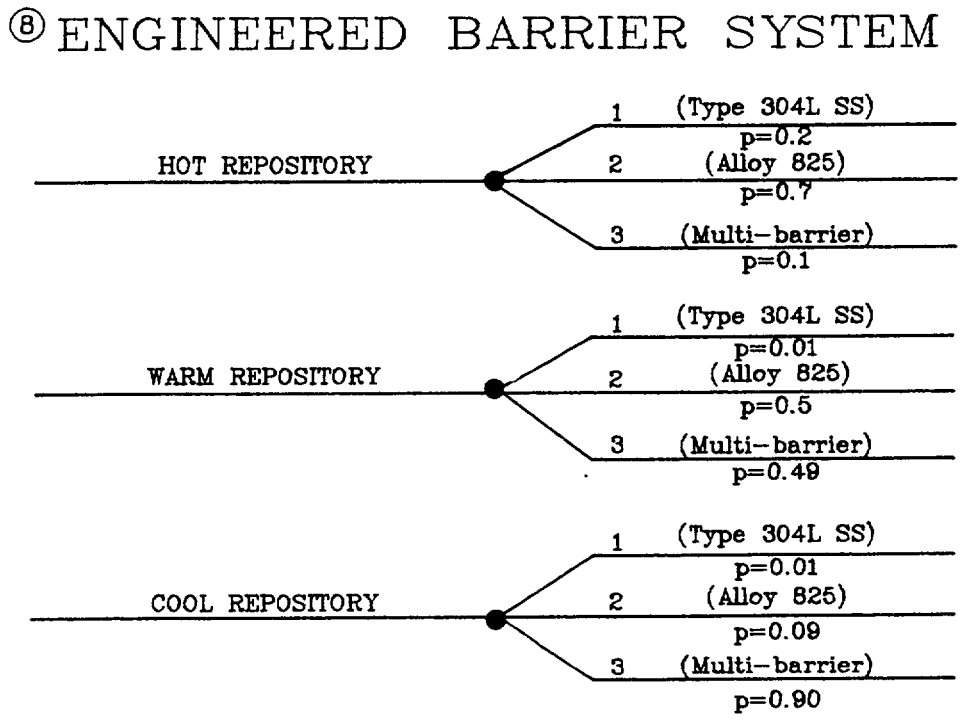

Figure 15-8. Logic tree node for engineered barrier system.

The major uncertainty in the source term derives from the solubility of radioelements and from the dissolution rate of the waste matrix. Specific values of solubilities and of the dissolution rate are reported in Section 11; the high, moderate, and low values are assigned probabilities of 0.05, 0.90, and 0.05, based on the interpretation of the extreme values as high confidence upper and lower bounds. These values are shown in Figure 15-9. Recall from the discussion in Section 11 that the source term calculations are governed by solubility limits for relatively insoluble radioelements, and by the waste dissolution rate for relatively soluble radioelements.

⑨ SOLUBILITY AND DISSOLUTION RATE

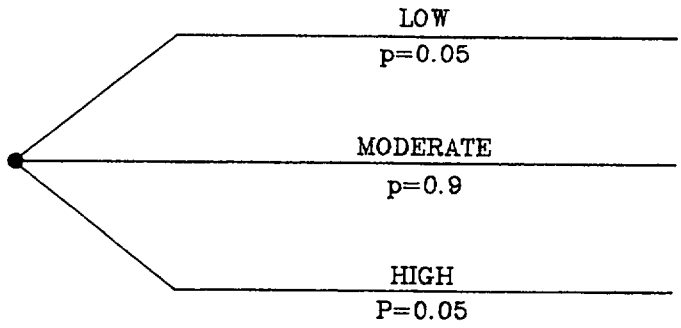

Figure 15-9. Logic tree node for solubility and dissolution rate.

The hydrologic model has four uncertain parameters associated with it: the possible lateral diversion of ground water away from the repository, the coupling between fracture and matrix flow, the matrix sorption of nuclides during transport, and the velocity of flow in the saturated zone. These parameters are described Section 12, and their uncertainties are summarized in Figure 15-10. The only change from the values presented in Section 12 is to combine the two lowest models for lateral diversion of ground water infiltration into one model. This achieves more efficient calculations with little loss in accuracy of the results (the lowest model for lateral diversion was weighted only 10%, as described in Section 12).

The final set of inputs for the performance assessment is the scenarios regarding human intrusion. These are taken from the description of the human intrusion model presented in Section 14. Four possible effects of human intrusion are modeled, as summarized in Figure 15-11: (1) no effects, (2) drilling that intersects waste containers but does not continue to the ground water, (3) drilling that intersect containers and continues to the ground water, and (4) excavation at the site. The latter three effects are assigned probabilities based on the tables presented in Section 14. For example, the probability assigned to scenario 3, drilling that intersects containers and continues to the water table, is just the sum of such probabilities presented in Table 14-9 for the period 0 to 10,000 years. The probability of drilling and intersecting containers and <u>not</u> continuing to the water table is calculated

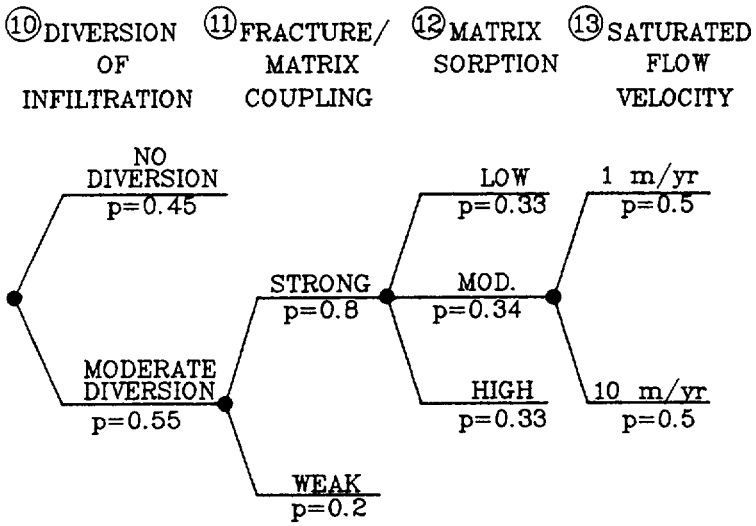

Figure 15-10. Logic tree nodes for hydologic parameters.

as the probability of drilling and intersecting containers (0.012, from Table 14-8) minus the probability from scenario 3. This results in a probability of 0.005. The probability of excavation (0.006) is taken directly from Table 14-10. The first scenario, no effects of human intrusion, is calculated as the complement of the sum of the probabilities from the other scenarios.

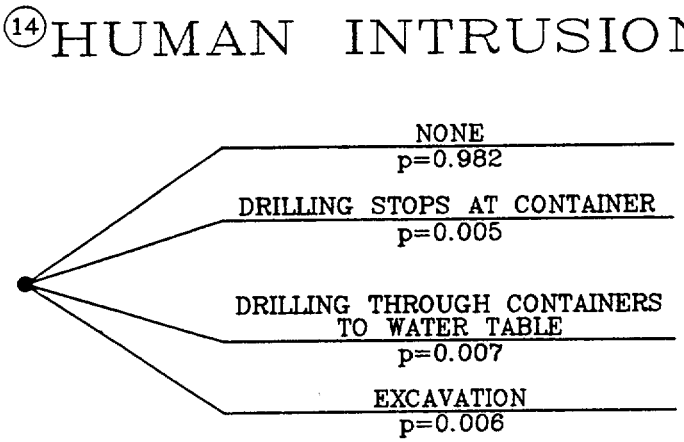

Figure 15-11. Logic tree node for human intrusion.

The possible releases corresponding to these effects are estimated as follows. For scenario 2, it is assumed that one container is intersected in the period 0 to 1000 years with probability 0.001, or that

one container is intersected in the period 1000 to 10,000 years with probability 0.004. These probabilities are determined from the recommended numbers reported in Tables 14-8 and 14-9, and using the result that it is unlikely that more than one container will be hit by drilling. This scenario results in the immediate release of waste material to the environment. For scenario 3, it is assumed that one container is involved in a drill hole that extends to the water table during the period 0 to 1000 years with probability 0.001, or that one container is involved in a drill hole that extends to the water table during the period 1000 to 10,000 years with probability 0.006. These numbers are taken from Table 14-9. In these cases it is assumed that the contents of the affected container are deposited in the ground water immediately upon drilling, and that transport takes place from there to the accessible environment at a rate of 1 or 10 m/yr (see node 13 on Figure 15-10). With a 5 km assumed horizontal distance to the accessible environment, this means that the release will take place either 500 or 5000 years after drilling. For the excavation scenario, it is assumed that excavation of one container will take place in the period 0 to 1000 years with probability 0.002, or that four containers will be excavated in the period 1000 to 10,000 years with probability 0.004. These values are taken directly from Table 14-10. Upon excavation it is assumed that immediate release occurs. Within each of the above time periods, a uniform distribution of occurrence of intrusion is assumed.

CALCULATIONAL METHODOLOGY

The above inputs are used in the program IMARC (Integrated Multiple Assumptions and Release Calculations) to generate multiple combinations of input parameters, for each combination to calculate releases as a function of time, and for these releases to generate a CCDF expressing the distribution of releases as a function of uncertainties in input. The IMARC software breaks the problem into three pieces, as shown in Figure 15-12. The first piece, labelled IMARC1, does hydrologic transport calculations; the second piece, IMARC2, does source term calculations; the last piece, IMARC3, loops over all uncertainties in the master logic tree, combines the source term with the transport calculations to obtain distributions of release. The gaseous release calculations are also performed in IMARC3, and the degradation of waste containers is taken into account in that program.

The hydrologic transport calculations in the first program follow the description in Section 12. Separate calculations are made for the variables that influence transport, specifically:

1. Infiltration level,
2. Lateral diversion of ground water flow,
3. Level of the water table,

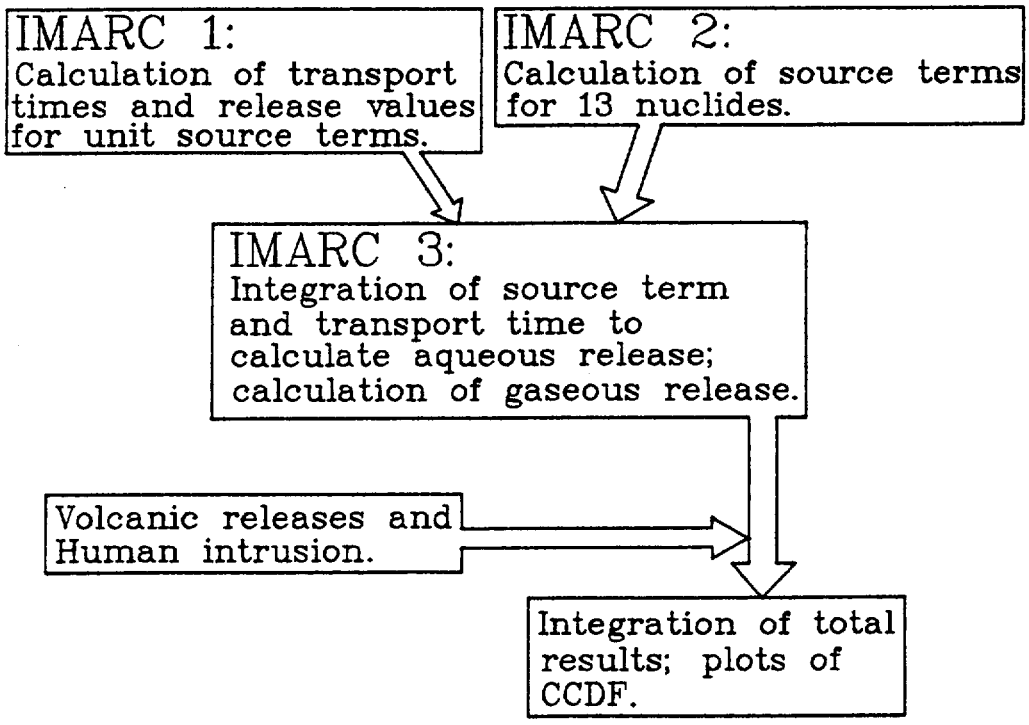

Figure 15-12. Major steps and program packages for performance assessment calculations.

4. Fracture-matrix coupling,
5. Horizontal velocity of water in the saturated zone, and
6. Retardation of nuclides in the matrix.

A logic tree format is used to organize and loop through all combinations of these parameters; for each, and for each nuclide, the transport time to the accessible environment is calculated, as well as the amount of nuclide that is released per unit amount of nuclide input at the source. The amount of nuclide released per unit input is affected by radioactive decay, particularly for radioelements with short half-lives (e.g. ^{226}Ra and ^{240}Pu). It was found that, although two infiltration levels are used by the calculations (0 to 1000 years and 1000 to 10,000 years), the hydrologic transport is almost stationary, (i.e., the transport time for release in year 1000 is virtually the same as the transport time for release in the year 2000, 3000, and so on), so a simple time step can be used to quantify the delay between introduction of a gram of radioelement to the system and release of that material to the accessible environment.

The second package estimates source term values over all values of the input variables critical to the quantity of radionuclides available for introduction to the hydrologic system. Again, a logic tree format is used to organize these variables and loop over all combinations of them. These variables are:

1. Infiltration level,
2. Lateral diversion of ground water flow,
3. Environment in the host rock (unsaturated flow, wet drip conditions, or saturated flow),
4. Solubility of radioelements or dissolution rate of the waste matrix, and
5. Fracture conditions of the bore holes (i.e. whether or not the air gap has failed).

For every combination of values of these variables, the amount of each radioelement available for transport is calculated, using the methods presented in Section 11. The last condition, the condition of the bore holes, determines whether transport is possible under unsaturated conditions. For the other environments (saturated and wet drip conditions), transport can take place whether or not the air gap has failed. As discussed in Section 11, the possible source terms are calculated by comparing results from both elemental solubility calculations and from waste dissolution rate calculations. This comparison is made at 10,000 years, which is not a critical choice as neither elemental solubilities nor waste dissolution rate is assumed to be temperature dependent. Whichever calculation indicates the least amount of element in solution is used as the governing equation for all times. The output of these calculations is the amount (grams) of each radioelement that is available for transport as a function of time for each possible environment of the host rock, assuming the waste container has lost integrity.

The source term and transport calculations are integrated in IMARC3. The entire master logic tree (Figure 15-13) is used to loop over all uncertainties and to calculate releases as a function of time for each combination of uncertain input variables. Time steps of 1000 years are used, consistent with the results calculated for the source term and travel times. The program determines the fraction of waste containers that fail at each time step for each set of input values, and this fraction is used to modify the source term from IMARC2. Also the "pulse" release of 1% of the inventory of ^{79}Se, ^{99}Tc, and ^{129}I are added as source terms, as described in Section 11. As a result of the previous calculations made in IMARC1 and IMARC2, the calculations in IMARC3 involve only additions and multiplications; hence a large number of combinations of values from the master logic tree (e.g. 25,000) can be handled with efficiency.

The gaseous release calculations are also made in IMARC3. For these, the distributions of travel times from Section 13 are quantified using a gamma probability function. These travel times are then convolved with the releases occurring during each time period as waste containers fail and release gaseous ^{14}C. As discussed in Section 11, it is assumed that 2% of the inventory of ^{14}C is available to be released from waste containers immediately upon failure, and that an additional 58% is released congruently with dissolution of the waste matrix. Both of these gaseous source terms are calculated for each time period, and the time and amount of gas that escapes at the ground surface is calculated using the travel time distributions. The total release of gaseous ^{14}C for each time step is the convolution of all possible source times and travel times that lead to escape at that time step.

In addition to the aqueous and gaseous release modes, possible releases are determined for volcanic occurrences (entrainment of waste material by basaltic dikes and transport to the surface) and by human intrusion. These estimates of release follow the method indicated above.

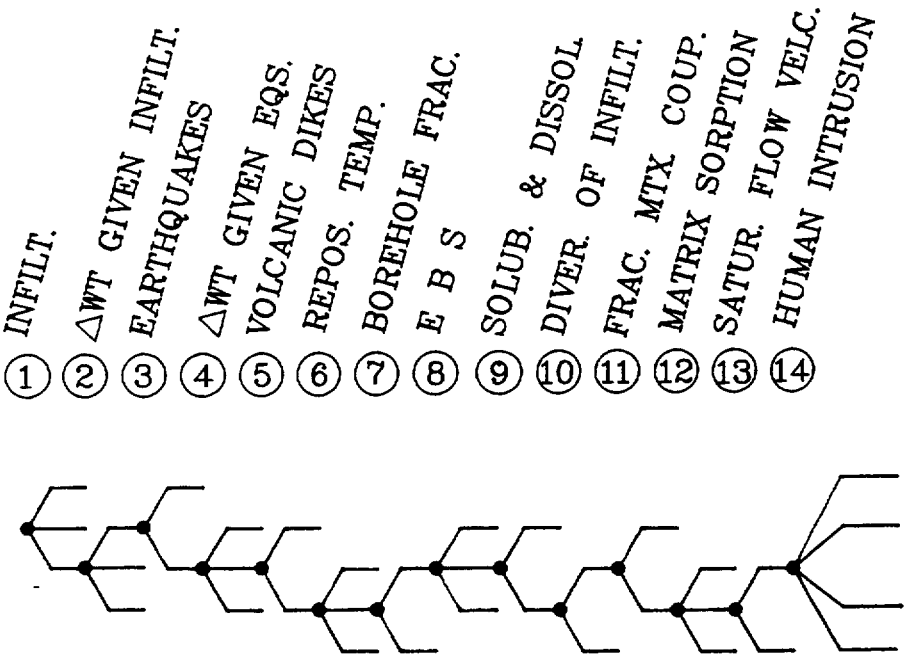

Figure 15-13. Master logic tree.

REFERENCES

1. R. K. McGuire (ed.). *Demonstration of a Risk-Based Approach to High-Level Waste Repository Evaluation*, Palo Alto, Calif.: Electric Power Research Institute, 1990. NP-7057, Research Project 3055-2.

2. M. E. Paté-Cornell. "Fault Trees Versus Event Trees in Reliability Analysis." *Risk Analysis*, vol. 4, no. 3, 1984, pp. 177-186.

Section 16

RESULTS AND SENSITIVITY ANALYSES

by

Robin K. McGuire

BASIC RESULTS

This Section presents results of the performance assessment carried out using the inputs described in Sections 2 through 14, with the methodology of Section 15. Releases to the accessible environment are calculated for the following 13 nuclides:

gaseous release:	^{14}C
aqueous release:	^{79}Se, ^{99}Tc, ^{129}I, ^{135}Cs, ^{226}Ra, ^{234}U, ^{235}U, ^{238}U, ^{237}Np, ^{239}Pu, ^{240}Pu, and ^{242}Pu
volcanic releases:	all of the above
human intrusion releases:	all of the above

Figure 16-1 shows the CCDFs of these 13 nuclides from gaseous and aqueous release pathways. Note that these plots use, as the abscissa, the release normalized by the EPA proposed limits for each nuclide. The gaseous pathway indicates the largest probability for low levels of release, but is limited in release to about 0.2 of the EPA limit. Higher releases are dominated by the aqueous pathways, with many nuclides having nearly similar releases. Among the highest are ^{237}Np and ^{79}Se, which have both relatively high solubilities and are present in large amounts in the waste material. These nuclides are used for sensitivity studies in this Section, as they are reasonably representative of the 13 nuclides studied.

Figure 16-2 presents CCDFs of release for ^{237}Np for aqueous pathways, volcanic dikes (logic tree node 5), and human intrusion (node 14). It is evident that aqueous pathways dominate the releases; volcanic occurrences and the human intrusion scenarios lead to low levels of release, by comparison. It is for this reason that the volcanic occurrences and human intrusion were treated as separate, independent mechanisms of release, even though it is more logical to combine these with aqueous and gaseous

releases. (In other words, if human intrusion does occur at the proposed repository, it is likely that other modes of release are also active, so the total release would be the combination of release from the two mechanisms. The lower relative releases from the human intrusion and volcanic scenarios means that the gaseous and aqueous pathways can be considered independently from the others when considering total releases to the environment, to good approximation.)

SENSITIVITY OF RELEASE DISTRIBUTION TO INPUT

The sensitivity of release to infiltration rate (node 1 on the master logic tree) is shown in Figure 16-3. This compares the CCDF for infiltration rates of 1.5 and 5.4 mm/yr to the "base case" CCDF obtained from calculations for the entire master logic tree. The CCDF for an infiltration rate of 0.5 mm/yr is too low to appear on the axes shown on Figure 16-3. In this figure, as well as in the other sensitivity studies illustrated below, the values for each individual curve have been renormalized by their probabilities, so the proper interpretation is that the curve for each infiltration rate is the CCDF that would be obtained if that rate were given a weight of unity and the alternatives were weighted zero. Thus the "base case" CCDF is a weighted average of the individual CCDFs. This figure indicates that there is not much difference between releases associated with 1.5 or 5.4 mm/yr, but these releases are much higher than those for 0.5 mm/yr.

The dominance of saturated conditions for high releases is evident in Figure 16-4, which shows sensitivity to changes in the water table. These changes may be caused by infiltration (node 2 of the master logic tree) or may be associated with tectonic stress release (node 4 of the logic tree). The total water table change is the sum of changes from the two causes, and Figure 16-4 indicates sensitivity to the total water table change. There is low sensitivity as long as there is unsaturated flow in the system, but if the repository is flooded, releases increase dramatically. Normalized releases exceeding unity on the abscissa consist entirely of cases with saturated flow.

Earthquakes have a minor effect on increasing releases, and this is demonstrated in Figure 16-5. The curve for scenarios including earthquake occurrences is close to that where earthquakes are not considered. Recall from the discussion in Section 5 that earthquakes are treated very conservatively, and that the associated releases are added to releases from other mechanisms. Even under these conservative conditions, earthquakes do not significantly increase the total releases. The primary way that earthquakes do affect releases is not by rupture of containers along fault zones but through potential increases in the water table which, when combined with moderate increases in the water table from changes in infiltration, lead to flooding of the repository. Note however that both the probability

of this sequence of events is low, and the possible effect is minor. Figure 16-5 makes that evident.

Repository temperature (node 6) is not a major factor in leading to differences in releases, as is evident from Figure 16-6; CCDFs for the three temperature scenarios are similar. There are two effects here. The cool repository scenario allows releases in the year 1000, whereas the warm and hot repository scenarios assume that temperatures at or above 96°C would prevent nuclides from being transported hydrologically. This is a minor effect, as all nuclides that are retained in year 1000 for the warm and hot scenarios are released in the next time step (year 2000). A more important effect is that the cool scenario implies that a multiple barrier waste container would be probably be used (see Figure 15-10), and this would significantly reduce the release of nuclides to the hydrologic system. Thus the effect we see in Figure 16-6 is caused primarily by differences in EBS selection, which is conditional on repository temperature.

The existence or non-existence of borehole fractures (node 7 in the logic tree) also does not affect releases greatly. This is illustrated in Figure 16-7. Even if the air gap remains intact and the repository is "dry" (i.e. it has unsaturated flow), 10% of the repository is assumed to have wet drip conditions, and these conditions lead to the predominant mode of release. Of course, for the largest releases where saturated conditions prevail, the existence or non-existence of borehole fractures is immaterial. All of this means that failure of the air gap through fracturing of the host rock surrounding each borehole would not lead to significantly larger releases.

The selection of the EBS (node 8) has a major impact on releases, particularly if the multiple barrier system is used as opposed to either of the single barrier systems. This is illustrated in Figure 16-8. Lower levels of release for the multiple barrier system result from the much longer time over which this EBS maintains its integrity, as described in Section 10.

Solubility and dissolution rate (node 9) is important for the releases of ^{237}Np, as illustrated in Figure 16-9. If the lowest values shown in Table 11-4 are justified, releases are significantly lower that the base case CCDF. There is less difference between the CCDF for the median and the high values of solubility and dissolution rate. Note that ^{237}Np is unusual in that there are orders of magnitude between the low and median values of solubility (see Table 11-4), and only a factor of two between the median and high solubilities. This is the case for several nuclides but not all, so Figure 16-9 is representative of some nuclides but not all of them.

Figure 16-10 shows the sensitivity to lateral diversion of ground water flux (node 10). There is substantial sensitivity at lower levels or release; at higher levels (above a normalized release of one) the scenarios involving high water tables and saturated conditions dominate releases. For saturated conditions the amount of lateral diversion is immaterial to the amount of waste released, and Figure 16-10 indicates this lack of sensitivity at high levels of release.

In a similar vein there is a strong dependence on the coupling between fractures and matrix in the host rock (node 11) at the lower levels of release where unsaturated flow dominates the release mechanism, and this is illustrated in Figure 16-11. At the higher releases (above a normalized release of unity), large releases are dominated by saturated conditions when saturated flow controls the transport of nuclides. Under these conditions the coupling between fractures and matrix is immaterial.

Matrix sorption (node 12) is not an important parameter in the way hydrologic transport is modeled here. This is illustrated in Figure 16-12; it results from the importance of weak coupling between fracture and matrix flow in leading to large releases. With weak coupling there is no chance for interaction between fracture and matrix flow, so retardation of nuclide velocities in the matrix is not an issue. Figure 16-12 illustrates this lack of sensitivity.

The saturated flow velocity, node 13, has a relatively minor impact on releases, and this is illustrated in Figure 16-13. Even for the case of a saturated repository, a large portion of waste containers have failed before year 5000 for the two single-barrier EBSs (see Figures 10-3 and 10-5), so nuclides reach the accessible environment under either assumed value of saturated flow. Thus level of release is not sensitive to this parameter.

Releases of ^{79}Se, ^{129}I, and ^{135}Cs have an additional factor apart from solubility and dissolution of the waste form; this is the initial release of these radioelements from the gap region of the cladding/matrix. Figure 16-14 shows how sensitive the CCDF of ^{79}Se is to the inclusion or exclusion of this pulse of release as described in Section 11. The fraction of ^{79}Se released upon initial contact with water is not a significant portion of the total release, at least for a pulse assumed to be 1% of the inventory.

SUMMARY

Overall, the CCDFs calculated and illustrated in this Section show several trends. First, potential releases of waste for aqueous pathways dominate the possible mechanisms by which nuclides may

travel from the proposed repository to the environment. Gaseous release of ^{14}C dominates the total release of nuclides at low levels of release but is exceeded by releases via aqueous pathways for large releases (Figure 16-1). Releases by volcanic scenarios and by human intrusion are relatively low compared to aqueous pathways (Figure 16-2). The latter conclusion may not be the case for ^{239}Pu and ^{240}Pu, however, which are present in relatively large quantities in the waste.

Input assumptions that have relatively low influence on large releases are the coupling between fractures and matrix, the degree of matrix sorption, the saturated flow velocity, the repository temperature, borehole fracturing, and effects of earthquakes. The large releases are dominated by extreme scenarios of high water table or flooded conditions, which make assumptions on unsaturated flow less critical.

Factors that are important are the level of infiltration, solubility and dissolution rate of the waste matrix, choice of the EBS, possible lateral diversion of the ground water flow (for lower levels of release), and possible initial pulses of release of radioelements associated with initial contact with water, for some radionuclides. These assumptions indicate a strong influence on the releases, and more sophisticated analysis is probably justified to model these effects.

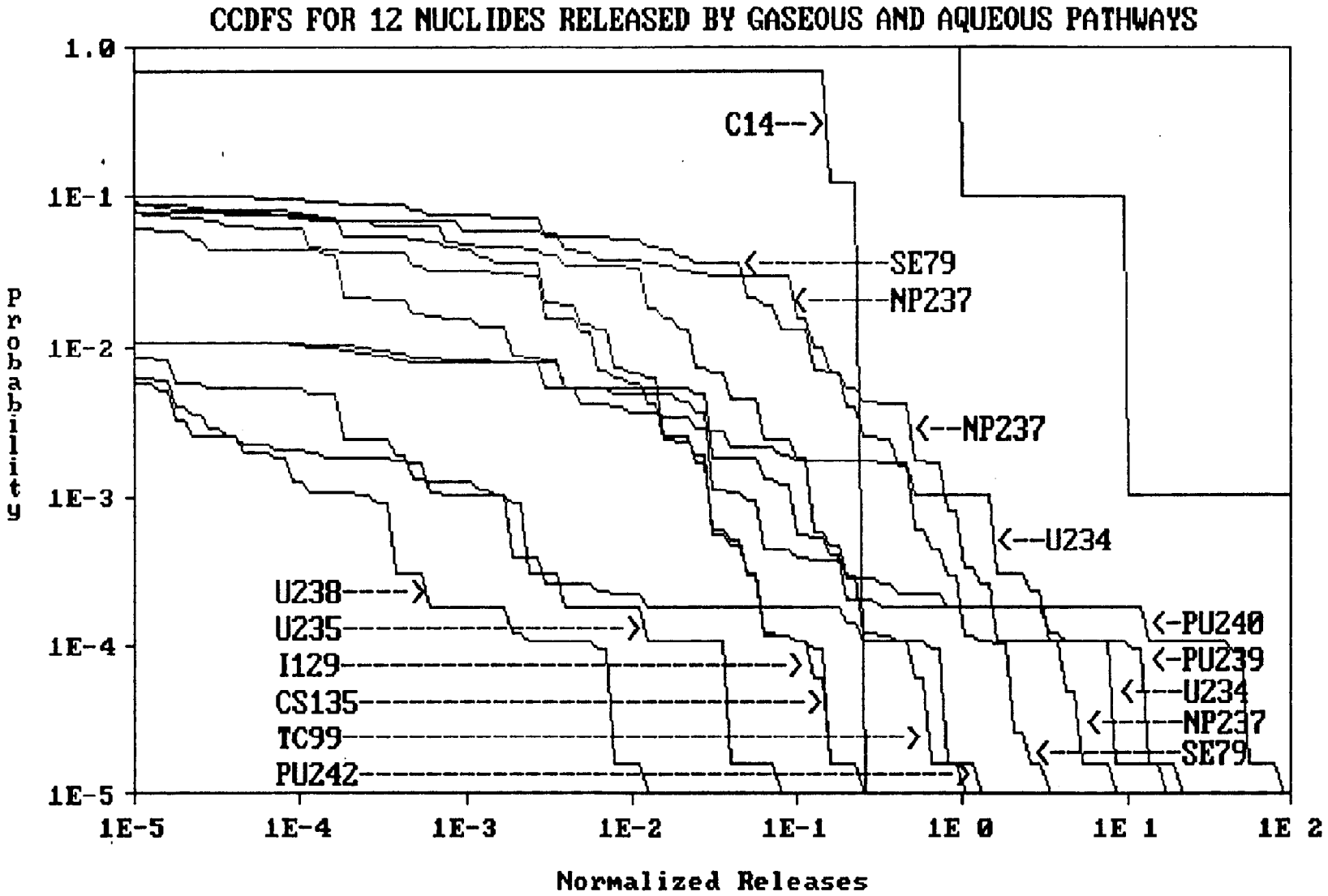

Figure 16-1. CCDFs for 12 nuclides released by gaseous and aqueous pathways.

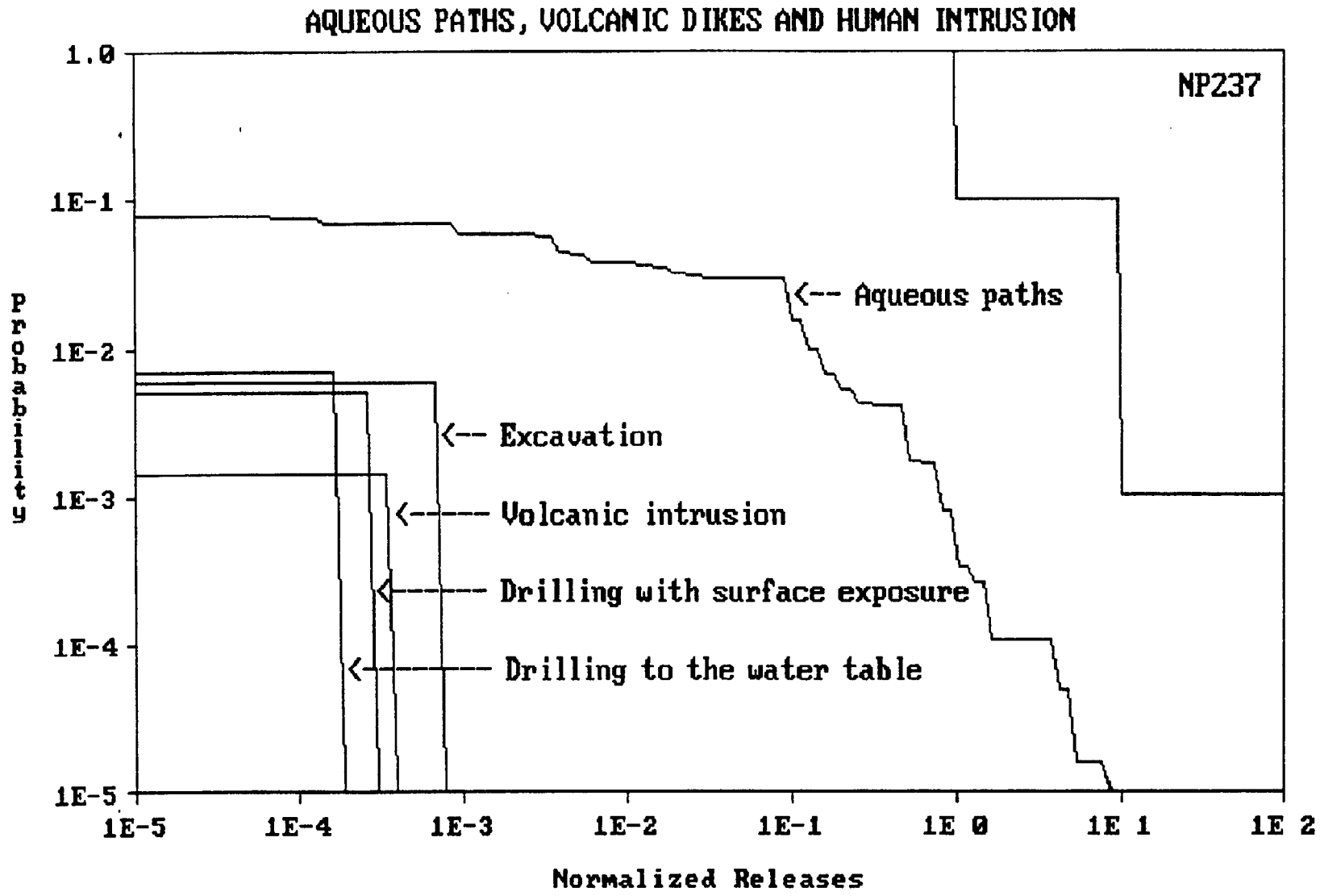

Figure 16-2. CCDFs for ^{237}Np for releases by aqueous paths, volcanic dikes and human intrusion.

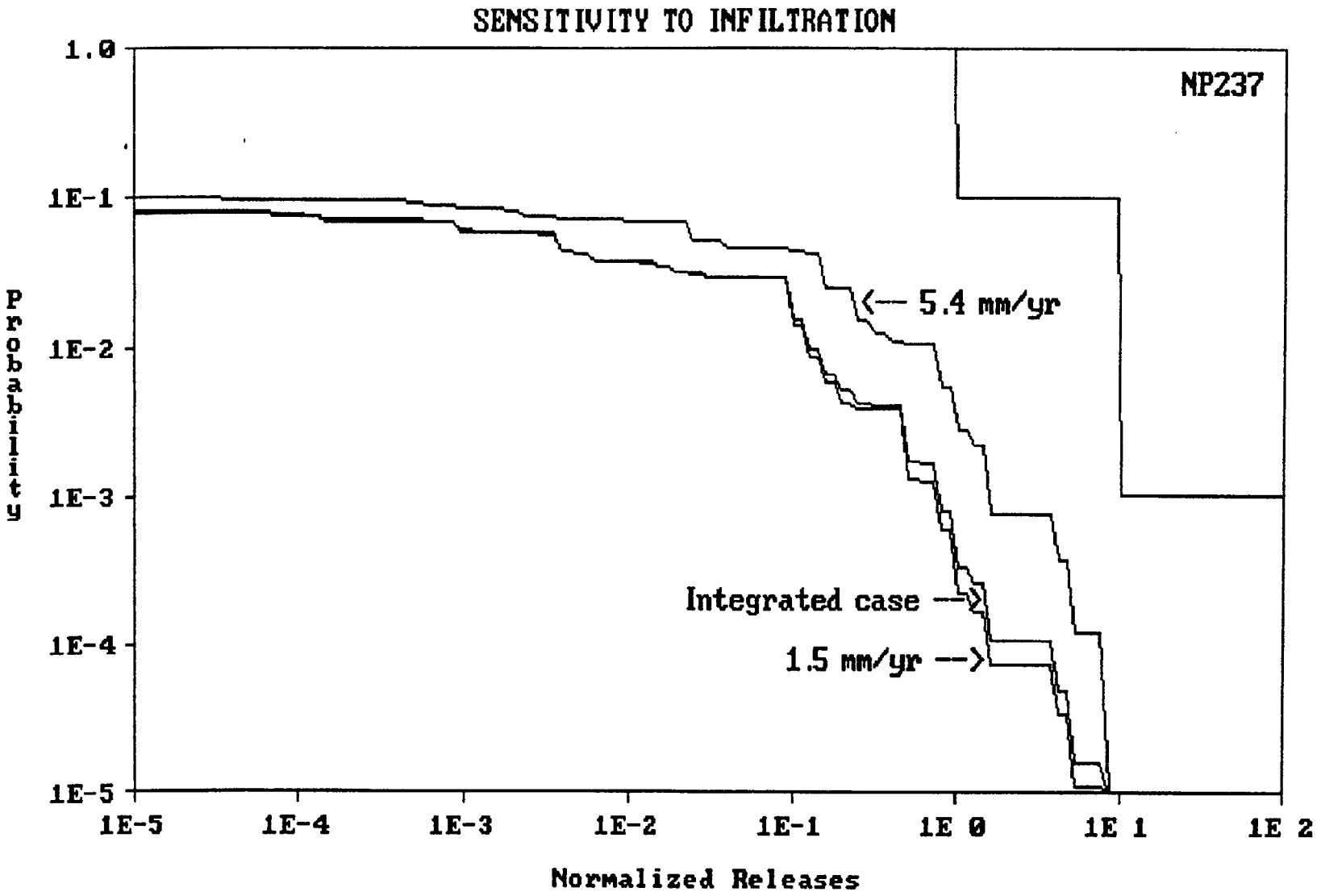

Figure 16-3. Sensitivity of CCDF for ^{237}Np to infiltration.

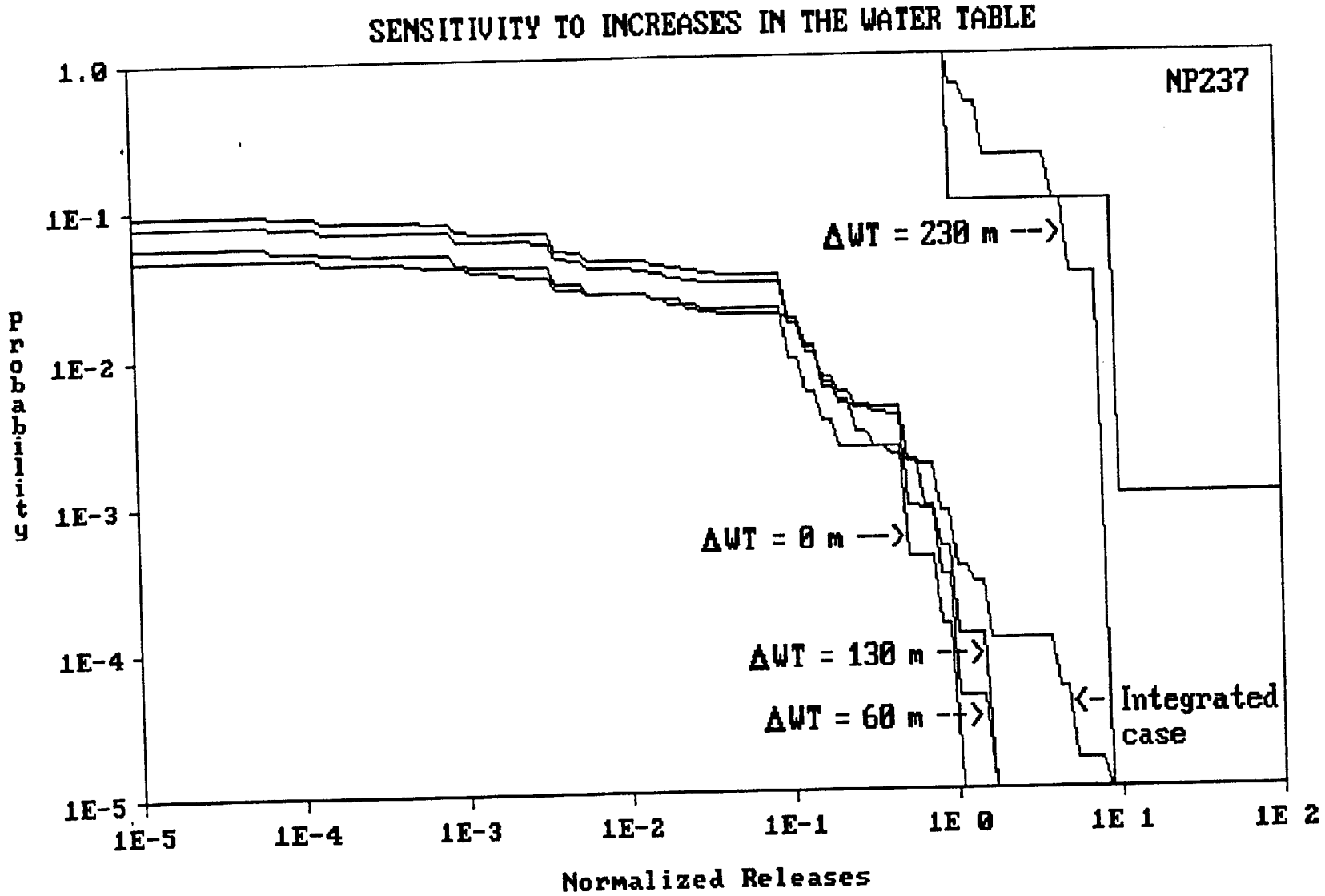

Figure 16-4. Sensitivity of CCDF for ^{237}Np to changes in water table.

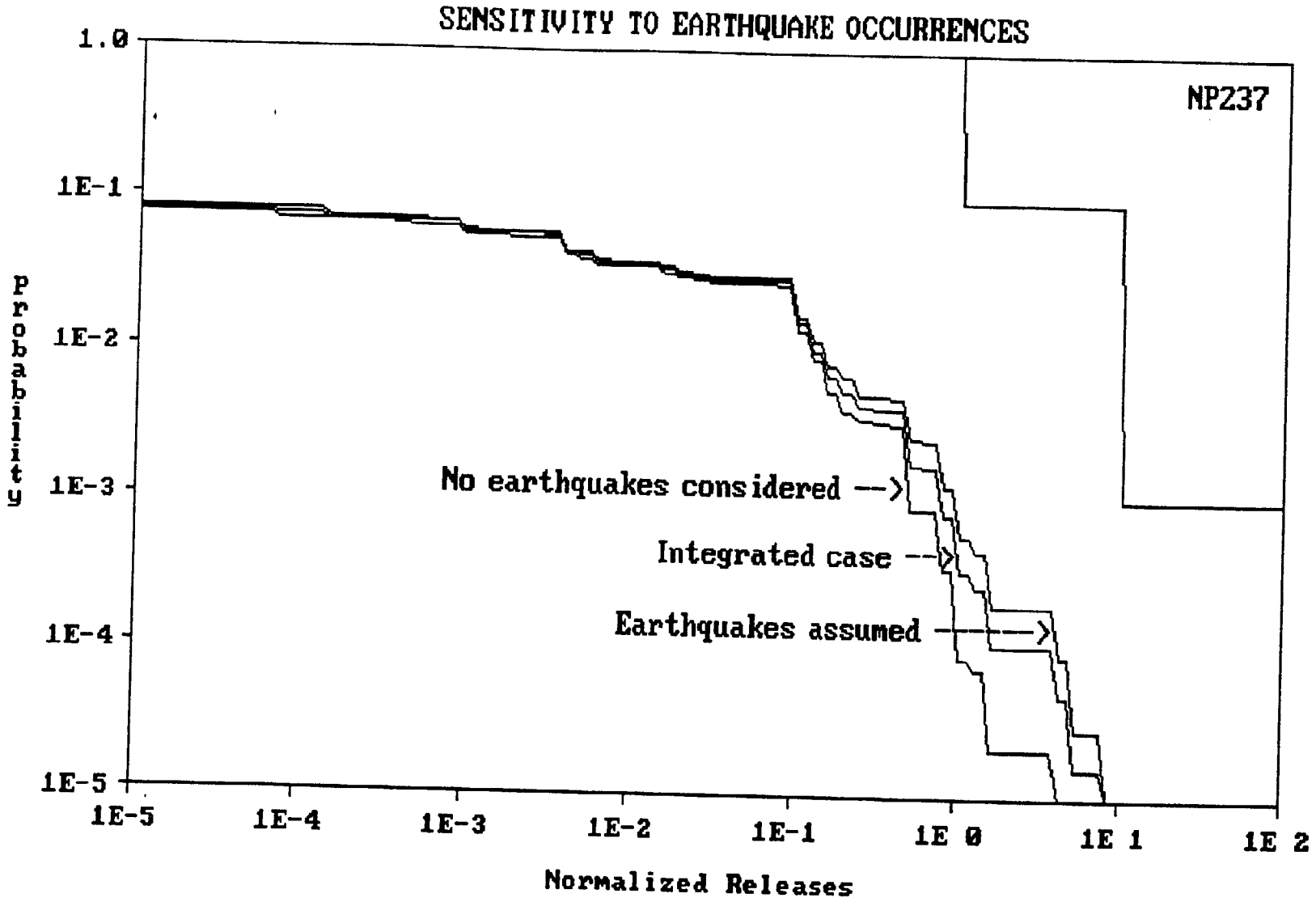

Figure 16-5. Sensitivity of CCDF for ^{237}Np to earthquake occurrences.

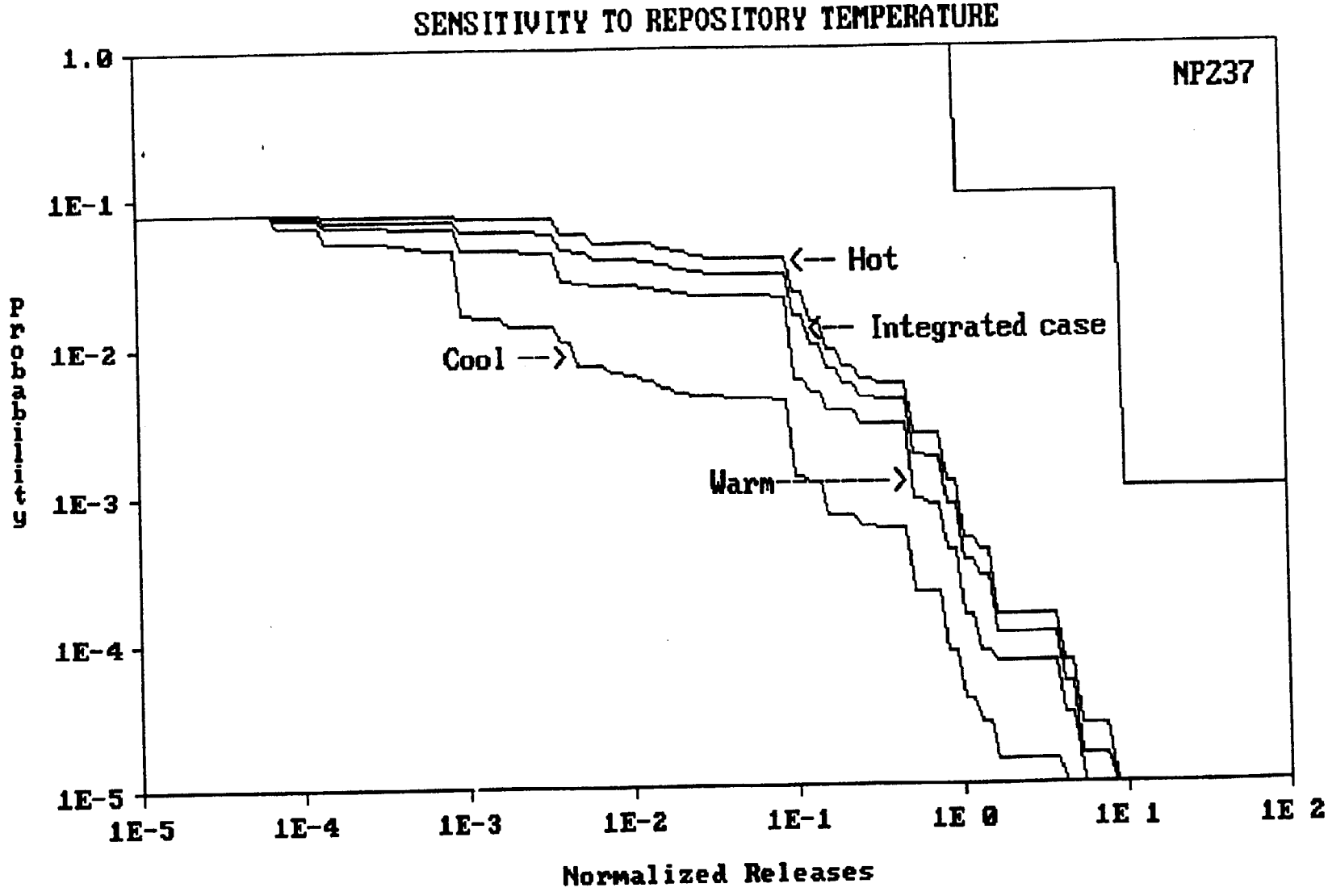

Figure 16-6. Sensitivity of CCDF for ^{237}Np to repository temperature.

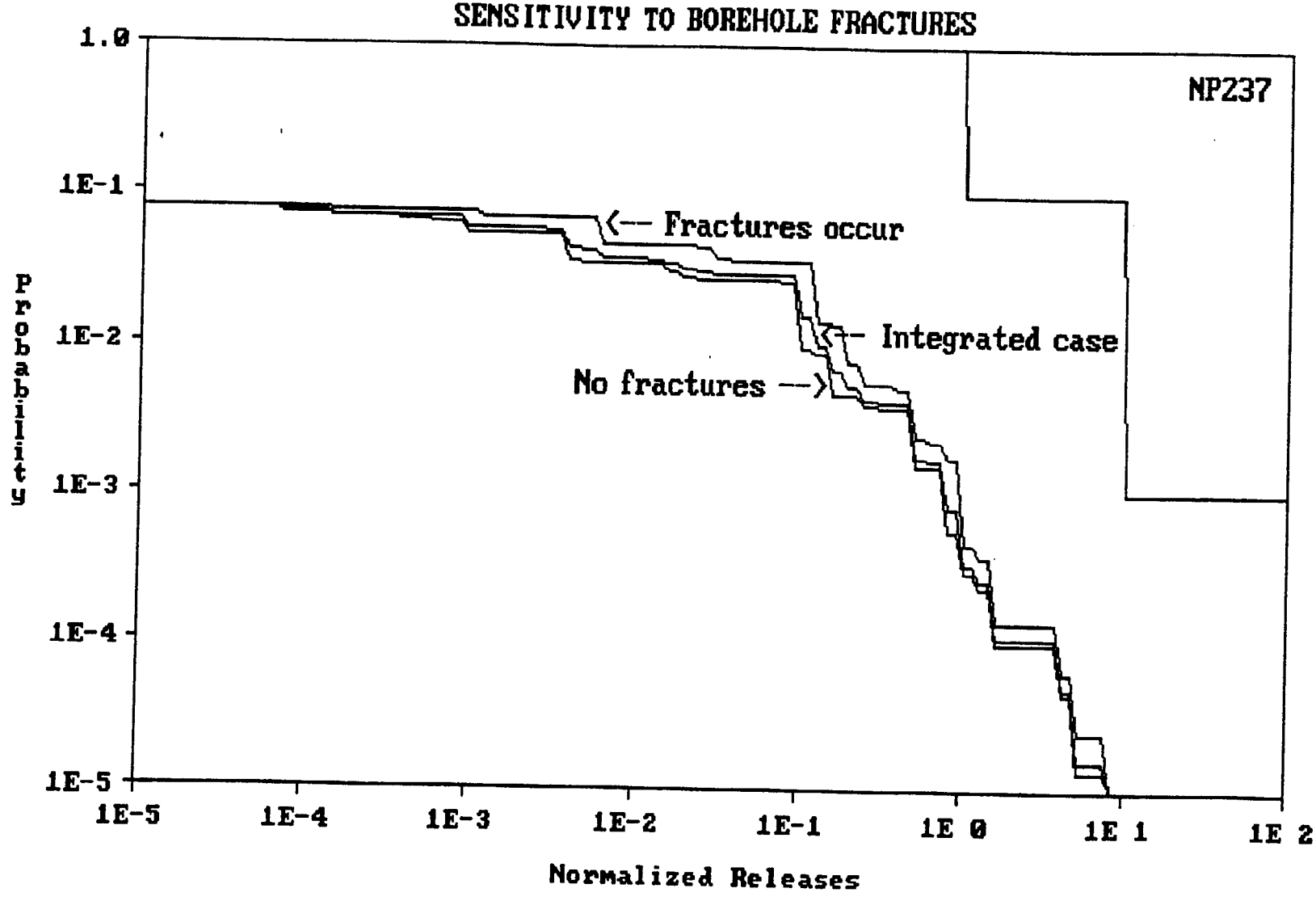

Figure 16-7. Sensitivity of CCDF for ^{237}Np to borehole fractures.

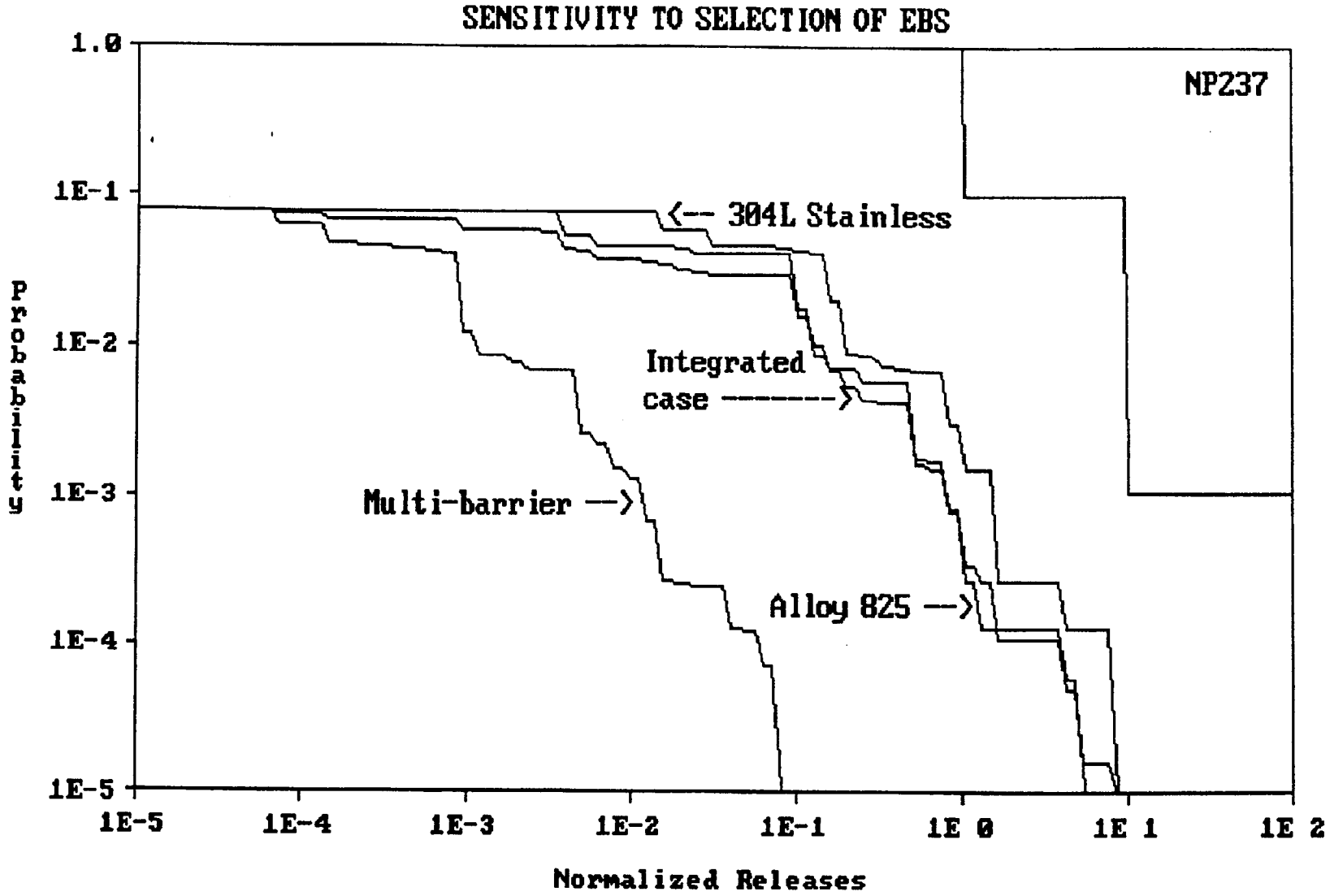

Figure 16-8. Sensitivity of CCDF for ^{237}Np to selection of EBS.

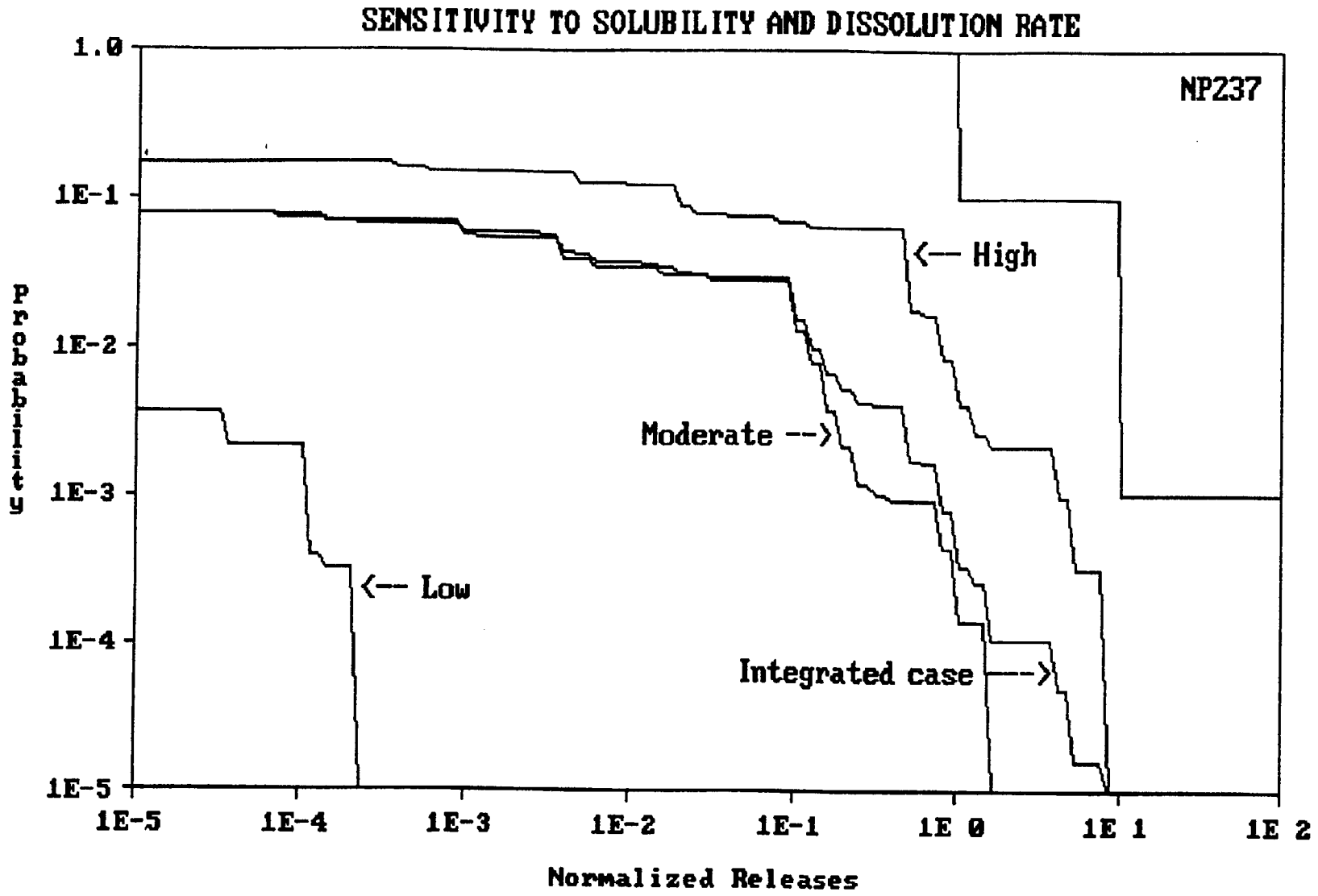

Figure 16-9. Sensitivity of CCDF for ^{237}Np to solubility and dissolution rate.

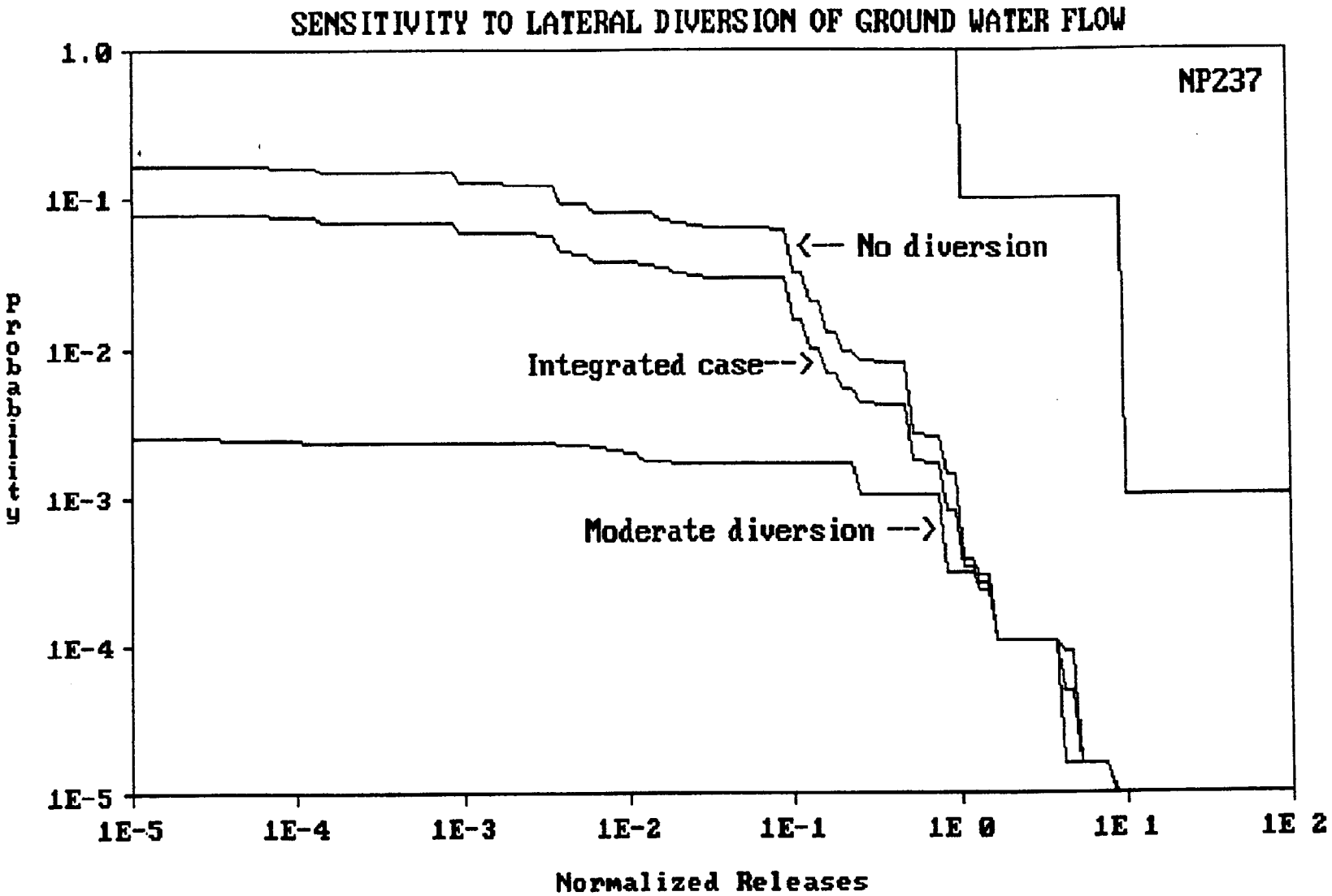

Figure 16-10. Sensitivity of CCDF for ^{237}Np to lateral diversion of ground water flow.

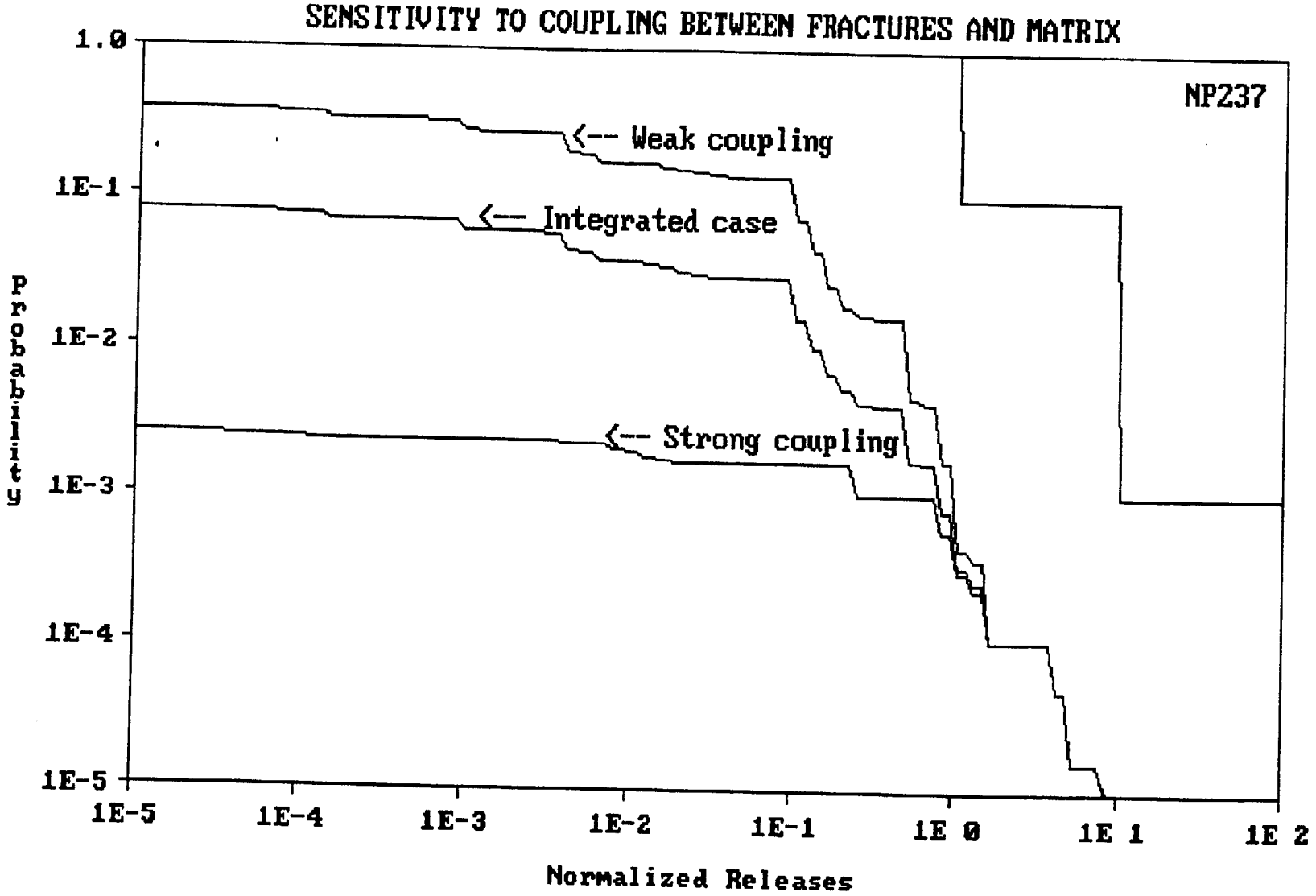

Figure 16-11. Sensitivity of CCDF for ^{237}Np to coupling between fractures and matrix.

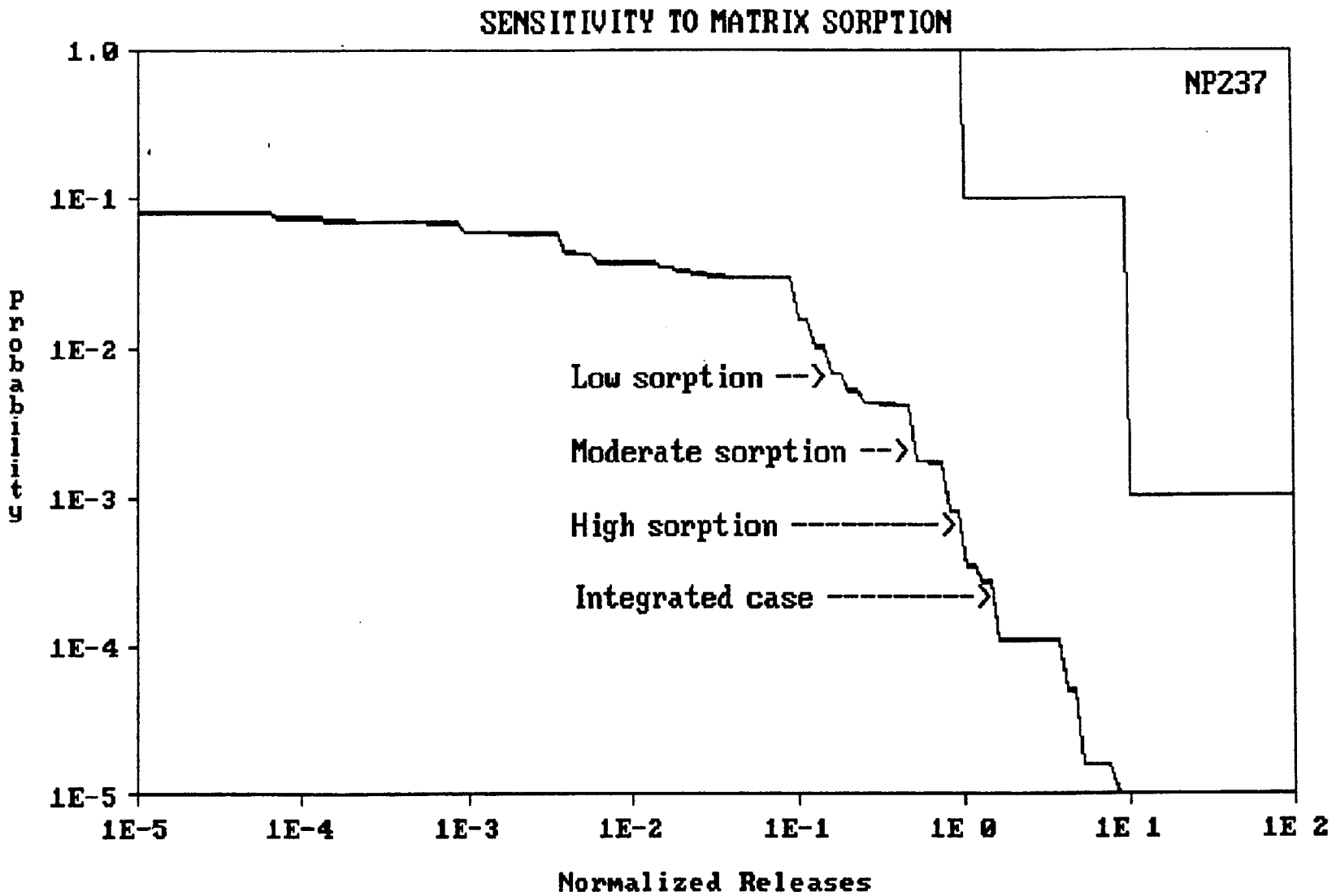

Figure 16-12. Sensitivity of CCDF for ^{237}Np to matrix sorption.

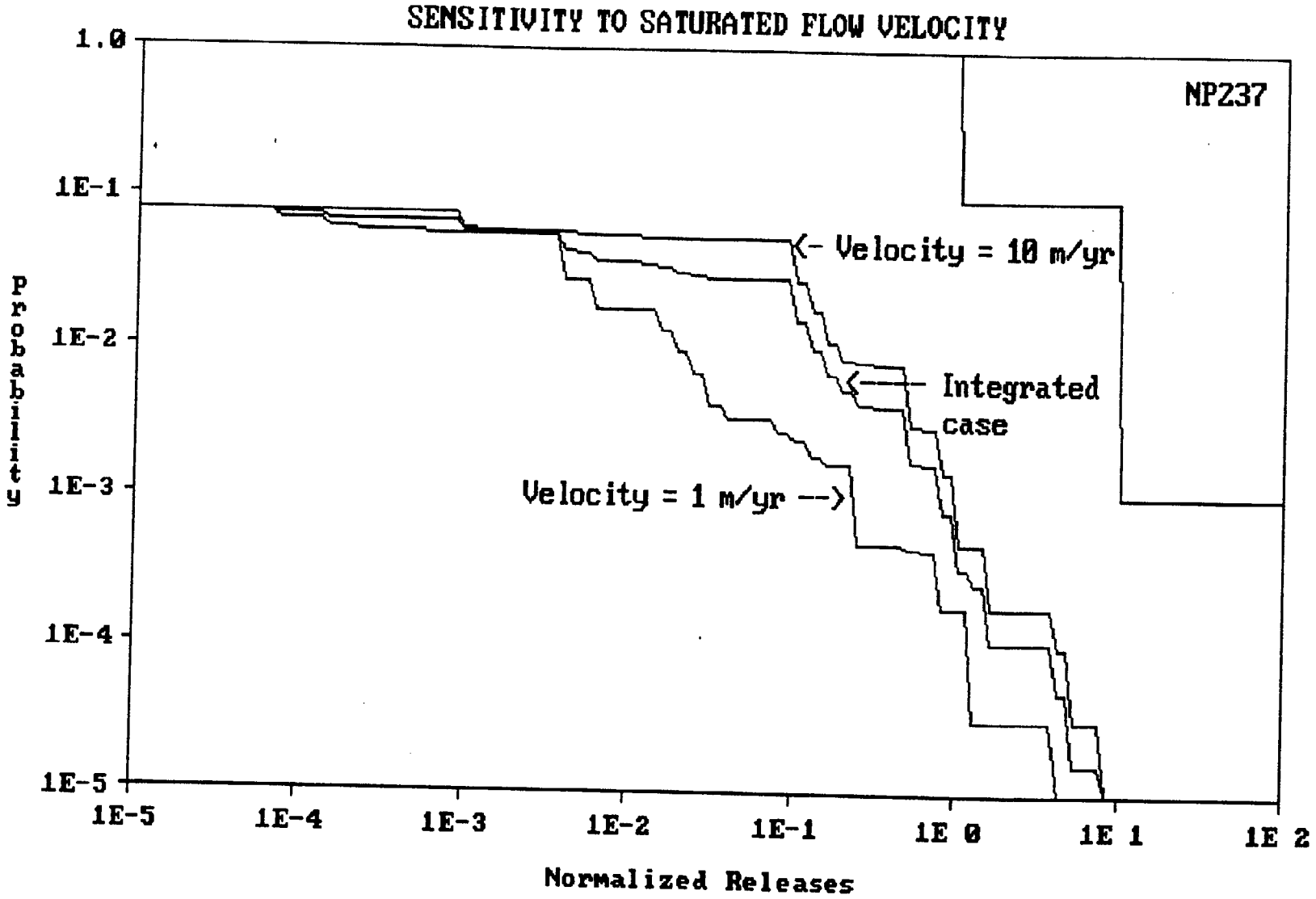

Figure 16-13. Sensitivity of CCDF for ^{237}Np to saturated flow velocity.

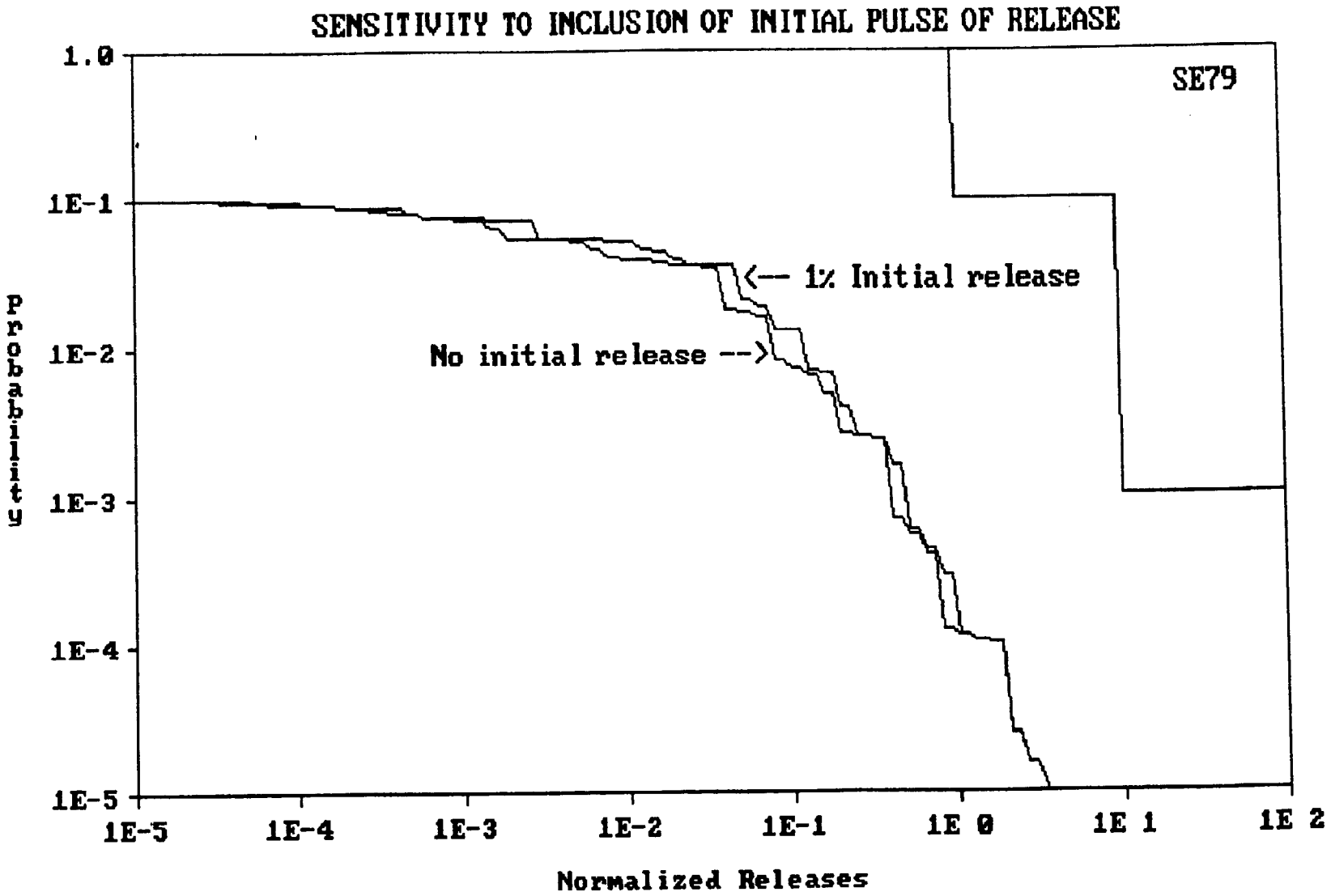

Figure 16-14. Sensitivity of CCDF for ^{79}Se to inclusion of initial pulse of release.

Section 17

CONCLUSIONS

by

Robin K. McGuire

Conclusions from this study are divided into two areas. First are results obtained from the development and application of new models in the various technical areas. These results come from the experience of development and application, and apply in a broad sense to risk-based performance assessments of waste repositories. Second are conclusions related specifically to the application of the methodology for the Yucca Mountain site; these relate to the specific results that are obtained and described in Section 16.

In the first category, several conclusions are evident from the scientific and engineering models. The modeling of surface water flow and infiltration was a useful exercise, and provides estimates that are more strongly based in soil science, even though the results do not change much from the previous application. Similar comments apply to the climatological model of precipitation events and future climate effects. The models of volcanic occurrences and earthquakes have advanced about as far as can be expected with single expert applications, and are general enough that they could accommodate a diversity of opinion from multiple experts. The source-term model is improved over the previous study, but the area of the near-field needs further development. We have made rather simple, conservative assumptions about the connection between nuclides that go into solution at the source and the input to hydrologic models, ignoring effects of the disturbed zone and any travel time or retardation that might take place there. The hydrologic model is still a simple one, as it must be for performance assessments involving many combinations of parameters, but it has been calibrated with more sophisticated calculations and is adequate for its purpose. The EBS model is a simple application of Weibull distributions that accounts for different EBS designs, materials, and barriers; it is a general-enough technique that the important characteristics of EBSs can be represented and evaluated. The gaseous release model uses a sophisticated methodology for calculation of gas travel times, and is adequate. The human intrusion model has been developed in a general format, with preliminary numbers assigned that are not site-specific; it would gain credibility with additional inputs

from a group of experts, rather than one expert as used in this study, but that is a general comment that applies to all of the models developed under this project.

Conclusions regarding the specific application to the proposed repository at Yucca Mountain are based on the results presented in the previous Section. Hydrologic pathways appear to be the largest source of release from repository; gaseous pathways are likely to be a source of low levels of release but not of large nuclide releases. By comparison to these two release nodes, volcanic events and human intrusion do not appear to lead to large releases of radionuclides. Comparing the calculated CCDFs to proposed standards of release from the EPA, there is not an exceedance of the standard, but alternative models or inputs than those used here could be constructed that lead to larger releases. The largest releases are associated with unlikely combinations of events: large hydrologic fluxes, no diversion of ground water flow around the repository, an increased water table that floods part of the repository, and high solubilities and dissolution rates. Factors that have a strong influence on release are the amount of hydrologic flux, potential lateral diversion of this flux (except at the highest levels of release), flooding of part of the repository, coupling between fractures and matrix (except at the highest levels of release), the EBS design, and the solubility and dissolution rate. Factors that are less influential on release are volcanic occurrences, earthquake occurrences, the thermal pulse, and potential borehole fractures that fail the air gap.

This application of a risk-based performance assessment methodology meets the three objectives for such a methodology, as described in Section 1: (1) results can be compared to regulatory standards, (2) the relative importance of uncertainties in the various models and parameter values used as input can be assessed, and (3) the overall performance of a repository, quite apart from any regulatory criteria, can be assessed in the context of the uncertainties resulting from lack of knowledge and data. In this sense the current application has been successful, notwithstanding the qualifications stated herein and the improvements in models that are always desired.

Appendix A

EARTHQUAKES AND TECTONICS CALCULATIONS

This appendix supplements Section 5 of the report and provides a discussion of the models used to characterize the potential for fault displacement offset of canister boreholes.

SECONDARY FAULTING DATABASE

The database of secondary faulting parameters compiled for normal faulting earthquakes consists of more than 40 historical normal slip earthquakes that had associated surface rupture. The earthquakes considered include those characterized by a dominant normal-slip surface displacement, as well as several strike slip earthquakes with a significant component of normal slip (strike slip to normal slip ratio of less than 2:1). For each earthquake, all available information on the coseismic surface deformation was reviewed. Of the larger database, 20 earthquakes for which measured displacements and detailed maps of the surface ruptures have been published were selected for characterization. For most of the additional earthquakes, the details of the surface deformation are too poorly known to be used in the analyses.

Source characteristics including moment magnitude, **M**, surface and subsurface rupture length, and maximum net surface displacement were evaluated for each earthquake (Table A-1). The primary rupture lengths listed in Table A-1 for all earthquakes that occurred prior to 1975, with the exception of the 1959 Hebgen Lake earthquake, represent the observed surface rupture length. For all other earthquakes, the rupture length was estimated from the spacial distribution of early aftershocks (typically those aftershocks recorded within the 24 hours after the mainshock). For the latter earthquakes, we consider the length of the early aftershock zone to be more representative of the actual extent of the coseismic rupture than the shorter mapped surface rupture lengths. There is no data on the extent of subsurface rupture for most of the listed earthquakes that occurred prior to 1975.

Maps of the surface ruptures were examined and criteria for identifying primary and secondary coseismic fault ruptures were defined using a similar methodology to that employed by Bonilla (1). A primary fault includes the main trace of the surface rupture, as well as allsubparallel ruptures occurring within a distance of approximately 0.2 kilometers from the main trace. Surface traces

Table A-1

FAULT RUPTURE PARAMETERS FOR NORMAL FAULTING EARTHQUAKES

Earthquake	Date	Mag	Rupture Length (km)		Fault Zone Width (km)		Fault Displacement (m)		
			Primary	Secondary	Hanging Wall	Foot Wall	Primary	Secondary	References
Owens Valley, Calif	1872.03.26	7.6	108.0	31.0	12.0	5.0	6.40	0.00	(2)
Pitaycachi, Mexico	1887.05.03	7.3	75.0	18.0	11.5	0.0	4.50	0.00	(3), (4)
Pleasant Valley, Nevada	1915.10.03	7.2	59.0	6.0	1.3	0.0	6.60	1.00	(5)
Salmas, Iran	1930.05.06	7.2	30.0	6.3	0.8	0.0	6.40	0.00	(6)
Hansel Valley, Utah	1934.03.12	6.6	11.5	9.0	5.0	0.0	0.52	0.00	(7), (8)
Ancash, Peru	1946.11.10	6.8	20.0	3.0	2.0	0.0	3.50	1.00	(9), (10)
Fort Sage Mtns, Calif	1950.12.14	5.7	9.2	0.4	0.4	0.0	0.20	0.08	(11)
Rainbow Mtn, Nevada	1954.07.06	6.2	18.0	5.1	0.2	0.5	0.31	0.15	(12)
Fairview Peak, Nevada	1954.12.16	7.2	67.0	47.8	4.0	2.5	4.80	1.30	(13)
Hebgen Lake, Montana	1959.08.18	7.3	36.0	33.2	13.8	1.5	6.10	0.90	(14), (15)
Alasehir Valley, Turkey	1969.03.28	6.8	32.0	11.0	5.0	4.0	0.82	0.00	(16), (17)
Gediz, Turkey	1970.03.28	7.1	41.0	18.4	4.0	1.4	2.80	2.25	(16), (18)
Oroville, Calif	1975.08.01	6.1	15.0	0.5	0.5	0.0	0.06	0.02	(19)
Corinth, Greece	1981.02.25	6.3	15.0	7.2	2.0	0.6	1.50	0.30	(20)
Corinth, Greece	1981.03.04	6.2	25.0	1.1	1.5	0.0	0.70	0.08	(20)
Dhamer, North Yemen	1982.12.13	6.3	20.0	3.2	5.5	7.5	0.03	0.00	(21)
Borah Peak, Idaho	1983.10.28	6.9	34.0	16.0	3.5	0.3	2.70	1.90	(22)
Guinea, West Africa	1983.12.22	6.4	27.0	0.2	0.4	0.0	0.13	0.10	(23)
Kalamata, Greece	1986.09.13	5.9	15.0	3.1	0.8	0.0	0.18	0.12	(24), (25)
Edgecumbe, New Zealand	1987.03.02	6.5	28.0	13.3	5.5	2.2	2.50	1.20	(26)

(2) Jennings (1975)
(3) Bull and Pearthree (1988)
(4) Natali and Sbar (1982)
(5) Wallace (1984)
(6) Tchalenko and Berberian (1974)
(7) Doser (1989)
(8) Neumann (1936)
(9) Bellier et al. (1991)
(10) Silgado (1951)
(11) Gianella (1957)
(12) Tocher (1956)
(13) Slemmons (1957)
(14) Myers and Hamilton (1964)
(15) Witkind (1964)
(16) Ambraseys and Tchakuko (1972)
(17) Eyidoyan and Jackson (1985)
(18) Tasdemiroglu (1971)
(19) Clark et al. (1976)
(20) Jackson et al. (1982)
(21) Plafker et al. (1987)
(22) Crone et al. (1987)
(23) Langer et al. (1987)
(24) Lyon-Caen et al. (1988)
(25) Papazachos et al. (1988)
(26) Beanland et al. (1989)

occurring within fault steps are considered to be primary faults. Branching faults, and other surface ruptures that occur at distances greater than 0.2 kilometers from the main trace are defined as secondary faults. Ruptures that are not tectonic in origin, including those formed as a result of slope failures, ground shaking, slumping or liquefaction, etc., are not considered to be secondary faults and are excluded from the database. For each earthquake, the length of individual secondary faults and the distance from the main fault trace to each secondary fault were measured. The location of each secondary fault with respect to location in the hanging wall block or the foot wall block were identified. The secondary rupture length listed in Table A-1 represents the sum of the lengths of all secondary faults identified for each earthquake. The maximum distance between the primary fault and associated secondary faults is defined as the fault zone width. The fault zone width is listed for both the hanging wall block and foot wall block (Table A-1). For secondary faults that are not subparallel to the primary fault, the fault zone width is taken as average of the maximum and minimum distance between the primary fault trace and each individual secondary fault trace. All reported displacements on secondary faults were evaluated to identify the maximum displacement on faults within each block.

The extent of secondary faulting, both with respect to total length of all secondary faulting and maximum displacement on secondary faults varied widely for individual earthquakes, irrespective of magnitude. It is possible that additional secondary faulting occurred for many of these earthquakes, but was not recorded for various reasons. Displacements were not reported for nearly half of the secondary faults, however, it is likely that displacements were significantly smaller than those that observed on the primary fault. The observed secondary faulting varies from individual faults up to 14 kilometers in length with displacements of up to 2.2 meters to 0.2 kilometer long fractures with no measured displacement. Shorter fractures cannot be accurately resolved at the scale of most published fault maps. A total of 94 secondary faults were identified for all 20 earthquakes, and as many as 14 secondary faults were identified for individual earthquakes.

A significant difference exists between the extent of secondary faulting that occurs in hanging wall and foot wall blocks. Of the secondary faults in the database, 70 or approximately 75 percent occur within the hanging wall block. The fault zone width is significantly larger for the hanging wall block, with a maximum of approximately 14 kilometers versus a maximum of 5 kilometers for the foot wall.

In addition, it is important to note that secondary deformation was observed for all earthquakes where detailed field studies were completed. There were no earthquakes in the larger database for which the occurrence of secondary deformation can be precluded.

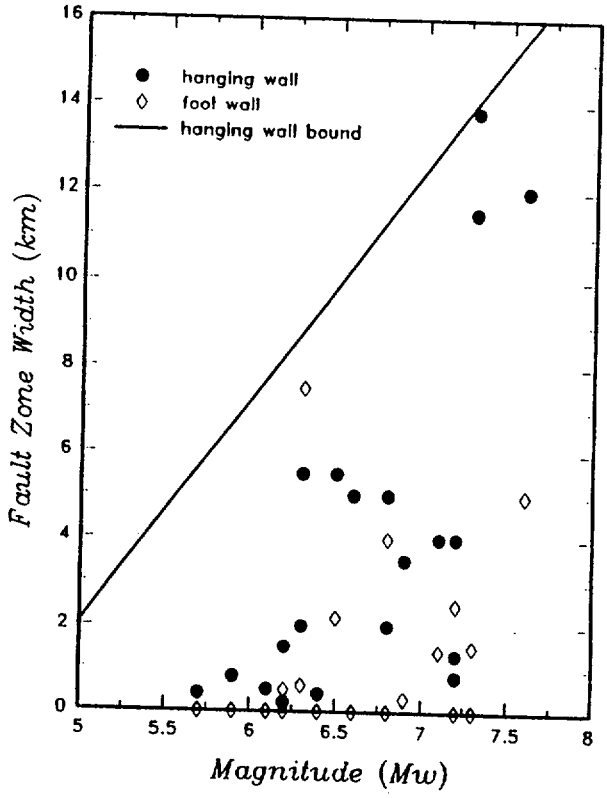

Figure A-1. Maximum width of zone of faulting, measured from primary fault trace, versus earthquake magnitude for normal faulting events listed in Table A-1.

LENGTH AND DISPLACEMENT OF FAULT RUPTURE IN REPOSITORY

The model for evaluating the length and displacement of fault rupture with the repository is based on the observed pattern of surface faulting in normal faulting earthquakes. The data show that the width in map view of the zone of faulting during normal-faulting earthquakes (Table A-1) varies from essentially zero to as much as 14 km. Figure A-1 shows the data for both the hanging wall and foot wall sides of the zone. The bound of the fault zone width for the hanging wall side is similar to the bound for fault zone half-width used in the Phase I study. Figure A-2 shows the ratio of foot wall to hanging wall fault zone width plotted against hanging wall width. As can be seen, there is little correlation between the ratio of foot/hanging wall zone with and the hanging wall fault zone width. Therefore, a discrete distribution independent of fault zone width was used in the analysis (right hand plot in Figure A-2).

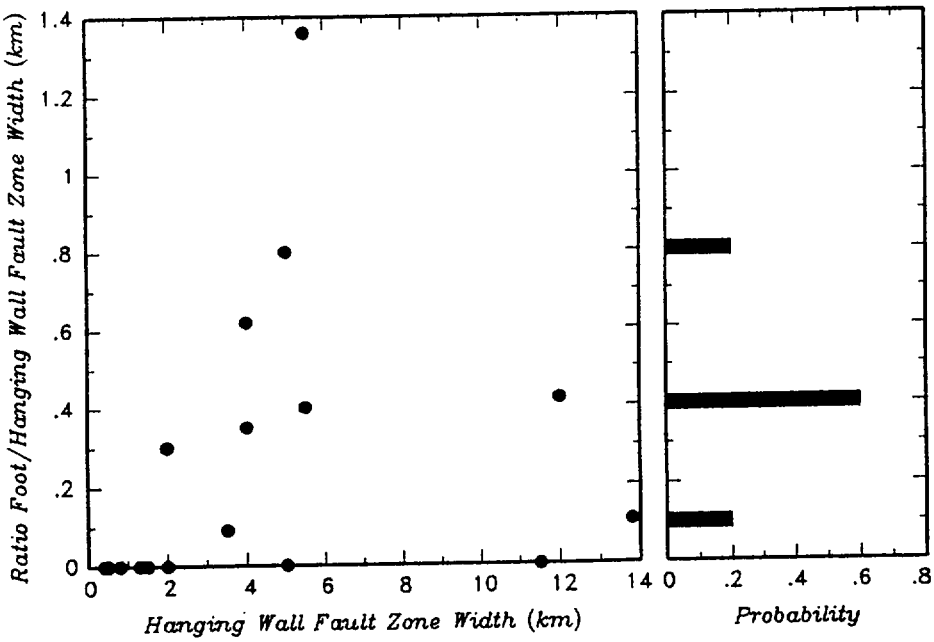

Figure A-2. Ratio of foot wall/hanging wall fault zone width (measured from primary rupture trace) for data shown in Figure A-1. Left hand plot shows the reported data, the right hand plot show the discrete distribution used in the simulations.

The zone of surface faulting can contain a single strand of secondary faulting, or multiple strands. Figure A-3 shows the ratio of the total length of secondary faulting to the length of primary faulting, $R_{S/P}$, plotted against the fault zone width. As can be seen, there is considerable scatter in the data and, once the fault zone has significant width, the ratio $R_{S/P}$ does not show a systematic increase with increasing width. Three relationships were used to represent the relationship between $R_{S/P}$ and fault zone width in the analysis with the weights indicated in Figure A-3.

The expected length of faulting within the repository for a magnitude m earthquake on fault n, $E[L_F(m)$ for fault $n]$, was evaluated using the simulation procedure illustrated schematically in Figure A-4. For a given fault and earthquake magnitude, the down-dip width and length of primary faulting are computed from an empirical relationship between rupture area and magnitude (27). The primary rupture area is then randomly located on the fault plane assuming all locations are equally likely. The hanging wall half-width in map view of the zone of faulting is randomly selected from a uniform

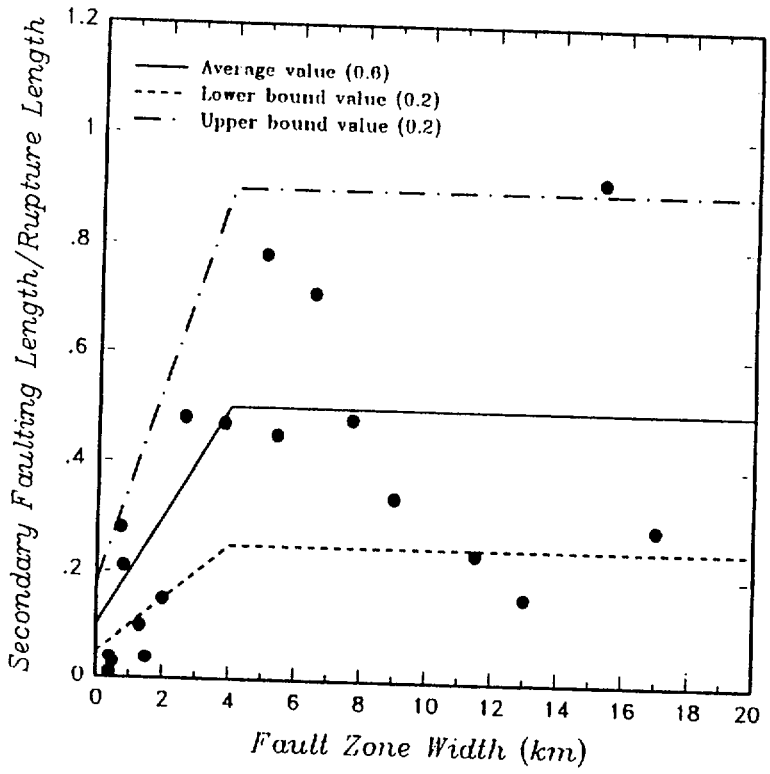

Figure A-3. Ratio of total length of secondary faulting to total length of primary faulting $R_{s/p}$, versus maximum width of zone of faulting. The three lines show the weighted relationships used in the simulations.

distribution between zero and the bound to the data shown in Figure A-1. The ratio of foot wall/hanging wall width is then selected from the discrete distribution shown on the right in Figure A-2. The two widths are then used to construct a zone of faulting around the primary rupture plane, as shown in Figure A-4.

The fraction of the total area of the zone of faulting that falls within the repository boundary, F_{RI}, is then computed. Assuming that secondary fault rupture is equally likely to occur anywhere within the zone of rupture, then the fraction of the total length of secondary rupture that is expected to occur within the repository is equal to the fraction of the total area of the zone of faulting that falls within the repository boundary, F_{RI}. The total length of secondary faulting as a percentage of the length of

the repository boundary, F_{RI}. The total length of secondary faulting as a percentage of the length of primary faulting, $R_{S/P}$ is selected from the weighted relationships shown in Figure A-3 and the selected half-width of the zone of faulting. The expected length of secondary faulting in the repository for simulation i, $E[L_{SF}]_i$, is given by

$$E[L_{SF}]_i = F_{RI} \cdot R_{S/P} \cdot L_R(m) \qquad \text{(A-1)}$$

where $L_R(m)$ is the length of primary faulting estimated above.

The previous step is repeated, selecting new values of the half-width of the zone of faulting to provide the expected length of secondary faulting for a given primary rupture location.

The primary rupture zone is then moved to a new location on the fault plane and the process repeated to give the expected length of secondary faulting in the repository for a randomly located earthquake on the fault plane. In this process, if the primary rupture does not extend upward to a depth within a rupture zone half-width below the repository depth, then no intersection with the repository is assumed to occur for that simulation.

The above process was repeated for all magnitude that could occur on the particular fault, and for all faults considered in the analysis. Figure A-5 shows typical results for the relationship between earthquake magnitude and the expected length of secondary fault rupture within the repository.

The amount of secondary faulting displacement was estimated as being a fraction of the primary faulting displacement. Figure A-6 shows the data for normal faulting earthquakes (Table A-1) which indicates that the ratio of secondary faulting displacement to primary faulting displacement can be as high as 0.8. For this analysis the ratio of secondary to primary displacement was randomly selected from a uniform distribution ranging from 0 to 0.8. The amount of primary displacement was estimated using a empirical relationship developed by Wells and Coppersmith (27).

The length of primary fault rupture was assessed using a similar procedure. Earthquake ruptures were randomly distributed over the fault plain and the length of the fault intersecting the repository horizon computed.

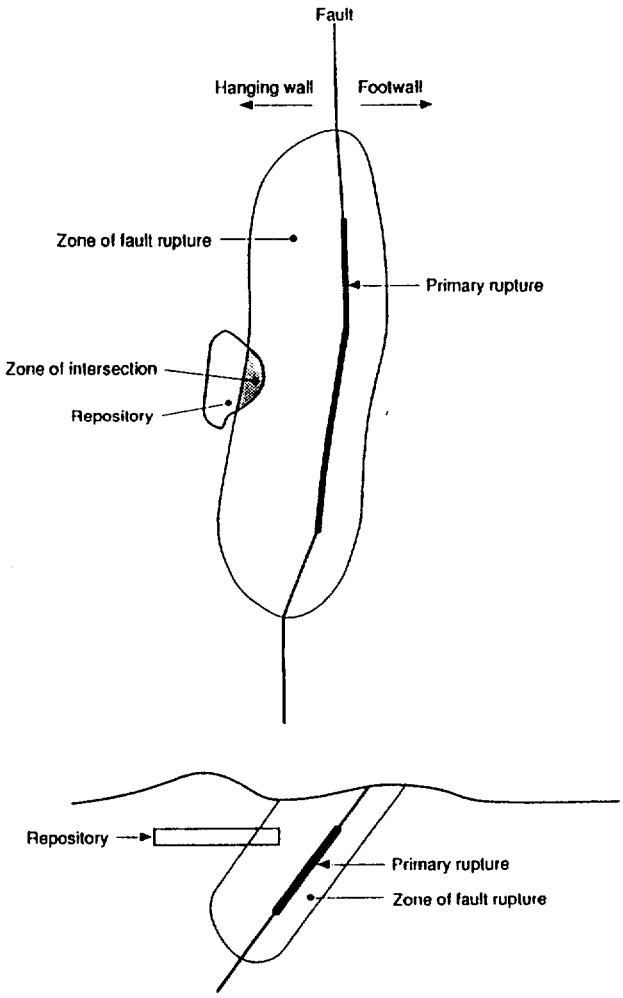

Figure A-4. Illustration of simulation of a zone of faulting for a single event occurring on a fault near the repository. Shaded area represents the area of intersection of the rupture zone with the repository footprint.

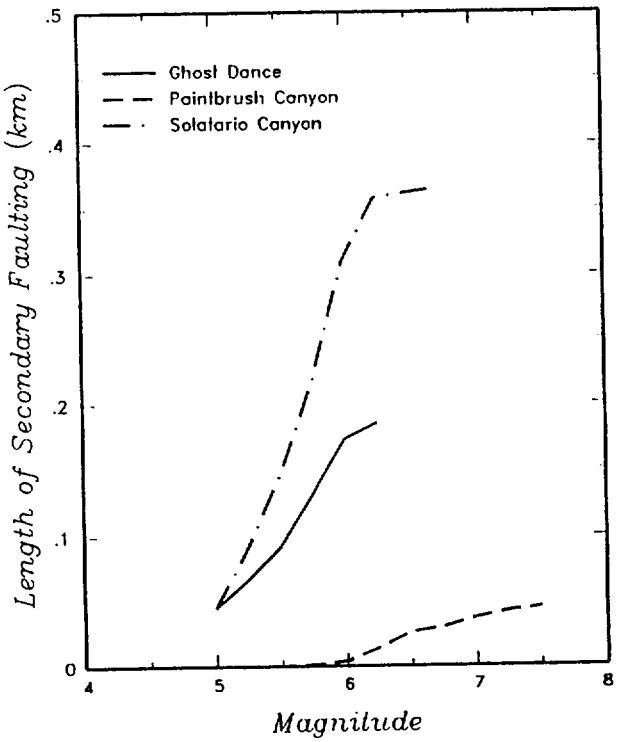

Figure A-5. Typical computed relationships between earthquake magnitude and the expected length of secondary faulting within the repository.

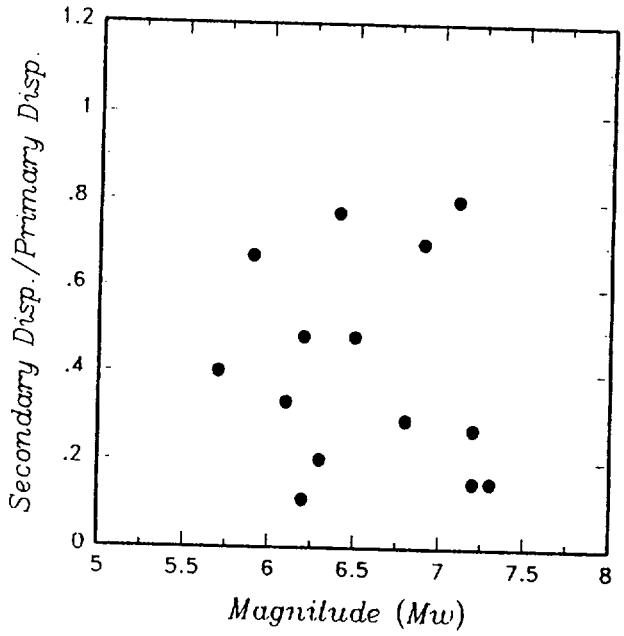

Figure A-6. Ratio of secondary faulting displacement to primary faulting displacement for various magnitude earthquakes. Data is from Table A-1.

REFERENCES

1. M. G. Bonilla. "Surface Faulting and Related Effects. In *Earthquake Engineering*. R. L. Wiegal (ed.). Englewood Cliffs, NJ: Prentice-Hall, Inc., 1974, pp. 47-74.

2. C. W. Jennings. *Fault map of California with Locations of Volcanoes, Thermal Springs, and Thermal Wells*. California Division of Mines and Geology, Geologic Data Map No. 1, scale 1:750,000, 1975.

3. W. B. Bull and P. A. Pearthree. "Frequency and Size of Late Quaternary Surface Ruptures of the Pitaycachi Fault, Northeast Sonora, Mexico." *Bulletin of the Seismological Society of America*, vol. 78, 1988, pp. 956-978.

4. S. G. Natali and M. L. Sbar. "Seismicity in the Epicentral Region of the 1887 Northeast Sonora Earthquake, Mexico. *Bulletin of the Seismological Society of America*, vol. 72, 1982, p. 181-196.

5. R. E. Wallace. *Faulting Related to the 1915 Earthquakes in Pleasant Valley, Nevada. U.S.*

Geological Survey Professional Paper 1274-A, 1984, 33 pp.

6. J. S. Tchalenko and M. Berberian. "The Salmas (Iran) Earthquake of May 6th, 1930." *Annali di Geofisica*, vol. 27, no. 1-2, 1974, pp. 151-212.

7. D. I. Doser. *The Character of Faulting Processes of Earthquakes in the Intermountain Region.* U.S. Geological Survey Open-File Report 89-315, 1989, pp. 163-180.

8. F. Neumann. *United States Earthquakes, 1934: Coast and Geodetic Survey.* Washington DC: U.S. Department of Commerce, 1936, pp. 13-14, 43-48.

9. O. Bellier, J. F. Dumont, Sébrier and J. L. Mercier. "Geological Constraints on the Kinematics and Fault-plane Solution for the Quiches Fault Zone Reactivated During the 10 November 1946 Ancash Earthquake, Northern Peru." *Bulletin of the Seismological Society of America*, vol. 81, 1991, no. 2, pp. 468-490.

10. F. E. Silgado. "The Ancash, Peru, Earthquake of November 10, 1946." *Bulletin of the Seismological Society of America*, vol. 41, no. 2, 1951, pp. 83-100.

11. V. P. Gianella. "Earthquake and Faulting, Fort Sage Mountains, California, December, 1950." *Bulletin of the Seismological Society of America*, vol. 47, 1957, pp. 173-177

12. D. Tocher. "Movement on the Rainbow Mountain Fault." *Bulletin of the Seismological Society of America*, vol. 46, 1956, pp. 10-14.

13. D. B. Slemmons. "Geological Effects of the Dixie Valley-Fairview Peak, Nevada, Earthquake of December 16, 1954." *Bulletin of the Seismological Society of America*, vol. 47, 1957, pp. 353-375.

14. W. F. Myers and W. Hamilton, W. *Deformation Accompanying the Hebgen Lake Earthquake of August 17, 1959.* U.S. Geological Survey Professional Paper 435, 1964, pp. 37-98.

15. I.J. Witkind. *Reactivated Faults North of Hebgen Lake.* U.S. Geological Survey Professional Paper 435-G, 1964, pp. 37-50.

16. N.N. Ambraseys and J. S. Tchalenko. "Seismotectonic Aspects of the Gediz, Turkey, Earthquake of March 1970. *Geophysical Journal of the Royal Astronomical Society of London*, vol. 30, 1972, pp. 229-252.

17. H. Eyidogan and J. Jackson. "A Seismological Study of Normal Faulting in the Demirci, Alasehir and Gediz Earthquakes of 1969-70 in Western Turkey--Implications for the Nature and Geometry of Deformation in the Continental Crust. *Geophysical Journal of the Royal Astronomical Society of London*, vol. 81, 1985, pp. 569-607.

18. M. Taşdemiroglu. "The 1970 Gediz Earthquake in Western Anatolia, Turkey. *Bulletin of the Seismological Society of America*, vol. 61, no. 6, 1971, pp. 1507-1527.

19. M. M. Clark, R. V. Sharp, R. O. Castle and P. W. Harsh. "Surface Faulting Near Lake Oroville, California in August, 1975." *Bulletin of the Seismological Society of America*, vol. 66, 1976, pp. 1101-1110.

20. J. A. Jackson, J. Gagnepain, G. Houseman, G. C. P. King, P. Papadimitriou, C. Soufleris, and J. Virieux. "Seismicity, Normal Faulting, and the Geomorphological Development of the Gulf of Corinth (Greece): The Corinth Earthquakes of February and March 1981." *Earth and Planetary Science Letters*, vol. 57, 1982, pp. 377-397.

21. G. Plafker, R. Agar, A. H. Asker and M. Hanif. "Surface Effects and Tectonic Setting of the 13 December 1982 North Yemen Earthquake." *Bulletin of the Seismological Society of America*, vol. 77, no. 6, 1987, pp. 2018-2037.

22. A. J. Crone, M. N. Machette, M. G. Bonilla, J. J. Lienkaemper, K. L. Pierce, W. E. Scott, and R. C. Bucknam. "Surface Faulting Accompanying the Borah Peak Earthquake and Segmentation of the Lost River Fault, Central Idaho." *Bulletin of the Seismological Society of America*, vol. 77, 1987, pp. 739-770.

23. C. A. Langer, G. A. Bollinger and J. M. Merghelani. "Aftershocks of the 13 December 1982 North Yemen Earthquake--Conjugate Normal Faulting in an Extensional Setting." *Bulletin of the Seismological Society of America*, vol. 77, 1987, no. 6, pp. 2038-2055.

24. H. Lyon-Caen and others. "The 1986 Kalamata (South Peloponnesus) Earthquake--Detailed Study of a Normal Fault, Evidences for East-West Extension in the Hellenic Arc." *Journal of Geophysical Research*, vol. 93, no. B12, 1988, pp. 14,967-15,000.

25. B. Papazachos, A. Kiratzi, B. Karacostas, D. Panagiotopoulos, E. Scordilis and D. M. Mountrakis. "Surface Fault Traces, Fault Plane Solution and Spatial Distribution of the Aftershocks of the September 13, 1986, Earthquake of Kalamata (Southern Greece)." *Pure and Applied Geophysics*, vol. 126, no. 1, 1988, pp. 55-68.

26. S. Beanland, K. R. Berryman and G. H. Blick, G. H. "Geological Investigations of the 1987 Edgecumbe Earthquake, New Zealand." *New Zealand Journal of Geology and Geophysics*, vol. 32, 1989, pp. 73-91.

27. D. Wells and K. J. Coppersmith. "New Earthquake Magnitude and Fault Rupture Parameters: Part I Surface Rupture Length and Rupture Area Relationships." (Abs.). *Seismological Research Letters*, vol. 60, n. 1, p. 27, paper submitted to *Journal of Geophysical Research.*

EPRI—*Leadership in Science and Technology*

ABOUT EPRI

The mission of the Electric Power Research Institute is to discover, develop, and deliver advances in science and technology for the benefit of member utilities, their customers, and society.

Funded through annual membership dues from some 700 member utilities, EPRI's work covers a wide range of technologies related to the generation, delivery, and use of electricity, with special attention paid to cost-effectiveness and environmental concerns.

At EPRI's headquarters in Palo Alto, California, more than 350 scientists and engineers manage some 1600 ongoing projects throughout the world. Benefits accrue in the form of products, services, and information for direct application by the electric utility industry and its customers.

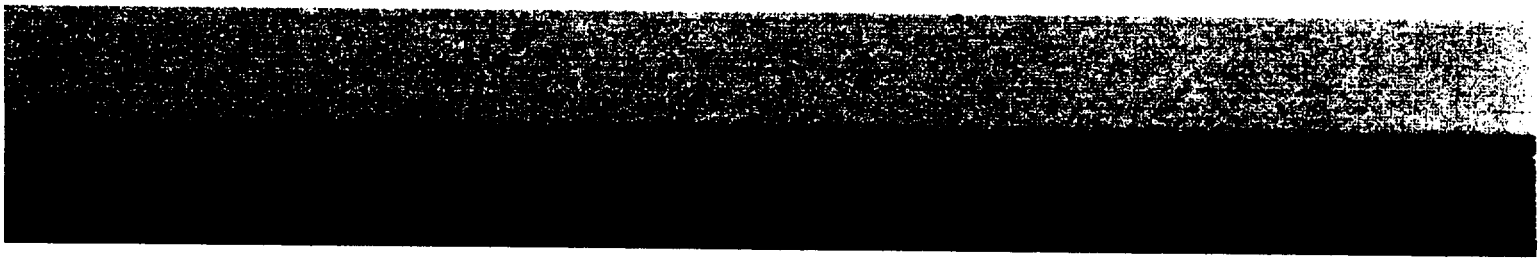

Printed on Recycled Paper
Printed in USA